Properties and evolution of dense structures in the interstellar medium

Anna Parikka

UNIVERSITÉ PARIS-SUD XI

ÉCOLE DOCTORALE 127
ASTRONOMIE ET ASTROPHYSIQUE D'ÎLE-DE-FRANCE

DOCTORAT : SCIENCE DE L'UNIVERS

ANNA PARIKKA

PROPERTIES AND EVOLUTION OF DENSE STRUCTURES IN THE INTERSTELLAR MEDIUM

DEFENDED SEPTEMBER 28TH 2015

THÈSE DIRIGÉ PAR:
ALAIN ABERGEL
EMILIE HABART
JERONIMO BERNARD-SALAS

JURY:
ANNIE ZAVAGNO (RAPPORTRICE)
JÉRÔME PETY (RAPPORTEUR)
JAQUES LE BOURLOT (EXAMINATEUR)
JAVIER GOICOECHEA (EXAMINATEUR)
VOLKER OSSENKOPF (EXAMINATEUR)
ALAIN ABERGEL (DIRECTEUR DE THÈSE)
EMILIE HABART (CO-DIRECTRICE DE THÈSE)
JERONIMO BERNARD-SALAS (CO-DIRECTEUR DE THÈSE)

In loving memory of Hillevi Kajavaara,
who lived long and prospered.

1924 – 2007

Keep your eyes on the stars,
and your feet on the ground.

— Theodore Roosevelt

ACKNOWLEDGMENTS

I want to thank my supervisors, Emilie Habart, Jeronimo Bernard-Salas, and Alain Abergel for all their work and advice. Especially I want to thank Jeronimo, who was always encouraging and a joy to work with. Thanks also to Melanie Köhler for answering all my questions in the beginning and, Nathalie Ysard for all the help when I came to France. In addition, I want to thank Mika Juvela, my Master's thesis advisor, who worked with me on the paper on cold clumps, for all his patience and advice. I also had support, especially in the late stages of my thesis, from the école doctorale. Especially, I want to mention Jaques Le Bourlot, Jacqueline Plancy, and Guillaume Pineau des Forêts, who gave me practical support. In IAS, I want to thank Rosario Brunetto, Matthieu Langer, and Nicole Nesvadba whose doors were always open.

I want to thank my jury, especially the "rapporteurs", Annie Zavagno and Jérôme Pety, but also Jaques Le Bourlot, Javier Goicoechea, and Volker Ossenkopf. I would like to thank Javier for all the comments and help with my CH^+ and OH paper, and Volker for the many interesting discussions in conferences. I also want to thank Benjamin Godard for his help with the CH^+ excitation. Other collaborators and friends that I want to mention are Zsofia Nagy, Silvia Vicente, and Olivier Berné. Thank you for your friendship and collaboration.

I want thank my friends in IAS, especially Lisseth and Elisabetta, who always made me feel better no matter what and offered many moments of peer support. Also, thank you, Marian, for introducing me to your wife. I also want to thank the other PhD students and postdocs in IAS. Especially I want to thank Agnès for the coffee breaks in French, and Cinthya and Raul for sharing the office with me. Outside IAS, Charlène was there when things were tough and Emeric, who took me climbing. Thank you for your friendship.

I want to thank all my friends outside of work: Anni, for all our discussions in Finnish, Aleksi, for being a friend and also introducing me to all his friends, and Helen, for all the Jane Austen geekiness and overall support. And in Finland: Laura, Riikka, and Jossu you have been there for me so many times. And everyone else, even though I don't mention you here, I do appreciate all the support and your friendship.

And last but not least, I want to thank my family: my parents, Aira and Erkki, and my sisters, including Iiris, for all the support through the years. Without you I wouldn't be here. Also, my grandparents, who I wish could have seen me, for all their love and encouragement. And especially my grandmother who taught me to be a geek.

ABSTRACT

In this thesis I present a study of two kinds of dense ISM structures: compact cold sources detected by Planck and dense condensations in a photodissociation region (PDR), namely the Orion Bar detected by ground-based and Herschel telescopes. Both kinds of structures are closely related to star formation. The cold sources are investigated as potentially gravitationally bound, prestellar, objects. The Orion Bar is a highly FUV-illuminated (G_0 ~10^4) prototypical PDR, with several known protoplanetary disks, illuminated by the young Trapezium stars.

First I introduce a paper published in A&A: *The Physical state of selected cold clumps*. In this paper we compared the Herschel dust continuum observations from the open time key program *Galactic Cold Cores* to ground based molecular line observations from the 20-m radio telescope of the Onsala Space Observatory in Sweden. The clumps were selected based on their brightness and low dust color temperatures (T~10−15 K). We calculated the virial and Bonnor-Ebert masses and compared them to the masses calculated from the observations. The results indicate that most of the observed cold clumps are not necessarily prestellar.

In my study of the Orion Bar, I use observations from PACS instrument onboard *Herschel* from the open time program *Unveiling the origin and excitation mechanisms of the warm CO, OH and CH^+*. I present maps of $110'' \times 110''$ of the methylidyne cation (CH^+ J=3-2), OH doublets at 84 μm, and high-J CO (J=19-18). This is the first time that these PDR tracers are presented in such a high spatial resolution and high signal-to-noise ratio.

The spatial distribution of CH^+ and OH shows the same clumpy structure of the Bar that has been seen in other observations. The morphology of CH^+ and H_2 confirms that CH^+ formation and excitation is strongly dependent on the vibrationally excited H_2, while OH is not. The peak in the OH 84 μm emission corresponds to a bright young object, identified as the externally illuminated protoplanetary disk 244-440.

I introduce mid-J (~20 K), and high-J (~1000 K) CO observations of the area. The high-J CO morphology shows a clumpy structure in the Bar and we establish a link between the dense core of the clumps, traced in CS J=2-1 by Lee et al. (2013) and in $H^{13}CN$ by Lis and Schilke (2003). We also show that the high-J CO is mainly excited by the UV heating.

RÉSUMÉ

Mon travail de thèse présente deux types de structures denses : des sources froides compactes détectées par Planck et des condensations denses dans une région de photodissociation (PDR), à savoir la Barre d'Orion. Les deux types de structures sont étroitement liées à la formation des étoiles. Les sources froides sont étudiées comme objets potentiellement gravitationnellement liés, c'est-à-dire comme objets préstellaires. La Barre d'Orion est intéressante en tant que PDR à fort champ UV (G_0 ~10^4) prototypique, avec plusieurs disques protoplanétaires connus, éclairés par les jeunes étoiles du Trapèze.

D'abord, je présente un article publié dans A&A: *The Physical state of selected cold clumps*. Dans cet article, nous avons comparé les observations du continuum de la poussière par Herschel provenant de l'open time key program *Galactic Cold Cores* (Herschel) aux observations de raies moléculaires par le radiotélescope de 20-m de l'Onsala Space Observatory en Suède. Les objets ont été sélectionnés en fonction de leur luminosités et faibles températures de couleur des poussières (T~10−15 K). Nous avons calculé les masses du viriel et de Bonnor-Ebert et les avons comparées aux masses déduites Ã partir des observations. Les résultats indiquent que la plupart des objets froids observés ne sont pas nécessairement préstellaires.

Dans mon étude de la Barre d'Orion, j'utilise des observations de l'instrument PACS d'Herschel du programme *Unveiling the origin and excitation mechanisms of the warm CO, OH and CH^+*. Je présente des cartes de $110'' \times 110''$ du cation méthylidyne (CH^+ J=3-2), des doublets de OH à 84 μm, et des raies de CO á hauts J (J=19-18). C'est la première fois que ces traceurs des PDR sont présentés avec une telle résolution spatiale et un tel rapport signal-sur-bruit.

La répartition spatiale de CH^+ et OH montre la même structure de la Barre qui a été vue dans d'autres observations. La morphologie du CH^+ et H_2 confirme que la formation et l'excitation de CH^+ est fortement dépendante du H_2 excité vibrationnellement. Le maximum d'émission de OH 84 μm correspond à un objet brillant jeune, identifié comme le disque protoplanetaire 244-440.

Je présente également des transitions rotationnelles de CO de moyenne (~20 K) et haute (~1000 K) énergie. La morphologie de l'émission du CO rotationnellement excité est corrélée avec la présence des petites structures denses irradiées. Nous établissons le lien entre le coeur de ces structures, tracé en CS J=2-1 par Lee et al. (2013) et $H^{13}CN$ par Lis and Schilke (2003) et le bord de la PDR, tracé en CO J=19-18 et le H_2 vibrationnellement excitée. Nous montrons également que le CO est principalement excité par le chauffage UV.

CONTENTS

Part I

INTRODUCTION

1

WHERE AND HOW DO STARS FORM?

1.1 STAR FORMATION IN THE ISM

Star formation takes place in the interstellar medium (ISM), which consists of gas and dust. It is a process that includes a complex mixture of gravity, turbulence, rotation, radiation, thermodynamics, and magnetic fields. The relative importance of these factors depend on the initial conditions in molecular clouds, and in dense cores which will eventually evolve into stars. Advances in our understanding of the star formation process has improved in the past decade as telescopes and equipment have improved the resolution and sensitivity of observations. While the general process of especially low- and intermediate star formation is known, we are still missing many details, e.g., how the gas assembles into dense cores, what sets the star formation rate and the mass of stars, how do substellar objects form, and why star formation is so inefficient in the ISM.

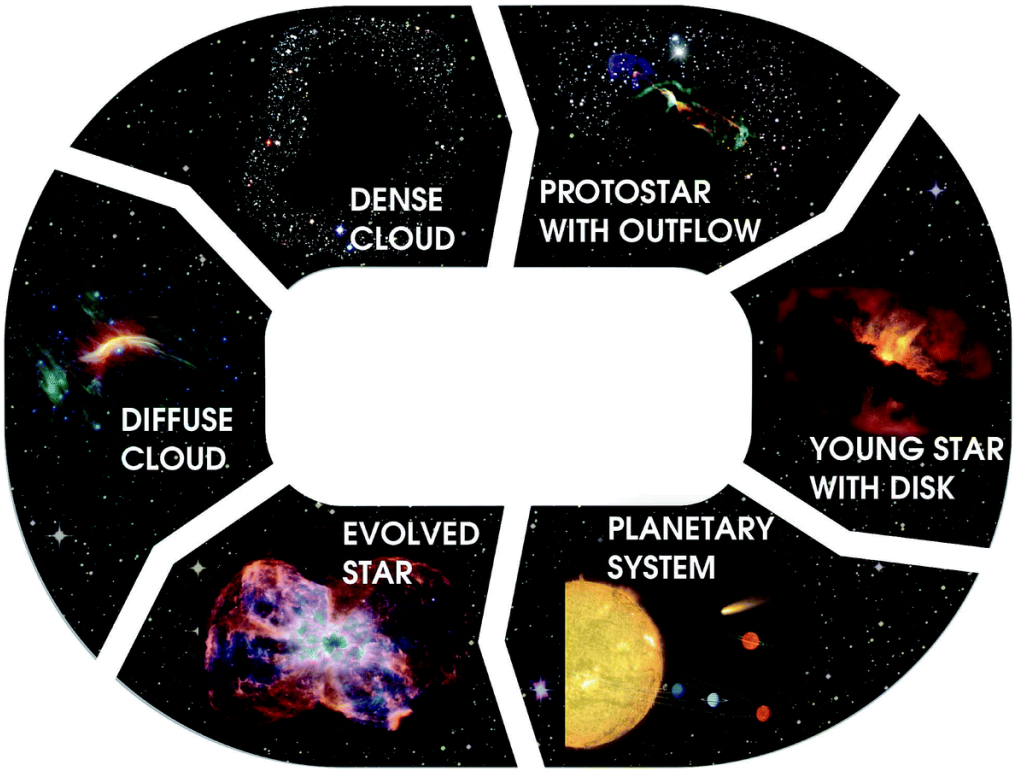

Figure 1.1: The lifecycle of gas, dust and ice in interstellar and circumstellar clouds. Credit: M. Persson, NASA/ESA/ESO/ALMA

Figure 1.1 shows the life cycle of galactic matter in the ISM. Much of the volume of ISM is low density clouds (n_H ~100 cm^{-3}) of diffuse ISM. However, the mass of the ISM is concentrated on dense clouds. Dense clouds can

stay in a stable state for a long time due to turbulence and magnetic fields, but finally with time (~1 Myr) the gravity will make the protostar collapse into a new star. The new star will have circumstellar disks around it, which will continue to evolve into planets and to form a planetary system. At this time the star has entered the stable main-sequence phase. At the end of their life the nuclear fuel of the star is exhausted. This causes the stars become larger while loosing part of their mass. Their radiation and the lost mass causes the surrounding environment to become warm and dense. This environment is favorable for the formation of molecules and the condensation of dust grains. At the final stage the star will produce a planetary nebula with a hot central star ionizing the previously ejected layers. Massive stars have a shorter life cycle and they will explode as supernovae and become black holes or neutron stars (e.g., Snow and McCall, 2006; van Dishoeck, 2014).

The efficiency of star formation in molecular clouds is not very high; only about 10–25 % of the gas in the dense clouds will end up in stars. Star formation is most efficient in the filaments that form the dense clouds. The filamentary distribution of gas is something that remains throughout the process of star formation (e.g., Leisawitz et al., 1989; Hartmann, 2002; Tachihara et al., 2002). The study of the star formation process involves the study of evolution from dense clouds to young stars. In my thesis, I concentrate on the early stages of star formation and the dense condensations (clumps and cores) in the dense clouds.

1.2 LOW VS. HIGH MASS STAR FORMATION

Many studies have been dedicated into the study of low star formation. Shu et al. (1987) detailed four stages of low-mass star formation as:

1. Fragmentation of the clouds and formation of slowly rotating cloud cores
2. Gravitational contraction as core passes the instability threshold and collapses dynamically from inside-out
3. The bipolar outflow phase, where the matter is accreted to the disk instead of the star, and stellar wind causes collimated jets and bipolar outflows
4. T Tauri star with a surrounding remnant nebular disk

A fifth stage can also be defined as the final disappearance of the nebular disk. In this stage the matter becomes incorporated into planets or stellar companions or is dispersed by the energetic outflow. While the general process of star formation is known, there are still questions about the specific underlying conditions that trigger the first stages of star formation and the role of turbulence, magnetic fields, clustering, and feedback is still unclear.

The formation of massive stars ($M>10\ M_{\odot}$) is not as well understood. It can be a scaled-up version of low-mass star formation, but only up to early

B stars. The massive star formation and further evolution is most likely to occur as follows, starting with a pre-existing giant molecular cloud (Zinnecker and Yorke, 2007):

1. Formation of cold dense filaments and cores
2. Nonhomologous[1] gravitational collapse of the cores into protostellar cores supported by pressure
3. Accretion of matter onto protostellar objects and their evolution towards the main sequence
4. Evolution of the star to become a supernova influenced by the winds, outflows, and UV radiation of the first high-mass stars

In the first stage, the UV radiation and stellar winds exert pressure on the accretion flow of massive stars. The second stage differs from the low-mass star formation stage of the dynamical inside-out collapse. Also in the accretion phase, the accretion for low-mass objects stops before the start of hydrogen burning, unlike with massive stars. And, of course, the low-mass stars do not evolve to supernovae. Other differences between low- and high-mass star formation include physical properties of clouds where they are formed. Massive star formation happens mainly in clouds that are warmer, larger, more massive, mainly located in spiral arms, and in clusters and associations while low-mass stars form mainly in cooler clouds throughout the Galactic disk as well as GMCs, and not necessarily in clusters. However, they can also coexist in the same region, like in the Orion cluster.

Massive stars are not as common as low-mass stars. They also evolve fast and are frequently obscured by or situated in dense clusters. Thus, studies of large populations are challenging, and only lately there are telescopes with high enough angular resolution to resolve these dense clusters. There is also the question of building up sufficient mass against the radiation pressure. Currently there are two competing models to explain this: monolithic collapse and competitive accretion. Monolithic collapse predicts massive stars to form relatively isolated but also in clusters. This is a scaled-up version of low-mass star formation. Competitive accretion predicts massive stars to form exclusively in dense cores or clusters of molecular clouds and expects a high-density environment for massive star formation.

The nearest place to us where massive star formation takes place is the Orion Nebula depicted in Fig. 1.2. In my thesis I will consider the effects of the UV radiation from the young massive stars (Trapezium) and their effect on their surroundings (see Chapters 7 and 8). The study on cold clumps (in Chapter 6) focuses on the early conditions of the low-mass star formation.

1.3 STAR FORMATION STUDIES WITH HERSCHEL AND BEYOND

Herschel Space Observatory was planned to observe the cool universe. Its key science objectives emphasized the formation of stars and galaxies. From

1 In this context, nonhomologous is used to indicate that the distribution of mass changes, as opposed to a homologous or self-similar collapse.

Figure 1.2: Orion Nebula (HST). Credit: NASA,ESA, M. Robberto (Space Telescope Science Institute/ESA) and the Hubble Space Telescope Orion Treasury Project Team

the 21 guaranteed time key programs 10 focused on the ISM and/or star formation and the numbers are the same for open time key programs (see list of ISM and/or star formation key programs in Appendix A). In addition there are key programs on the extragalactic star formation and numerous non-key programs that address star formation and ISM.

Herschel observations have confirmed the filamentary structure of the cold ISM and given new information on the connection of filaments to star formation (e.g., André et al., 2010; Men'shchikov et al., 2010; Molinari et al., 2010). Filaments are present everywhere, even in diffuse gas and, thus, precede the actual star formation (Miville-Deschênes et al., 2010; Ward-Thompson et al., 2010). They form networks and have also sub-filaments (Peretto et al., 2012; Palmeirim et al., 2013, e.g.,). Filaments have also been shown to be velocity coherent structures (e.g., Hacar and Tafalla, 2011; Arzoumanian et al., 2013). These structures are shown in all Herschel images of star forming regions, like the image of W3 in Fig. 1.3.

In addition to filaments, the properties of dense cores where the star formation takes place has been the subject of many programs with *Herschel*.

Figure 1.3: Star forming region W3 in the constellation of Cassiopeia. The figure combines Herschel bands at 70 µm (blue), 160 µm (green) and 250 µm (red). Credit: ESA/PACS & SPIRE consortia, A. Rivera-Ingraham & P.G. Martin, Univ. Toronto, HOBYS Key Program (F. Motte)

Both the Gould Belt Survey (André et al., 2010) and the Galactic Cold Cores survey (Juvela et al., 2010) studied these cores. With the *getsources* method of Men'shchikov et al. (2010), many dense condensations have been identified in both surveys and I will take a closer look at part of the condensations from the Galactic Cold Cores survey in Chapter 6. These condensations are classed as starless, prestellar, or protostellar cores[2] depending on their self-gravitation potential and existence of a protostellar source. *Herschel* studies have also found a close relation between the initial mass function (IMF) and core mass function (CMF) suggesting a close link between cloud properties and star formation (e.g. Motte et al., 1998; André et al., 2010; Könyves et al., 2010).

Herschel observations of the ISM have detected a rich chemistry, including CO (e.g., Chapter 8 and Köhler et al., 2014) water (van Dishoeck et al., 2011), and CH^+ and OH (e.g., Chapter 7 and Goicoechea et al., 2011; Godard et al., 2012). While *Herschel* is no longer in operation, there are still new studies published with the existing data bringing us more information

2 See Chapter 2.2.2 for definitions.

on the physical and chemical processes in the ISM and especially in star forming regions. There are also several studies that focus on the later stages of star formation like the DIGIT program on protoplanetary disks (Sturm et al., 2010).

After *Herschel*, the research goes on. Stratospheric Observatory for Infrared Astronomy (SOFIA) is the largest airborne observatory in the world. It covers wavelengths of 0.3−1600 μm at an altitude of 12−14 km reducing the effect of the atmosphere on observations. Specific advantage to *Herschel*/PACS follow-up studies is the GREAT instrument which operates at similar wavelengths (60−240 μm) to PACS (55−210 μm), but with a higher velocity resolution (0.03 km s^{-1}, Pérez-Beaupuits et al., 2012). Several studies have already observed CO lines in different environments (e.g., Requena-Torres et al., 2012; Okada et al., 2015; Ossenkopf et al., 2015) and OH 119 μm doublet has been observed in ultracompact HII/OH maser regions (Csengeri et al., 2012). Thus, the 119 μm lines used in Chapter 7 and several mid-/high-J CO lines are already observable with SOFIA.

Another important telescope, where one of the main objectives is the study of star formation is the Atacama Large Millimeter/submillimeter Array (ALMA). ALMA has a high angular (0.7″ at 675 GHz to 4.8″ at 110 GHz in the most compact configuration) and velocity resolution (highest resolution at 110 GHz is 0.01 km s^{-1}). ALMA has been used to study the chemistry in the ISM, especially the chemistry related to deuterated molecules and complex organic molecules (e.g., Belloche et al., 2014; Öberg et al., 2015; Sakai et al., 2015) and there is also evidence of disks surrounding a number of high mass protostars (e.g., Sánchez-Monge et al., 2013; ALMA Partnership et al., 2015; Zapata et al., 2015). In addition, there are studies on dense structures, like hot cores, massive starless cores, and filamentary fragmentation in the process of star formation, as well as CO freezeout in the densest parts of the ISM (Lee et al., 2012; Tan et al., 2013; Mathews et al., 2013; Sakai et al., 2013, 2015)

In addition to ALMA, NOrthern Extended Millimeter Array (NOEMA), located in the French Alps, consists of seven 15-m antennas. When the construction is finished NOEMA will have 12 antennas. The new improved resolution of four times higher than its predecessor, Plateau du Bure observatory, and ten times better sensitivity will make NOEMA the most advanced millimeter radio astronomy observatory in the Northern Hemisphere. At the current state the resolution is 0.5″ at wavelength of 1.3 mm (230 GHz).

These and other ground based telescopes in use provide a combination of angular resolution, spectral coverage, sensitivity, and spectroscopic and imaging capabilities to further the understanding of the star formation processes. For the next decade, we will also have the James Webb Space Telescope (JWST) and most likely SPICA, which is a project proposed by ESA. Although often talked as a replacement for Hubble, JWST is not identical and will continue the work in infrared instead of optical wavelengths. Infrared and sub-mm wavelengths include most of the dust and gas emission in the ISM. SPICA will operate in the same wavelengths as *Herschel*, but with an improved sensitivity allowing observations of fainter regions than

Herschel. Thus, JWST and SPICA will also be ideal for star formation studies along the other telescopes already in use.

1.4 AIMS OF THE THESIS

Dalgarno (2008) states that astrochemistry, or molecular astrophysics, studies *'the formation, destruction, and excitation of molecules in astronomical environments and their influence on the structure, dynamics, and evolution of astronomical objects'*. This is a good definition of the subject as it includes the molecules as tools to probing the physical conditions and processes of the regions. Van Dishoeck (2014) states the main questions in astrochemistry as:

1. How, when, and where molecules are produced and excited?
2. How far does the chemical complexity go?
3. How are the molecules cycled through the various phases of stellar evolution, from birth to death?
4. Can the molecules become part of new planetary systems and form the building blocks for life elsewhere in the Universe?

In this thesis I will concentrate mainly on the microphysics and the initial conditions of the star formation (questions 1. and 2.), and thus, on the astrochemistry or physical and chemical conditions of the dense structures in the ISM. In Chapter 2 I will introduce the dense structures of the ISM in different gas phases. I will take a closer look on what is known about the cold clumps and cores, photodissociation regions (PDRs), and protoplanetary disks. In chapter 3 I will introduce the molecular tracers used in this thesis and the RADEX model used for analysis in Chapter 8.

In Chapters 4 and 5 I introduce the telescopes used in this thesis and the observations made on them. I will look at the physical properties and self-gravitation of cold clumps in Chapter 6. I will also investigate the influence of UV radiation on the structure, chemistry and thermal balance of the clouds, or more specifically PDRs, and the nature, properties and evolution of irradiated dense structures inside PDRs in Chapters 7 and 8.

2 DENSE STRUCTURES IN THE ISM

In this chapter I introduce the structure of the gas in the ISM, focusing on the dense structures important to star formation. In Sect. 2.1 I discuss the gas in general and in Sect. 2.2 I discuss the molecular clouds, clumps, and cores. Distinction between clumps and cores is especially important for Chapter 6. In Sect. 2.3 I introduce the photodissociation regions and the Orion Bar in particular, which is the target of the observations of Chapters 7 and 8. Finally, Sect. 2.4 focuses on externally illuminated protoplanetary disks, since we can see one of the known proplyds in the Orion Bar in our map of OH 84 μm emission. The last two sections introduce the context for Chapters 7 and 8.

2.1 GAS PHASES OF THE ISM

The ISM consists of baryonic matter, electromagnetic radiation, gravitational field, and magnetic field. In the ISM, ~99 % of the mass is gas: 70 % of the matter is hydrogen, 28 % helium, and 2 % heavier elements like oxygen, carbon, and nitrogen.

The ISM can be classified according to its temperature and density. Field et al. (1969) divided the ISM into the cold and warm neutral medium of the ISM. McKee and Ostriker (1977) expanded the model to include the hot and ionized gas. Currently, the gas in the ISM is divided into five phases (see reviews, e.g. Ferrière, 2001; Cox, 2005):

- *The molecular gas* consists mainly of H_2. It is cold and found mostly in the dense inner core part of the cloud. It is sometimes categorized as a sub-phase of cold neutral medium.
- *The cold neutral medium (CNM)* consists of cold, neutral, and mainly atomic gas. If the molecular gas is separated to its own phase, the CNM is less dense and warmer than the molecular gas.
- *The warm neutral medium (WNM)* surrounds small clouds and connects them to others forming cloud complexes. It is roughly in pressure equilibrium with CNM (Field et al., 1969). The WNM is characterized with low density and high temperature.
- *The warm ionized medium (WIM)* is ionized by stellar radiation from O and B stars. The transition from the ambient ISM to the WIM is abrupt due to the absorption of the ionizing UV photons by neutral hydrogen. The radiation forms an HII region that surrounds the stars.
- *The hot ionized medium (HIM)* is formed by supernova explosions and stellar winds. Hot gas forms only a small fraction of the interstellar mass due to its low density.

Table 2.1 summarizes the properties of the different gas phases, and Fig. 2.1 provides an example of how the phases relate to a small cloud.

Table 2.1: Phases of the ISM (Stahler and Palla, 2004). Listed in the table: total density [cm^{-3}], temperature [K], mass [$M_\odot$], and fraction of volume.

Phase	n_{tot} [cm^{-3}]	T [K]	M [10^9 $M_\odot$]	f
Molecular	> 300	10	2.0	0.01
Cold neutral (CNM)	50	80	3.0	0.04
Warm neutral (WNM)	0.5	8×10^3	4.0	0.30
Warm ionized (WIM)	0.3	8×10^3	1.0	0.15
Hot ionized (HIM)	3×10^{-3}	5×10^5	-	0.50

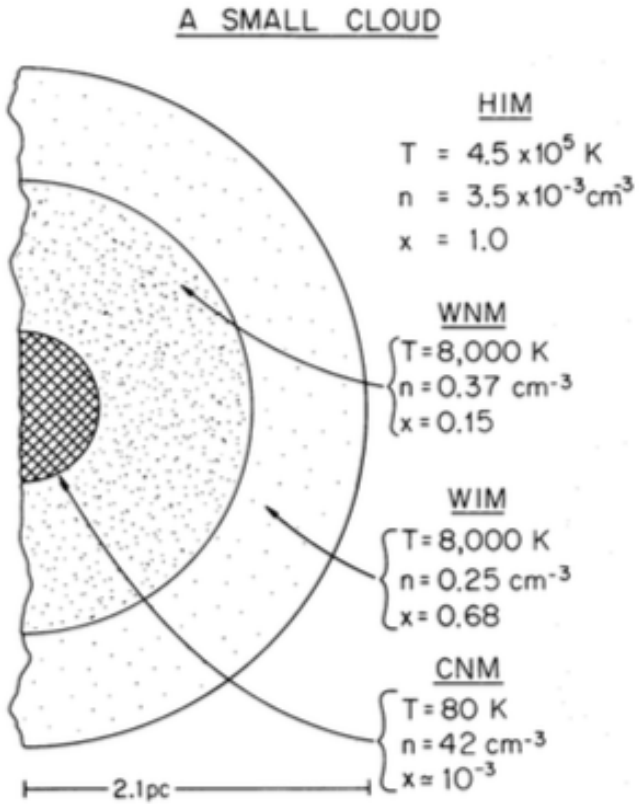

Figure 2.1: Cross section of a characteristic small cloud (McKee and Ostriker, 1977)

This thesis focuses on the dense structures in the ISM. I mainly focus on CNM including molecular gas as the densest phases of the ISM. Snow and McCall (2006) classified different types of molecular clouds that can be found in the CNM and molecular gas. This denser gas contains variety of physical and chemical conditions, and the properties listed in Table 2.1 cover only part of the picture. The four types of clouds or gas based on a

photodissociation region (PDR) model (with $n_H = 100$ cm^{-3} and $\chi_{UV} = 1$[1], see Fig. 2.2 and Table 2.2[2]):

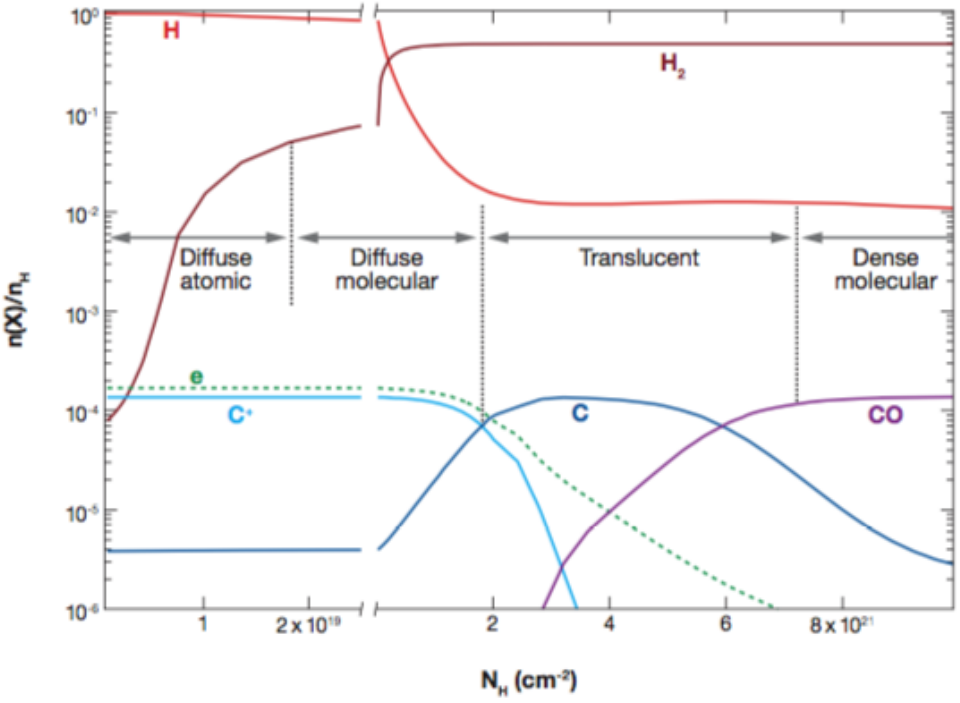

Figure 2.2: Definitions of cloud types (Snow and McCall, 2006)

Table 2.2: Classification of cloud types (Snow and McCall, 2006)

	Diffuse atomic	Diffuse molecular	Translucent	Dense molecular
Defining characteristic	$f^n_{H_2} < 0.1$	$f^n_{H_2} > 0.1$ $f^n_{C^+} > 0.5$	$f^n_{C^+} < 0.5$ $f^n_{CO} < 0.9$	$f^n_{CO} > 0.9$
A_V (min.)	0	~0.2	~1–2	~5–10
Typ. n_H [cm^{-3}]	10–100	100–500	500–5000(?)	$>10^4$
Typ. T [K]	30–100	30–100	15–50(?)	10–50

- *Diffuse atomic gas* is exposed to the interstellar radiation field. Thus, photodissociation destroys all molecules quickly. In diffuse atomic clouds hydrogen is mainly neutral and atomic. The atoms whose ionization potentials are less than that of hydrogen, are almost fully ionized. These clouds can be observed via optical and UV absorption, since there are many lines which are optically thin. Typical densi-

1 In this model a radiation field equals to the average interstellar value given by (Draine, 1978). The PDR model used in Neufeld et al. (2005), which was a modified version of the models of Kaufman et al. (1999), Wolfire et al. (1990), and Tielens and Hollenbach (1985a).

2 f^n_x are fractions of number densities: e.g., $f^n_{H_2} = 2n_{H_2}/n_H$ and $f^n_{CO} = n(CO)/n_C$

ties and temperatures for diffuse atomic gas are 10–100 cm^{-3} and 30–100 K, respectively.

- *Diffuse molecular gas* is affected by the interstellar radiation field, but it is attenuated enough by dust for the fraction of molecular hydrogen to become substantial (> 0.1). Carbon is still predominately C^+ due to photoionization of atomic carbon and photodissociation of CO. Diffuse molecular gas is always surrounded by diffuse atomic gas. This can be observed in UV, optical, IR, and mm wavelengths. Typical densities and temperatures for diffuse molecular gas are 100–500 cm^{-3} and 30–100 K, respectively.

- *Translucent gas* is protected from the interstellar radiation and the carbon is transitioned to neutral C or molecular CO form. The chemistry changes in comparison to the diffuse molecular clouds, when the electron fraction decreases and C atoms become highly abundant.

- *Dense molecular gas* has a higher extinction and carbon is mostly molecular (CO). Dense gas is likely to be surrounded by translucent gas and the low electron abundance changes the chemistry when cosmic ray ionization becomes the dominant source of ionization. Dense clouds are generally self-gravitating (see Section 2.2.1). They are mostly observed in IR absorption and mm emission. Typical densities and temperatures for dense molecular gas in quiescent regions are over 10^4 cm^{-3} and 10–50 K, respectively.

This is a simplified view of the cloud types. In reality clouds are most likely a mixture of these types as they are inhomogeneous. Also, one should keep in mind that the properties listed here are not line-on-sight properties.

2.2 MOLECULAR CLOUDS, FILAMENTS, CLUMPS, AND CORES

2.2.1 *Larson's relations and molecular clouds*

Larson (1981) identified some of the key features of giant molecular clouds which are often referred as Larson's laws or relations. These laws are: 1) molecular clouds obey a line-width - size relation, 2) they are gravitationally bound, and 3) they all have similar column densities. These relationships are not independent and any two imply the third. Larson's relations are purely empirical. Basically, they state how the masses, the radii, and the velocity dispersions of molecular clouds relate to each other.

Figure 2.3 illustrates the first law: velocity dispersion is dependent on the size of the cloud. The scale used is logarithmic and the figure gives the measured velocity dispersion as a function of cloud diameter. The correlation is clearly seen in figure 2.3 and the relation found from the fit is $\sigma \propto L^{0.38}$, where L is the region size in parsecs. The corresponding relation between velocity dispersion and mass can be seen in figure 2.4. For mass, the observed relation is $\sigma \propto M(M_\odot)^{0.20}$. These relations of velocity dispersions

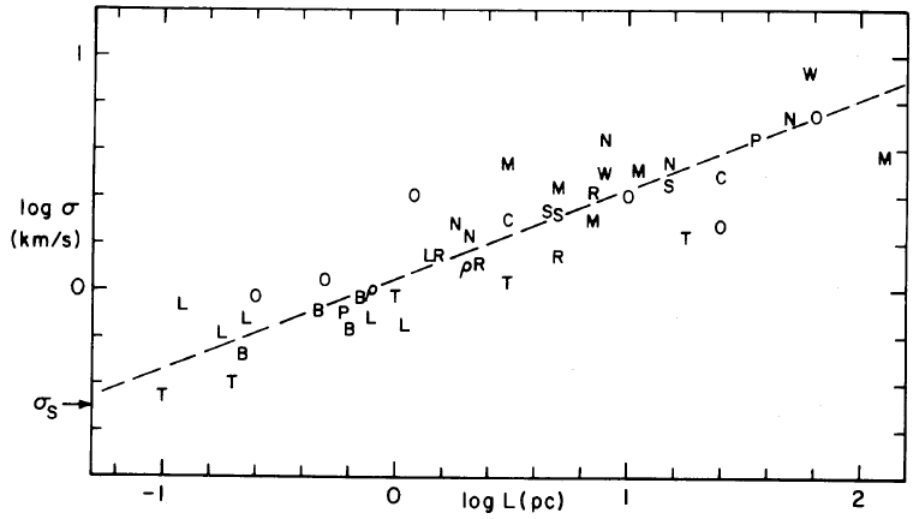

Figure 2.3: Velocity dispersion as a function of cloud diameter (Larson, 1981)

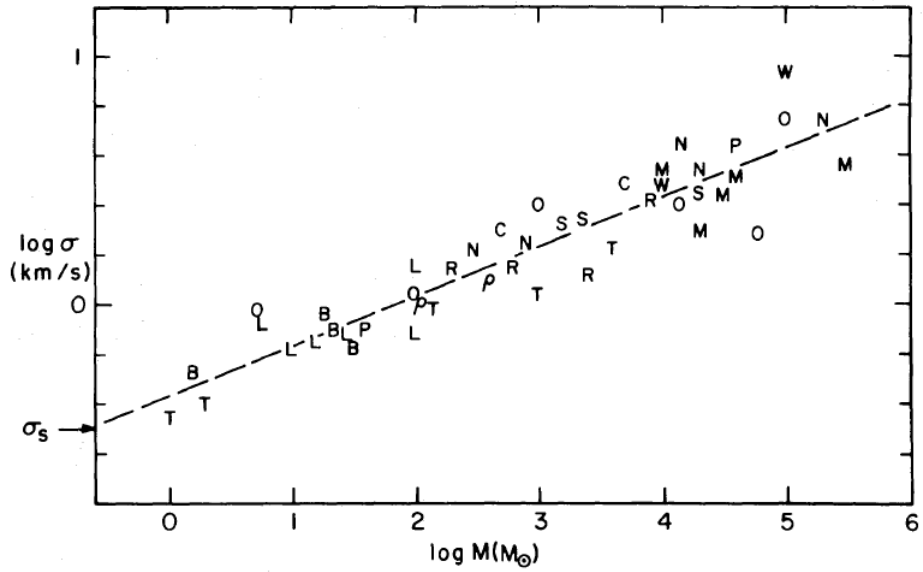

Figure 2.4: Velocity dispersion as a function of the cloud mass (Larson, 1981)

to size and mass hold for the whole cloud, but also for the subregions of an individual cloud or a cloud complex.

The second law states that the giant molecular clouds are gravitationally bound and approximately satisfy the virial theorem. However, along with gravity, turbulent hydrodynamics play an important role in the formation of substructures in molecular clouds. The relation between virial ratio and cloud diameter is given by:

$$\frac{2GM}{\sigma^2 L} \propto L^{0.14}. \tag{2.1}$$

This ratio is valid for a spherical cloud with a mass M, diameter L, and velocity dispersion σ. G is the gravitational constant 6.67384×10^{-11} m^3 kg^{-1} s^{-2}. This relation can be seen in figure 2.5.

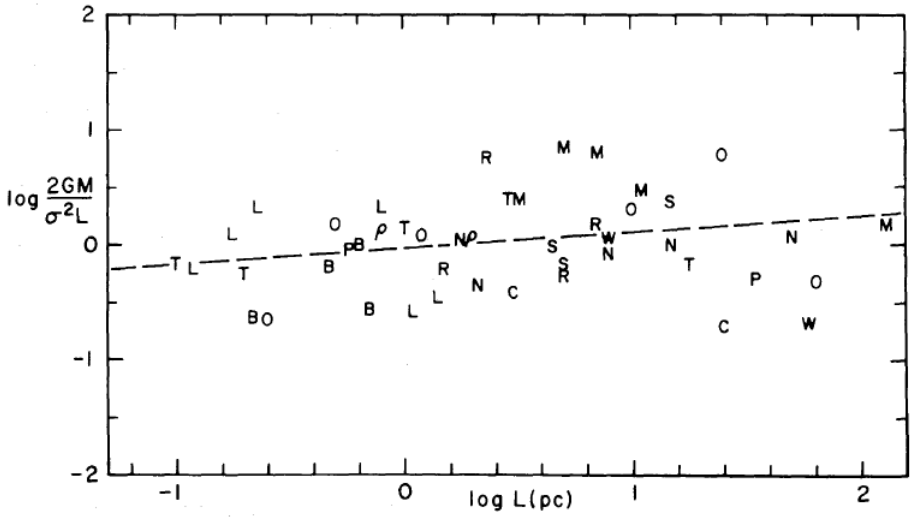

Figure 2.5: Virial ratio as a function of cloud diameter (Larson, 1981)

Finally, the third law states that all giant molecular clouds have similar column densities. The found relation between column density and size was

$$\langle n(H_2) \rangle (cm^{-3}) \propto L^{-1.10}. \tag{2.2}$$

For this relation the average density is calculated for a sphere with mass

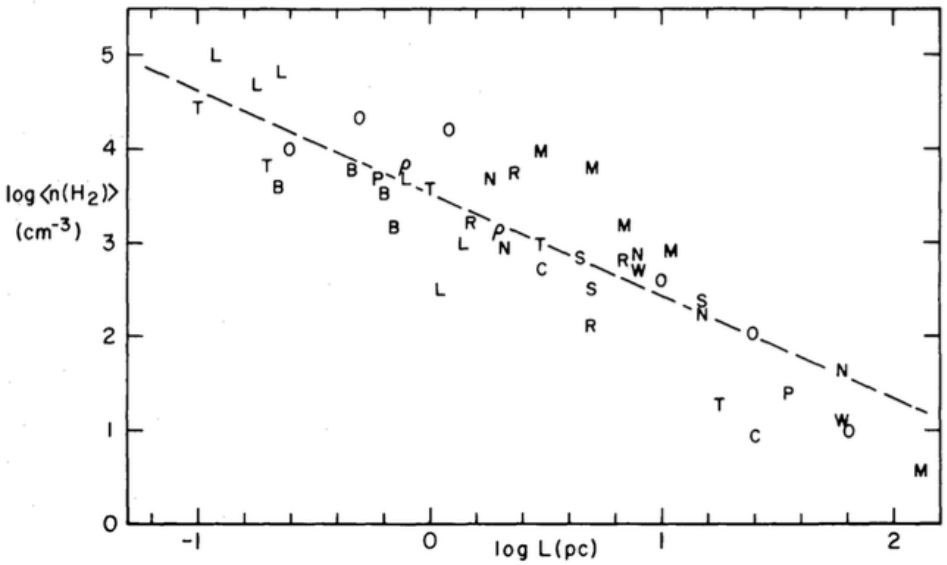

Figure 2.6: Column density versus region size in diameter (Larson, 1981)

M and diameter L.

Larson's relations have been tested with new data from surveys with higher resolution. Solomon et al. (1987) confirmed the relationships, although they found a steeper power index for the first relation: $\sigma \propto L^{0.5}$. Heyer et al. (2009) found different surface densities, but also in their investigation the laws hold qualitatively quite well. Lombardi et al. (2010) found that the third law does hold for molecular cloud complexes, but in smaller structures, like clumps and cores, and individual clouds the column densities vary. Bolatto et al. (2008) studied the laws in the extragalactic context and found that the laws hold for extragalactic giant molecular clouds as well. Finally, simulations have found support for a turbulent interpretation of the laws (Kritsuk et al., 2013). This interpretation implies that the line width-size and mass-size correlations are determined by the inertial cascade, that is a transfer of energy from large scales of motion to the small scales caused by the turbulent nature of internal motions.

2.2.2 *Smaller structures in the molecular clouds*

The structures in the molecular clouds can be classified by their physical properties. Although these definitions are not strict, in general, the filaments are larger denser structures in the clouds and can contain clumps and/or cores. In Table 2.3 is listed the approximate properties for molecular clouds as a whole, the clumps, and the cores. The largest entities are molecular

Table 2.3: Physical properties of molecular clouds, clumps, and cores (Bergin and Tafalla, 2007)

	Clouds	Clumps	Cores
Mass [$M_\odot$]	10^3–10^4	50–500	0.5–5
Size [pc]	2–15	0.3–3	0.03–0.2
Mean density [cm^{-3}]	0–500	10^3–10^4	10^4–10^5
Velocity extent [km s^{-1}]	2–5	0.3–3	0.1–0.3
Crossing time [Myr]	2–4	~1	0.5–1
Gas temperature [K]	~10	10–20	8–12
Examples	Taurus, Oph, Musca	B213, L1709	L1544, L1498, B68

clouds. They have clumps, which are smaller in size and mass, and finally, cores, which are the densest parts of clumps making them the smallest of the three. Thus, the higher the density, the smaller the structures are. That is why the cores are sometimes called dense cores even if their mean density (n_{H_2}) is only 10^4–10^5 cm^{-3}. They are dense compared to their surroundings with an average cloud density of ~500 cm^{-3}. In this thesis I will talk about clumps, that can be smaller in size than here. It is used for condensations that can be cores, but their nature is not possible to define from our observations.

There are different definitions to what is considered a clump or a core, but in this thesis I refer to the Table 2.3 in general. When talking about **cold clumps** in Chapter 6, I am referring to the *Planck*-detected cold clumps with a dust color temperature $T_{dust} \lesssim 14$ K (Planck Collaboration XXIII, 2011). Clump is also used to refer to denser structures in filaments in general, although some of the condensations referred to as clumps might be cores or contain unresolved cores.

There are different types of dense cores in the molecular clouds. A **starless core** is a dense core which has no protostellar object associated to it. **Prestellar core** is a starless core which is also gravitationally bound, and can potentially form a star by gravitational collapse. If the gravitational collapse happens, the prestellar core evolves to a **protostellar core**, which is a dense core with a formed protostar (e.g., Ward-Thompson et al., 1994, 2007; André et al., 2000; di Francesco et al., 2007). In Chapter 6 my goal is to investigate if the cold clumps observed with *Planck* and *Herschel* are, in fact, prestellar cores, that might evolve to protostellar cores.

2.3 PHOTODISSOCIATION REGIONS

2.3.1 *General background*

Most of the gas in the ISM is in neutral form. A photodissociation region (PDR) is created when intense far-ultraviolet (FUV) field illuminates a molecular cloud. Thus, FUV photons are present in PDRs and they can dissociate most molecules. They are not energetic enough to ionize hydrogen and create HII regions. PDRs are neutral surface layers at the interface of HII regions and molecular clouds.

STRUCTURE OF THE PDR. In Fig. 2.7 is a schematic diagram of a PDR. The PDR is illuminated with FUV flux from the left and extends to $A_V \sim 10$. The PDR starts where hydrogen is not ionized anymore, but is found in atomic form. Oxygen, which has similar ionization potential to hydrogen is also neutral. Carbon is still ionized as C^+. Neutral atomic hydrogen extends to H/H_2 transition. Atomic carbon exists mainly where carbon loses the ionization and changes to molecular CO form.

The typical kinetic temperature of the gas T_{gas} is also shown in the Fig. 2.7. The gas is hotter at the edge of the PDR where the UV flux is greater and the temperature decreases towards the molecular cloud. In the bottom of the figure the optical depth, A_V, and column density of hydrogen, N_H, are also shown. Hydrogen in the PDR is mainly in the form of H_2 and carbon in the form of CO. Warm O, C, C^+, H_2, and CO are produced in the PDR.

CHEMISTRY OF THE PDR. Due to the high FUV flux, photoreactions are are important in PDRs, in addition to the reactions with atomic hydrogen. H_2 chemistry is also very important to PDRs. After H_2 forms on grain surfaces, other species form in the PDR through H_2 chemistry. Sternberg and

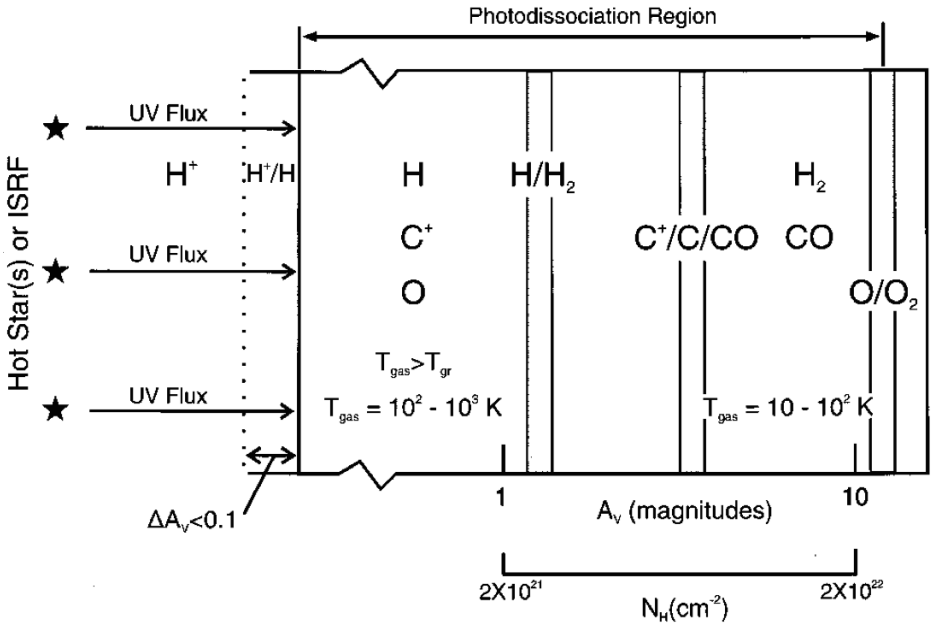

Figure 2.7: A schematic diagram of a PDR (Hollenbach and Tielens, 1997).

Dalgarno (1995) have discussed the chemical processes in PDRs in detail. The main reactions for oxygen- and carbon-bearing compounds are shown in Fig. 2.8. The chemistry is further discussed in Chapter 3, and Chapter 7

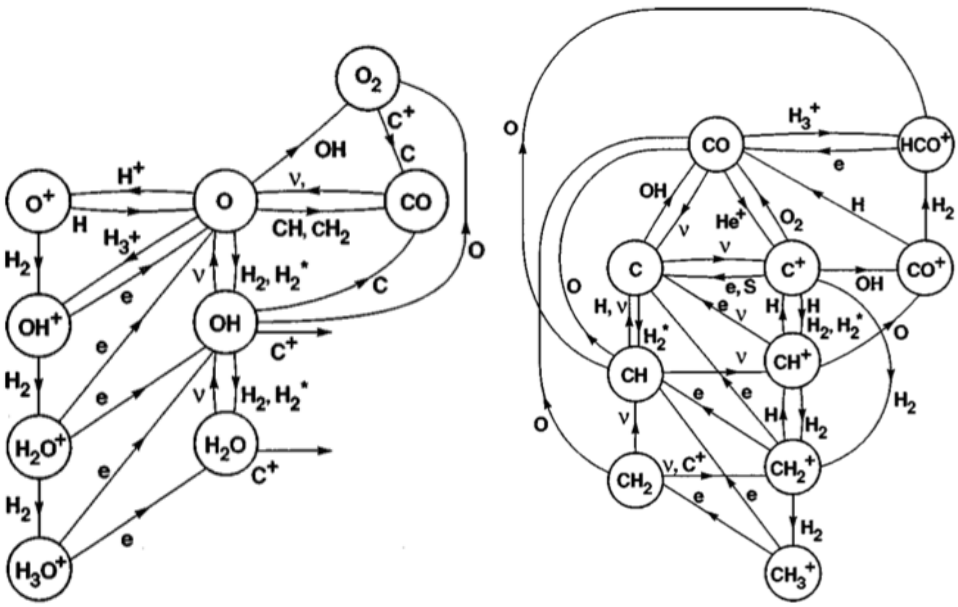

Figure 2.8: PDR chemistry of oxygen- (left) and carbon-bearing (right) compounds (Sternberg and Dalgarno, 1995).

concerning the formation and excitation of CH+ and OH.

HEATING AND COOLING OF THE PDR. The FUV photons (6 eV $< h\nu <$ 13.6 eV) dominate the heating of the PDR. The UV radiation heats either through the photoelectric effect on polycyclic aromatic hydrocarbons (PAHs)

and small dust grains or collisional de-excitation of UV-pumped H_2 molecules. Other heating mechanisms, such as H_2 formation, ionization of atoms (C) and molecules, cosmic ray ionization and excitation, pumping of gas particles to excited states by the FIR radiation field of the warm dust followed by collisional de-excitation, and gas collisions with warm grains can play a small role in the heating of the PDR when $T_{dust} > T_{gas}$ (Tielens and Hollenbach, 1985a; Hollenbach and Tielens, 1999).

The cooling of PDRs is dominated by FIR fine structure cooling lines. Especially important are [OI] lines at 63 and 145 μm and [CII] line at 158 μm at the edge of the PDR. Other cooling lines are the fine structure lines [SiII] 35 μm, [CI] 609, and 370 μm and molecular lines like CO and H_2. CO tends to dominate cooling in the denser part of the cloud. In high gas densities important cooling mechanisms can also include collisions with cooler dust grains and the recombination of electrons in positively charged particles.

2.3.2 *The Orion Bar*

The Orion Bar is a prototypical hot and dense PDR. In Fig. 2.9 we can see the *Herschel* image of Orion A, where the filamentary structure of the cloud is clearly seen. The 250 μm SPIRE map shows the Orion Bar, that

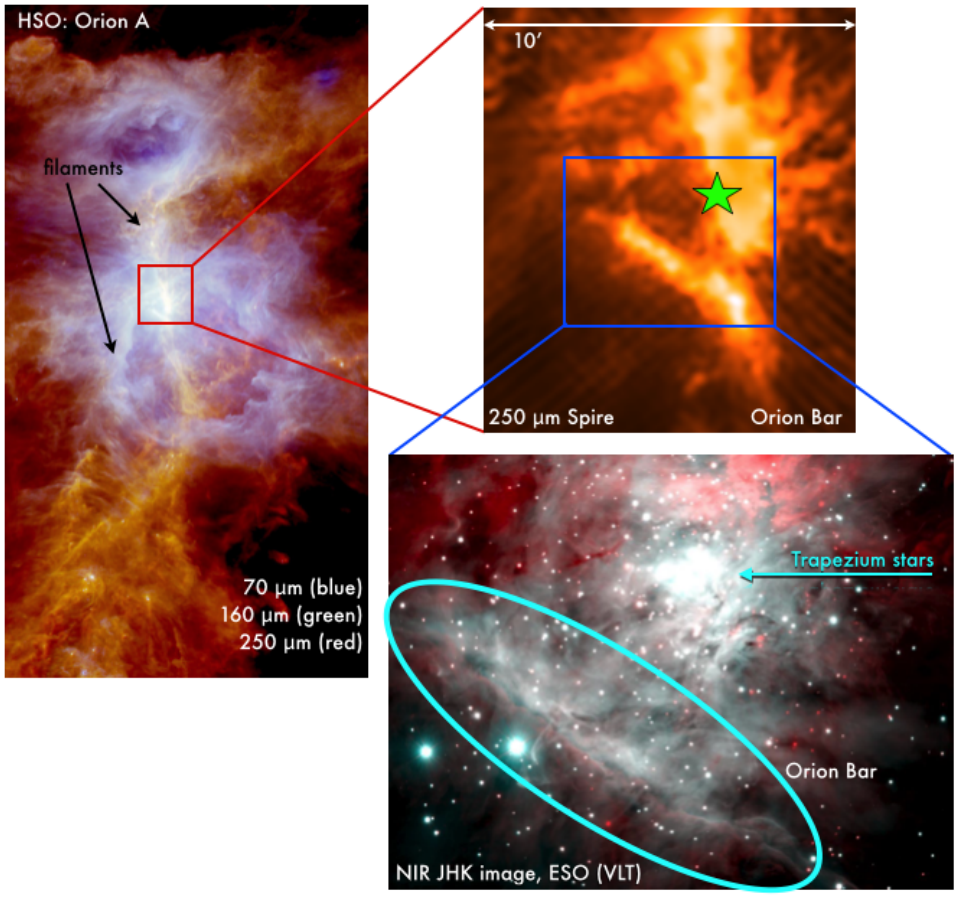

Figure 2.9: Orion Bar

can be classified as a filament as well (Walmsley et al., 2000), and finally a NIR image shows the Bar and the Trapezium stars creating HII region and the strong UV field 2.5×10^4 times the standard interstellar radiation field (Draine, 1978; Marconi et al., 1998) affecting the Bar. The Trapezium stars are a cluster of four stars of which one, θ^1 Orionis C, is the principal source of UV photons illuminating the Orion Nebula. The Bar or its ionization front is situated 111″ (0.23 pc, Pellegrini et al., 2009) South-East of the Trapezium stars.

Besides being bright, the Orion Bar is also located near, at a distance of 414 ± 7 pc (Menten et al., 2007). In addition, it is positioned nearly edge-on in the line of sight. The proximity, high luminosity, and the edge-on orientation makes it an ideal PDR to study. Thus, it has been extensively observed for more than four decades (e.g., Courtès and Viton, 1965; Andrillat and Duchesne, 1974; Russell et al., 1980; Tielens et al., 1993; Hogerheijde et al., 1995; van der Werf et al., 1996; Walmsley et al., 2000; Young Owl et al., 2000; Lis and Schilke, 2003; Habart et al., 2010; Arab et al., 2012; Bernard-Salas et al., 2012; Nagy et al., 2013).

Together with modeling, we have information on the physical structure, excitation, and dust and gas emission in the region. The studies have revealed stratified structure which is typical for edge-on geometry (e.g., Tielens et al., 1993; Lis and Schilke, 2003). The Bar is most likely a cylinder-like structure in the plane of the sky (Walmsley et al., 2000).

There are two gas components in the Bar: dense clumps of $n_H \sim 10^6$ cm^{-3}, and a less dense interclump medium $n_H \sim 5 \times 10^4$ cm^{-3} (e.g., Burton et al., 1990; Parmar et al., 1991; Tauber et al., 1994; Young Owl et al., 2000). Bernard-Salas et al. (2012) also observed a background PDR in [OI] and [CII] lines. The condensations in the Bar may collapse to form low-mass stars (Lis and Schilke, 2003) and there are known protoplanetary disks in the Bar (O'Dell and Hu, 1994).

2.4 PROPLYDS

Externally illuminated protoplanetary disks or **proplyds** (O'Dell et al., 1993) are PDR-like cometary structures with en elongated tail extending away from the illuminating star. They form around young stars and the external UV radiation produces a fully ionized surface for the disk. These objects are at high density and temperature, but a strong pressure gradient causes them to lose material into the nebula. Already Laques and Vidal (1979) found partially ionized globules with a neutral core, while ionization front penetrated inside the condensations and the ionized matter becoming progressively diluted in the general medium. Proplyds were first detected in Orion Nebula and they were called proplyds by O'Dell et al. (1993) and O'Dell and Hu (1994). Originally this was the term for all protoplanetary disks, but in time the term has come to refer only to disks that are externally illuminated and photoevaporated by UV radiation.

A schematic representation of the photoevaporating model, showing the principal components is shown in Fig. 2.10. In the figure, the ionizing star

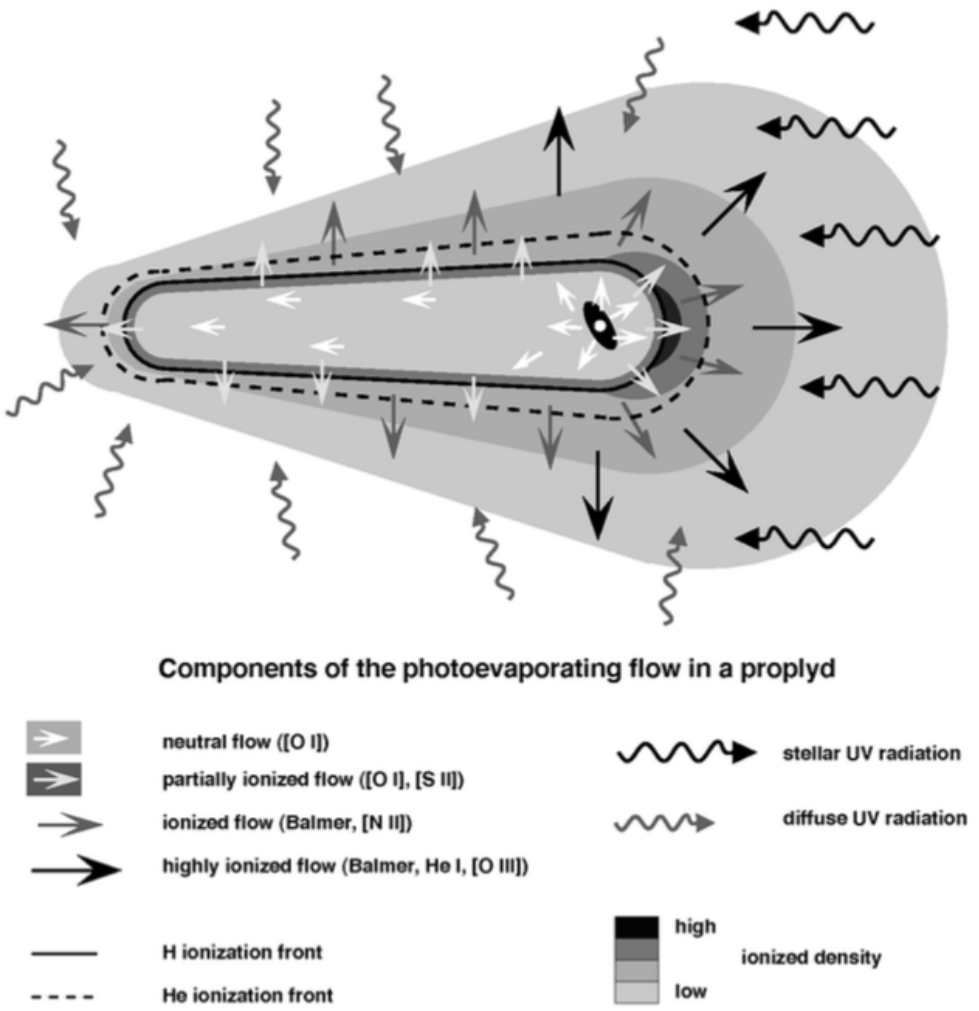

Figure 2.10: Schematic representation of the photoevaporating model, showing the principal components (Henney and O'Dell, 1999).

is on the right and the UV radiation from the star is entering from the right side. The surface of the proplyd is penetrated by the UV photons. This accelerates the gas to mildly supersonic velocities shocking before the ionization front. Inside the ionization front the gas accelerates to ~10 km s^{-1} and continues to accelerate further from the ionization front. After the ionization front, the gas becomes predominantly neutral in the inner molecular disk, and is fed by diffuse UV radiation. Thus, the tail is again ionized further away from the disk and the matter from the disk photoevaporates in the tail of the proplyd. Fig. 2.10 shows a general representation of a proplyd. The actual appearance of proplyds varies and depends on the orientation of the inner disk, the amount of ionization from the external sources, and the possible shielding of the proplyd from the ionizing photons (Henney and O'Dell, 1999; O'Dell et al., 2008).

There have been over 150 proplyds detected to date (e.g., O'Dell and Wong, 1996; Bally et al., 1998, 2000). Observations show less PAHs in proplyds than expected (Geers et al., 2007; Oliveira et al., 2010; Vicente et al., 2013). The underabundance is still unexplained, although hypothesis exists

on clustering of PAHs or destruction of PAHs by FUV photons in the PDR or X-rays emitted by the central star. However, the PAHs are still expected to be mainly responsible for the photoelectric heating of proplyds (Vicente et al., 2013). Proplyds and other protoplanetary disks have been observed in atomic and molecular lines, namely [OI] (Bally et al., 1998, 2000) and H_2 (Chen et al., 1998). Recent study with *Herschel* has shown that protoplanetary disks can be observed in several other lines as well, e.g., [CII], [OI], CO, CH^+, and OH (Sturm et al., 2010; Fedele et al., 2011; Thi et al., 2011; Champion et al. in prep.).

3

MOLECULAR TRACERS IN THE ISM

In this chapter I give an introduction to the spectroscopy and the molecules observed for the work presented in Chapters 6, 7, and 8. I also introduce RADEX that is used for the analysis of CO in Chapter 8.

3.1 SPECTROSCOPY OF MOLECULES IN THE ISM

The ISM is mostly studied using radio and infrared observations, since the peak of the radiation of the matter is mostly in these wavelengths and also dust extinction causes problems at short wavelengths. Spectroscopic studies provide information on molecules and atoms probing physical and chemical conditions in the ISM. Most of the interstellar gas is hydrogen (~70 %) and helium (~30 %). The most abundant molecule is H_2, followed by CO, OH, and NH_3, although the abundances of the latter molecules are only fractions of H_2. Molecules are formed by atoms and simpler molecules by chemical reactions either in the gas-phase or in the surfaces of grains. Dust is abundant in molecular clouds. This is essential for the appearance of molecules because H_2 forms on the dust particles and helps to build other molecules. In addition, dust absorbs the UV radiation that would otherwise destroy the molecules.

The interaction of radiation with matter is a complex subject, combining molecular spectroscopy, excitation and radiative transfer. Here I only introduce the photon interactions with atoms. It is possible for the photon to interact with atoms and molecules as a particle or a wave. The main ways for this interaction to happen are:

- *elastic scattering*, where the energy of the photon is not changed by the interaction,
- *non-elastic scattering*, where the photon is absorbed in the interaction and re-emitted at a different wavelength while the atom or molecule absorbs or gives energy to the emitted photon,
- *stimulated absorption*, where photon is destroyed while the atom or molecule absorbs the energy and momentum of the photon,
- *stimulated emission*, where the atom or molecule is in an excited state. This happens when a photon of appropriate energy passes by, and the atom or molecule emits photon of the same frequency as the passing photon, and
- *spontaneous emission*, where a photon is created when an atom or a molecule relaxes to a lower energy state.

Every line emitted in a given atomic or molecular transition has its natural line width that depends on the *Heisenberg's uncertainty principle* according to which the coordinate x and the impulse parallel to x-axis p_x have uncertainties Δx and Δp_x for which

$$\Delta x \Delta p_x \approx \hbar \tag{3.1}$$

where $\hbar$ =1.0546$\times 10^{-27}$ erg s, and the uncertainties for energy and time are

$$\Delta E \Delta t \approx \hbar. \tag{3.2}$$

These uncertainties cause the natural width of the spectrum. This natural width is defined as

$$\gamma = \frac{\Delta E_i + \Delta E_f}{\hbar} = \frac{1}{T_i} + \frac{1}{T_f}, \tag{3.3}$$

where the subscript i indicates the initial and f final energy and time. γ is the full width at half maximum (FWHM) of the spectrum.

In reality the FWHM is usually much wider than the natural width of the spectrum, though. This is due to the Doppler effect. Thermal broadening happens because the atoms in the gas move the faster the hotter the gas is. When the observed object is moving away from the observer, the frequency is shifted to longer wavelength (red-shifted) and when the object is moving towards the observer, the frequency is shifted to shorter wavelength (blue-shifted). This causes further widening in the spectra. Also microturbulent motions in the gas and macroscopic motions can cause the widening of the spectra.

3.2 CO

Since its detection in 1970 (Wilson et al., 1970), carbon monoxide (CO) has been used to trace the molecular component of the interstellar medium both in the Milky Way (e.g., Dame et al., 1987) and in extragalactic (e.g., Rickard et al., 1977) environments. While H_2 is the most abundant molecule in the ISM, it is, however, very difficult to observe, since it is a homonuclear diatomic molecule, i.e., it has no permanent electric dipole moment and its electric dipole transitions are forbidden. CO, being the most abundant molecule after H_2 ($^{12}CO/H_2$ abundance 2×10^{-4}, Lacy et al., 1994), and its isotopologues, like ^{13}CO and $C^{18}O$, are used as a tracer of the molecular gas instead of H_2.

In addition to being fairly abundant in the ISM, the CO molecule and its isotopologues are relatively stable. They also have a small dipole moment and a large moment of inertia, which means that the energy levels of CO and its isotopologues are closely spaced and easily excited at low temperatures. The lines are at millimeter wavelengths and the lowest transitions can be easily observed from the ground. Extensive surveys have been done in ^{12}CO and ^{13}CO over the Galactic plane and of nearby star-forming clouds (see, e.g., Combes, 1991, for review).

CO is a simple molecule that forms only through gas-phase reactions and it is fairly stable with a strong binding energy of 11.1 eV. CO has several observable isotopes and the seven lowest rotational transitions are observable from the ground (van Dishoeck and Black, 1987). Fig. 3.1 shows an energy level diagram of CO featuring some of the rotational transitions. The ro-

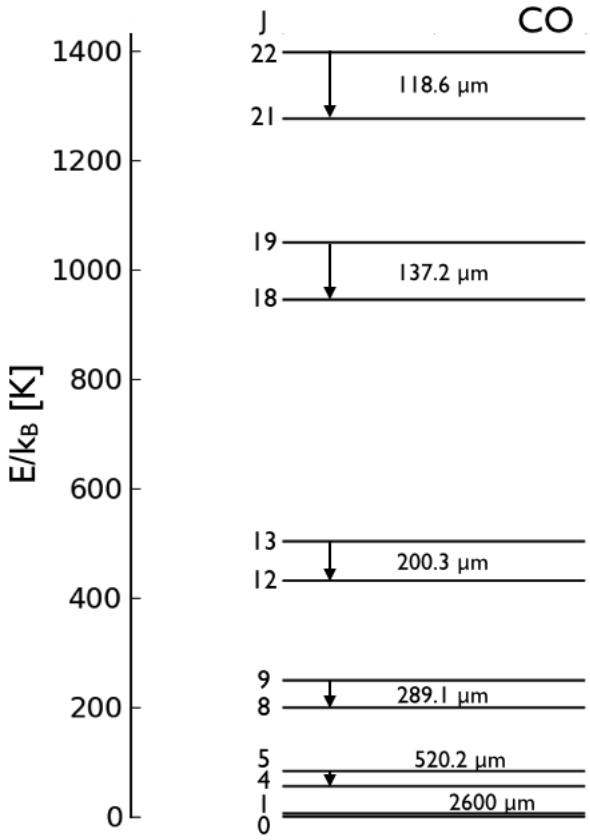

Figure 3.1: Level diagram of the rotational levels of CO.

tational levels of CO are very closely spaced, which is why only selected transitions are shown in the diagram. The moment of inertia of the CO molecules is high compared to, e.g. H_2, thus, the CO transitions can be excited even at low temperatures. The energies for the rotational levels are given by:

$$E_{rot} = \frac{\hbar^2}{2I} J(J+1) \equiv BhJ(J+1) \tag{3.4}$$

where $h = 6.6261 \times 10^{-27}$ erg s, and the rotational constant $B = \frac{h}{8\pi^2 I}$ in units of frequency.

From CO observations the temperature and column density of the gas can typically be derived. ^{12}CO is optically thick in the low- and mid-J transitions, but its isotopologues, like ^{13}CO and especially C^{18}O, are often not. Thus, they can be used in combination or instead of ^{12}CO.

3.3 N_2H^+

The diazenylium (N_2H^+) was first detected in the ISM in 1974 (Turner, 1974; Green et al., 1974) and the finding confirmed and the predicted hyperfine structure resolved a year later (Thaddeus and Turner, 1975). Since N_2, the neutral precursor to N_2H^+ lacks a dipole moment and is, thus, hard to detect, N_2H^+ can be used to derive the N_2 abundance in molecular clouds (see, e.g., Herbst et al., 1977; Hotzel et al., 2004)

Especially the J=1-0 transition has also been used to estimate physical conditions in the interstellar gas (e.g., Bergin et al., 2002; Tafalla et al., 2004; Lippok et al., 2013). In particular, it has been used to identify cold cores. N_2H^+ traces the high density regions of dark clouds as it is less depleted onto dust grain surfaces than CO and many other molecular species because of the low binding energy of its precursor molecule, N_2. Thus, it can be found in prestellar and protostellar clumps (Bergin and Langer, 1997; Hotzel et al., 2004; Daniel et al., 2006).

The fractional abundance of N_2H^+ is expected to be constant or even increase inside the cores (Hotzel et al., 2004; Alonso-Albi et al., 2010), although in some studies it has been found to be depleted in the densest part of the cores (Bergin et al., 2002; Pagani et al., 2007). However, it is formed primarily via reaction $H_3^+ + N_2 \rightarrow N_2H^+ + H_2$, which is a "dense-cloud" process, thus making N_2H^+ a good tracer of dense gas (Turner, 1995).

3.4 CH^+

The methylidyne cation (CH^+) was the first interstellar molecular ion observed in the interstellar medium via its optical spectrum (Dunham, T., 1937; Douglas and Herzberg, 1941). Although it is commonly observed, it is not very well understood. This is partly due to the fact that its rotational levels lie in the submillimeter range. The energies of the rotational levels can be calculated from the Eq. 3.4 and the first rotational transitions are shown in Fig. 3.2.

The pure rotational spectrum was finally observed in ISM by Cernicharo et al. (1997). They observed CH^+ in the PDR of planetary nebula NGC 7027 and estimated a CH^+ column density of 8×10^{13} cm^{-2} assuming a size of 6″ for the PDR. Among other transitions, they observed the transition J=3-2, which also is used in this thesis, but it was blended with the nearby OH (doublet at 119.2 and 119.4 μm). *Herschel* has finally provided observations of the unblended rotational transitions.

CH^+ is highly reactive and easily destroyed by reactive collisions with H_2, H, and electrons. However, observations have shown a greater abundance of CH^+ than what steady-state chemical models in quiescent molecular clouds have predicted (e.g., van Dishoeck and Black, 1986). The excitation of CH^+ has been suggested to be dominated by chemical pumping after reaction of C^+ with vibrationally excited H_2 which would lead to greater abundance of CH^+ (Godard and Cernicharo, 2013; Nagy et al., 2013). This formation route has a very high endothermicity of 0.37 eV (4640 K), and it has been

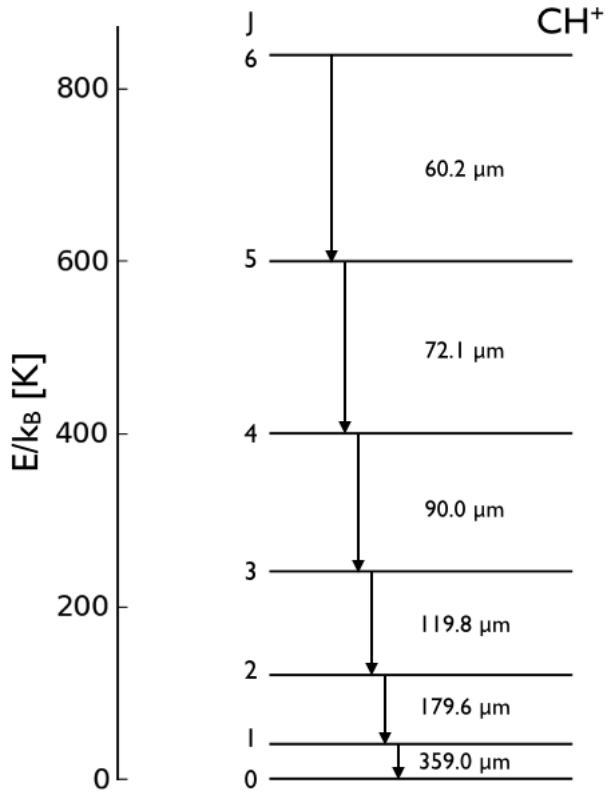

Figure 3.2: Level diagram of the lowest rotational levels of CH^+.

suggested that the ro-vibrational energy of the vibrationally excited H_2 can be used when available in strong irradiated PDRs and that this energy actually changes the reaction from endothermic to exothermic (e.g., Lambert and Danks, 1986; Jones et al., 1986; Agúndez et al., 2010; Naylor et al., 2010; Godard and Cernicharo, 2013; Nagy et al., 2013; Zanchet et al., 2013). Alternatively, in diffuse interstellar clouds with low FUV radiation field and very low density, shocks (e.g., Pineau des Forets et al., 1986) and turbulence (e.g., Godard and Cernicharo, 2013) have been proposed to overcome the high endothermicity.

Lately, the excitation of CH^+ observations of the Orion Bar have been compared to models (Godard and Cernicharo, 2013; Nagy et al., 2013; Zanchet et al., 2013). Chemical pumping via vibrationally excited H_2 is predicted to be important to the excitation of all the CH^+ rotational lines in the physical conditions prevailing in the warm molecular zone of the Orion Bar. Chemical excitation starts to be significant at transition J=3-2 and for higher transitions it seems to be the driving force (Godard and Cernicharo, 2013; Zanchet et al., 2013). Still, wider maps of CH^+ emission and further comparison with models are needed to fully comprehend the excitation of CH^+.

3.5 OH

Hydroxyl (OH) is a simple, but an important molecule for the study of the ISM. It is the first molecule that was observed in ISM in radio frequencies (Weinreb et al., 1963). It is a building block of more complex chemistry in the far ultraviolet (FUV) illuminated gas. Its reaction with H_2, C^+, O, N, and S^+ leads to the formation of H_2O, CO^+, O_2, NO, and SO^+, respectively. In addition, OH is the product of H_2O photodissociation, the main destruction route of water vapor in the gas unshielded against FUV radiation. With OH observations it is, thus, possible to constrain different chemical routes of oxygen chemistry. OH is strongly paramagnetic and, thus, also widely used to measure the magnetic field in the ISM through the Zeeman effect.

The use for magnetic field measurements is based on the nature of OH as a free radical, having one unpaired electron and, thus, a nonzero electronic angular momentum. While the rotational levels of OH have energies that can be calculated from the Eq. 3.4, the rotational levels are also divided into sublevels of nearly equal energy. This Λ-doubling is an interaction between the nuclei rotation and the unpaired electron motion around its orbit. The rotational levels and their sublevels for the transitions relevant to this thesis, can be seen in Fig. 3.3. The use for magnetic measurements is due to the magnetic hyperfine splitting, which can be seen as sublevels of the Λ-doubling in Fig. 3.3. Hyperfine splitting is caused by the interaction with the unpaired spin of the proton. The two ladders in the figure correspond to the opposite orientations of the unpaired electron's spin.

Hydroxyl was first detected in the Orion Bar by Goicoechea et al. (2011). They observed several transitions towards the CO^+ peak ($\alpha_{J2000} = 05^h35^m20.6^s$, δ_{J2000} = -05°25′14″) in the Bar (Störzer et al., 1995). These were pointed observations of the Orion Bar and not fully sampled maps. The measured intensities can be seen in Table 3.1. I have included here only the transitions relevant to this thesis, but also transitions at 65 μm and 79 μm were observed.

Table 3.1: PACS OH line intensities towards the Orion Bar PDR (Goicoechea et al., 2011).

λ [μm]	OH transition	I_{obs} (σ_{obs}) [10^{-5} erg s^{-1} cm^{-2} sr^{-1}]
119.441	$^2\Pi_{3/2}$ J= $5/2^+ - 3/2^-$	10.09 (0.21)
119.234	$^2\Pi_{3/2}$ J= $5/2^- - 3/2^+$	9.44 (0.21)
84.597	$^2\Pi_{3/2}$ J= $7/2^- - 5/2^+$	4.07 (0.79)
84.420	$^2\Pi_{3/2}$ J= $7/2^+ - 5/2^-$	2.38 (0.91)
163.396	$^2\Pi_{1/2}$ J= $3/2^- - 1/2^+$	1.34 (0.17)
163.015	$^2\Pi_{1/2}$ J= $3/2^+ - 1/2^-$	2.74 (0.16)

All the observed transitions were clearly detected in the Orion Bar. The transitions at 84 μm and 163 μm are of similar intensity, which is not sur-

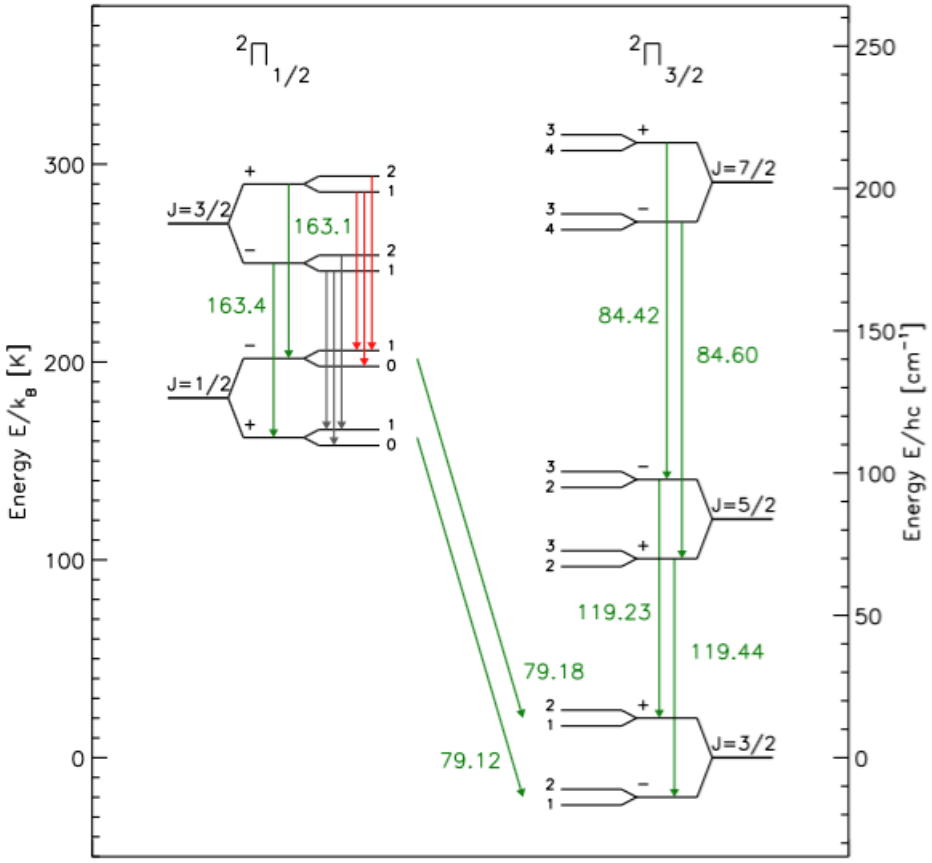

Figure 3.3: Level diagram of the lowest excited states of OH. Splitting of the levels because of Λ-doubling and hyperfine structure is not to scale. (Wampfler et al., 2010)

prising as they have similar upper level energy temperatures as seen in Fig. 3.3. Goicoechea et al. (2011) found OH emission to be extended, but correlating well with CO and CH^+ observations, thus, suggesting a common origin. They also interpreted that the OH emission originates in unresolved dense structures instead of the lower density "interclump" medium. The observations discussed in Chapter 7 cover a larger area and we are thus able to better compare the morphologies of these lines.

The fact that OH has also been found in young stellar objects, Herbig stars, and protoplanetary disks (Wampfler et al., 2010; Fedele et al., 2012; Wampfler et al., 2013; Lindberg et al., 2014) supports the idea, that OH in the ISM originates in dense structures, although the effect of shocks cannot be always ruled out. It does need a luminous star, since it is difficult to excite the rotational states of OH in quiescent clouds. However, it has been previously thought to be a tracer of diffuse gas (e.g., Neufeld et al., 2002; Dawson et al., 2014; Porras et al., 2014), and has been used widely as a probe of the local magnetic strength (e.g., Troland and Crutcher, 2008; Asanok et al., 2010; Crutcher et al., 2010; Maeda et al., 2015).

3.6 RADEX: MODEL FOR ANALYSIS OF MOLECULAR TRACERS

RADEX[1] (van der Tak et al., 2007) is a one-dimensional non-LTE radiative transfer code[2]. It uses uniform density and temperature layer and solves the statistical equilibrium equations assuming local excitation. The equations include collisional and radiative processes including background radiation and it treats optical depth with an escape probability method. The program uses the Leiden Atomic and Molecular Database (LAMDA, Schöier et al., 2005), which is being expanded and improved continuously.

RADEX is more sophisticated than the rotational diagram which does not solve the radiative transfer (e.g., Blake et al., 1987; Helmich et al., 1994; Goldsmith and Langer, 1999) and comparable to escape probability method and LVG method (Sobolev, 1947; de Jong et al., 1975; Goldreich and Scoville, 1976), but simpler and, in consequence faster, than more complex codes, like the PDR Meudon code (Le Petit et al., 2006) which computes the physical conditions in the PDR, namely, density and temperature. It also constrains the column densities of the emitting species. Thus, RADEX is useful in providing a quick estimation of the physics in PDRs. It calculates the escape probability assuming a homogenous medium. It predicts the emitted spectrum for the molecular lines, but cannot calculate flux or specific luminosity because it has no knowledge of the geometry of the source. Also, it calculates the intensities for one species at a time, thus, the effects of the line-overlap or different molecules are not taken into account.

The collision rates used depend on temperature and only limited range of temperatures are covered. RADEX uses interpolation or extrapolation to find the temperatures not covered in the database. Temperatures are handled well up to 500 K, but higher temperatures as well as high column densities can be problematic. In our CO modeling the high column densities and temperatures did not give reasonable results for hydrogen density of 10^4 cm^{-3}.

The input parameters for RADEX are 1) the spectral range for the output for which the program then calculates all transitions of the given molecule, 2) the kinetic temperature of the molecular cloud, 3) number of collision partners (maximum of 7 partners), 4) density of each collision partner, 5) equivalent black body temperature of the background radiation (usually taken to be T_{CMB}=2.73 K), 6) molecular column density, and 7) line width of the molecular lines (assumed the same for all lines).

Radex solves T_{ex} and calculates the intensity, I_ν^t, in erg s^{-1} cm^{-2} Hz^{-1} sr^{-1} of the given species in the given range given by:

$$I_\nu^t = B_\nu(T_{ex})[1 - e^{-\tau_0}] + e^{-\tau_0} I_\nu^b. \tag{3.5}$$

1 Available at: http://www.sron.rug.nl/~vdtak/radex/index.shtml

2 RADEX manual available at: http://home.strw.leidenuniv.nl/~moldata/radex_manual.pdf

In the equation I_ν^b is the background emission at line frequency, reduced by any absorption in the line. $B_\nu(T_{ex})$ is given in convenient units:

$$B_\nu(T_{ex}) = \frac{3.973 \times 10^{-16}\tilde{\nu}^3}{\exp(1.43883\tilde{\nu}/T) - 1} erg^{-1}cm^{-2}Hz^{-1}sr^{-1}, \tag{3.6}$$

where $\tilde{\nu}$ is the wave number in cm^{-1}. In the Eq. 3.5 T_{ex} is the excitation temperature, τ_0 is the optical depth in the line at the line center. Similarly to LVG programs, the optical depth, and consequently RADEX results, depend only on the ratio of column density to line width.

In addition to the calculated intensity, RADEX results list the quantum numbers of the upper and lower states, the line frequency, the excitation temperature of that line, the optical depth at the line center, and the Rayleigh-Jeans equivalent of the intensity of the line minus the background intensity.

In chapter 8 I compare the calculated intensities from RADEX with the intensities of CO observations. The comparison gives us the likely CO column density and kinetic temperature for the considered H_2 density.

Part II

OBSERVATIONS

4

HERSCHEL OBSERVATIONS

In this chapter I introduce the telescope and describe the observations of the Orion Bar which were used in Chapters 7 and 8. The work on cold clumps in Chapter 6 is also based on *Herschel* observations. The molecular lines in the cold clumps were observed from the ground in Onsala. The 20-m radio telescope in Onsala is introduced and observations described in Chapter 5.

4.1 INTRODUCTION TO THE TELESCOPE

4.1.1 *Herschel Space Observatory*

Herschel Space Observatory is the largest space telescope ever launched with a primary mirror of 3.5 m. It was launched in 14 May 2009. The mission was named after Sir William Herschel, who discovered the infrared radiation in 1800. The mission continued until 29 April 2013, when last of the helium used for cooling the instrumentation of the telescope was evaporated. During these four years over 35 000 observations were made. This included more than 25 000 hours of science data for ~600 observing programs. Over 1 300 scientific papers have been published by the end of February 2015[1].

The telescope was built to do photometry and spectroscopy in 55–671 μm range, a previously mostly unobserved region of the electromagnetic spectrum[2]. The evaporation of the liquid helium was keeping the instruments close to absolute zero, enabling the observations of the cool universe. The main objectives of *Herschel* were photometric surveys of extragalactic and galactic sky to measure dust-enshrouded star formation, detailed photometric and spectroscopic studies of the physics and chemistry of ISM, observational astrochemistry to understand stellar and interstellar lifecycle, and spectroscopic and photometric study of solar system objects and their atmospheres. The mission has also brought us technological advancements for future space missions which are already in use in ESA's new space missions, including Gaia.

The *Herschel Space Observatory* measures 7.5 m in height and 4 m in width and weighs ~3.4 tons. It is constructed almost entirely (~90 % of mass) of silicon carbide (SiC). The different parts of the satellite are shown in Fig. 4.1. The telescope is a Cassegrain telescope with a primary mirror, 3.5 m in diameter, and a smaller secondary mirror, 30.8 cm in diameter. These are protected by the sunshade. The detectors and receivers (HIFI) of the scientific instruments are located in the cryostat. The detectors are kept at very low and stable temperatures by liquid superfluid helium to make the

1 SAO/NASA Astrophysics Data System (ADS) http://adsabs.harvard.edu/

2 *Infrared Space Observatory (ISO)* Long Wavelength Spectrometer has a range of 45–200 μm.

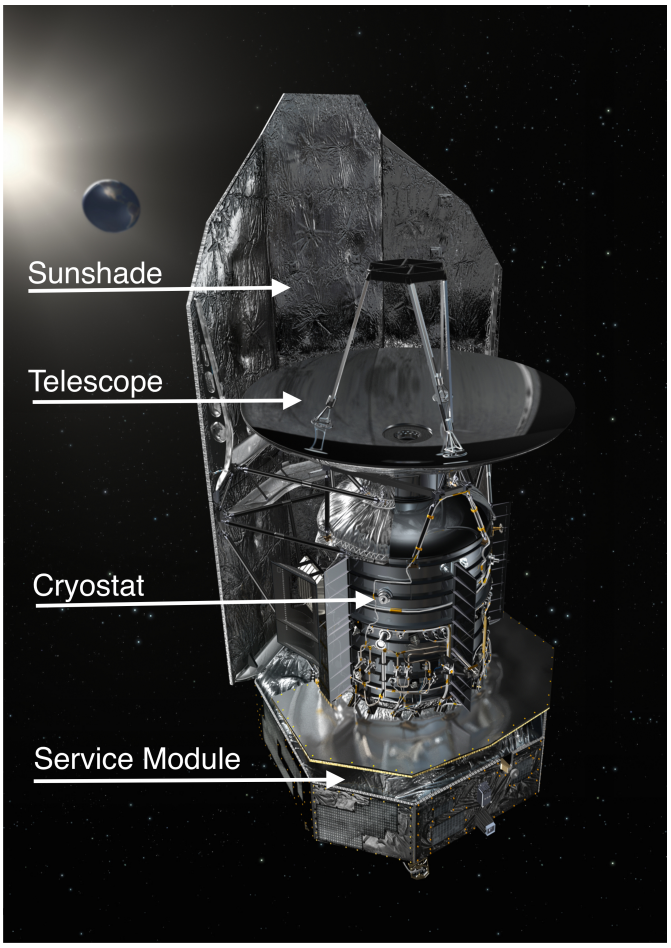

Figure 4.1: Artist view of the *Herschel* satellite. Credit: ESA/AOES Medialab

detectors as sensitive as possible. The service module houses instrument electronics and components responsible for satellite function.

4.1.2 *Herschel science instruments*

The three detectors in *Herschel Space Observatory* are the Photodetector Array Camera and Spectrometer (PACS, Poglitsch et al., 2010), the Spectral and Photometric Imaging REceiver (SPIRE, Griffin et al., 2010), and the Heterodyne Instrument for the Far Infrared (HIFI, de Graauw et al., 2010). In my thesis I concentrate on the data observed with the PACS spectrometer, but I also use SPIRE FTS observations and some complementary HIFI observations. All instruments are introduced here.

4.1.2.1 *The Photodetector Array Camera and Spectrometer: PACS*

The PACS instrument consists of two sub-instruments which are mutually exclusive: a color camera to obtain photometric observations and an imag-

ing grating spectrometer. It operates at wavelength range of 55–210 μm. A functional block diagram is shown in Fig. 4.2

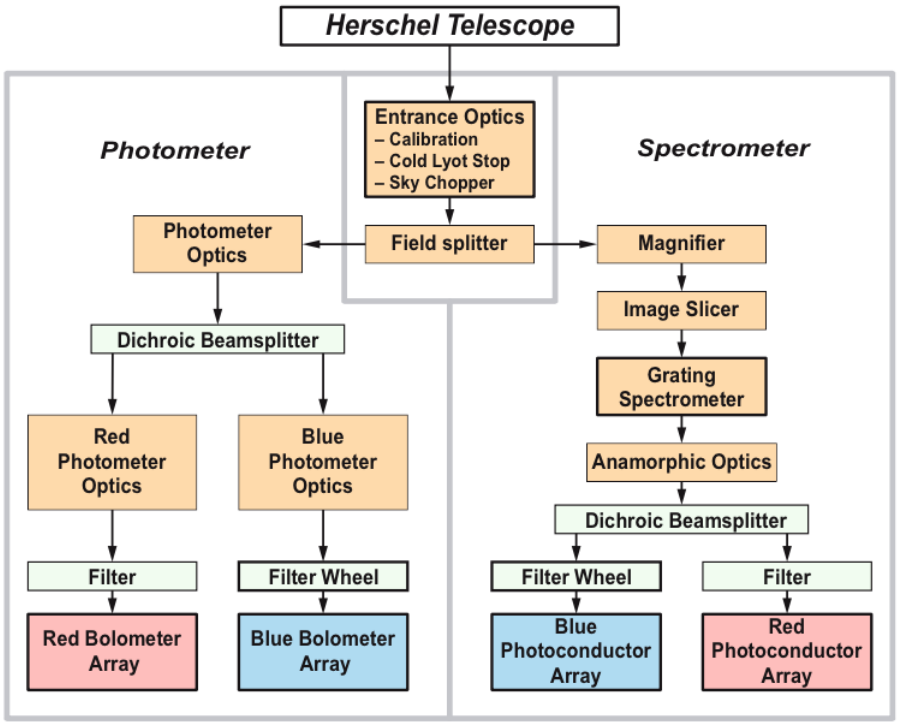

Figure 4.2: PACS focal plane unit (FPU) functional block diagram. The arrows visualize the optical paths through the instrument. Imaging optics and filter components are shown in different colors. Active components (mechanisms, electronics) are outlined in bold. (Poglitsch et al., 2010)

The front or entrance optics provide an intermediate image of the telescope secondary mirror with the cold Lyot stop and the first blocking filter. These front optics are common to all instrument channels. After the chopper, a fixed field mirror splits the light for the spectroscopy channel and the remaining field of view is passed on into the photometry channels.

SPECTROMETER. The PACS integral-field-unit spectrometer covers a wavelength range of 55–210 μm. The field of view of 47″×47″ is resolved into 5×5 spatial pixels (spaxels) with simultaneous imaging. This is not a spatially fully sampled array. The instantaneous spectral coverage is 1500 km s^{-1} and spectral resolution 55–320 km s^{-1}. In this thesis I analyze the PACS spectrometer observations from the open time project *Unveiling the origins and mechanisms of the warm CO, OH and CH^+* (PI: Emilie Habart).

The spectrometer has three observing modes: 1) chopped line spectroscopy for single lines, 2) chopped range spectroscopy for spectra over larger wavelength ranges, and 3) wavelength switching mode for single lines on extended sources without clean background for chopping[3]. In addition, there are specific adjustments for bright and faint lines with bright lines chopping-

3 Deprecated after the first year.

nodding mode and unchopped faint line mode. All the modes can be used in a single pointing or in a raster pattern for a larger map. A single pointing or footprint is composed of 5×5 spaxels. This configuration is shown in Fig. 4.3.

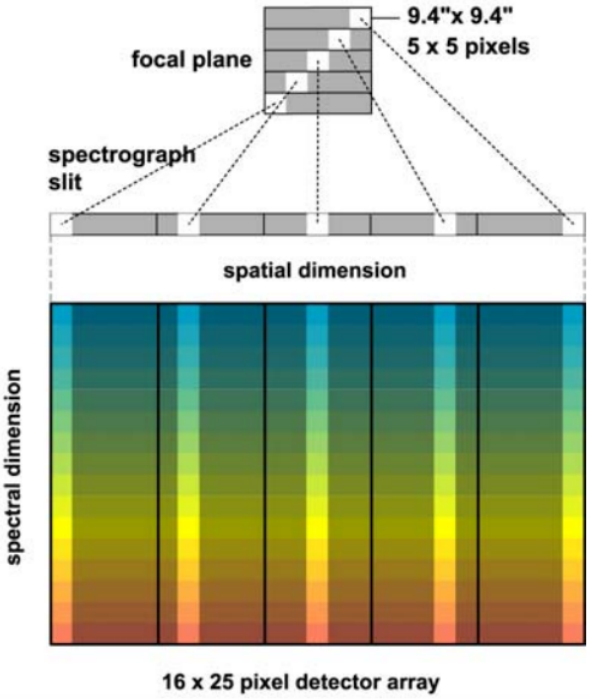

Figure 4.3: Projection of focal plane onto spectrometer arrays. The image slicer rearranges the 2D field along the entrance slit of the grating spectrograph in such a way that the spectra are observed simultaneously for all spatial elements in the field[4].

Sensitivity is the most important parameter for PACS spectrometer optimization. Single FIR spectral lines are normally several orders of magnitudes lower than the dust continuum over a typical photometric band. Thus, PACS spectrometer is optimized to detect faint FIR spectral lines at a high spatial resolution.

PHOTOMETER. The photometer images two bands, 60—85 μm or 85—125 μm (short wave bands, blue and green, respectively) and 125—210 μm (long-wave or red band), simultaneously. The field of view is $1.75' \times 3.5'$ with close to full Nyquist beam sampling in each band. The simultaneous observation of two band multiplies the observing efficiency. The same field of view is observed in all wavelengths, with red having 32×16 pixels of $6.4'' \times 6.4''$ and green and blue having 64×32 pixels of $3.2'' \times 3.2''$ each.

The PACS photometer uses three different observing modes: 1) point-source photometry mode in chopping-nodding technique, 2) scan map tech-

4 The Photodetector Array Camera and Spectrometer (PACS) for the *Herschel Space Observatory* presentation from SPIE June 2008, Marseille, France. Available at: http://herschel.esac.esa.int/Docs/Flyers/PACS_flyer_21May2010.pdf

nique, and 3) scan map technique within the PACS/SPIRE parallel mode (Poglitsch et al., 2010). The chop-nod mode is ideal for intermediately bright sources (50 mJy–50 Jy) due to its small relative pointing error of 0.3″ and high photometric reliability. It uses the PACS chopper to move the source ~50″ with a chopper frequency of 1.25 Hz. Satellite movement produces the nodding of the same amplitude but in a direction perpendicular to the chopping. Most observations use scan speed of 20″ s^{-1} where the bolometer performance is best and the pre-flight sensitivity estimates are met. This mode is ideal for mapping large areas, but is used also for small areas and even point sources. The maps are produced by slewing the spacecraft at a constant speed along parallel lines.

Deep and/or large scale photometric surveys take much of *Herschel* observing time. For large scale surveys mapping efficiency is essential. The efficiency is determined by the field of view and the sensitivity per pixel. The PACS photometer was built to include the largest detector arrays available at the time without compromising sensitivity.

4.1.2.2 *Spectral and Photometric Imaging REceiver: SPIRE*

SPIRE consists of a imaging photometer and a low to medium resolution Fourier Transform Spectrometer (FTS) complementing PACS for wavelengths in the range 194–672 μm, thus overlapping with PACS for ~15 μm. The SPIRE architecture as a block diagram is shown in Fig. 4.4.

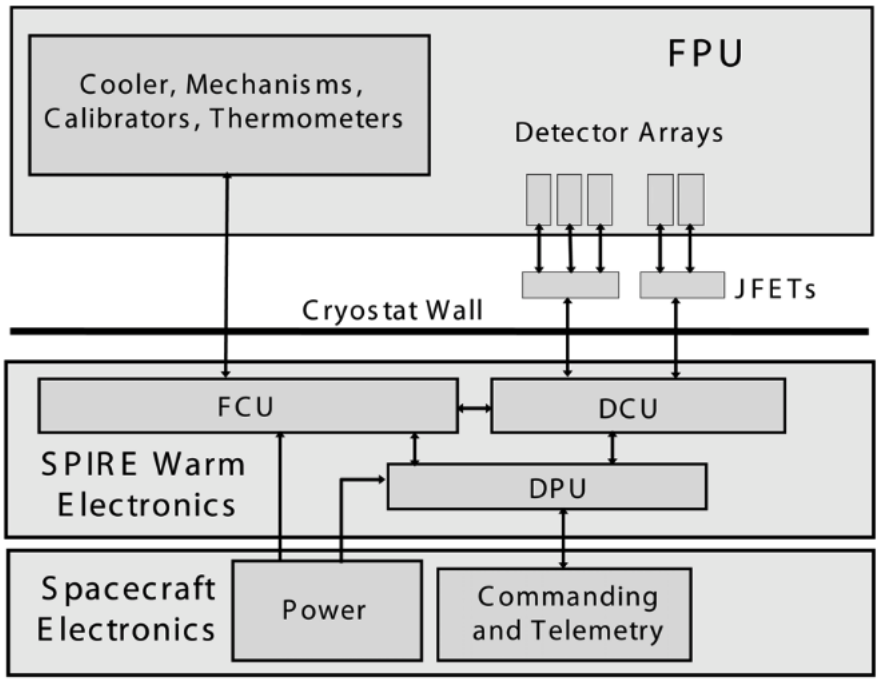

Figure 4.4: The SPIRE architecture (Griffin et al., 2010)

The focal plane unit (FPU) contains the optics, three detector arrays for the photometer and two for the spectrometer, an internal ^{3}He cooler for

operating temperature of ~0.3 K, filters, mechanisms, internal calibrators, and housekeeping thermometers.

The SPIRE warm electronics units include the Detector Control Unit (DCU), the FPU Control Unit (FCU), and the Digital Processing Unit (DPU). DCU provides the bias and signal conditioning for the arrays, cold electronics demodulates and digitizes the detector signals, FCU controls the cooler and the mechanisms, and DPU runs the on-board software and interfaces with the spacecraft. A summary of most important instrument characteristics of the photometer and FTS spectrometer is shown in Table 4.1.

Table 4.1: SPIRE instrument characteristics[5]

Sub-instrument	FTS Spectrometer		Photometer		
Array	SSW	SLW	PSW	PMW	PLW
Band (μm)	194–313	303–671	250	350	500
Resolution ($\lambda/\Delta\lambda$)	~40–1000 at 250 μm		3.3	3.4	2.5
Field of view	2.0′ (diameter)			4′ × 8′	
Beam FWHM (″)	17–21	29–42	17.6	23.9	35.2

The SPIRE observations concentrate on two main scientific goals: 1) The investigation of the statistics and physics of galaxies and large scale structure formation at high redshift and 2) The study of the earliest phases of star formation and the evolutionary life cycle of stars to their end phase. The SPIRE observations used in this thesis come from two *Herschel* key programs *Galactic Cold Cores* (PI: Mika Juvela) and *Evolution of interstellar dust* (PI: Alain Abergel), both concentrating on the earliest phases of star formation. Both of the main goals require deep photometric imaging surveys at far-infrared and submillimeter wavelengths over a large area and follow-up spectroscopic observations of selected sources.

SPIRE-FTS. The FTS covers a wavelength range of 194–671 μm with two overlapping bands: SSW (194–313 μm) and SLW (303–671 μm). The short-wavelength array contains 37 and the long-wavelength array contains 19 hexagonally packed detectors, each with its individual feedhorn. The configuration is shown in Fig. 4.5. The spectrometer has a field of view of 2.0′ and a low spectral resolution up to $\Delta\sigma = 0.04$ cm^{-1}. The beam size depends on the observed wavelength and is 17″–21″ for SSW and 29″–42″ for SLW (see Table 4.1).

With FTS the spectra can be measured in single pointing or by making a raster map by moving the telescope. Single pointing creates a sparse map (see Fig. 4.5), but intermediate or full sampling can be achieved without moving the telescope using the SPIRE beam steering mirror to provide the pointing changes while telescope pointing is fixed. If the region is larger

5 From the SPIRE Handbook. This can be found at http://herschel.esac.esa.int/Docs/SPIRE/spire_handbook.pdf

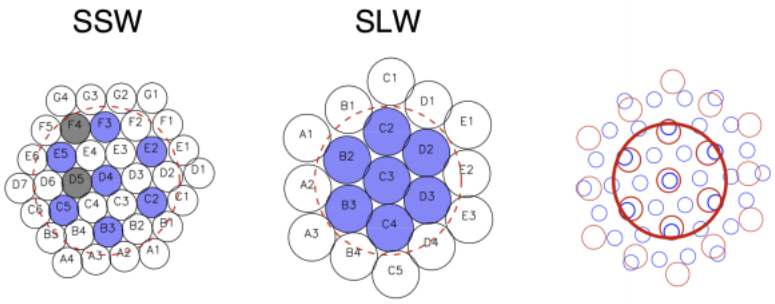

Figure 4.5: A schematic view of the FTS bolometer arrays. Each circle represents a detector feedhorn. The 2.0′ unvignetted field of view of each array is delineated by a red dashed circle. The two arrays overlap on the sky as shown in the rightmost figure, where the SLW and SSW are depicted by red and blue circles, respectively. The circle sizes in the rightmost figure correspond to the FWHM of the beam[6].

than the field, rastering combined with spatial sampling using the beam steering mirror is needed.

PHOTOMETER. The SPIRE photometer is a three band imaging photometric camera with bands centered on 250 μm (SPIRE Photometer Short Wavelength Array, PSW), 350 μm (SPIRE Photometer Medium Wavelength Array, PMW), and 500 μm (SPIRE Photometer Long Wavelength Array, PLW). The bolometer arrays contain 139, 88, and 43 detectors, respectively. The configuration is shown in Fig. 4.6. The photometer has a field of view of 4′×8′ (see Table 4.1).

The photometer has three observing modes: point source photometry, field mapping, and scan mapping. Scan mapping is optimal for most observations as it provides better data quality over a larger area than the chopped modes. It can also produce a sky background confusion limited map in a total observing time that is still dominated by telescope slewing overheads. The *Herschel* observations used in Chapter 6 used the scan mapping mode. All three SPIRE bands can be observed simultaneously and the scan mode can be also used simultaneously with PACS, which makes this mode very efficient in making multi-band maps.

4.1.2.3 *Heterodyne Instrument for the Far Infrared: HIFI*

HIFI is a high-resolution heterodyne receiver spectrometer covering wavelength ranges of 157– 212 μm and 240–625 μm. It observes a single beam on the sky at a time. HIFI consists of two spectrometers: the high resolution spectrometer (HRS, several possible resolutions from 0.125 to 1.00 MHz) and the HIFI wideband spectrometer (WBS, single resolution of 1.1 MHz). HRS is a digital autocorrelator that provides a high spectral resolution over a limited bandwidth. It also has a high flexibility. WBS uses the acousto-

6 From the SPIRE Handbook. This can be found at http://herschel.esac.esa.int/Docs/SPIRE/spire_handbook.pdf

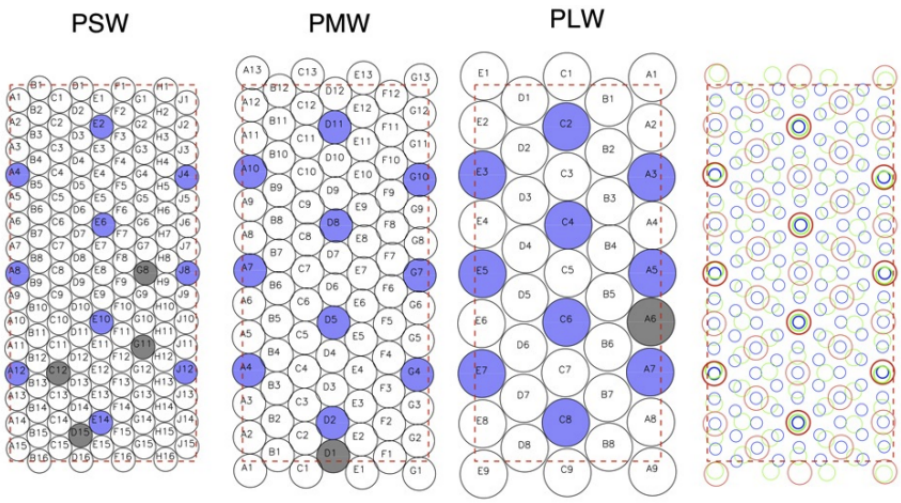

Figure 4.6: A schematic view of the photometer bolometer arrays. Each circle represents a detector feedhorn. The $4' \times 8'$ unvignetted field of view of each array is delineated by a red dashed rectangle. The three arrays overlap on the sky as shown in the rightmost figure, where the PLW (500 μm), PMW (350 μm) and PSW (250 μm) are depicted by red, green and blue circles respectively. The circle sizes in the rightmost figure correspond to the FWHM of the beam[7].

optical technique that provides a wide frequency coverage for low power and low mass.

HIFI observations include single-point observations, mapping observations, and spectral scans. These observations are achieved by different observing modes of the instrument: position switch, dual beam switch, frequency switch, and load chop. When position switch mode is used the beam alternates between the target position and a reference position. The reference position should preferably be without emission in the band in question. Dual beam switch mode is similar to the position switch mode, but uses internal chopper mirror to direct the beam between target and reference positions. In the frequency switch mode the local oscillator frequency is changed by a few tens of MHz. The shift is small enough that the lines of interest remain observable in both frequencies, which makes this mode very efficient, since the lines can be observed both in ON and OFF positions. In the load chop mode an internal cold source is used as a reference. A chopping mirror is used to alternate between the target in the sky and the internal load. This method can be used if there are no emission-free regions near the target.

The main science goals of HIFI are related to cyclic interrelation of stars and the interstellar medium in galaxies. HIFI is optimized for three specific areas that require a high spectral resolution and the wide frequency range available with HIFI: 1) to observe the water lines essential to the absorption

7 From the SPIRE Handbook. This can be found at http://herschel.esac.esa.int/Docs/SPIRE/spire_handbook.pdf

studies of cold water, 2) to survey the molecular complexity of the Universe, and 3) to observe the ionized Carbon [CII] at 158 μm.

4.2 OBSERVATIONS

In this section I provide an overview of the *Herschel* observations used in Chapters 7 and 8. The *Herschel* observations used in Chapter 6 were originally published by (Juvela et al., 2012) and although reduced with a more current version (v.10.0) of Herschel Interactive Processing Environment (HIPE) by Mika Juvela, are not further introduced here.

4.2.1 *PACS observations*

To the best of our knowledge, the Bar is the only PDR where the CH^+, OH, and high-J CO lines can be mapped with high enough signal-to-noise and spatial resolution, so that we can, for the first time, look at their morphology as a function of the physical conditions (FUV radiation, temperature, and density) and try to understand how these specific molecules are formed, excited and destroyed. Our maps are the only fully-sampled maps of FIR CH^+ and OH lines.

We observed the CO J=19-18 transition (137 μm), CH^+ J=3-2 transition (120 μm), and OH 84 μm doublet (84.4 and 84.6 μm, transitions $^2\Pi_{3/2}$ J=7/2$^+$-5/2$^-$ and $^2\Pi_{3/2}$ J=7/2$^-$-5/2$^+$, respectively) in the Orion Bar with *Herschel*/PACS spectrometer (Poglitsch et al., 2010). Due to the instantaneous wavelength window covered, in addition to CH^+ J=3-2 at 119.8 μm, the OH 119 μm doublet (119.2 and 119.4 μm, transitions $^2\Pi_{3/2}$ J=5/2$^-$-3/2$^+$ and $^2\Pi_{3/2}$ J=5/2$^+$-3/2$^-$, respectively) were observed. The observations were carried out on September 14, 2012 for CH^+ J=3-2 and on September 15, 2012 for the OH 84 μmm and CO J=19-18.

All the lines were observed using the unchopped mode. An off-position was selected ∼30′ North-East of the source. The observations consist of a fully Nyquist-sampled raster map of 4×4 footprints targeting CH^+ J=3-2 and CO J=19-18, and a fully Nyquist-sampled raster map of 5×5 footprints targeting OH 84 μm. The observations result to maps of a total area of 110″×110″ similar to what was observed in atomic lines by Bernard-Salas et al. (2012) and included in the total area of dust observations of Arab et al. (2012). The configuration of the observations is shown in Chapter 7 in the attached article. Due to the overlapping footprints the quality of the data is better in the middle of the map than in the edges, where we only have the data from one footprint.

The line widths of the observed lines are not resolved. Also, the hyperfine structures of the OH Λ-doublets are not resolved in our observations. The spatial resolution is 10″ for the CO J=19-18, 9″ for the CH^+ J=3-2 line and the OH 119 μm doublets, and 6″ for the OH 84 μm doublets.

4.2.2 *SPIRE and HIFI*

In addition to the PACS observations we have used observations made with SPIRE (Griffin et al., 2010) in the high-resolution full-sampling mode of the SPIRE FTS on September 20, 2010. From this wavelength range we use the lower-J CO lines from J=4-3 to J=13-12 and ^{13}CO lines from J=5-4 to J=11-10. In addition, CH^+ J=1-0 at 359 μm and water lines 1_{11}-0_{00} at 269 μm and 2_{11}-2_{00} at 399 μm, and the $C^{18}O$ J=8-7 line at 342 μm are also used. These observations cover larger area (including the Trapezium stars) than the PACS observations, but only the area of PACS observations is used in this study.

The Heterodyne Instrument for the Far Infrared (HIFI, de Graauw et al., 2010) was used to observe the CH^+ J=2-1 line at 180 μm (1669 GHz) along a cut perpendicular to the Orion Bar (see Fig. 2 in the article in Chapter 7). The cut is centered at the position α_{J2000}= $05^h35^{min}20.61^s$, δ_{J2000}= -05°25′14″ and extends for 2′ with an inclination PA=52°. We used the on-the-fly observing mode using half-beam sampling, less good than Nyquist-sampling, using the nominal HIFI beam size at this frequency (12.3″). The data was obtained with the high-resolution spectrometer (HRS).

4.3 DATA REDUCTION

Data reduction for the HIFI observations was led by Paolo Pilleri (IRAP-CNRS, Toulouse), thus I will concentrate here on the PACS and SPIRE observations.

4.3.1 *PACS observations: Maps with PACSman*

The PACS observations used in this study were first reduced with HIPE 10.0.2843 to a level 1 cube. At this level the data is calibrated in flux and in wavelength. The final maps were further reduced and analyzed using IDL-based software PACSman version 3.55 (Lebouteiller et al., 2012). This is an alternative to the reduction and analysis steps performed in HIPE after the level 1 cube. PACSman includes transient correction, line fitting, map projection, and map analysis. All the observation modes are currently supported.

When cosmic rays hit the detector they can modify the pixel response over a given period of time. These hits are called transients. PACSman uses a multiresolution algorithm to correct for transients, which results in a more robust correction for transients, specially when several transients overlap in time. Transients need to be corrected only for unchopped observations, since the fast chopping allows their reliable removal. The corrections are not needed for chopped observations, because the telescope observes alternatively the source and an off position. The difference automatically gets rid of detector's response variations. Thus, extra correction in the data reduction phase is not needed.

In PACSman the lines are fitted with a Gaussian profile using a polynomial baseline. First, the continuum is fitted around the line and then using this as a starting point, the final fit with continuum and line are performed. Line fluxes are measured for each spatial pixel independently. Errors are not calculated for individual measurements, but estimated by calculating the dispersion of measurements in a given wavelength bin (defined as 1/5 of the line FWHM). Thus, the error is not calculated for individual spectrum, but the averaged final spectrum combined from all the measurements. Prior to line fitting 5σ clipping is performed. Clipping is needed to get rid of clear outliers and allows to fit the line better. To produce the final map, PACSman recreates an oversampled pixelated grid of the observations with 3″ pixel resolution and calculates the average fractional contribution of the given spatial pixels to the relevant position.

We calculated the statistical uncertainties for the PACS observations with PACSman. The uncertainties include the dispersion in the reduction process and the rms of the fit. These uncertainties are small and usually amount to 5–20 % for the, high-J CO, CH^+ and OH lines. The relative accuracy between spatial pixels given in the manual is 10 %[8]. We assume a conservative total error of 22 % for the integrated line intensities in the fainter regions, that is the upper limit of a combination of the calibration uncertainties (10 %) and the line fitting errors (5–20 %). For the Bar, the error is the less than 11 %.

4.3.2 *SPIRE observations: SUPREME*

The beam size and shape of the FTS varies depending on the wavelength. This is due to the multi-moded feedhorns of the spectrometer arrays (Makiwa et al., 2013). The super-resolution method SUPREME (Ayasso et al., in prep)[9] has been developed to overcome this problem. It uses a realistic physical instrument model and regularized inversion. SUPREME is used here to achieve better angular resolution. The gain in resolution with the SUPREME method is a factor of ~1–2, dependent on the wavelength. For instance, the resolution is improved at 400 μm from a FWHM from 32.6″ to 19.0″.

The first version of a method using realistic physical instrument model and regularized inversion was developed for the Spitzer Space Telescope spectrograph (Rodet et al., 2008). This was further developed and applied to SPIRE instrument by Orieux et al. (2012). They also tested the method with real SPIRE data. Estimates of the hyperparameters and instrument parameters in a Bayesian framework have been presented in Orieux et al. (2013). The current version of SUPREME (Ayasso et al., in prep) uses unsupervised Bayesian approach with enhanced beam and offset models.

The SUPREME method was applied to all SPIRE observations used in this study. Further, the lines were fitted with HIPE Spectrometer Cube fitting

8 From the PACS spectroscopy performance and calibration manual. This can be found at http://herschel.esac.esa.int/twiki/bin/view/Public/PacsCalibrationWeb

9 A SUPer REsolution Mapmaker for Extended emission: http://www.ias.u-psud.fr/supreme/home.php

procedure. This procedure uses a Gaussian fit. It should be noted, however, that the PSF is non-Gaussian and a FWHM does not account for the shape of the beam. We assume a total error of 36 % for the integrated line intensities, which includes the calibration uncertainties and the line fitting errors.

5

GROUND BASED OBSERVATIONS IN ONSALA

In this chapter I introduce the telescope and describe the observations of cold clumps which were used in Chapter 6 and in the included article.

5.1 INTRODUCTION TO THE TELESCOPE

The Swedish National Facility for Radio Astronomy, Onsala Space Observatory (OSO), at Chalmers University of Technology hosts a 20-m radio telescope built in 1975–1976 and upgraded in 1992. It is a mm- and cm-wave antenna with a range up to 116 GHz, enclosed in a radome. Because of the radome, the wind speeds and sun do not cause any restrictions on the use of the telescope. The receivers available at the time of the observations were SIS-mixer for the range 85–116 GHz and HEMT amplifiers for 18–50 GHz. The telescope is an elevation-azimuth mounted Cassegrain antenna. It has a diameter of 20.1 m, surface accuracy of 130 μm (rms), and pointing accuracy of 3″ rms in azimuth and elevation. In addition to being a single-dish instrument, the telescope is used in VLBI observations.

The 100 GHz receiver is based on a cryogenically cooled SIS sideband separation mixer and actually consists of two complementary mixers. The system covers 84–116 GHz and has an SSB receiver temperature of 100 K. The backend instruments include two reconfigurable hybrid autocorrelators and a Fast Fourier transform (FFT) spectrometer. These can all run simultaneously. The available spectrometers are the broadband autocorrelator (RCC) with a maximum bandwidth of 1280 MHz (corresponding to a velocity coverage of 3300 km s^{-1} at 115 GHz) with highest spectral resolution of 30 Hz (available on special request, normally resolution of 12.2 kHz is the highest available), and the FFT spectrometer for resolutions of 12 and 61 kHz at 100 and 1000 MHz bandwidths. The data used in Chapter 6, however, is the RCC data, since it yielded better results.

The telescope offers three observational methods: beam switching, position switching, and frequency switching. Beam switching gives the best baselines, since the switching is relatively fast. However, the baseline tends to show curvature. It is mainly used for weak and broad lines. Position switching is slower, because the whole antenna moves in switching and the baseline is highly dependent on the atmospheric conditions. It is used for complex spectra and large source extents. Of the offered modes frequency switching is the most efficient considering the signal-to-noise ratio, provided that the signal and reference frequencies both fall within the band of the spectrometer. Thus, we chose this method for the cold clumps observations.

With this telescope the calibration used is the chopper wheel method (described, e.g., in Jewell, 2002). The intensity scale of the spectrum is given

in T_A^*, which is an approximate, corrected antenna temperature. The main beam brightness temperature is given by $T_{mb} = TA^* \times F_{eff}/B_{eff}$, where F_{eff} is the forward efficiency and B_{eff} is the beam efficiency.

5.2 OBSERVATIONS AND DATA REDUCTION

The selection of 21 clumps in 20 fields was based on fields previously mapped with the *Herschel Space Observatory*, *Galactic Cold Cores* key program (PI Juvela), and *Planck*. In these surveys the selected clumps show a significant excess of cold dust emission (Planck Collaboration XXIII, 2011). The clumps are cold (color temperature at $T_{dust} \lesssim 14$ K, 40″ resolution) but also bright at submillimeter wavelengths. The fields are located in the Milky Way at galactic latitudes |b|=$9-17°$, which ensures minimal confusion from background emission.

The observed lines were ^{13}CO (1-0), C^{18}O (1-0), and N_2H^+ (1-0) at the frequencies 110.2, 109.8, and 93.2 GHz. Larger areas were mapped in ^{13}CO, and one-dimensional strips across the clumps were observed in C^{18}O. N_2H^+ was observed in the ^{13}CO peak position. More comprehensive listing of the fields and targeted lines is in Chapter 6 in the attached article. While the clouds typically have a general cometary or filamentary morphology, the higher resolution *Herschel* submillimeter data show that, at small scales, the clouds can be resolved into several clumps.

All the observations used were made with a frequency switching method with a frequency throw of 10 MHz for ^{13}CO and C^{18}O and 5 MHz for N_2H^+. Considering the lines observed, for 86 GHz (N_2H^+) the half power beam-width (HPBW) is 44″ and the main beam efficiency is 0.65. For 109 GHz (^{13}CO and C^{18}O), the HPBW is 35″ and the main beam efficiency is 0.45. The expected noise for the ^{13}CO line was σT_{MB}=0.27 K, for the C^{18}O line σT_{MB}=0.18 K, and σT_{MB}=0.08 K for the N_2H^+ line at a velocity resolution of Δv ~0.14 km s^{-1}. The expected noise levels were reached as the observed noise for the ^{13}CO line was on average σT_{MB} ~0.27 K, and the observed noise for the C^{18}O line was on average σT_{MB} ~0.06 K, and for the N_2H^+ line was on average σT_{MB} ~0.05 K. N_2H^+ was only detected in six fields, however. There is a clear difference between ^{13}CO and C^{18}O σT_{MB}. Even though these lines are close to each other in wavelength, they cannot be observed simultaneously in Onsala. The C^{18}O signal is weaker than the ^{13}CO and we get a detection even with worse signal-to-noise ratio.

Due to bad weather, the integration time estimates on the observation request were optimistic, and the sizes of the ^{13}CO map sizes were reduced from the original to keep in the allocated observing time and desired signal-to-noise ratio. Example of this adjustment is shown in Fig. 5.1. Calibration observations were made every day after sunrise and sunset. The main calibration source was R Cassiopeiae, line SiO. U Orionis, with the same line, was also used.

I reduced the data with GILDAS/CLASS software package[1]. The frequency switched spectra were first folded and averaged. Then the baselines

1 Institut de Radioastronomie Millimétrique (IRAM): http://iram.fr/IRAMFR/GILDAS/

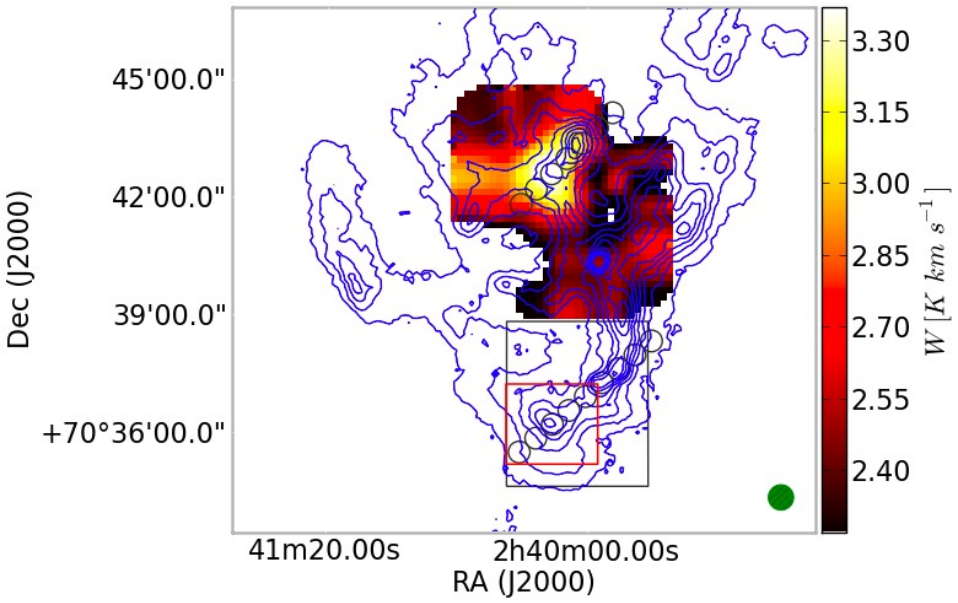

Figure 5.1: The field G131.65+9.75. The color image is the ^{13}CO(1-0) line area from Onsala observations in 2010. The contours show the intensity of the 250 μm dust emission measured with Herschel. The rectangle shows the area planned for ^{13}CO mapping, the smaller rectangle the revised plan, and the circles show the positions of the two C^{18}O strips.

were modeled and subtracted using third order polynomials, except for C^{18}O in sources G108.28+16.68, G131.65+9.75 north and south, and G161.55-9.30 where fifth order polynomials were used. Examples of the reduced spectra can be seen in Chapter 6, in the Appendix of the attached article.

Part III

DENSE STRUCTURES IN COLD ISM

6 PHYSICAL PROPERTIES OF COLD CLUMPS

The relative importance of different processes of star formation depends on the initial conditions in the gravitationally bound cores, often referred to as prestellar cores[1], where the actual star formation takes place. The core evolves towards a higher condensation, eventually leading to the formation of a protostellar object. Studying prestellar cores, thus, gives us insight on the initial conditions of star formation.

In this chapter I observed 21 clumps in the Milky Way at galactic latitudes $|b| = 9-17^\circ$ to find out if the cold clumps observed are indeed prestellar cores. The word *clump* is used as a general term for the dense structures investigated. However, some of these structures are likely to be cores themselves or contain unresolved cores.

6.1 PROPERTIES OF PRESTELLAR CORES

How the prestellar cores actually form is under a debate. The central role of self-gravity is evident, but the roles of the magnetic field and turbulence are still controversial. Currently, core formation is understood to happen either through linear or non-linear turbulent perturbations that initiate the formation (see e.g., André et al., 2009). These models are divided further depending on the magnetic field and if it is dynamically dominant[2]. Turbulence seems to have an important role in the core formation, but is too wide a subject to discuss here. Different core formation models have been discussed, e.g., by Padoan and Nordlund (2002), Bate and Bonnell (2005), Klessen and Burkert (2000), Tilley and Pudritz (2004), and Vázquez-Semadeni et al. (2005).

The role of magnetic field in molecular clouds and star formation, and, thus, in core evolution is not well understood. There is evidence that magnetic field offers magnetical support, while stars form preferentially in the regions which lack this support (Vázquez-Semadeni et al., 2011). Like turbulence, the role of the magnetic field is a wide subject and not discussed here in detail. Its role in star formation is studied continuously both in observations and by modeling (see, e.g., Myers et al., 2014; Chen and Ostriker, 2014; Soam et al., 2014; Alves et al., 2014; Davidson et al., 2014).

In this chapter I study the intrinsic physical properties of the cold clumps and the interaction with the molecular cloud and external factors are not

1 More discussion on the terminology and definition of cores and clumps is found in Chapter 2

2 Dynamically dominant magnetic field is here understood as a magnetic field that is strong enough, that the magnetic force is the most significant force influencing the system in question.

discussed in great detail. The following sections will introduce the main physical properties of prestellar cores.

6.1.1 *Size and density*

Prestellar cores vary greatly in size and mass. Generally the cores have mass of 0.5−5 $M_\odot$ and size of 0.03−0.2 pc, while clumps have a mass of 50−500 $M_\odot$ and size of 0.3−3 pc (Bergin and Tafalla, 2007). It is possible to have bigger and more massive cores, but small cores are far more common. The mass of the born stars is very similar to the mass of the prestellar core, and the stellar initial mass function (IMF) and prestellar core mass function resemble each other (André et al., 2009). This suggests that the mass required for the formation of individual stars is already there at the prestellar core.

The prestellar core is mainly identified from its density, i.e. the core is much denser than its surroundings. When the core is dense enough and quieter than its surroundings it becomes a gravitationally bound object. Cores have a mean density of 10^4 - 10^5 molecules per cm^{-3} and clumps 10^3−10^4 cm^{-3} (Bergin and Tafalla, 2007). The density of the cores exceed the density of the surrounding gas by a factor $\gtrsim$ 5-10. The observed density profiles for the cores tend to be flattened in the middle. Alves et al. (2001) mapped the B68 globule and were able to fit almost perfectly the Bonnort-Ebert (BE) density profile, which actually has a flattening middle. While some cores and globules can be fitted with the BE model, there are also many examples of cores that lack spherical symmetry, thus, having a non-symmetrical force component or lacking perfect equilibrium. In addition, the thermal pressure is important but not the only factor influencing core structure. Thus, the prestellar cores are usually more complex than the simple BE spheres (see Bergin and Tafalla, 2007, and references therein).

6.1.2 *Temperature*

The dust temperatures in the cores result from the balance between heating and cooling of the dust grains. The interstellar radiation field (ISRF) is responsible for heating the grains and the cooling is affected by thermal radiation from the grains (Mathis et al., 1983). In general the cores are colder than their surroundings. The core values being typically 10−12 K and surrounding cloud 15−20 K (average over ~1′). Denser cores can have even lower temperatures, close to 8 K (Bergin and Tafalla, 2007, and references therein). The gas temperature is also determined by the balance between heating and cooling. Heating happens mostly due to cosmic rays (photoelectric heating due to the external UV field being important only at cloud surfaces) while cooling is mainly caused by line radiation from the atomic and molecular species, namely [CII], [OI], H_2, and CO (Goldsmith and Langer, 1978).

The equilibrium between heating and cooling is what regulates the kinetic temperature of the gas and dust inside the core (see e.g., Bergin and Tafalla, 2007; Juvela et al., 2011). The collisions of gas and dust particles start

the thermal coupling at typical core densities $\gtrsim 10^5$ cm^{-3} and this leads to the converging of the two temperatures. This process will heat or cool the gas depending on the difference of the gas and dust temperatures. Whether the gas and dust temperatures actually converge enough to equalize, depends on the exact density of the core and the external radiation field (Galli et al., 2002).

6.1.3 *Velocity*

The internal velocity motions in prestellar cores are low ($\sim$1 km s^{-1}, largest intrinsic line widths being $<$10 km s^{-1}) compared to molecular clouds as a whole. Despite the low intrinsic speed, the cores are complex, and there is no single dominant element causing these motions (Myers, 1983; Jijina et al., 1999).

In turbulent regions Larson's law for the line-width - size relation generally applies: molecular clouds are supersonically turbulent with velocity dispersions that increase as a power of the size[3]. This, however, might not be true within individual cores or clumps (McKee and Ostriker, 2007). The line widths of core-tracing molecular species tend to be very close to the thermal line width, which indicates that the turbulence is only a minor factor affecting core support and that thermal component has a bigger effect on the gas pressure (Bergin and Tafalla, 2007, and references therein). Also, when the internal turbulence in the core is sufficient compared to the self-gravity, the core will disperse instead of collapsing to form stars. Thus, prestellar cores are known to have a very low level of turbulence and subsonic internal motions.

Velocity changes that indicate an outflow are seen as a possible sign of a protostellar source in a core. This is because young stellar objects can cause very powerful winds and jet-like outflows. Besides rotation and outflows, inward motions are a typical velocity pattern in the cores (see e.g., Bergin and Tafalla, 2007). These are seen as self-absorbed spectral line profiles with a red-shifted dip and a brighter blue peak that can signify a subsonic contraction of the core. In addition, other physical processes have been suggested to explain the line broadening, e.g., asymmetric velocity fields with inward and outward motions (Lada et al., 2003), residual internal motions from asymmetric contraction (Keto et al., 2006; Tafalla and Santiago, 2004), and relative velocities between the core and the surrounding interstellar medium (Walsh et al., 2004).

6.1.4 *Chemistry*

The effects on the cloud's ability to cool and radiate away its internal energy, which are required processes for the collapse of the core and subsequently the star formation, are not well understood. The chemistry affects, for instance, the ionization level and the gas-grain microphysics of the molecular

3 see Chapter 2.2.1

cloud. Changes in ionization level affect the magnetic field which can have slowing effect on the collapse that forms the star.

In the prestellar phase, the dominant processes affecting the abundances of molecules are the molecular freeze-out and the following deuterium fractionation caused by the low temperature (see e.g., Bacmann et al., 2002; Flower et al., 2005; Tafalla et al., 2006). In the freeze-out molecular species deplete from the gas phase by freezing onto the dust grains. This depletion can have a great effect on the line intensities and profiles. For example, the N_2H^+ and deuterated species are enhanced due to the CO freeze-out (see, e.g., Lee et al., 2003; Tafalla et al., 2004; Lippok et al., 2013).

The N_2H^+ chemistry is dominated by the decrease of CO and this is why N_2H^+ is significantly more abundant in the dense cores in gas phase than at typical core densities, which makes N_2H^+ an excellent tracer of dense cores. The CO depletion is also expected to cause deuterium fractionation. In fact, atomic deuterium is mainly produced by $H_2D \xrightarrow{CO} DCO^+ \xrightarrow{e^-} D$ (Roberts and Millar, 2000). The reaction of H_2D and CO passes the deuterium atom to different molecular species, in particular to form DCO^+, and when the CO depletes, the D atom is passed on to produce species like H_2D^+, D_2H^+, and D_3^+ (see, e.g., Roberts et al., 2003; Walmsley et al., 2004).

6.2 STABILITY OF CORES

The prestellar core was defined in Chapter 2.2.2 as a starless core which is also gravitationally bound. Thus, the stability of the clumps is an important characteristic in determining if the clumps are actually prestellar cores.

The Jeans mass is a critical mass, which, if exceeded, should cause a collapse of the cloud. This would happen if the cloud is only thermally supported. The Jeans mass can be calculated as:

$$M_J = \left(\frac{\pi k T_K}{\mu m_H G}\right)^{1.5} \rho^{-0.5} = 18 M_\odot T_K^{1.5} n^{-0.5}, \tag{6.1}$$

where k is the Boltzmann constant 1.3806488×10^{-23} m^2 kg s^{-2} K^{-1}, T_K is the kinetic temperature (K), μ is the mean mass per particle, G is the gravitational constant 6.67384×10^{-11} m^3 kg^{-1} s^{-2}, ρ is the mass density (g cm^{-3}), and n is the total particle density (cm^{-3}). Total particle density can be calculated as ρ/μ. In molecular clouds, the hydrogen nuclei are almost exclusively in H_2 molecules, thus, $n \simeq n_{H_2} + n_{He}$ (Jeans, 1928; Evans, 1999).

There are some problems with the use of the Jeans mass as the critical mass, however. In particular, no uniform static clouds have ever been observed. Molecular clouds tend to have substructures, clumps, and filaments. Also supersonic turbulence has been observed in the clouds and that can provide additional support against gravity, although in the actual cores only low turbulence levels have been detected. Thus, Jeans mass is still not sufficient to determine cloud stability.

One of the key concepts concerning cloud stability is the virial theorem. The virial theorem states that, for a stable, self-gravitating, spherical distri-

bution of equal mass objects, the potential energy U must equal the kinetic energy T within a factor of two: $T = -\frac{1}{2}U$. According to the virial theorem the virial mass and virial parameter can be calculated. These help us to determine the nature of core stability. The virial theorem is in essence:

$$\frac{1}{2}\ddot{\mathcal{I}} = \Omega_G + 2\mathcal{K} = 0 \tag{6.2}$$

where $\ddot{\mathcal{I}}$ is the second derivative of the moment of inertia of the cloud, Ω_G is the cloud's self-gravitational potential energy, and $\mathcal{K}$ is the net translational kinetic energy of the particles of the cloud due to random thermal motions and bulk motions, such as turbulence and rotation.

For a spherical cloud the kinetic energy is $\frac{1}{2}M\sigma^2$ and the self-gravitational potential energy is $-\frac{GM^2}{r}$. In these equations M is the cloud mass, r is the radius of the cloud, and σ is the velocity dispersion (see Eq. 6.5). When these are substituted into the virial theorem we get the virial mass:

$$M_{vir} \sim \frac{\sigma^2 r}{G}. \tag{6.3}$$

For a spherical, but no homogenous cloud, the virial mass can be estimated from the formula (MacLaren et al., 1988):

$$M_{vir} = \frac{k\sigma^2 r}{G}, \tag{6.4}$$

where σ is the full three dimensional velocity dispersion, averaged over the whole system given by (Lehtinen et al., 2004):

$$\sigma = \sqrt{3\left(\frac{kT_k}{\bar{m}} + \left(\frac{\Delta V^2}{8\ln(2)} - \frac{kT_k}{m}\right)\right)} \tag{6.5}$$

where $\bar{m}$ is the mean molecular mass and m the mass of the molecule used for observations and k depends on the density distribution as a function of distance from the cloud center $\rho(r)$. For $\rho(r) \propto r^{-n}$, where $n<3$:

$$k = \frac{5-2n}{3-n}. \tag{6.6}$$

We assume a spherically symmetric source, thus, the density profile defines the value of k, as the virial mass is dependent on how the mass is divided. If the cloud's mass is close to the virial mass, the cloud is in a virial equilibrium. If it exceeds the virial mass, the cloud will collapse unless it has another mode of support. If the mass of the cloud is less than the virial mass, it is not gravitationally bound and without external pressure for support, it will disperse.

When the core has no other form of support and has a significantly greater mass than the virial mass, the core will collapse due to self-gravity. The shortest possible time scale of this collapse is called the free-fall time scale and is given by

$$t_{ff} = \left(\frac{3\pi}{32G\rho}\right)^{0.5} = 3.4 \times 10^7 n^{-0.5} \text{years}. \tag{6.7}$$

Alternatively, if the mass of the core is much less than the virial mass, the core will disperse in the absence of external pressure by the dispersion time scale $t_{disp} \simeq \frac{r}{\sigma}$.

Core stability can also be investigated with BE spheres which are isothermal gas spheres that are bound by external pressure and are in hydrostatic equilibrium. They have been used to reproduce the column density profiles of cold, dense cores (e.g., Alves et al., 2001; Kandori et al., 2005). A mass can be calculated for the BE spheres and this BE mass can be used as an alternative to the virial mass. The critical BE mass is

$$M_{BE} \approx 2.4 R_{BE} \frac{\sigma^2}{G} \tag{6.8}$$

where R_{BE} is the BE radius, G is the gravitational constant, and σ is defined by Eq. 6.5.

6.3 PREVIOUS WORK ON COLD CORES

The study of dense cores has advanced greatly in the last decades due to the availability of new telescopes with improved sensitivity and better resolution. Previous work, thus, concentrated on global properties like total masses and average densities (see, e.g., Clemens and Barvainis, 1988; Benson and Myers, 1989). New large-scale optical, infrared, and radio observations have finally allowed resolution under 1′ and given possibilities to study the molecular clouds in more detail. These studies of molecular clouds and cores rely on information from extinction, dust continuum emission, and molecular lines (see reviews, e.g., Bergin and Tafalla, 2007; Evans, 1999).

6.3.1 *Measuring extinction*

Extinction can be measured to some extent on optical wavelengths, but near-infrared (IR) observations can give more detailed information on regions of high column density which are completely opaque at optical wavelengths. Extinction can be mapped with the star counting method (e.g., Cambrésy, 1999; Dobashi et al., 2005) or by a color-excess method (e.g., Lombardi and Alves, 2001; Indebetouw et al., 2005; Nishiyama et al., 2009).

With both methods near-infrared (NIR) observations have become increasingly important. They can be used to extend the optical extinction measurements to most opaque regions in molecular clouds (Bergin and Tafalla, 2007). With higher extinction values (A_V ~20) star count method can be applied to NIR observations, but at lower A_V-values color-excess gives better spatial resolution (Juvela et al., 2008).

The mapped extinction can be used to identify the clumps and to derive hydrogen column densities for the mapped region. The hydrogen column densities are estimated by assuming a linear relationship between extinction and the hydrogen column density measured from the inter cloud medium (e.g., Reina and Tarenghi, 1973; Gorenstein, 1975; Predehl and Schmitt, 1995; Güver and Özel, 2009).

6.3.2 *Dust observations*

New telescopes in the IR and FIR have brought the possibility to observe dust emission instead of just the extinction. The *Planck* satellite has provided maps of thermal dust emission from the whole sky. These maps include the molecular clouds within the Milky Way. From the *Planck* data and the IRAS (100 μm) survey, the Cold Clump Catalogue of *Planck* Objects (C3PO) has been compiled. This Catalogue has been reduced to 915 most reliable detections (high S/N sources) in Early Cold Clumps Catalogue (353−857 GHz, 350−850 μm), ECC (see, e.g., Planck Collaboration XXIII, 2011; Planck Collaboration XII, 2011; Planck Collaboration VII, 2011). Recently the catalogues have been updated and the Planck Catalogue of Galactic Cold Clumps (PGCC), an all-sky catalogue of Galactic cold clump candidates detected by Planck has been published (Planck Collaboration XXVIII, 2015). It provides a global view of the cold clump population over the whole sky.

Herschel observations of star-forming clouds, e.g., the Gould Belt Survey (André et al., 2010; Könyves et al., 2010) and the *Herschel imaging survey of OB Young Stellar objects* (HOBYS)[4] program (Motte et al., 2010), have led to the numerous detections of starless and protostellar condensations. Könyves et al. (2010) found 541 starless cores in the entire Aquila field. Most of these cores seem to be prestellar[5]. In Polaris only unbound starless cores were observed (André et al., 2010) and in the HOBYS fields more than 250 high-mass protostars are expected to be found (Motte et al., 2010). The condensations are particularly observed in nearby (d<500 pc) molecular clouds where *Herschel*'s resolution is high enough (SPIRE resolution 20−50″ depending on the wavelength: assuming 40″ → resolution of 0.97 pc at 500 pc) to resolve the densest parts. The condensations tend to be found in filaments, which are abundant in the molecular clouds (André et al., 2013).

6.3.3 *Molecular line observations*

The molecular line observations in general are discussed in Chapter 3. Here I discuss the studies relevant to the paper by Parikka et al. (2015). Arzoumanian et al. (2013) investigated the gas velocity dispersions of a sample of filaments in the IC 5146, Aquila, and Polaris interstellar clouds. For the measurement, ^{13}CO, $C^{18}O$, and N_2H^+ lines were used. The filaments were found to contain both supercritical gravitationally bound structures and subcritical structures that are likely to disperse with time. This result confirms the use of gravitational instability as a criteria of a prestellar core that was used by André et al. (2010) in the earlier analysis of these fields (Arzoumanian et al., 2013). Hacar et al. (2013), who observed 10-pc long filamentary complex in Taurus, found that although the structure contained

4 see http://hobys-herschel.cea.fr

5 Prestellar core as defined in Chapter 2: the core is gravitationally bound and is evolving but no protostellar objects exist yet within the core.

many filaments, the dense core formation was concentrated in few of the filaments and the distribution was not random, but seemed to depend on an intrinsic property of each velocity-coherent filament.

Wu et al. (2012) surveyed 674 sources of the ECC catalogue with single-point observations of ^{12}CO (1-0), ^{13}CO (1-0), C^{18}O (1-0) and mapped 10 clumps with 22 identified potential cold cores. ^{12}CO and ^{13}CO were detected in 673 sources. C^{18}O was detected in 68 % of the sample. They found excitation temperatures of 4−27 K. These temperatures were generally slightly higher than the ones derived from the dust. The average abundance ratio for ^{13}CO and C^{18}O was found to be 7.0±3.8, absolute value being higher than the terrestrial value of 5.5, though still within the uncertainties. Seven cores of the 22 identified potential cores were found to be likely gravitationally bound. In a follow-up study (Meng et al., 2013), 71 of the sources observed only with single-point observations were examined and the majority of the cores were found to be not bound and will likely disperse and therefore no star will be formed. However, 51 clumps were also mapped in ^{12}CO and ^{13}CO in Orion Complex. In this case 82 dense cores were found and most of these seemed to be gravitationally bound (Liu et al., 2012).

My study is a follow-up study of Juvela et al. (2012), where 71 fields were examined with *Herschel* and in infrared with AKARI and WISE. These observations were performed to examine the cloud structure and confirm the presence of cold dust in the selected fields identified from *Planck* observations (Planck Collaboration XXIII, 2011). Point sources were found in the mid-infrared observations in about half of these fields indicating active star formation. The cold dust still dominates the submillimeter spectra, thus, making these fields optimal to study early stages of star formation (Juvela et al., 2012).

6.4 PARIKKA ET AL.: THE PHYSICAL STATE OF SELECTED COLD CLUMPS

The aim of this paper is to understand the preliminary conditions which lead to star formation in interstellar clouds. For this purpose I have compared molecular line spectrum and dust continuum emission observations. In the interpretation of the data CRT[6] and Cppsimu[7] numerical models of radiative transfer were used (Juvela and Padoan, 2003; Juvela, 2005). This part was mainly conducted by Mika Juvela.

From *Planck* data more than 10,000 compact cold sources have been detected of which a large fraction are believed to be prestellar cores. For a subsample of clumps, the detections of cold dust have been confirmed by late *Herschel* observations. In this study, 20 fields which contained 21 clumps of those already mapped with *Herschel* at wavelengths 100−500 μm, were chosen for more detailed follow-up. The fields are believed to represent an early prestellar phase of star formation. These regions were mapped in the ^{13}CO(1-0) spectral line using the Onsala 20-m radio telescope. Across

6 https://wiki.helsinki.fi/display/~mjuvela@helsinki.fi/CRT
7 https://wiki.helsinki.fi/display/~mjuvela@helsinki.fi/Cppsimu

these ^{13}CO maps were observed strips of C^{18}O(1-0) lines, and N_2H^+ was observed in the center position. The observations were done by me (50 %) and Veli-Matti Pelkonen (50 %).

These observations enable me to determine the physical parameters of the gas component, examine the stability of the cores, and measure molecular depletion. More precisely, (1) to estimate core stability from line-widths based on kinematic and turbulent support, (2) to determine the column density of C^{18}O (and ^{13}CO) and to compare it with column densities derived from submillimeter dust emission, and (3) to estimate the column density of N_2H^+ across the clumps. Since we did not find N_2H^+ in most of the clumps and due to the bad weather during observations, we could only measure one point (beam size 40″) instead of the planned strip through the clump detected by *Herschel*, thus, the N_2H^+ was used only as an indication of a dense clump in comparison with the densities and masses calculated from the ^{13}CO and C^{18}O observations. I performed the data reduction and analysis on the ^{13}CO and C^{18}O observations and wrote most of the article except for the analysis on N_2H^+ and the appendix on modeling.

A further aim of this work was to compare the molecular line data with the dust emission and with theoretical model. The *Herschel* dust continuum data from the selected fields were used for the comparisons. The modeling was limited to two clumps that are located in one field. This field was chosen to enable comparison of clumps at the cloud edge and its center.

A&A 577, A69 (2015)
DOI: 10.1051/0004-6361/201423428

Astronomy & Astrophysics

The physical state of selected cold clumps⋆,⋆⋆

A. Parikka[1,2], M. Juvela[1], V.-M. Pelkonen[1,3], J. Malinen[1], and J. Harju[1]

[1] Department of Physics, PO Box 64, 00014 University of Helsinki, Finland
e-mail: anna.parikka@ias.u-psud.fr
[2] Institut d'Astrophysique Spatiale, Université Paris Sud, 91405 Orsay Cedex, France
[3] Finnish Centre for Astronomy with ESO (FINCA), University of Turku, Väisäläntie 20, 21500 Piikkiö, Finland

Received 15 January 2014 / Accepted 5 February 2015

ABSTRACT

Context. The study of prestellar cores is essential to understanding the initial stages of star formation. With *Herschel* more cold clumps have been detected than ever before. For this study we have selected 21 cold clumps from 20 *Herschel* fields observed as a follow-up on original *Planck* detections. We have observed these clumps in ^{13}CO (1−0), C^{18}O (1−0), and N_2H^+ (1−0) lines.
Aims. Our aim is to find out if these cold clumps are prestellar. We have examined to what extent independent analysis of the dust and the molecular lines lead to similar conclusions about the masses of these objects.
Methods. We calculate the clump masses and densities from the dust continuum and molecular line observations and compare these to each other and to the virial and Bonnor-Ebert masses calculated for each clump. Finally we examine two of the fields with radiative transfer models to estimate CO abundances.
Results. When excitation temperatures could be estimated, the column densities derived from molecular line observations were comparable to those from dust continuum data. The median column density estimates are 4.2×10^{21} cm^{-2} and 5.5×10^{21} cm^{-2} for the line and dust emission data, respectively. The calculated abundances, column densities, volume densities, and masses all have large uncertainties and one must be careful when drawing conclusions. Abundance of ^{13}CO was found in modeling the two clumps in the field G131.65+9.75 to be close to the usual value of 10^{-6}. The abundance ratio of ^{13}CO and C^{18}O was ∼10. Molecular abundances could only be estimated with modeling, relying on dust column density data.
Conclusions. The results indicate that most cold clumps, even those with dust color temperatures close to 11 K, are not necessarily prestellar.

Key words. ISM: clouds – submillimeter: ISM – molecular data

1. Introduction

The details of the initial stages of star formation are still poorly known, despite many observational and theoretical studies. This is in part because star formation involves a very complex mixture of effects of gravity, turbulence, rotation, radiation, thermodynamics, and magnetic fields. Both large representative samples of clumps and detailed studies of their properties and relations to their cloud environment are needed.

Herschel observations of star-forming clouds, e.g., those conducted within the Gould Belt Survey (André et al. 2010) and HOBYS program (Motte et al. 2010), have lead to the detections of hundreds of starless and protostellar condensations. This is particularly true for nearby star forming clouds where the *Herschel* resolution is sufficient to resolve gravitationally bound cores. The objects appear preferentially within filaments, which are a conspicuous feature of all interstellar clouds (André et al. 2014). The filaments themselves contain both supercritical gravitationally bound structures and subcritical filaments that are likely to disperse with time (Arzoumanian et al. 2013).

The *Planck* satellite has performed an all-sky survey to map anisotropies of the cosmic microwave background (Tauber et al. 2010). At the same time *Planck* is providing maps of thermal dust emission from molecular clouds within the Milky Way. From these data more than 10 000 compact cold sources have been detected and a large fraction of these are believed to be prestellar cores or larger structures harboring prestellar cores (Planck Collaboration XXIII 2011). The *Planck* and IRAS (100 μm) surveys have been used to compose the Cold Clump Catalogue of *Planck* Objects (C3PO), from which 915 most reliable detections were published as the Early Cold Clumps Catalogue (353−857 GHz, 350−850 μm), ECC (see, e.g., Planck Collaboration VII 2011; Planck Collaboration XXII 2011). The sources were detected with the method described in Montier et al. (2010) and the initial results on the Planck detections were described in Planck Collaboration XXII (2011), Planck Collaboration XXIII (2011). The final version of C3PO is currently in preparation and will provide a global view of the cold clump population over the whole sky.

A number of *Planck* detections of cold clumps have been confirmed with the *Herschel* Space Observatory observations (100−500 μm) to be cold ($T_{\rm dust} \sim 14$ K or below) and also dense. For the present study, we selected clumps from fields covered in the *Herschel* open time key program Galactic Cold Cores (Juvela et al. 2010). The aim of this *Herschel* program is to examine a representative cross section of the source population of cold clumps observed with *Planck* and to determine the physical properties of these clumps. The *Herschel* results suggest that many of the sources are already past the prestellar

⋆ *Herschel* is an ESA space observatory with science instruments provided by European-led Principal Investigator consortia and with important participation from NASA.
⋆⋆ Appendices are available in electronic form at http://www.aanda.org

phase (Juvela et al. 2010, 2011). In this paper, we refer to sources that are gravitationally bound as prestellar objects. If the estimated mass exceeds the virial mass, the object is expected to be gravitationally bound. Bonnor-Ebert (BE) spheres are used as an alternative model to recognize prestellar cores (André et al. 2010; Könyves et al. 2010).

In an earlier study, a sample of 71 fields at distances ranging from ~100 pc to several kiloparsecs were examined. The *Herschel* observations, together with AKARI and WISE infrared data, were used to confirm the presence of cold dust. In about half of the observed fields, point sources were found in the mid-infrared, indicating active star formation. However, the cold dust still dominated the submillimeter spectra in these active star formation areas (Juvela et al. 2012b).

Some of the *Planck*-detected clumps have already been studied in molecular lines. Wu et al. (2012) surveyed 673 sources with single-point observations and mapped 10 clumps with 22 identified potential cold cores. They found seven cores that are likely to be gravitationally bound and, thus, on the verge of collapse. In a follow-up study, 71 of the sources observed only with single-point observations were examined and 90% of the found cores were starless (Meng et al. 2013). The clumps studied by Wu et al. (2012) and Meng et al. (2013) did not include the clumps chosen for this paper.

The definition of dense structures in the ISM is still an ongoing process. The clumps are small and dense condensations in the molecular clouds, often inside filaments. Cores are even smaller and denser. Bergin & Tafalla (2007) defined the clumps to have a mass of 50−500 $M_{\odot}$, size of 0.3−3 pc, and density of 10^3−10^4 cm^{-3}. Cores were defined to have mass of 0.5−5 $M_{\odot}$, size of 0.03−0.2 pc, and density of 10^4−10^5 cm^{-3}. We use the word clump as a general term for the dense structures we investigate here, however, some of these structures are likely to be cores themselves or contain unresolved cores.

Extensive surveys have been done in ^{12}CO and ^{13}CO over the Galactic plane and of nearby star-forming clouds (see, e.g., Combes 1991, for review). However, general surveys are not the best method to research possible compact sources. For the first time, with *Planck* and *Herschel*, we can identify the coldest and densest clumps in the known molecular clouds complexes and focus on dedicated molecular line observations targeting the most interesting dense clumps in these regions.

We combine *Herschel* data with molecular line observations to examine the physical properties of several cold clumps and their likelihood to evolve into star-forming cores. To investigate the gravitational stability of the objects, molecular line observations are essential to providing direct information of the kinetic and turbulent forces and, thus, on the current stability of the clumps and the cores. The objects can become gravitationally unstable by cooling and accretion, possibly aided or hindered by turbulence and external forces (Bergin & Tafalla 2007; Ballesteros-Paredes et al. 2007).

We investigate the physical state of a few clumps that were originally selected based on the cold dust signature detected by the *Planck* satellite. We derive the CO column densities, volume densities, and clump masses and estimate the gravitational stability. The potential prestellar nature of the objects is investigated by comparing their mass estimates with virial masses. We look for signs of CO abundance variations as further evidence of the nature of the sources. Analysis assuming a local thermodynamic equilibrium (LTE) will be complemented with modeling. We selected one target for radiative transfer modeling where continuum data are used to constrain the models so that direct estimates of CO abundance are possible. The results also provide insights into the nature of the larger *Planck* cold clump population.

The paper is organized as follows. The observations are described in Sect. 2. Further, we go through the methods in Sect. 3. The results are presented in Sect. 4 and they are discussed in more detail in Sect. 5. Finally, the conclusions are summarized in Sect. 6.

2. Observations

2.1. The clump sample

We examine 21 clumps in 20 fields previously observed with *Herschel* at wavelengths 100−500 μm. The fields mapped with *Herschel* were originally selected based on the *Planck* survey, in which these clumps showed a significant excess of cold dust emission (Planck Collaboration XXIII 2011). Our selection was based on the *Herschel* data from the Galactic Cold Cores *Herschel* key program (PI Juvela) that carried out follow-up observations of 116 fields, each with one or more *Planck* cold clumps. We chose the bright clumps, which based on *Herschel* data also contain very cold dust (color temperature at $T_{\rm dust} \lesssim$ 14 K, 40″ resolution). The fields are located in the Milky Way at galactic latitudes $|b| = 9$−$17°$, which ensures minimal confusion from background emission. While they typically have a general cometary or filamentary morphology, the submillimeter data show that at small scales the clouds are fragmented to several clumps.

2.2. Molecular line observations

We mapped the selected clumps in the ^{13}CO (1−0) spectral line using the 20-m radio telescope in Onsala Space Observatory, Sweden, in February and March 2012. Toward the ^{13}CO peaks, we also observed C^{18}O (1−0) and N_2H^+ (1−0) lines. Part of the northern clump in field G131.65+9.75 was mapped in ^{13}CO (1−0) in February 2011 (Planck Collaboration XXIII 2011). The observed clumps are summarized in Table 1 and the observed spectra are shown in Appendix A. We carried out the observations in frequency switching mode, with frequency throws of ±10 MHz for ^{13}CO and C^{18}O and ±5 MHz for N_2H^+. For N_2H^+ in the 86 GHz band the half-power beam width (HPBW) is 44″ and the main beam effciency, η_B, is 0.65. For ^{13}CO and C^{18}O in the 109 GHz band the HPBW is 35″ and η_B is 0.45.

The telescope has a pointing accuracy of 3″ rms. The pointing was checked with SiO spectra toward bright sources R Cassiopeiae and U Orionis. The calibration was achieved through the chopper-wheel method, and the system gives antenna temperatures in units of $T_{\rm A}^*$ (Kutner & Ulich 1981). The backend was a low-resolution digital autocorrelator spectrometer (ACS) with a bandwidth of 40 MHz divided into 1198 channels. This gave a channel width of 25 kHz, corresponding to 0.068 km s^{-1} at the frequency of the ^{13}CO(1−0) line.

On average the rms noise for the observed ^{13}CO lines was ~0.27 K per channel on the main beam temperature ($T_{\rm MB}$) scale. The corresponding values for the observed C^{18}O and N_2H^+ lines are ~0.06 K and ~0.05 K, respectively. The data were reduced with GILDAS/CLASS software package[1]. The frequency switched spectra were folded, averaged, and the spectral baselines were modeled and subtracted using third

[1] Institut de Radioastronomie Millimétrique (IRAM): http://iram.fr/IRAMFR/GILDAS/

Table 1. Summary of observations.

Field	d (pc)	$T_{\rm dust}$	α (J2000)	δ (J2000)	^{13}CO (sq′)	C^{18}O (N)	N_2H^+ (N)
G86.97–4.06	700	11.5 ± 0.9	21 17 44.22	+43 18 47.1	4.55	1	1
G92.04+3.93	800	10.4 ± 0.8	21 02 23.43	+52 28 38.3	3.96	1	1
G93.21+9.55	440	10.6 ± 0.8	20 37 19.98	+56 54 42.6	6.79	2	1
G94.15+6.50	800	12 ± 1	20 59 04.80	+55 34 33.4	6.67	1	1
G98.00+8.75	1100	12 ± 1	21 04 22.70	+60 08 55.1	3.79	1	1
G105.57+10.39	900	10.9 ± 0.8	21 41 01.79	+66 34 40.9	8.33	1	1
G108.28+16.68	300	14 ± 1	21 09 08.60	+72 53 43.2	8.01	7	1
G110.80+14.16	400	14 ± 1	21 57 35.84	+72 46 49.1	6.88	2	1
G111.41–2.95	3000	13 ± 2	23 22 28.78	+57 36 44.5	7.77	1	1
G131.65+9.75 N	1070	11 ± 1	02 40 03.30	+70 43 20.1	6.79	4	1
G131.65+9.75 S	1070	13 ± 1	02 40 11.20	+70 36 09.5	8.89	7	1
G132.12+8.95	850	10.6 ± 0.9	02 41 49.64	+69 50 12.9	5.92	2	1
G149.67+3.56	170	13 ± 1	04 17 08.20	+55 13 40.6	4.89	1	1
G154.08+5.23	170	11.2 ± 0.9	04 48 08.73	+53 07 23.1	20.2	3	1
G157.92–2.28	2500	10.9 ± 0.8	04 28 48.30	+45 24 22.5	8.33	2	1
G159.34+11.21	1590	14 ± 1	05 42 17.30	+52 08 16.4	1 point	1	1
G161.55–9.30	250	13 ± 1	04 16 15.30	+37 45 35.0	2.22	5	1
G164.71–5.64	330	13 ± 1	04 40 44.43	+37 45 14.3	5.39	1	1
G167.20–8.69	160	12 ± 1	04 35 26.88	+34 18 25.6	6.88	2	1
G168.85–10.19	2610	13 ± 1	04 37 07.59	+31 43 01.2	1 point	1	0
G173.43–5.44	150	13 ± 1	05 07 49.46	+31 20 46.3	1 point	1	0

Notes. The table lists the 21 targets, kinematic distances for the fields (Montillaud et al. 2015), temperature of the dust, coordinates for the ^{13}CO (1–0) peak temperature (where the C^{18}O (1–0) and N_2H^+ (1–0) were observed), area in square arc minutes selected for the ^{13}CO (1–0) mapping, and number of observed points for C^{18}O (1–0) and N_2H^+ (1–0).

order polynomials, except for C^{18}O in sources G108.28+16.68, G131.65+9.75 north and south, and G161.55–9.30 where fifth order polynomials were used.

2.3. Dust continuum observations with Herschel

We observed the dust continuum data with the *Herschel* SPIRE instrument (Griffin et al. 2010) between November 2009 and May 2011. These observations consist of surface brightness maps of 250, 350, and 500 μm. The raw and pipeline-reduced data are available via the *Herschel* Science Archive, the user-reduced maps are available via ESA site[2]

We reduced these data similar to (Juvela et al. 2012b) and only a summary of these reduction steps is given here. We completed the reduction using the *Herschel* Interactive Processing Environment HIPE v.10.0 and the official pipeline with the iterative destriper and extended emission calibration options. The resulting maps are the product of direct projection onto the sky and averaging of the time-ordered data. The resolutions of the maps are 18″, 25″, and 37″ at 250, 350, and 500 μm, respectively.

The accuracy of the gain calibration of *Herschel* data is better than 7% in absolute terms and probably better than 2% band-to-band[3]. The surface brightness data do not have an absolute zero point and therefore, before temperatures or column densities can be estimated, we must set a consistent zero point across all *Herschel* bands. One alternative is to compare *Herschel* data with *Planck* and IRAS measurements (using IRAS data tied to DIRBE scale) and to make use of the zero points of those surveys (see, e.g., Juvela et al. 2012b). We opt for the more straightforward procedure of selecting a reference area with a radius of 1.5′ within the *Herschel* map and measuring surface brightness values relative to the average value found in the reference area. The central coordinates of the reference areas can be seen in Table 2. The derived dust temperature and column density estimates ignore the very diffuse medium to the extent that is visible in the reference region. The reference regions have low extinction ($A_V \sim 2$ or less) and therefore probably a lower fractional abundance of CO. Thus, even after background subtraction, the continuum data may probe a volume larger than the actual molecular cloud. Therefore, the extrapolation of the relations like in Fig. 1 does not necessarily go via the origin of that plot. This should not be a significant problem, however, because we are interested in the densest clumps that are far above the column density of the reference regions.

Table 2. Center coordinates of the 1.5′ radius reference areas.

Field	α (J2000)	δ (J2000)
G86.97–4.06	21 16 40.8	+43 34 45
G92.04+3.93	21 01 17.9	+52 34 45
G93.21+9.55	20 37 44.3	+56 44 49
G94.15+6.50	20 59 48.7	+55 56 19
G98.00+8.75	21 05 59.4	+59 51 19
G105.57+10.39	21 43 14.5	+66 26 12
G108.28+16.68	21 08 16.0	+72 51 20
G110.80+14.16	21 59 05.7	+72 37 40
G111.41–2.95	23 20 11.9	+57 35 20
G131.65+9.75	02 42 10.5	+70 45 20
G132.12+8.95	02 37 04.7	+69 53 43
G149.67+3.56	04 18 42.2	+55 29 55
G154.08+5.23	04 47 58.8	+53 14 42
G157.92–2.28	04 30 02.5	+45 25 50
G159.34+11.21	05 41 07.7	+51 54 33
G161.55–9.30	04 15 46.2	+37 40 56
G164.71–5.64	04 42 47.6	+38 22 45
G167.20–8.69	04 35 10.1	+34 11 09
G168.85–10.19	04 36 06.8	+31 50 54
G173.43–5.44	05 07 55.2	+31 04 55

[2] http://herschel.esac.esa.int/UserReducedData.shtml
[3] SPIRE Observer's manual http://herschel.esac.esa.int/Documentation.shtml

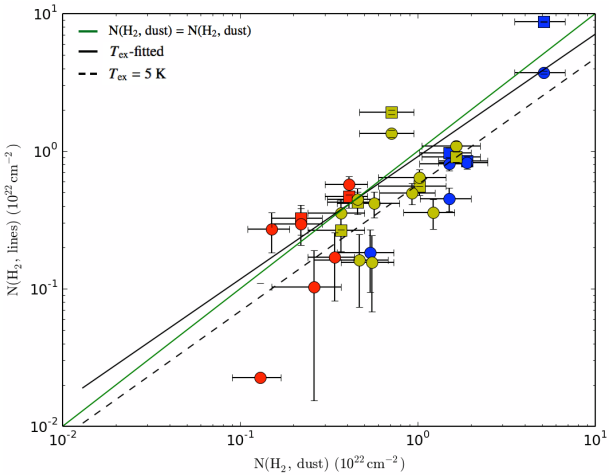

Fig. 1. Comparison of the column densities derived from molecular line and dust continuum observations. The squares are the column densities, where the excitation temperature could be calculated, and the circles are the column densities calculated with an assumed excitation temperature of 5 K. The colors indicate the dust color temperature. Blue is below 11 K, yellow is 11–13 K, and red is warmer than 13 K. The solid line is the linear least-squares fit to the column densities derived from the calculated excitation temperature, and the dashed line fits the $T_{\rm ex}$ = 5 K values. The green line indicates a line where $N\mathrm{H}_{2\rm dust} = N\mathrm{H}_{2\rm line}$.

The resolution of *Herschel* column density maps is 40″. The beam size is 35″ in CO observations and 40″ in N_2H^+ observations. Because of the relatively small differences and the extended nature of our sources, the data were compared directly without further convolution.

3. Methods

For the calculation of the CO column densities, we used the method described by Myers et al. (1983). Based on the data analysis, we calculated the optical depth at the peak of $C^{18}O$ line, τ_{18}, the excitation temperature of the $C^{18}O$ line, T_{18}, and the column density of the $C^{18}O$ in the cloud, N_{18}. To derive the total column density of H_2, the column density of $C^{18}O$, N_{18}, is divided by the commonly assumed abundance ratio $[C^{18}O]/[H_2] = 10^{-7}$.

The optical depths of ^{13}CO and $C^{18}O$ are related by (Myers et al. 1983, Eq. (2))

$$\tau_{13} = \tau_{18} \frac{n_{13}(J=1)}{n_{18}(J=1)} \frac{L_{13}}{L_{18}} \frac{\Delta V_{18}}{\Delta V_{13}} \frac{J(T_{18})}{J(T_{13})}. \quad (1)$$

In the equation $J(T) = T_0[\exp(T_0/T)-1]^{-1}$, where T_0 = 5.27 K for $C^{18}O$ and 5.29 K for ^{13}CO and T is the excitation temperature. The $n_{13}(J=1)$ and $n_{18}(J=1)$ are the number of molecules at J = 1 levels of the ^{13}CO J = 1–0 and $C^{18}O$, respectively. The L_{13} and L_{18} are the line-of-sight extent of the emitting gas and the ΔV_{13} and ΔV_{18} are the line widths of the ^{13}CO and $C^{18}O$ line, respectively. The equation assumes the same excitation temperature for both lines, the same beam filling (both lines originate in the same region), and the same velocity gradient. We also assume the terrestrial abundance ratio of 5.5 between ^{13}CO and $C^{18}O$ and we use the line width of $C^{18}O$ for the calculations. For a more comprehensive explanation of the method, see Myers et al. (1983).

We also derived the column density with the *Herschel* dust continuum observations. The observed intensity can be stated as

$$I_\nu = B_\nu(T_{\rm dust})(1-\mathrm{e}^{-\tau}) \approx B(T_{\rm dust}) \times \tau, \quad (2)$$

where I_ν is the observed intensity at a frequency ν, $B_\nu(T_{\rm dust})$ is the blackbody brightness of the object as a function of color temperature $T_{\rm dust}$, and τ is the source optical depth. The equation assumes a homogeneous source. In the far-infrared and at longer wavelengths the optical depths of the clouds are clearly below one. This justifies the approximation made in Eq. (2). The optical depth can be written as

$$\tau = \kappa_\nu \times N(\mathrm{H}_2) \times \mu, \quad (3)$$

where μ is the average particle mass per H_2 molecule, 2.8 u. We assume a dust opacity of $\kappa = 0.1(f/1000.0 \times 10^9)^{2.0}\,\mathrm{cm}^2/\mathrm{g}$, where f is the frequency (Beckwith et al. 1990). The constant 2.0 is the dust opacity spectral index, β. While it may vary from source to source, the value 2.0 we used is consistent with many observations of dense clumps although the average value in molecular clouds is likely to be closer to ∼1.8 (Beckwith et al. 1990; Boulanger et al. 1996; Hildebrand 1983; Planck Collaboration XXV 2011; Planck Collaboration XXIII 2011; Planck Collaboration XXII 2011). Again, the column density of hydrogen is $N(H_2)$. From Eqs. (2) and (3) we can derive the molecular column density

$$N(\mathrm{H}_2) = \frac{I_\nu}{B_\nu(T_{\rm dust})\kappa_\nu\mu}. \quad (4)$$

The derived column densities from molecular lines and dust can be used to calculate the mass and density of a cloud or a clump as

$$M_{\rm c} = N(\mathrm{H}_2) \times \pi R^2 \times \frac{\mu}{M_\odot}, \quad (5)$$

where R is the radius of the clump. The average density, n, is calculated using the hydrogen column density

$$n = \frac{N(\mathrm{H}_2)}{2R}, \quad (6)$$

where the clump diameter $2R$ is the full-width at half maximum (FWHM) from the *Herschel* column density map.

We derived the estimated virial mass from the formula (MacLaren et al. 1988)

$$M_{\rm vir} = \frac{k\sigma^2 R}{G}, \quad (7)$$

where k depends on the density distribution. We choose k = 1.333, which corresponds to density distribution $\rho(r) \propto r^{-1.5}$. The velocity dispersion is given by the equation

$$\sigma = \sqrt{\frac{kT_{\rm kin}}{\overline{m}} + \left(\frac{\Delta V^2}{8\ln(2)} - \frac{kT_{\rm kin}}{m}\right)}, \quad (8)$$

where $\overline{m}$ is the mean molecular mass (2.33 u assuming 10% He), and m is the mass of the molecule used for observations. The temperature, $T_{\rm kin}$, is the kinetic temperature, which is assumed to be 10 K. The velocity dispersion provides an estimate of the nonthermal motions that provide further support against gravity (Planck Collaboration XXIII 2011; Bertoldi & McKee 1992). If the cloud's mass is less than the virial mass, it is not gravitationally bound, and without external pressure for support, it will disperse.

We can also examine the stability using the model of BE spheres. The BE mass assumes a static isothermal cloud with no magnetic field (McKee & Ostriker 2007). We include the nonthermal component and use the effective sound speed instead of

Table 3. Clump sizes (FWHM from dust column density), column densities derived from dust and line data, and estimated $C^{18}O$ excitation temperatures.

Field	*FWHM* [′]	*FWHM* [pc]	$N(H_2)$ dust [10^{21} cm^{-2}]	T_{ex} [K]	$N(H_2)$ lines [10^{21} cm^{-2}]	$N(H_2)$, T_{ex} = 5 K lines [10^{21} cm^{-2}]
G86.97–4.06	0.4	0.17	12 ± 4	–	–	4 ± 1
G92.04+3.93	0.8	0.38	50 ± 20	4 ± 2	90 ± 40	37 ± 8
G93.21+9.55	0.6	0.15	19 ± 6	4.9 ± 0.4	9 ± 2	8 ± 1
G94.15+6.50	0.9	0.41	7 ± 2	4 ± 1	19 ± 8	13 ± 2
G98.00+8.75	0.5	0.35	10 ± 4	6 ± 1	6 ± 1	6.5 ± 0.9
G105.57+10.39	0.5	0.28	15 ± 5	–	–	8 ± 1
G108.28+16.68	0.8	0.15	1.5 ± 0.4	–	–	2.7 ± 0.8
G110.80+14.16	1.0	0.24	2.2 ± 0.7	4.7 ± 0.3	3.3 ± 0.8	3.0 ± 0.3
G111.41–2.95	0.6	1.09	6 ± 2	–	–	4.2 ± 0.1
G131.65+9.75 N	0.6	0.38	9 ± 3	–	–	5 ± 1
G131.65+9.75 S	0.3	0.17	4 ± 1	–	–	3.6 ± 0.5
G132.12+8.95	1.3	0.64	15 ± 5	–	–	5 ± 1
G149.67+3.56	0.4	0.04	5 ± 2	–	–	1.6 ± 0.4
G154.08+5.23	0.9	0.09	17 ± 6	5.5 ± 0.5	9 ± 2	11 ± 1
G157.92–2.28	0.4	0.55	5 ± 2	–	–	1.8 ± 0.6
G159.34+11.21	1.4	1.33	4 ± 1	–	–	6 ± 2
G161.55–9.30	0.5	0.07	6 ± 2	–	–	1.6 ± 0.4
G164.71–5.64	0.8	0.15	3 ± 1	–	–	1.7 ± 0.3
G167.20–8.69	1.2	0.12	5 ± 2	5.1 ± 0.4	4 ± 1	4.7 ± 0.5
G168.85–10.19	1.6	2.43	1.3 ± 0.4	–	–	0.2 ± 0.1
G173.43–5.44	2.6	0.23	3 ± 1	–	–	1.0 ± 0.2

Notes. We plot the column densities calculated from molecular observations in comparison with the column density calculated from dust continuum observations in Fig. 1.

the isothermal sound speed. As a difference to the virial mass, the BE model includes the external pressure. The critical BE mass (Bonnor 1956) is

$$M_{BE} \approx 2.4 R_{BE} \frac{\sigma^2}{G}, \quad (9)$$

where R_{BE} is the BE radius, and G is the gravitational constant.

4. Results

4.1. Comparison of dust continuum and molecular line data

First we compare the column densities calculated from the molecular line observations to the column densities calculated from the dust continuum observations. The sizes of the clumps were estimated as a FWHM from the dust column density maps and the physical sizes in pc are in Table 3. Twelve of the clumps are larger than the size criteria (0.03−0.2 pc) given by Bergin & Tafalla (2007) for cores, and, thus, are larger structures that could contain further substructures.

We did not get a result for the excitation temperature in all of the cases. This is most likely because of the greater ratio between ^{13}CO and $C^{18}O$ abundances than the 5.5 that was assumed in the calculations. Thus, we initially used an estimate of T_{ex} = 10 K (see, e.g., Dobashi et al. 1994; Alves et al. 1999). The results from the calculations showed, however, that when T_{ex} could be estimated, it was typically 5 K (see Table 3). Therefore, we show in Table 3 column densities for a fixed value of T_{ex} = 5 K. We plot the column densities calculated from molecular observations in comparison with the column density calculated from dust continuum observations in Fig. 1.

In Fig. 1, the cases where T_{ex} could be derived are plotted with square symbols, the solid line showing the corresponding linear least-squares fit. The column densities calculated with T_{ex} = 5 K are plotted with circles and fitted with a dashed line. In the cases where the excitation temperature could be calculated from the observations, the T_{ex} = 5 K values are usually within the margin of errors. The column densities calculated from dust are typically higher but also often within the margin of error. For example, for G159.34+11.21, for which $N(H_2)_{dust} = 4 \pm 1 \times 10^{21}$ cm^{-2} and $N(H_2)_{5K} = 6 \pm 2 \times 10^{21}$ cm^{-2}. In some cases the column densities are quite different, however. This is the case for G86.97–4.06, where $N(H_2)_{dust} = 1.2 \pm 0.4 \times 10^{22}$ cm^{-2}, while the value derived from the line data is much lower, $N(H_2)_{5K} = 4 \pm 1 \times 10^{21}$ cm^{-2}. Uncertainty of the background subtraction could contribute to some of these differences. For example, in G86.97–4.06 the reference region is estimated to have a column density of $\sim 10^{21}$ cm^{-2}, which corresponds to a diffuse part of the cloud with little CO. However, the presence of a small column density of gas without CO molecules cannot explain the difference in the column density estimates of several times 10^{21} cm^{-2}.

The dust color temperatures of the clumps are shown in Fig. 1 in different colors: blue for clumps below 11 K, yellow for the range of 11−13 K, and red above 13 K. The column densities derived from dust show an anticorrelation with the dust color temperature as denser regions are cooler. This anticorrelation on the dust color temperature was not seen as clearly in the column densities derived from molecular line observations, as there are several column densities $\sim 0.5 \times 10^{22}$ cm^{-2} independent of the dust color temperature.

The maps of $T_{mb}(^{13}CO)$ are shown in Fig. 2. The contours correspond to the column densities derived from dust continuum data (subtracting the local diffuse background). The statistical error in the column density maps of the dust is at level 2×10^{20} cm^{-2}. All the contours are at more than 10σ level and, thus, statistically significant. The S/N of ^{13}CO maps is lower. In a few cases, we get over 5σ detection for the whole map, namely

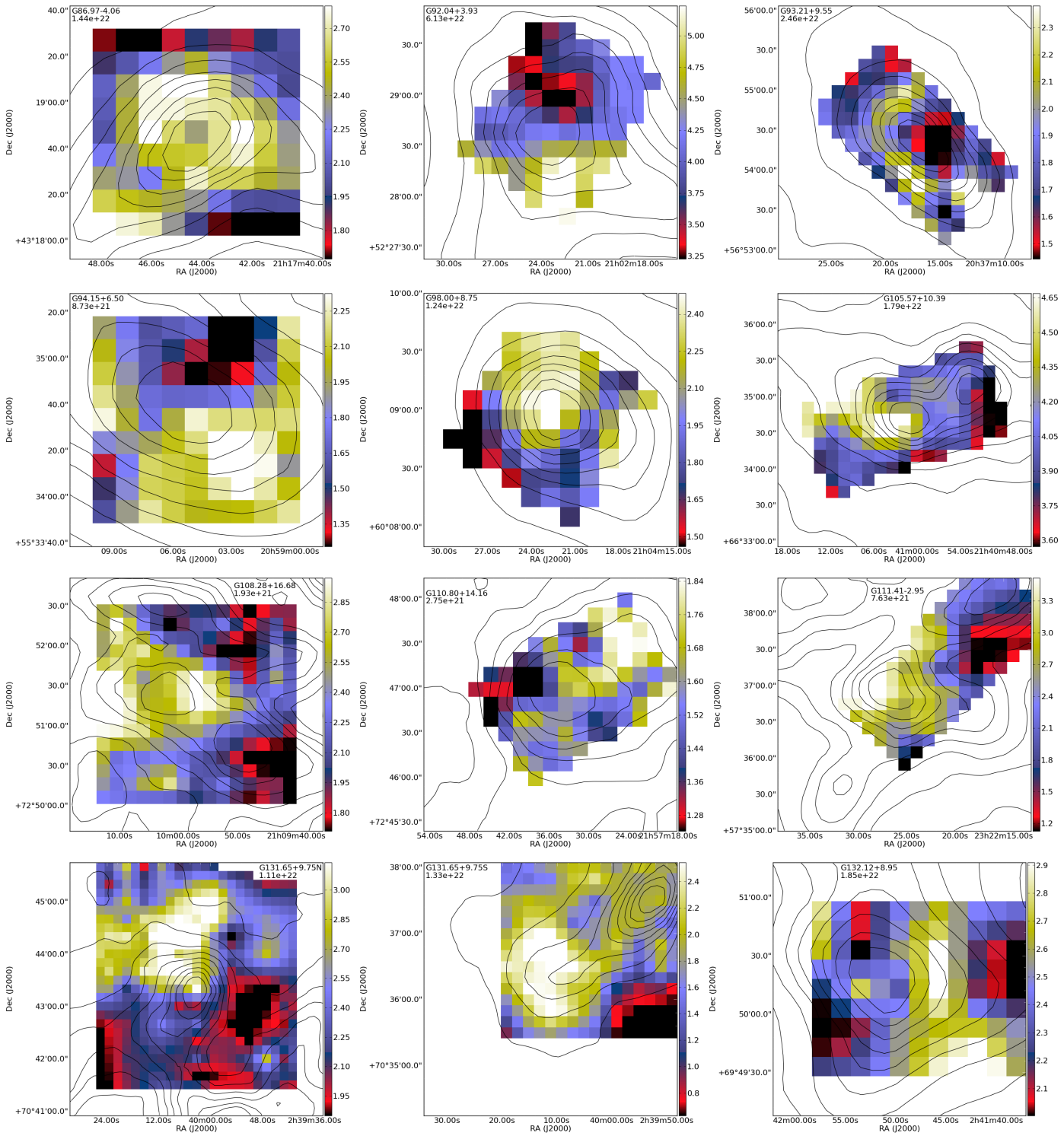

Fig. 2. Maps of ^{13}CO main beam temperature (T_{mb} [K], resolution 35″). The contours show the column density derived from dust continuum observations (resolution 40″), with contour steps 10% of the peak value. The name of the field and the maximum value of $N(H_2)$ derived from dust emission are marked in each frame.

for fields G105.57+10.39 and G149.67+3.56. In five fields, G86.97–4.06, G108.28+16.68, G131.65+9.75 S, G157.92.28, and G164.71–5.64, the signal drops below 2σ in part of the field.

In all the maps, we see a peak in the main beam temperature of ^{13}CO close to the dust column density peak. For few fields, e.g., G98.00+8.75 (Fig. 2), the peaks coincide, but for most cases there is a small shift, which can be up to 0.5′. In most cases the shift is smaller than the resolution of the observations. In some cases, as in G149.67+3.56, the peaks coincide partly, but are still shifted. The shifts are small in physical sizes as well, ~0.01−0.22 pc, and less than the radius of the clumps.

Significant differences in the peak positions of dust and line emission are often observed because of molecular depletion, other chemical gradients, or because of temperature differences. Marsh et al. (2014) found shifts with a median distance of 59″ for $H^{13}CO^+$ and dust (250 μm). The dust and gas have been

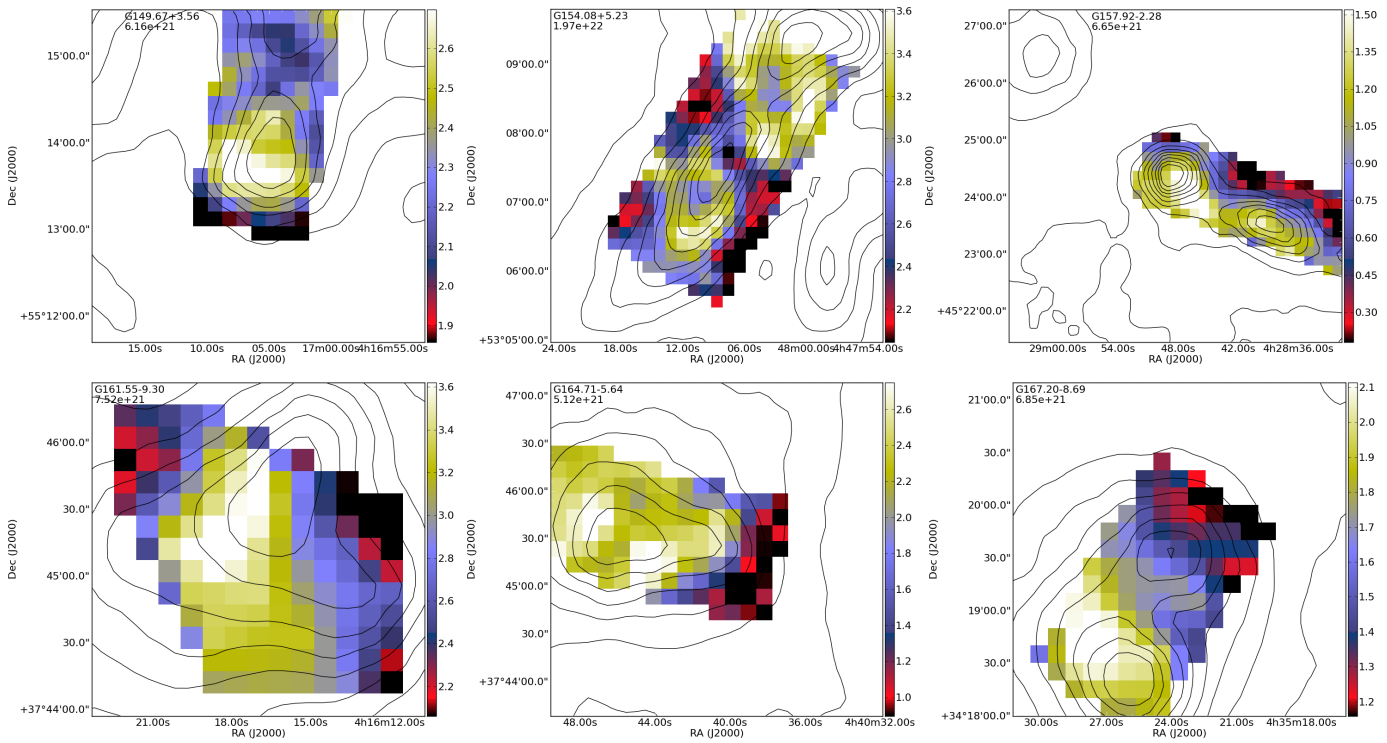

Fig. 2. continued.

found to be coupled in the interior of cores with densities above 3×10^4 cm^{-3}. At lower densities the temperature difference between the two components depends on the strength of the external UV field and not on density (Galli et al. 2002). Also, the depletion can increase the gas temperature in low and moderate densities (Goldsmith 2001). If we compare the densities calculated from the molecular line observations in Table 4, the clumps are less dense and, thus, dust and gas are not likely coupled in these clumps. However, the asymmetric displacement of the ^{13}CO emission in the densest clumps is more likely to be a sign of variations of ^{13}CO abundance.

4.2. Clump masses

The masses and densities along with the virial and BE masses are listed in Table 4. The uncertainties for densities and masses were determined with the Monte Carlo method. The uncertainties are big in many cases, up to 53%, and we must be careful when drawing conclusions from the density and masses. The mass errors do not include the error for distance (~30%, in the case of G168.85–10.19 the error is closer to ~50%), which further increases the uncertainty. In addition, in most cases the excitation temperature could not be calculated and the excitation temperature of 5 K was assumed. In the cases where the excitation temperatures could be calculated, the derived densities and masses are within the margin of error of those derived from the dust emission data. The field G92.04+3.93 is the only exception.

The calculated masses vary greatly between the clumps, from one tenth of a solar mass to a couple of hundred. Thus, they clearly cover a mix of different structural scales. Following the mass criteria of Bergin & Tafalla (2007), 11 of them are more massive than typical cores (>5 $M_\odot$). However, most of them show a single kinematic component and are therefore consistent with the idea of clumps as velocity coherent objects. If both $M_{\rm line}$ and $M_{\rm dust}$ are larger than the virial and BE mass, we consider them to be gravitationally bound, and thus (potentially) on the verge of collapse. If $M_{\rm line}$ or $M_{\rm dust}$ exceeds BE mass, the object is potentially bound, but if the estimated mass is smaller than both the virial and BE mass, we consider the object not to be prestellar.

Two clumps, G92.04+3.93 and G159.34+11.21, appear to be on the verge of collapse. The mass of G92.04+3.93 calculated with $T_{\rm ex}$ = 5 K is lower than the virial mass, but when excitation temperature could be calculated it exceeds the virial mass clearly. For the field G159.34+11.21, the excitation temperature could not be calculated, thus, the calculated mass is based on the assumption of $T_{\rm ex}$ = 5 K. Three other clumps, G94.15+6.50, G98.00+8.75, and G105.57+10.39, are supercritical, albeit not significantly, if we consider the BE mass. The remaining 16 clumps seem to be near equilibrium.

4.3. Observations of N_2H^+

To estimate the N_2H^+ column densities, we performed fits of the hyperfine structure of the J = 1–0 lines. The fits were carried out assuming a single excitation temperature. We treated the excitation temperature, optical depth of the 23–12 component, and the radial velocity and width of the spectral lines as free parameters (see Pirogov et al. 2003). Because of the low signal-to-noise ratio, the optical depths and excitation temperatures were uncertain. Therefore we calculated the column density assuming a fixed value of the excitation temperature, $T_{\rm ex}$ = 5 K, and optically thin emission (Caselli et al. 2002). The line parameters and obtained column densities are listed in Table 5. We estimated the error estimates with the Monte Carlo method, however, excluding the effect of the uncertainty of $T_{\rm ex}$. Apart from G86.97–4.06, shown in Fig. 3, the N_2H^+ spectra are shown in Appendix B.

For most of the studied clumps, N_2H^+ line was not detected, suggesting that these clumps are not dense enough for significant CO depletion and the associated rise of N_2H^+ abundance

Table 4. The used line width of $C^{18}O$, densities, masses, virial masses, and BE masses for all the targets using molecular line observations and mass value calculated from the dust observations.

Field	$\Delta V_{C^{18}O}$ [km s^{-1}]	n [10^3 cm^{-3}]	n [10^3 cm^{-3}] (T_{ex} = 5 K)	M_{line} [$M_\odot$]	M_{line} [$M_\odot$] (T_{ex} = 5 K)	M_{dust} [$M_\odot$]	M_{vir} [$M_\odot$]	M_{BE} [$M_\odot$]
G86.97–4.06	0.74	–	7 ± 2	–	1.7 ± 0.5	6 ± 2	10 ± 2	6 ± 2
G92.04+3.93	1.79	70 ± 20	32 ± 8	230 ± 70	100 ± 20	130 ± 40	110 ± 30	70 ± 10
G93.21+9.55	0.65	19 ± 4	18 ± 2	3.2 ± 0.7	3.1 ± 0.4	7 ± 2	7.5 ± 0.8	4.5 ± 0.5
G94.15+6.50	0.85	15 ± 8	11 ± 2	60 ± 30	39 ± 7	20 ± 7	31 ± 6	18 ± 3
G98.00+8.75	0.76	5 ± 1	6.0 ± 0.8	12 ± 2	13 ± 2	22 ± 9	22 ± 3	13 ± 2
G105.57+10.39	0.76	–	9 ± 1	–	11 ± 2	21 ± 7	18 ± 3	11 ± 1
G108.28+16.68	1.07	–	6 ± 2	–	1.0 ± 0.3	0.6 ± 0.2	16 ± 4	10 ± 2
G110.80+14.16	0.31	4.4 ± 0.9	4.0 ± 0.5	3.3 ± 0.7	3.0 ± 0.4	2.2 ± 0.7	5.6 ± 0.6	3.4 ± 0.4
G111.41–2.95	2.27	–	1.2 ± 0.3	–	90 ± 20	120 ± 50	500 ± 100	290 ± 80
G131.65+9.75 N	1.22	–	4 ± 1	–	13 ± 3	23 ± 8	50 ± 10	30 ± 8
G131.65+9.75 S	0.53	–	7 ± 1	–	1.7 ± 0.2	1.8 ± 0.6	6.5 ± 0.9	3.9 ± 0.6
G132.12+8.95	1.39	–	2.3 ± 0.5	–	32 ± 7	110 ± 30	110 ± 30	70 ± 20
G149.67+3.56	0.64	–	12 ± 3	–	0.05 ± 0.01	0.15 ± 0.07	2.1 ± 0.5	1.3 ± 0.3
G154.08+5.23	0.56	33 ± 7	40 ± 4	1.3 ± 0.3	1.5 ± 0.2	2.3 ± 0.8	3.7 ± 0.5	2.2 ± 0.3
G157.92–2.28	0.87	–	1.1 ± 0.3	–	9 ± 3	30 ± 10	40 ± 10	26 ± 8
G159.34+11.21	0.84	–	1.4 ± 0.4	–	180 ± 60	130 ± 30	100 ± 30	60 ± 20
G161.55–9.30	0.48	–	7 ± 2	–	0.13 ± 0.04	0.4 ± 0.1	2.3 ± 0.7	1.4 ± 0.4
G164.71–5.64	0.50	–	3.6 ± 0.7	–	0.7 ± 0.1	1.4 ± 0.4	6 ± 1	3.4 ± 0.7
G167.20–8.69	0.32	12 ± 2	12 ± 1	1.0 ± 0.2	1.1 ± 0.1	0.47 ± 0.05	2.8 ± 0.3	1.7 ± 0.2
G168.85–10.19	0.21	–	0.03 ± 0.01	–	20 ± 10	130 ± 40	50 ± 30	30 ± 10
G173.43–5.44	0.24	–	1.4 ± 0.2	–	0.9 ± 0.1	2 ± 1	4.5 ± 0.7	2.7 ± 0.4

Notes. The values from molecular line observations are derived with T_{ex} calculated from $C^{18}O$ observations and with a fixed value of T_{ex} = 5 K.

Table 5. The main beam temperature, velocity, noise and column density of N_2H^+ in the fields it was detected.

Field	T_{mb} [K]	V [km s^{-1}]	ΔV [km s^{-1}]	rms [K]	N [10^{12} cm^{-2}]
G86.97–4.06	0.34 ± 0.03	5.50 ± 0.02	0.43 ± 0.04	0.06	1.1 ± 0.3
G92.04+3.93	0.17 ± 0.01	−1.80 ± 0.02	0.51 ± 0.04	0.04	3.0 ± 0.2
G93.21+9.55	0.23 ± 0.04	−1.73 ± 0.03	0.41 ± 0.08	0.07	2.1 ± 0.5
G98.00+8.75	0.23 ± 0.02	4.98 ± 0.03	0.54 ± 0.04	0.06	2.3 ± 0.6
G105.57+10.39	0.31 ± 0.02	−10.10 ± 0.02	0.46 ± 0.04	0.05	2.0 ± 0.5
G132.12+8.95	0.32 ± 0.02	−12.41 ± 0.02	0.51 ± 0.04	0.04	1.1 ± 0.3

(Bergin & Langer 1997; Charnley 1997). The line was detected in six clumps: G86.97–4.06, G92.04+3.93, G93.21+9.55, G98.00+8.75, G105.57+10.39, and G132.12+8.95 (see Fig. 3 for an example of the spectra and Table 5). These clumps were among those with coldest dust temperatures. The main line in the fields was T_{mb} ~0.2−0.8 K and the satellites are barely visible above the noise of ~0.05 K. The low excitation temperature of the CO lines can also be an indication of a low density, as in lower densities the molecules are less thermalized and the excitation temperature is much lower than the kinetic temperature. In the studied clumps, the excitation temperature of the $C^{18}O$ in most cases was ~5 K indicating a clear difference between the excitation and kinetic temperatures.

The calculated N_2H^+ column densities are only a few times 10^{12} cm^{-2}. These can be compared with the N_2H^+ survey of nearby, low-mass cores conducted by Caselli et al. (2002). In that study, for the low-mass cores, $M_{vir} \sim 10\ M_\odot$, the average N_2H^+ column density was ~7×10^{12} cm^{-2}, and they found starless cores had a marginally lower column density than protostellar cores. Our column densities correspond to a lower end of those values. Conversely, Pirogov et al. (2003) observed a sample of 35 massive molecular cloud cores (mean virial mass over 600 solar masses) and found an average column density of 29×10^{12} cm^{-2}. Our low column density values are consistent with the low mass of the clumps, but also suggest that the densities (and CO depletion) are not significant enough for a large N_2H^+ abundance.

4.4. Modeling

The observations were compared to radiative transfer models of CO lines and of dust continuum emission. The modeling is explained in more detail in Appendix C and we present only the main results. The modeling was limited to the two positions in the field G131.65+9.75. These positions were chosen as they were in the same field and, thus, enable comparison of clumps at the cloud edge and in its center.

The calculations that are based on the dust model of Ossenkopf & Henning (1994) find ^{13}CO abundances that are close to the value of 10^{-6}. Because the abundances depend greatly on the column density estimated from continuum data, the values are uncertain. The abundance ratio for ^{13}CO and $C^{18}O$ was found to be ~10, instead of the 5.5 assumed in Sect. 3, independent of the different assumptions used in the modeling (see Table C.1). Harjunpää & Mattila (1996) and Anderson et al. (1999) have also found similar abundance ratios in dark clouds and cores.

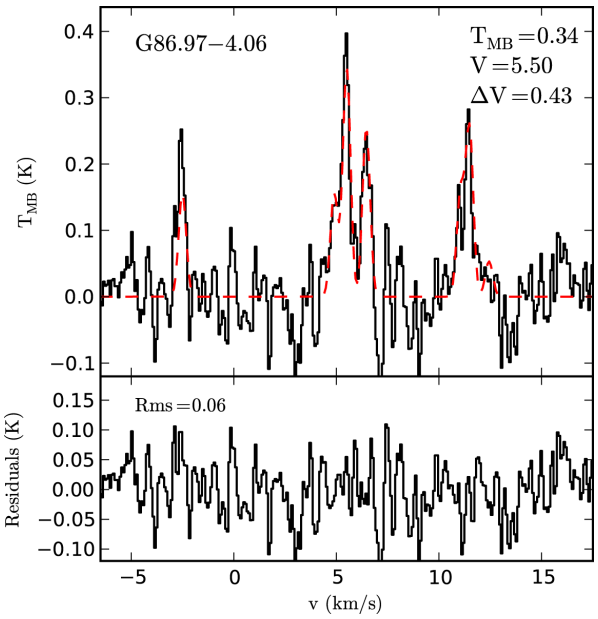

Fig. 3. N_2H^+ spectrum observed toward G86.97–4.06. The red dashed line is the fit to the hyperfine spectra and the lower subframe shows the fit residuals. The main beam temperature of the 23−12 component, the fitted radial velocity, the FWHM line width (km s^{-1}), and the residual rms noise (as main beam temperature) are given in the frames.

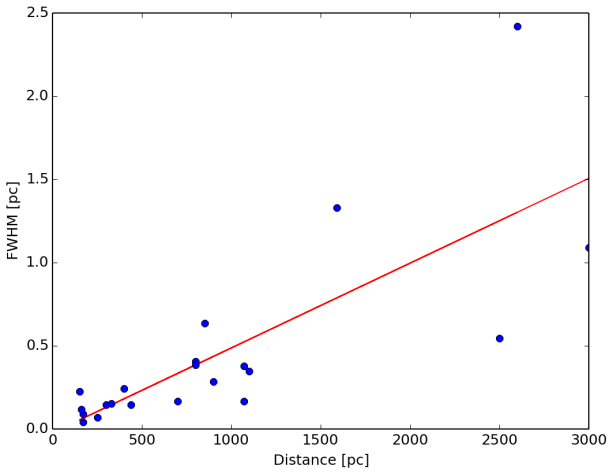

Fig. 4. FWHM (pc) vs. distance with the best fit.

5. Discussion

In about one third of the clumps, where excitation temperature could be estimated, the column densities are similar to those derived from dust (see Fig. 1 and Table 3). The column densities calculated with T_{ex} = 10 K, were lower by a factor of three. Using T_{ex} = 5 K, which was more in line with those that could be calculated, we get very similar results, especially with the cases where column densities are lower ($\sim 10^{21}$ cm^{-2}). Higher column densities tend to have larger uncertainties. For example, the column density for clump G92.04+3.93, 5 ± 2 × 10^{22} cm^{-2} from dust and 9 ± 4 × 10^{22} cm^{-2} from molecular lines is still inside the margin of errors. The cases where T_{ex} = 5 K were assumed to have mostly lower column densities than those where T_{ex} was solved. One explanation for this could be that CO has been depleted in these areas and, thus, the column density and the volume density calculated from CO observations are too low. The most likely explanation for the difference to the dust estimates is, however, the excitation temperature that is likely to vary from clump to clump.

The distances vary from 150 pc to 3 kpc across the sample, but the physical sizes (see Table 3 and Fig. 4) of the objects are, with one exception, ∼1 pc or below and thus comparable to typical clump scales as defined by Bergin & Tafalla (2007). The largest sizes include those of the most distant clouds, namely, G111.80+14.16, G157.92–2.28, G159.34+11.21, and G168.85–10.19. On average, the physical size is proportional to 0.77 times the distance, a natural result of our resolution at larger distances corresponding to larger structures.

Although there are large uncertainties in the column densities derived from the lines, even with the calculated T_{ex} values, the mass and column density estimates indicate that the selected clumps might not be very dense, and subsequently may not be actual prestellar cores. The lack of N_2H^+ emission also supports this conclusion, with upper limits $T_{mb}(N_2H^+) = 0.05–0.2$ K for the 16 of 21 clumps.

The fact that the excitation temperature could not be calculated in all of the selected positions could be caused by the abundance ratio of ^{13}CO and $C^{18}O$, which was actually higher than the assumed upper limit of 5.5. When extinction A_V is small, the abundance ratio can range much above the terrestrial value (Minchin et al. 1995). The abundance ratio we found in our models was ∼10, compared to the used terrestrial value of 5.5. We found the abundance for ^{13}CO, however, to be close to the canonical 10^{-6}, provided that we trust the dust-derived column densities. The difference in the estimated abundance ratio can be caused by a real differences in the abundances or excitation temperatures or by optical depth effects. The modeling, however, roughly takes the effect of optical depth and the expected difference in the excitation temperature of the isotopomers into account. This difference is caused by the difference in the photon trapping resulting from the difference in the optical depth of the lines. The assumption of the homogeneous source in the LTE analysis is inaccurate and, in reality, the excitation temperature of $C^{18}O$ is probably below the excitation temperature of ^{13}CO (and not equal as assumed) and drops precipitously toward the cloud surface. If the ^{13}CO is optically thick, the observed intensity originates in a different part of the cloud than the $C^{18}O$. Our calculations did not show ^{13}CO to be optically thick, but we calculated the optical thickness using the assumption that the excitation temperatures are equal. Because of the smaller optical depth, more of the $C^{18}O$ line photons escape, leading to a smaller excitation temperature. This is also clearly significant when the kinetic temperature varies within the cloud (Juvela et al. 2012a).

Based on the line data, 16 of the studied clumps are subcritical and, even considering the uncertainties of the mass estimates, only five sources could be gravitationally bound. In three cases, G92.04+3.93, G94.15+6.50, and G159.34+11.21, the calculated mass is larger than the virial and BE mass even when considering the uncertainty. Two other clumps, G98.00+8.75 and G105.57+10.39, are within error margins when we consider the BE mass. The five clumps are from the entire temperature range. However, only one clump, namely G92.04+3.93, had a mass larger than the virial and BE masses on a level >1σ, although G92.04+3.93 does not exceed this level if we assume T_{ex} = 5 K. If we consider the error in the distance of the object, none of the sources exceed the 1σ-level. However, only four clumps have masses below the virial and BE masses on a level >1σ. In the coldest supercritical clumps, G92.04+3.93 (T_{dust} = 10.4 K), G98.00+8.75 (T_{dust} = 11.6 K), and G105.57+10.39 (T_{dust} = 10.9 K), we detect the N_2H^+ line, which would support

the idea that these are being denser and possibly prestellar. The N_2H^+ emission seemed in general to be connected to the coldest clumps of ~10−11 K, although it was not observable in all the clumps of these temperatures. For the clumps where N_2H^+ was detected, we get a FWHM line width of $\lesssim$0.5 km s^{-1}, values typically found in prestellar cores (Johnstone et al. 2010).

If we rely on the mass estimates derived from dust observations instead of CO lines, the results are similar, only three clumps are below the virial mass and BE mass limits. Four of the clumps were larger by more than the error margins and could be classified as prestellar. The four clumps were G92.04+3.93, G105.57+10.39, G159.34+11.21, and G168.85–10.19. Thus, most of the clumps that were detected for low dust color temperature appear to disperse with time rather than form stars. Meng et al. (2013) and Wu et al. (2012) had similar results in their cold cores surveys: only a small fraction of the clumps were found to be prestellar. Of the 673 sources, 10 clumps were mapped and 22 potential cold cores were identified by Wu et al. (2012). Of these 22 cores, seven were found to be gravitationally bound. Our results are in general agreement with these results on the fractions of starless and prestellar cores (5 out of 21 were gravitationally bound). Meng et al. (2013) studied a subset of Wu et al. (2012) in more detail, and 90% of them were found to be starless (4 cores out of a sample of 38 were associated with sources). Studies of protostellar sources should be extended to a larger set of Planck clumps, including the 21 clumps that we discuss.

6. Conclusions and summary

We investigated 21 clumps, that show low dust color temperatures $T \sim 10-15$ K and are therefore potential places of star formation. To study the conditions in the clouds, we used molecular line and dust continuum observations. Our comparison of the two tracers shows that, even though the gas and dust emission are mainly morphologically compatible, the dust peak is sometimes shifted up to 30″ relative to the ^{13}CO maximum. The data were examined with standard LTE analysis and with radiative transfer modeling to understand better the physical and chemical state of the clumps.

The column density calculations from molecular lines were mostly within the uncertainties to those calculated from dust, when the excitation temperature could be calculated. With an assumed fixed excitation temperature value of $T_{ex} = 5$ K, the derived column densities were only slightly below the dust estimates.

Using modeling to compare dust continuum and line data, the abundance of ^{13}CO was found to be close to the typically assumed value of 10^{-6}. However, the abundance ratio of ^{13}CO and C^{18}O was ~10, higher than the terrestrial value 5.5.

The calculated masses had big uncertainties and one must be careful when drawing conclusions. When the masses were compared to virial and BE masses, only five clumps had a high enough mass to be gravitationally bound. In three of these clumps, we also found N_2H^+, so the clumps found in the fields G92.04+3.93, G98.00+8.75, and G105.57+10.39 could be prestellar. G92.04+3.93 and G105.57+10.3 were also among the coldest $T_{dust} \sim 10-11$ K, while G98.00+8.75 was slightly warmer $T_{dust} = 12$ K. The highest temperatures in the examined clumps were $T_{dust} \gtrsim 13$ K.

The stability of the clumps requires further study. Observations of higher CO isotopomer transitions and further density and temperature tracers are needed to better quantify the gas component in these cold clumps.

References

Alves, J., Lada, C. J., & Lada, E. A. 1999, ApJ, 515, 265
Anderson, I. M., Caselli, P., Haikala, L. K., & Harju, J. 1999, A&A, 347, 983
André, P., Men'shchikov, A., Bontemps, S., et al. 2010, A&A, 518, L102
André, P., Di Francesco, J., Ward-Thompson, D., et al. 2014, in Protostars and Planets VI, Henrik Beuther, eds. S. Klessen, C. P. Dullemond, & Th. Henning (Tucson: University of Arizona Press), 27
Arzoumanian, D., André, P., Peretto, N., & Könyves, V. 2013, A&A, 553, A119
Ballesteros-Paredes, J., Klessen, R. S., Mac Low, M.-M., & Vazquez-Semadeni, E. 2007, Protostars Planets V, 951, 63
Beckwith, S. V. W., Sargent, A. I., Chini, R. S., & Guesten, R. 1990, AJ, 99, 924
Bergin, E. A., & Langer, W. D. 1997, ApJ, 486, 316
Bergin, E. A., & Tafalla, M. 2007, ARA&A, 45, 339
Bertoldi, F., & McKee, C. F. 1992, ApJ, 395, 140
Bonnor, W. B. 1956, MNRAS, 116, 351
Boulanger, F., Abergel, A., Bernard, J.-P., et al. 1996, A&A, 312, 256
Caselli, P., Walmsley, C. M., Zucconi, A., et al. 2002, ApJ, 565, 344
Charnley, S. B. 1997, MNRAS, 2911, 455
Combes, F. 1991, ARA&A, 29, 195
Dobashi, K., Bernard, J.-P., Yonekura, Y., & Fukui, Y. 1994, ApJS, 95, 419
Galli, D., Walmsley, M., & Gonçalves, J. 2002, A&A, 394, 275
Goldsmith, P. F. 2001, ApJ, 557, 736
Griffin, M. J., Abergel, A., Abreu, A., et al. 2010, A&A, 518, L3
Harjunpää, P., & Mattila, K. 1996, A&A, 305, 920
Hildebrand, R. H. 1983, QJRAS, 24, 267
Johnstone, D., Rosolowsky, E., Tafalla, M., & Kirk, H. 2010, ApJ, 711, 655
Juvela, M. 1997, A&A, 322, 943
Juvela, M. 2005, A&A, 440, 531
Juvela, M., Ristorcelli, I., Montier, L. A., et al. 2010, A&A, 518, L93
Juvela, M., Ristorcelli, I., Pelkonen, V.-M., et al. 2011, A&A, 527, A111
Juvela, M., Harju, J., Ysard, N., & Lunttila, T. 2012a, A&A, 538, A133
Juvela, M., Ristorcelli, I., Pagani, L., et al. 2012b, A&A, 541, A12
Juvela, M., Malinen, J., & Lunttila, T. 2013, A&A, 553, A113
Könyves, V., André, P., Men'shchikov, A., et al. 2010, A&A, 518, L106
Kutner, M. L., & Ulich, B. L. 1981, ApJ, 250, 341
Li, A., & Draine, B. T. 2001, ApJ, 554, 778
MacLaren, I., Richardson, K. M., & Wolfendale, A. W. 1988, ApJ, 333, 821
Malinen, J., Juvela, M., Collins, D. C., Lunttila, T., & Padoan, P. 2011, A&A, 530, A101
Marsh, K. A., Griffin, M. J., Palmeirim, P., et al. 2014, MNRAS, 439, 3683
Mathis, J. S., Mezger, P. G., & Panagia, N. 1983, A&A, 128, 212
McKee, C. F., & Ostriker, E. C. 2007, ARA&A, 45, 565
Meng, F., Wu, Y., & Liu, T. 2013, ApJS, 209, 37
Minchin, N. R., White, G. J., & Ward-Thompson, D. 1995, A&A, 301, 894
Montier, L. A., Pelkonen, V.-M., Juvela, M., Ristorcelli, I., & Marshall, D. J. 2010, A&A, 522, A83
Montillaud, J., Juvela, M., Rivera-Ingraham, A., et al. 2015, A&A, submitted
Motte, F., Zavagno, A., Bontemps, S., et al. 2010, A&A, 518, L77
Myers, P. C., Linke, R. A., & Benson, P. J. 1983, ApJ, 264, 517
Ossenkopf, V., & Henning, T. 1994, A&A, 291, 943
Pirogov, L., Zinchenko, I., Caselli, P., Johansson, L. E. B., & Myers, P. C. 2003, A&A, 405, 639
Planck Collaboration VII. 2011, A&A, 536, A7
Planck Collaboration XXII. 2011, A&A, 536, A22
Planck Collaboration XXIII. 2011, A&A, 536, A23
Planck Collaboration XXV. 2011, A&A, 536, A25
Plummer, H. C. 1911, MNRAS, 71
Tauber, J. A., Norgaard-Nielsen, H. U., Ade, P. A. R., et al. 2010, A&A, 520, A2
Whitworth, A. P., & Ward-Thompson, D. 2001, ApJ, 547, 317
Wu, Y., Liu, T., Meng, F., et al. 2012, ApJ, 756, 76

Pages 11 to 15 are available in the electronic edition of the journal at http://www.aanda.org

Appendix A: ^{13}CO and C^{18}O spectra

A sample spectrum of ^{13}CO of all the fields are shown in Fig. A.1 and A.2. The spectra are from the ^{13}CO peak position of each field. The C^{18}O spectrum is shown from the same position; the baseline has been moved to −2.0 K.

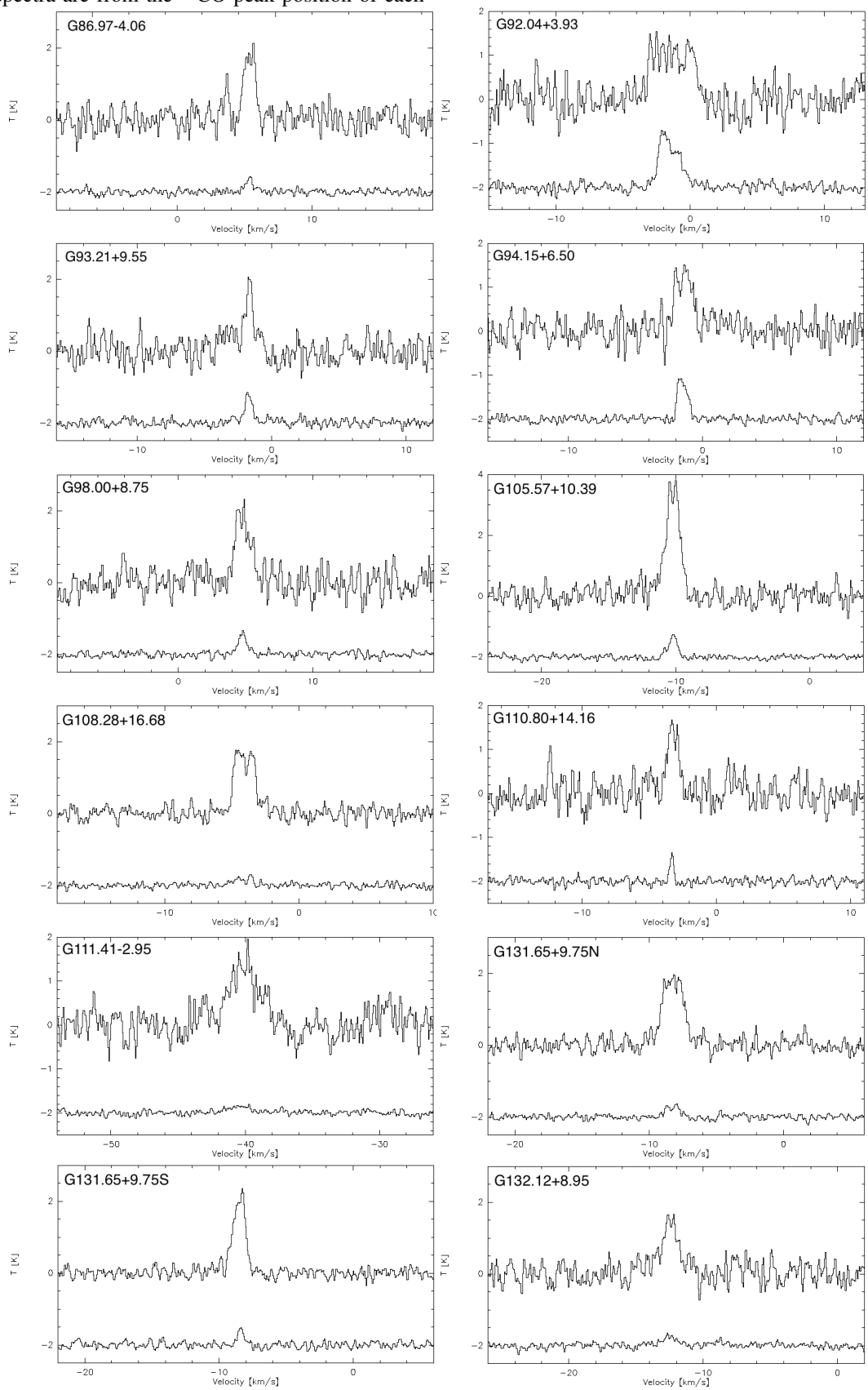

Fig. A.1. Observed ^{13}CO and C^{18}O spectra at the ^{13}CO peak position. The *x*-axis shows the velocity and the *y*-axis shows the main beam temperature. For plotting, the C^{18}O spectra have been shifted by 2 K.

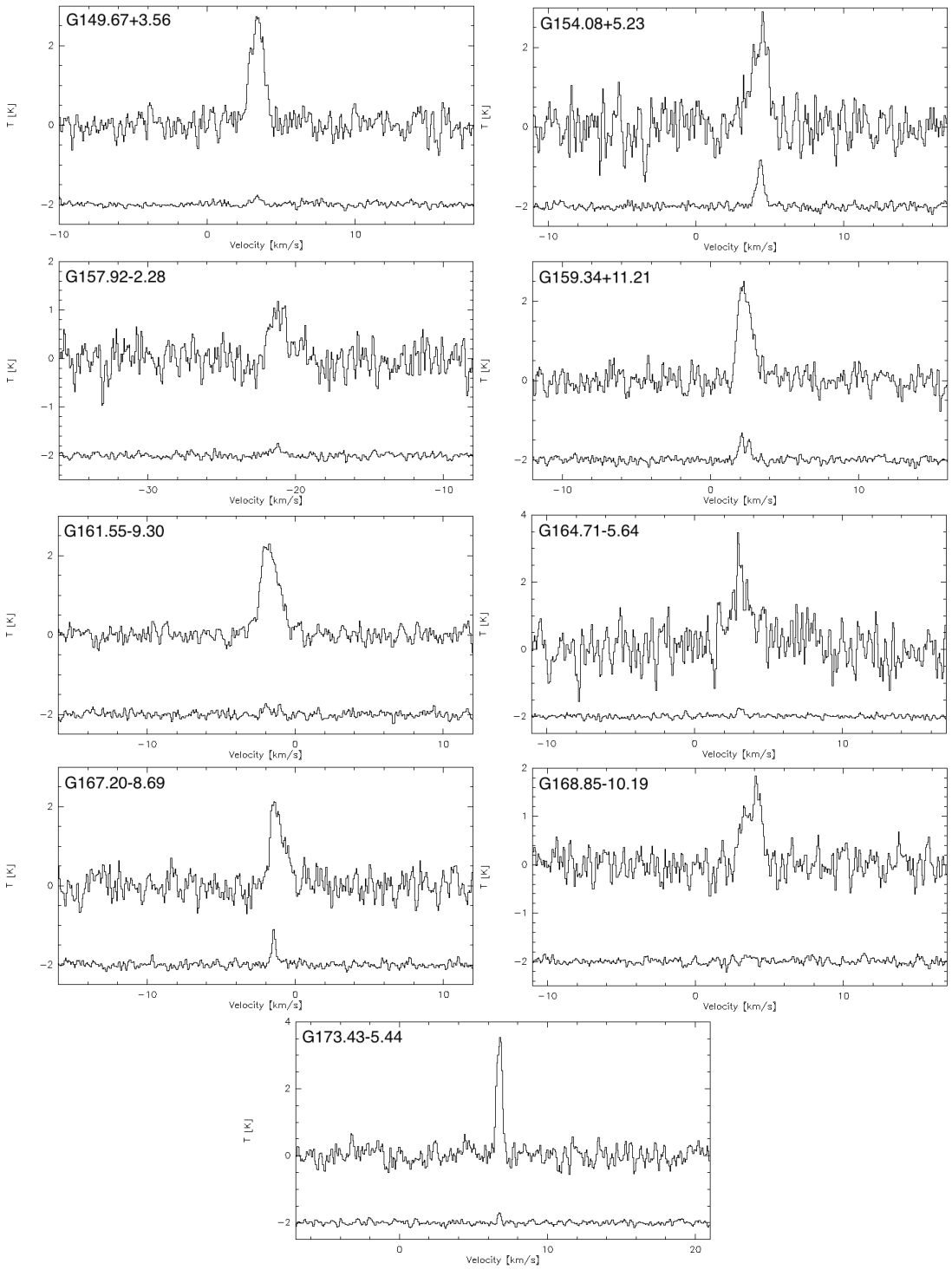

Fig. A.1. continued.

Appendix B: N_2H^+

The spectra with N_2H^+ detections, besides the field G86.97–4.06 in Fig. 3, are shown in Fig. B.1.

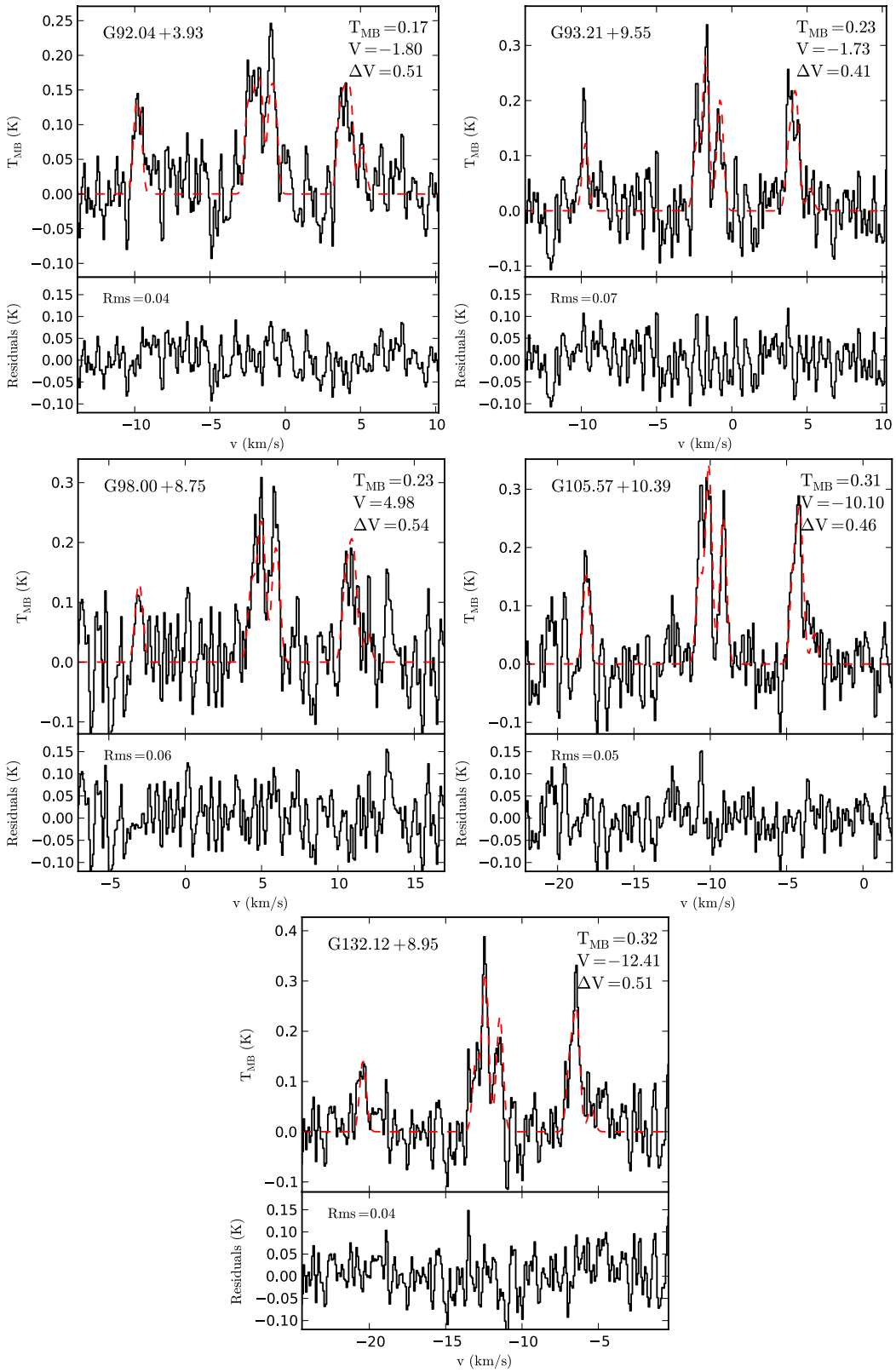

Fig. B.1. N_2H^+ spectra observed toward G92.04+3.93, G93.21+9.55, G98.00+8.75, G105.57+10.39, and G132.12+8.95. The field G86.97–4.06 is shown in Fig. 3. The red dashed line is the fit to the hyperfine spectra and the lower subframe shows the fit residuals. The main beam temperature of the 23−12 component, the fitted radial velocity, the FWHM line width (km s^{-1}), and the residual rms noise (as main beam temperature) are given in the frames.

Appendix C: Radiative transfer models

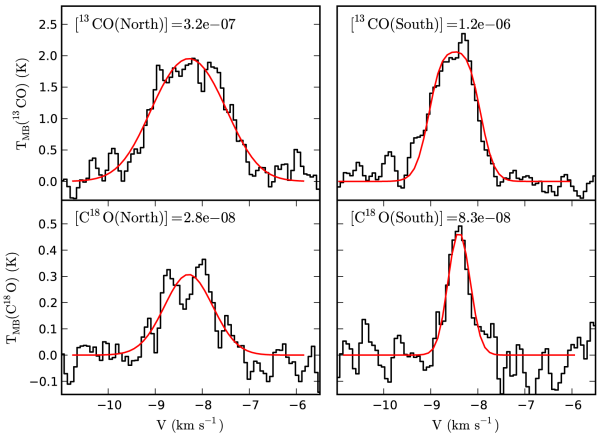

Fig. C.1. Examples of the modeled ^{13}CO (*upper frames*) and C^{18}O spectra (*lower frames*) for the northern (*left frames*) and southern (*right frames*) positions in the field G131.65+9.75. The histograms show the observed spectra and the continuous red lines the model predictions. The model densities were derived from continuum modeling with OH dust, assuming a narrow LOS density profile.

In Sect. 4 the dust emission was analyzed assuming a constant temperature along the line-of-sight (LOS), but this may underestimate the true column density of externally heated, optically thick clumps (Malinen et al. 2011; Juvela et al. 2013). Similarly, the ^{13}CO(1–0) and C^{18}O(1–0) lines were analyzed using the LTE assumption, without the possibility of independent estimates of their relative abundances. To examine these questions, we carried out radiative transfer modeling where the density distribution was first derived from dust continuum observations and was then used as a basis for modeling the lines. The modeling was limited to the two positions in the field G131.65+9.75.

C.1. Modeling of dust surface brightness

We extracted 5′×5′ continuum surface brightness maps centered on the selected positions and resampled the data on 3″ pixels. The maps are 100×100 pixels in size and corresponding model clouds were constructed using a Cartesian grid of 100×100 cells. In the LOS direction the density distribution was assumed to follow a Plummer-like (Whitworth & Ward-Thompson 2001; Plummer 1911) function $\rho(r) \sim \frac{1}{[1+(r/R_{\rm flat})^2]}$, with a central flat part with $R_{\rm flat}$ equal to 0.03 pc (not well resolved with the employed discretization). Corresponding to the apparent clump sizes in the plane of the sky, the FWHM of the density distribution was set to ∼17 pixels, which corresponds to ∼50″ or a linear scale of 0.25 pc at the distance of 1070 pc. This may overestimate the size because of the effects of beam convolution and radial temperature gradients in the clumps. For this reason, and to check the general sensitivity to the LOS extent, we also calculated another set of models with FWHM at half of the value given above. Note that the clump size can also be significantly larger along LOS than in the plane of the sky. There is even some bias in this direction because the emission from elongated clumps and filaments becomes stronger when they are aligned along LOS.

We performed the calculations iteratively, and on each iteration we solved the dust temperature distributions and calculating model predictions of the surface brightness that we then convolved to the resolution of the observations. The calculations were carried out with a Monte Carlo radiative transfer program (Juvela 2005). The initial external radiation field corresponded to that of Mathis et al. (1983). The modeling was performed with two dust models. The first, in the following MWD, represents dust in normal diffuse interstellar medium (Li & Draine 2001). The other one, in the following OH, was taken from Ossenkopf & Henning (1994) and corresponds to dust that has coagulated and accreted thin ice mantles over a period of 10^5 yr at a density 10^6 cm^{-3}. In our calculations, the dust opacities $\kappa(250\,\mu{\rm m})$ were 0.045 cm^2 g^{-1} for MWD and 0.22 cm^2 g^{-1} for OH, the value of Sect. 4 falling between the two. The value of κ is crucial because it affects the column density, an important parameter of the subsequent line modeling.

In the plane of the sky, the column density corresponding to each map pixel was adjusted by comparing the observed 350 μm surface brightness with the model prediction. The external radiation field was adjusted so that finally the 160 μm and 500 μm predictions also agreed with the observations to within 10%. The observations could be fitted well with both dust models, with an external radiation field 70−80% of the Mathis et al. (1983) values. Because we used background-subtracted surface brightness data, the model represents only the inner parts of the cloud without the diffuse envelope. Therefore, the radiation field in the models is somewhat weaker that the full radiation field outside the cloud. The column densities are listed in Table C.1.

The values obtained with the OH dust model are close to the column densities estimated in Sect. 4. With MWD, the column densities are higher and in the northern point by more than the ratio of dust opacities, ∼5. For a given dust opacity and radiation field, there is a maximum surface brightness that can be produced with any column density. Thus, for a too small value of κ, the column density of the model might be grossly overestimated. When estimated with the NICER method (using 2MASS stars, a spatial resolution of two arcminutes, and a value of $R_V = 3.1$), the visual extinction of northern clump is less than 3 mag. Taking the difference in the resolution into account, this is still consistent with the Sect. 4 estimates and the result from the models with OH dust. However, the A_V measurement appears to rule out the values obtained with MWD dust (assuming the A_V is not severely underestimated either because of very clumpy column density structure or the presence of foreground stars) and give some support to the idea of dust opacity higher than that of diffuse medium.

C.2. Modeling of the ^{13}CO(1–0) and C^{18}O(1–0) lines

We modeled the ^{13}CO(1–0) and C^{18}O(1–0) lines separately, taking the density distribution directly from the continuum models. We only modeled the spectra toward the center of the clumps. The fractional abundance and kinetic temperature were assumed to be constant but in the non-LTE models the excitation temperature does vary and gives more weight to the dense regions. The velocity field was initialized by giving each cell a random velocity vector with $\sigma_{\rm 3D} = 1.0$ km s^{-1} and assuming a turbulent line width with Doppler velocity $\Delta v_{\rm D} = \sqrt{2}\sigma_{\rm 1D} = 1.0$ km s^{-1}. Thus the initial "microturbulence" within the cells is slightly larger than the "macroturbulence" between the cells. In the actual calculations, to match the observed line widths, both velocity components are scaled by the same number, typically by ∼0.3−0.4, and the thermal line broadening is added to the turbulent line widths. The predictions of the models are optimized regarding the line width (the scaling mentioned above) and the line

Table C.1. Result from radiative transfer modeling.

Position	$N(H_2)$ (10^{21} cm^{-2})	LOS width	Dust	$N(H_2)$ (10^{21} cm^{-2})	T_{kin} (K)	[^{13}CO] (10^{-6})	[^{13}CO]/[C^{18}O]
G131.65+9.75 N	9.3	Wide	OH	10.9	10.0	0.36	11.4
G131.65+9.75 N	9.3	Narrow	OH	12.3	10.0	0.32	11.3
G131.65+9.75 N	9.3	Wide	MWD	85.8	10.0	0.04	10.4
G131.65+9.75 N	9.3	Narrow	MWD	93.3	10.0	0.04	10.5
G131.65+9.75 S	3.7	Wide	OH	3.4	10.0	1.50	16.2
G131.65+9.75 S	3.7	Narrow	OH	3.7	10.0	1.22	14.8
G131.65+9.75 S	3.7	Wide	MWD	20.3	10.0	0.12	10.7
G131.65+9.75 S	3.7	Narrow	MWD	22.2	10.0	0.11	10.8
G131.65+9.75 N	9.3	Wide	OH	10.9	12.0	0.32	10.7
G131.65+9.75 N	9.3	Narrow	OH	12.3	12.0	0.29	10.8
G131.65+9.75 S	3.7	Wide	OH	3.4	12.0	1.11	13.3
G131.65+9.75 S	3.7	Narrow	OH	3.7	12.0	0.94	12.7

Notes. The columns are (1) observed position; (2) column density estimated in Sect. 4; (3) width of the LOS density profile; (4) dust model; (5) column density of the continuum model; (6) assumed kinetic temperature; (7) ^{13}CO abundance of the model; and (8) relative abundance [^{13}CO]/[C^{18}O].

intensity that is adjusted by changing the molecular abundance. There are four cases for each position corresponding to two different assumptions of the LOS cloud extent and the two different dust models. Furthermore, some models were also calculated with a kinetic temperature of T_{kin} = 12.0 K, instead of the default assumption of T_{kin} = 10.0 K. Again, the true kinetic temperature is unknown, but the comparison between T_{kin} = 10.0 K and T_{kin} = 12.0 K gives some idea of the associated uncertainties.

We performed the line calculations with the Monte Carlo program described in Juvela (1997). The obtained abundances are listed in Table C.1. Concentrating on the models based on continuum modeling with OH dust, the ^{13}CO values are on the order of the canonical value of 10^{-6} and the estimates are similar for both assumed values of T_{kin}. However, because the abundances directly depend on the assumed column density, and thus the values of dust κ, the absolute values are very uncertain. The relative abundance between ^{13}CO and C^{18}O should be more reliable, as suggested by the similarity between the OH and MWD cases and the two cases of LOS density distribution. The abundance ratio is ∼10 and thus larger than the value of 5.5 that was assumed in Sect. 3.

6.5 PERSPECTIVES

In this paper 21 clumps were chosen for a more detailed follow up. The chosen clumps show low dust color temperatures T~10−15 K and are therefore potential places of star formation. We used molecular line and dust continuum observations.

Similar studies with different targets have been conducted by Wu et al. (2012) and their follow-up study by Meng et al. (2013). Our found ratio of the ^{13}CO to $C^{18}O$ (~10) in the clumps is within the certainties of the value found by Wu et al. (2012), 7.0 ± 3.8. These studies, like ours, also found only a small fraction of prestellar cores (90 % being starless). They had a greater variation to the excitation temperatures: 4−27 K. We found the excitation temperatures to be ~5 K for the clumps were able to calculate it.

The stability of the clumps requires further study. These are now further studied together with writers of Wu et al. (2012) and Meng et al. (2013). This collaboration (Liu et al., 2014) has observed and planned observations of other clumps, other properties of the clumps, and other tracers. A summary of these follow-up observations are given in Table 6.1.

Table 6.1: Summary of follow-up observations (Liu et al., 2014)

Telescopes	Tracers	Aims	Status
PMO 13.7-m	J=1-0 of ^{12}CO, ^{13}CO, $C^{18}O$, HCN, and HCO^+	dense clumps	674 PCCs surveyed
CSO 10-m	J=1-0 of ^{12}CO, ^{13}CO, $C^{18}O$	CO depletion & outflows	20 PCCs mapped
APEX 12-m	J=1-0 of ^{12}CO, ^{13}CO, $C^{18}O$	CO depletion & outflows	proposal accepted
NANTEN2 4-m	^{12}CO (4-3) & (7-6)	shock evidence	proposal accepted
IRAM 30-m	J=2-1 of ^{12}CO, ^{13}CO, & $C^{18}O$ J=1-0 of HCN, HCO^+, & N_2H^+	starless cores chemistry	24 PCCs mapped
Mopra 22-m	J=1-0 of HCN, HCO^+, & N_2H^+ SiO (2-1), HC_3N (10-9)	chemistry	30 PCCs mapped
Effelsberg 100-m	NH_3 (1,1) & (2,2) HC_7N (21-20)	kinetic temperature & chemistry	proposal accepted
The SMA	continuum and molecular lines at 230 GHz band	fragmentation & kinematics of G207.3-19.8	proposal accepted

Part IV

DENSE STRUCTURES IN WARM ISM

7

CH^+ AND OH IN THE ORION BAR

In this chapter and the attached paper the aim is to examine the spatial distribution of the methylidyne cation (CH^+) and hydroxyl (OH), in the Orion Bar, which is one of the nearest nearly edge-on luminous PDR. These simple molecules are important building blocks for many complex molecules in the ISM and they represent the first steps of the ISM chemistry. CH^+ is important, since carbon and hydrogen are the basic blocks of interstellar chemistry. OH, on the other hand, is an intermediary molecule in forming other important tracers like H_2O, CO^+, O_2, NO and SO^+in the ISM.

CH^+ and OH are among the first molecules that were observed in the ISM and also among the first to be observed in the FIR range (Dunham, T., 1937; Douglas and Herzberg, 1941; Weinreb et al., 1963; Storey et al., 1981; de Vries and van Dishoeck, 1988). In addition to being building blocks of more complex chemistry, these molecules are important tracers of warm interstellar chemistry. Their formation and excitation mechanisms are still not well understood. CH^+ and OH rotational lines have similar critical densities and upper level energies which makes them ideal for comparison. The similar properties should lead to similar morphologies if their origin and excitation mechanism is the same. Fig. 7.1 plots the critical density of sev-

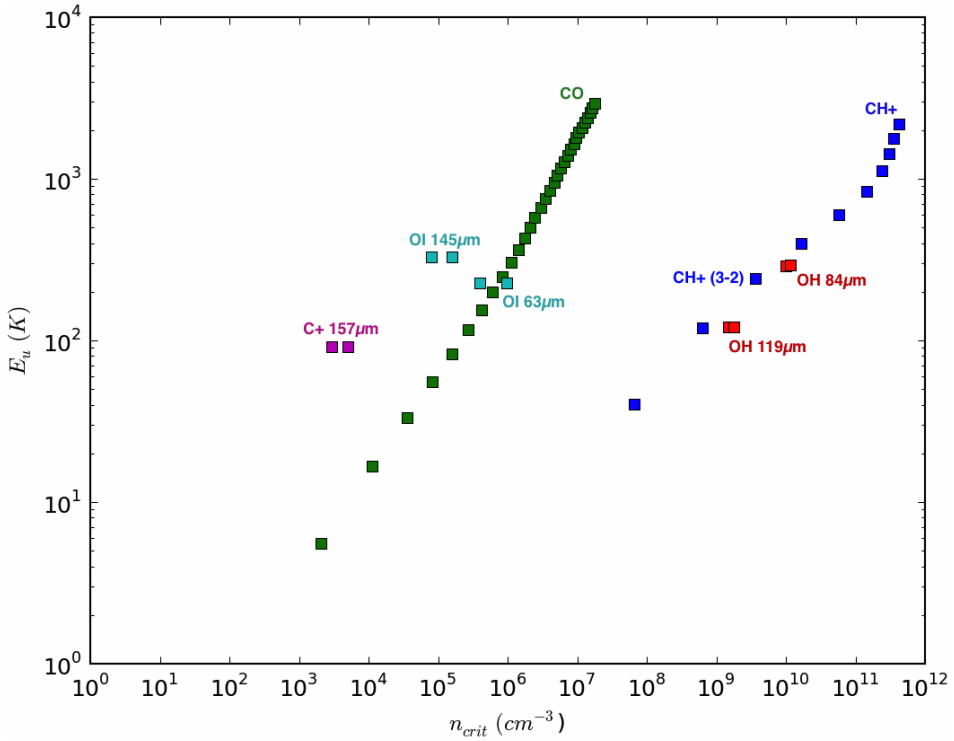

Figure 7.1: Critical densities and upper level energy temperatures of key molecules in the ISM.

eral atomic and molecular lines in the ISM as a function of their upper level energy. The figure shows that the critical density and upper level energy of CH$^+$ and OH lines are similar and this is especially true for our observed lines: OH 84 μm (n_{crit}=10^{10} cm^{-3}, E_u/k=291 K) and CH$^+$ J=3-2 at 119.8 μm (n_{crit}=4×10^{10} cm^{-3}, E_u/k=240 K).

In PDRs with high incident radiation field and moderate densities, the chemical reaction with FUV-pumped vibrationally excited H_2 is expected to have a substantial impact on the abundance and excitation of some molecules, especially CH$^+$ which is highly reactive (Agúndez et al., 2010, and references therein). In dense gas, excitation of FIR molecular lines may originate from nonreactive collisions with H_2, H, and electrons. Previous *Herschel* observations of a smaller area hint at a possible correlation between the high-J CO[1], OH and CH$^+$ lines and suggest that their emission is associated with the presence of small irradiated dense structures (Goicoechea et al., 2011).

7.1 CH$^+$ IN THE ISM

CH$^+$ was observed in the ISM, albeit unidentified, in 1937 (Dunham, T., 1937), and later identified by Douglas and Herzberg (1941) in optical range. Since then it has been observed at optical wavelengths in absorption (e.g., Bates and Spitzer, Lyman, 1951; Douglas and Morton, 1960; Hobbs, 1973; de Vries and van Dishoeck, 1988; Vladilo and Centurion, 1990). Because the pure rotational spectrum lies in the far-infrared range, CH$^+$ was for the first time observed through its pure rotational spectrum with the *Infrared Space Telescope (ISO)* by Cernicharo et al. (1997). They observed rotational lines from J=2-1 up to J=6-5 in the planetary nebula NGC 7027. They also derived a CH$^+$ column density of 8×10^{13} cm^{-2} assuming a size of 6″ (0.2 pc) for the PDR.

With the improved sensitivity and angular resolution of *Herschel* the rotational lines of CH$^+$ were easier to observe than ever before. The J=1-0 transition has been studied in several star forming regions (Bruderer et al., 2010; Falgarone et al., 2010a,b). Naylor et al. (2010) detected CH$^+$ with *Herschel*/SPIRE from near to distant star forming regions, while Godard et al. (2012) analyzed the ground rotational state observations with *Herschel*/HIFI in distant star forming regions. CH$^+$ rotational lines have also been found in UV-irradiated disks (Thi et al., 2011), J=5-4 being the clearest detection, but J=6-5 and J=3-2 were also detected with a lower signal-to-noise ratio. Nagy et al. (2013) studied the rotational lines up to J=6-5 in a small region of the Orion Bar (one PACS footprint[2] 47″$\times$ 47″) towards the CO$^+$ peak. This paper is closely related to my work.

PDR models predict a low ISM abundance, because the reaction $H_2(v=0)+C^+$ is very endothermic. CH$^+$ is also highly reactive and easily destroyed by reactive collisions with H_2, H, and electrons. However, the obser-

1 Here the high-J CO observations are discussed only in relation to CH$^+$ and OH. For discussion of high-J CO, see Chapter 8

2 see Chapter 4.1.2.1 and Fig. 4.2 for more information on the footprint.

vations have found a higher abundance than predictions. Thus, it has been suggested (Agúndez et al., 2010; Godard and Cernicharo, 2013; Zanchet et al., 2013; Nagy et al., 2013) that CH^+ can be formed via the endothermic reaction:

$$H_2 + C^+ \rightarrow CH^+ + H. \tag{7.1}$$

The endothermicity of the reaction is very high, 0.37 eV (4300 K), but this can be overcome by shocks (e.g., Elitzur and Watson, 1978; Pineau des Forets et al., 1986) or turbulence (Godard et al., 2009, 2012; Falgarone et al., 2010a,b). In strong irradiated PDRs, like the Orion Bar, this barrier can be overcome by the vibrationally excited H_2, because the vibrational energy from H_2 changes the reaction from endothermic to exothermic (White, 1984; Lambert and Danks, 1986; Jones et al., 1986; Agúndez et al., 2010; Naylor et al., 2010; Godard and Cernicharo, 2013; Nagy et al., 2013; Zanchet et al., 2013). However, Lim et al. (1999) found that the observed abundances of CH^+ by Cernicharo et al. (1997) could be explained by inelastic collisions alone. They found that inelastic collisions can lead to significant CH^+ populations, particularly when the electron density is 10^3 cm^{-3} or higher and the gas is hot, >1000 K. In this case most of the production is through thermal reaction $C^+ + H_2(v = 0)$.

7.2 OH IN THE ISM

OH was first detected in 18-cm absorption lines by Weinreb et al. (1963). The first FIR observations were made by Storey et al. (1981) with the *Kuiper Airborne Observatory*. They observed the 119.2 and 119.4 μm lines towards Sgr B2, where the lines were seen in absorption, and Orion KL, where the lines were seen in emission. Although the FIR OH lines have been observed with the *Kuiper Airborne Observatory* (e.g., Storey et al., 1981; Melnick et al., 1987) and *ISO* (e.g., Ceccarelli et al., 1998; Larsson et al., 2002; Goicoechea et al., 2006) to trace warm neutral gas in shocked gas, *Herschel* finally brought the angular resolution needed to study these lines in PDRs, protostellar outflows, and disks.

Goicoechea et al. (2011) studied OH 84 and 119 μm lines in Orion Bar, in a small area (one PACS footprint $47'' \times 47''$) towards the CO^+ peak. Through detailed excitational and photochemical modeling, they found that OH arises from a small dense ($n_H \sim 10^{6-7}$ cm^{-3}) structures in warm (160–220 K) gas. This is supported by studies of protoplanetary disks, where OH were also observed, which suggests that OH arises from the protoplanetary disk itself, rather than the outflow (Sturm et al., 2010; Fedele et al., 2012).

The Meudon PDR code for the high UV irradiation conditions prevailing in the Orion Bar predicts that the OH traces the PDR surface reaching its peak abundance at $A_V \lesssim 1$ within small spatial scales similar to CH^+ (Goicoechea et al., 2011). On the PDR surface, the OH formation is most likely dominated by the endothermic reaction (Agúndez et al., 2010):

$$H_2 + O \rightarrow H + OH \tag{7.2}$$

The endothermicity of the route is 0.08 eV (900 K), but it has an even higher activation barrier of 0.4 eV (4800 K) than the endothermicity of CH^+. It has been suggested that the FUV-pumped vibrationally excited H_2 could, like for CH^+, enhance the abundance and excitation of OH. Although, Agúndez et al. (2010) do conclude that the effect of vibrationally excited H_2 is more important in $H_2 + C^+$ reaction than $H_2 + O$ reaction. Alternatively, owing to the strong FIR radiation field in Orion, excited OH levels could be populated through radiative pumping in the lower density interclump medium. However, Goicoechea et al. (2011) concluded that this was not the case for Orion Bar.

7.3 PARIKKA ET AL.: SPATIAL DISTRIBUTION OF FIR ROTATIONALLY EXITED CH$^+$ AND OH EMISSION LINES IN THE ORION BAR PDR

In the attached paper we use fully sampled maps of $110'' \times 110''$ with *Herschel* (PACS) of the CH^+ J=3-2 line at 120 μm and the OH-doublet ($^2\Pi_{3/2}$ J=7/2$^-$-5/2$^+$ and $^2\Pi_{3/2}$ J=7/2$^-$+5/2$^+$) at 84 μm in the Orion Bar with a spatial resolution between $6''$ and $9''$. For the first time we have fully sampled maps of these lines from such a large area with high spatial resolution. So far, this is only possible in the Orion Bar, because it is so near (~400 pc, (Menten et al., 2007)) and bright (10^4 times the standard radiation field (Marconi et al., 1998)). Fully sampled maps are needed to properly trace the spatial distribution of the lines.

The observed CH^+ and OH lines have been connected to dense irradiated clumps due to their high critical density and upper level energy temperature (Goicoechea et al., 2011; Nagy et al., 2013). Warm and dense gas is prevalent in PDRs making these lines critical in understanding the structures of the PDRs and their chemical processes. These molecules are the first steps of ISM chemistry. Their reactions with other molecules and atoms remove H_2, C^+ and O from the gas. The interstellar chemistry is important, since it reflects the physical processes in the ISM.

We are interested in investigating the formation and excitation mechanisms of both CH+ and OH. Although these have been studied, more observations are still needed to fully understand the physical and chemical evolution of these molecules. The comparison of CH^+ 120 μm and OH 84 μm is especially interesting having similar critical densities (~10^{10} cm^{-3}) and upper level energy temperatures (~250 K). Due to the similar properties, their morphologies should be similar if their formation and excitation mechanisms are also similar.

This study allows us for the first time to discuss the observed spatial distribution and variation of these lines as a function of the distance to the ionizing star (i.e., UV flux) and the density structure. We investigate what are the main formation and excitation mechanisms (chemical pumping versus nonreactive collisions) for CH^+ and OH, and what is the physical origin of their emission within the limits of the spatial resolution obtained with *Herschel*.

We compare the spatial distribution of these molecules with the components of their main formation routes (H_2 $v > 0$, C^+ and O) and tracers of the warm and dense gas (high-J CO). This allows us to study how the formation and chemical pumping via reactions with vibrationally excited H_2 affects differently CH^+ and OH. Having access to the line profile of CH^+ J=2-1 gives us information on the CH^+ excitation. These HIFI observations are not a fully sampled map, but a strip across the Bar, which shows us how and if the line profile changes from the more diffuse gas in front of the Bar to the dense part of the Bar.

In this paper I have analyzed the data. The pipeline reduction for the SPIRE cubes was done by Karine Dassas and Boualam Hasnoun. For the SPIRE observations I have used the SUPREME method (Ayasso et al., in prep.) for the final reduction steps and then fitted the lines with the HIPE Spectrometer Cube fitting procedure. This procedure uses Gaussian profile. SPIRE profile is not exactly Gaussian, but is used widely in the line fitting of SPIRE observations. Concerning PACS observations I used the level 2.0 cube from the HIPE pipeline reduction and made the line emission maps with PACSman. The HIFI observations were fully reduced by Paolo Pilleri. I am the main author of the article and led discussion with co-authors to improve it.

Astronomy & Astrophysics manuscript no. CHpOH_paper
November 6, 2015

Spatial distribution of FIR rotationally exited CH^+ and OH emission lines in the Orion Bar PDR⋆

A. Parikka[1], E. Habart[1], J. Bernard-Salas[2], J. R. Goicoechea[3], P. Pilleri[4], E. Dartois[1], C. Joblin[5,6], C. Pinto[7], M. Gerin[8], and B. Godard[8]

[1] Institut d'Astrophysique Spatiale, Université Paris Sud, 91405 Orsay Cedex, France
[2] Department of Physical Sciences, The Open University, Milton Keynes MK7 6AA, UK
[3] Instituto de Ciencia de Materiales de Madrid, CSIC, Sor Juana Inés de la Cruz, 3, 28049 Madrid, Spain.
[4] Los Alamos National Laboratory, P.O. Box 1663, Los Alamos, NM 87545, USA
[5] Université de Toulouse, UPS-OMP, IRAP, 31400 Toulouse, France
[6] CNRS, IRAP, 9 Av. Colonel Roche, BP 44346, 31028 Toulouse Cedex 4, France
[7] Laboratoire d'Astrophysique de Marseille, 38 rue Frédéric Joliot-Curie, 13 388 Marseille Cedex 13, France
[8] LERMA, Observatoire de Paris, 61 Av. de l'Observatoire, 75014 Paris, France

Received <date>/ accepted <date>

ABSTRACT

Context. In Photodissociation regions with high incident radiation field, the presence of vibrationally excited H_2 or the presence of hot gas (>1000 K) are predicted to enhance the abundance of CH^+ and OH in PDRs. However, excitation of these species may originate also from dense gas ($> 10^5$ cm^{-3}) followed by nonreactive collisions with H_2, H and electrons.
Aims. Our goal is to examine the spatial distribution of CH^+ and OH emission lines in the Orion Bar. We investigate the main formation and excitation mechanisms for CH^+ and OH, and the physical origin of their emission.
Methods. We use fully sampled maps with *Herschel* (PACS) of the CH^+ J=3-2 line at 119.8 μm and the OH Λ-doublet at 84 μm in the Orion Bar. We compare the spatial distribution of these molecules with those of their chemical precursors, C^+, O and H_2, and tracers of the warm and dense gas (high-J CO). *Herschel* HIFI data of the CH^+ J=2-1 line at 180 μm obtained along a cut perpendicular to the Orion Bar is used to assess the spatial variation of the velocity line profile.
Results. The spatial distribution of CH^+ and OH confirms the density enhancements in the Bar at a 10″ scale, also seen in CO observations and atomic lines. The morphology of CH^+ and H_2 emission distribution confirms that CH^+ formation and excitation is strongly dependent on the vibrationally excited H_2. Velocity-resolved observations of CH^+ J=2-1 show that these line widths (3–4 km s^{-1}) are much larger than CO because of the fast destruction of CH^+. Interestingly, the peak of the OH 84 μm emission corresponds to a bright young object, identified as a proplyd 244-440.
Conclusions. Both formation pumping and non reactive collisions in a UV-irradiated dense gas are important excitation processes of these molecules. This gives strong constraints for the modeling the physical conditions of the far-infrared (FIR) rotationally excited molecular lines in the presence of FUV fields.

Key words. ISM: individual objects: Orion Bar, ISM: lines and bands, photon-dominated region (PDR)

1. Introduction

The methylidyne cation (CH^+) and hydroxyl (OH) have been observed in different environments from the local (e.g., Storey et al. 1981; Nagy et al. 2013; Dawson et al. 2014) to the extragalactic ISM (e.g., Schmelz et al. 1986; Baan et al. 1992; Darling & Giovanelli 2002; Spinoglio et al. 2012; Rangwala et al. 2014). They are key molecules in the warm interstellar chemistry, and because they require specific conditions to form, they trace specific physical processes in the ISM. Thus, it is expected that, in addition to the physical conditions, the spatial distribution of the FIR emission of these species might give clues on their formation and excitation processes. *Herschel* allows, for the first time, to observe the rotationally excited FIR emission lines of OH and CH^+ in photodissociation regions (PDRs).

Carbon atoms and hydrogen molecules and radicals are the first chemical building blocks in the ISM. The main formation route of CH^+ is believed to be via reaction of C^+ with H_2. This formation route has a very high endothermicity of 0.37 eV (4300 K), and it has been suggested that this barrier could be overcome by the vibrationally excited H_2 in strongly irradiated PDRs (e.g., White 1984; Lambert & Danks 1986; Jones et al. 1986; Agúndez et al. 2010; Naylor et al. 2010; Godard & Cernicharo 2013; Nagy et al. 2013; Zanchet et al. 2013). However, Lim et al. (1999) found that the observed abundances of CH^+ by Cernicharo et al. (1997) could be explained by inelastic collisions alone, particularly when the electron density is 10^3 cm^{-3} or higher. Alternatively, in diffuse interstellar clouds with low FUV radiation field and very low density, shocks (e.g., Elitzur & Watson 1978; Pineau des Forets et al. 1986) and turbulence (e.g., Godard et al. 2009, 2012; Falgarone et al. 2010a,b) have been proposed to overcome the high endothermicity.

CH^+ is highly reactive and easily destroyed by reactive collisions with H_2, H, and electrons. The reaction $C^+ + H_2$ becomes

⋆ *Herschel* is an ESA space observatory with science instruments provided by European-led Principal Investigator consortia and with important participation from NASA.

exothermic when $v > 0$ (Godard & Cernicharo 2013; Nagy et al. 2013). Godard & Cernicharo (2013) find that with the chemical destruction rates considered typical for PDR environments, the low-J populations of CH^+ are sensitive to the formation pumping. Collisional excitation with H_2, H and electrons could, however, be important for the lowest rotational transitions. In contrast, the radiative pumping is predicted to have only a marginal effect even in the FIR radiation field of the Orion Bar PDR.

The OH radical is a key intermediary molecule in forming other important tracers like H_2O, CO^+, O_2, NO and SO^+in the ISM. On the surface of high FUV-flux PDRs and similarly to CH^+, the OH formation is expected to be dominated by the endothermic reaction with H_2 and O (Goicoechea et al. 2011; Hollenbach et al. 2012). The endothermicity of the route is 0.08 eV (~900 K) but it has an even higher activation barrier than CH^+ of 0.4 eV (~4800 K). Similarly to CH^+ the possibility of the FUV-pumped vibrationally excited H_2 enhancing the abundance and excitation of OH has been suggested. In addition, excited OH levels could be populated through radiative pumping in the lower density interclump medium ($n_H < 10^5$ cm^{-3}).

Goicoechea et al. (2011) made the first detection of rotationally excited OH and CH^+ emission lines of pointed observations towards the *CO^+ peak* at the edge of the Orion Bar PDR using the Photoconductor Array Camera and Spectrometer (PACS, Poglitsch et al. 2010) onboard *Herschel* Space Observatory. They hint at a possible spatial correlation between these lines and suggested that the rotational OH emission originates in small irradiated dense structures (densities of $n_H \sim 10^{6-7}$ cm^{-3}, and $T_k \sim 160-220$ K from a non-LTE, nonlocal model). In addition, the emission seems not to be confined behind the dissociation front but spatially extended at scales larger than homogeneous PDR model predictions. In this case, the correlations and extended emission could be interpreted as the result of unresolved dense structures exposed to FUV radiation near the edge of the Bar. Using high spectral resolution *Herschel*/HIFI observations, Nagy et al. (2013) found that the CH^+ J=1-0 and J=2-1 line have line widths of $\Delta \sim 5$km s^{-1}, larger than than those of all molecular lines (typically showing line widths of 2−3 km s^{-1}). This line broadening could result from the formation pumping. Conversely the CH^+ emission could arise from the interclump medium.

In this paper, we study the spatial distribution of the rotationally excited CH^+ and OH emission lines using fully sampled PACS maps of CH^+ transition J=3-2 and OH 84 μm towards the Orion Bar (see Fig. 3), one of the nearest, nearly edge-on luminous PDRs. These are the first fully sampled maps of these emission lines in a PDR. Constraints on the excited CH^+ spatial distribution and comparison with tracers of warm and dense gas are needed to disentangle between interclump and dense clump origins. Given the similar critical densities (10^{10} cm^{-3}) and upper level energies (250 K) of these lines, our observations allow us to study how the chemical reaction affects the formation and excitation of CH^+ and OH.

We describe the *Herschel* observations and data reduction of the CH^+ and OH lines, as well as the lines observed for comparison, in Sect. 2. We discuss the line detection and spatial morphology of the CH^+ J=3-2 and OH 84 μm lines in Sect. 3. In Sect. 4 we discuss the origin of the emission of these lines comparing their morphology to that of excited CO line. Sect. 5 investigates the CH^+ and OH formation and chemical pumping excitation via reaction with vibrationally excited H_2 and compares OH with H_2O. In Sect. 6, we discuss the CH^+ velocity dispersion as a function of its excitation. The detection of a proplyd in the OH map is described in Sect. 7. Finally, we conclude and summarize the findings of the paper in Sect. 8.

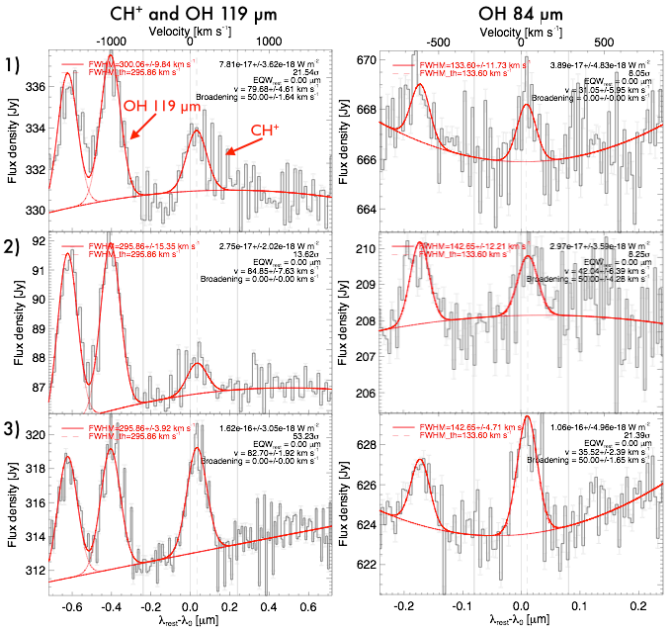

Fig. 1. Spectra of CH^+ J=3-2 (120 μm) and OH 119 μm (left) and OH 84 μm (right) at three positions indicated in panel a) of Fig. 3.

2. Observations and data reduction

2.1. CH^+ J=3-2 and OH lines observed with PACS

We observed the Orion Bar with PACS onboard *Herschel* Space Observatory. Table 1 lists the observed lines and their wavelengths, observed transitions, critical densities, upper level energy temperatures, and Einstein coefficients. Fig. 1 gives an example of the observations and line fitting routine. To the best of our knowledge, the Bar is the only PDR where the rotational lines of CH^+, OH, and high-J CO lines can be mapped with high enough signal-to-noise and spatial resolution, so that we can, for the first time, look at their morphology as a function of the physical conditions (FUV radiation, temperature, and density).

We observe a 110″×110″ region of CH^+ J=3-2 and OH 84 μm and 119 μm Λ-doublets towards the Orion Bar (see Fig. 3). The observations consist of a fully Nyquist-sampled raster map of 4×4 footprints targeting CH^+ J=3-2 and a fully Nyquist-sampled raster map of 5×5 footprints targeting OH 84 μm. These footprints are composed of 5×5 spatial pixels (spaxels). For each spaxel the line is observed in 16 different spectral scans, each with an up and down scan. The configuration is shown in Fig. 2, where the raster map is overlaid on top of the 8 μm IRAC image of the Orion Bar. Due to the overlapping footprints the quality of the data is better in the middle of the map than in the edges, where we only have the data from one footprint. The observations were carried out on September 14, 2012 for CH^+ J=3-2 and on September 15, 2012 for the OH 84 μm and the total observation time for both of these lines were 749.875 s. For CH^+ J=3-2 and OH 84 μm the typical σ outside the Bar is ~ 10 − 15 and in the Bar ~ 15 − 30. For OH 119 μm the typical σ outside the Bar is ~ 50 and in the Bar > 100. The rms for CH^+ J=3-2 depending on the position is ~ 0.07 − 0.26, for OH 84 μm ~ 0.04 − 0.13, and for OH 119 μm ~ 0.11.

Table 1. The properties of the observed lines: wavelength (λ), transition, critical density (n_{crit}), upper level energy temperature (E_u/k), and Einstein coefficient (A_{ij}). Numbers in parenthesis are power of 10. The critical densities have been calculated with *a*) ortho-H_2 (Offer et al. 1994), *b*) helium (Hammami et al. 2008, 2009), *c*) ortho-H_2 (Flower 2001), *d*) ortho-H_2 (CDMS, Müller et al. 2005), *e*) molecular hydrogen (Green et al. 1993) and with a temperature of 100 K, except for the H_2O, where 120 K was used.

	λ [μm]	transition	n_{crit} [cm^{-3}]	E_u/k [K]	A_{ij} [s^{-1}]
OH	84.6	$^2\Pi_{3/2}$ J=7/2$^-$-5/2$^+$	1 (10)^a	291	5.20 (-01)
OH	119.4	$^2\Pi_{3/2}$ J=5/2$^+$-3/2$^-$	2 (09)^a	121	1.38 (-01)
CH^+	119.8	J=3-2	4 (09)^b	240	2.20 (-01)
CH^+	179.6	J=2-1	6 (08)^b	120	6.10 (-02)
CH^+	359.0	J=1-0	6 (07)^b	40	6.36 (-03)
CO	137.3	J=19-18	5 (06)^c	1050	5.70 (-04)
$C^{18}O$	341.5	J=8-7	6 (06)^d	190	4.47 (-05)
[CII]	157.7	$^2P_{3/2}$-$^2P_{1/2}$	3 (03)^e	91	2.29 (-06)
[OI]	145.5	$^3P_0$-$^3P_1$	2 (05)^e	99	1.66 (-05)
H_2O	269.3	1_{11}-0_{00}	5 (08)^e	53	1.84 (-02)
H_2O	398.7	2_{11}-2_{00}	3 (11)^e	137	7.05 (-03)

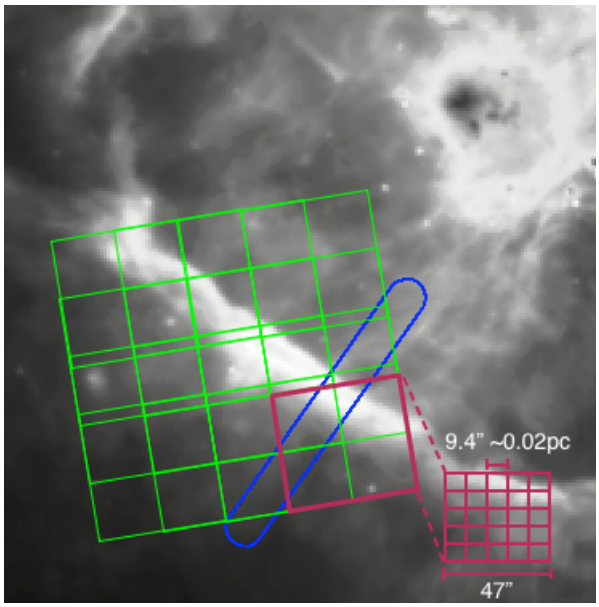

Fig. 2. Overlay of the PACS observations and HIFI observations on a Spitzer IRAC 8 μm image of the Orion Bar. A 4 × 4 raster map of CH^+ J=3-2 16 overlapping footprints is shown in green and an example of a footprint is shown in red. The strip of CH^+ J=2-1 is shown in blue.

PACS instrument has a spectral resolution of ~135 km s^{-1} for 85 μm and ~300 km s^{-1} for 120 μm, thus, the line widths of the observed lines are not resolved. We mapped the following lines: CH^+ J=3-2 (120 μm), OH 84 μm Λ-doublet (84.4 and 84.6 μm, transitions $^2\Pi_{3/2}$ J=7/2$^+$-5/2$^-$ and $^2\Pi_{3/2}$ J=7/2$^-$-5/2$^+$, respectively), OH 119 μm Λ-doublet (119.2 and 119.4 μm, transitions $^2\Pi_{3/2}$ J=5/2$^-$-3/2$^+$ and $^2\Pi_{3/2}$ J=5/2$^+$-3/2$^-$, respectively). The hyperfine structures of the OH Λ-doublets are not resolved in our observations. The spatial resolution for the CH^+ 120 μm line and the OH 119 μm Λ-doublets is 9″, and 6″ for the OH 84 μm Λ-doublets. The observations were carried out on September 14, 2012 for CH^+ 120 μm and on September 15, 2012 for the OH 84 μm.

The data were processed using the version 10.0.2843 of the reduction and analysis package HIPE. The line fitting was done using IDL-based software PACSman version 3.55 (Lebouteiller et al. 2012). Using a polynomial baseline, the lines were fitted with a Gaussian profile and the flux measured. PACSman measures the line fluxes for each spatial pixel independently. To produce the final map, PACSman recreates an oversampled pixelated grid of the observations with 3″ pixel resolution and calculates the average fractional contribution of the given spatial pixels to the relevant position.

PACSman also calculates the statistical uncertainties, including the dispersion in the reduction process and the rms of the fit. These uncertainties are small and usually amount to 5−20 % for the CH^+ and OH lines. The relative accuracy between spatial pixels given in the manual is 10%[1]. We assume a conservative total error of 22 % for the integrated line intensities in the fainter regions, that is the upper limit of a combination of the calibration uncertainties (10 %) and the line fitting errors (5−20 %). For the Bar, the error is the less than 11 %.

2.2. HIFI and SPIRE observations

In order to obtain information about the velocity structure of the CH^+ lines, we used the Heterodyne Instrument for the Far Infrared (HIFI, de Graauw et al. 2010) to observe the CH^+ J=2-1 line at 180 μm along a cut perpendicular to the Orion Bar (see Fig. 2). The cut is centered at the position α_{J2000}= $05^h35^{min}20.61^s$, δ_{J2000}= -05°25′14″ and extends for 2′ with an inclination PA=52°. We used the on-the-fly observing mode using half-beam sampling, using the nominal HIFI beam size at this frequency (12.3″). The data were obtained with the high-resolution spectrometers (HRS). After porting the FITS data into GILDAS format (Pety 2005)[2], the data processing consisted of a scan-by-scan linear baseline subtraction and resampling to a common frequency grid with a resolution of 0.3 km s^{-1}.

We have also observed CH^+ J=1-0 at 359 μm and water lines 1_{11}-0_{00} at 269 μm and 2_{11}-2_{00} at 399 μm with the Spectral and Photometric Imaging Receiver (SPIRE, Griffin et al. 2010) in the high-resolution full-sampling mode of the SPIRE FTS on September 20, 2010. We include the waterlines as OH can also form via the photodissociation of H_2O. Within the SPIRE range of these observations, the $C^{18}O$ J=8-7 line at 342 μm has also been detected. The data of CH^+ J=1-0 and the water lines were processed using HIPE 11.0.1. To achieve a better angular reso-

[1] From the PACS spectroscopy performance and calibration manual. This can be found at `http://herschel.esac.esa.int/twiki/bin/view/Public/PacsCalibrationWeb`

[2] Institut de Radioastronomie Millimétrique (IRAM): `http://iram.fr/IRAMFR/GILDAS/`

lution, the super-resolution method SUPREME was applied to the FTS data as in Köhler et al. (2014). In Figs. 3 and 9 we give a FWHM using a Gaussian fit with the same bandwidth of the equivalent beam. It should, however, be noted that the PSF is non-Gaussian and a FWHM does not account for the shape of the beam. The gain in resolution with the SUPREME method is, e.g., from a FWHM from 32.6″ to 19.0″ at 400 μm.

The spatial resolution for the CH^+ J=1-0, H_2O 399 μm, and $C^{18}O$ J=8-7 is 19″, and 13″ for the H_2O 269 μm after SUPREME processing. For the detailed description of the reduction procedure method, fitting routines, and PSF see Ayasso et al. (in prep)[3]. The lines were fitted with HIPE Spectrometer Cube fitting procedure. We assume a total error of 36 % for the integrated line intensities, which includes the calibration uncertainties and the line fitting errors.

3. Line emission detection and spatial morphology

In this section we present the observations of CH^+ J=3-2 at 120 μm and J=1-0 at 359 μm, as well as OH 84 μm and 119 μm Λ-doublets observed with PACS. For OH one line map is presented for each Λ-doublet, namely 84.6 μm ($^2\Pi_{3/2}$ J=7/2$^-$-5/2$^+$) and 119.4 μm ($^2\Pi_{3/2}$ J=5/2$^+$-3/2$^-$), as the two lines of the Λ-doublets have the same distribution and almost the same intensities. In both OH 119 μm and 84 μm Λ-doublets the intensities of the two lines vary only slightly by ~30 % (see Fig. 1). Asymmetries are predicted to be small when collisions with ortho-H_2 dominate (i.e., in the warm gas) and when FIR radiative pumping plays a role (Offer & van Dishoeck 1992; Offer et al. 1994; Goicoechea et al. 2011). We have chosen the Λ-doublet with higher integrated intensity for a higher signal-to-noise ratio. Maps of the integrated line intensities are shown in Fig. 3. The black pixels in the maps mark the areas where there is no detection. We show spectra for the CH^+ J=3-2 and OH 119 μm in the left panel and OH 84 μm in the right panel in Fig. 1. These spectra are from the three positions specified in the maps in Fig. 3.

The CH^+ J=3-2 line is well detected in the Bar (see panel a in Fig. 3 and position 2 in the left panel of Fig. 1). The spatial profile of the line emission across the Bar is resolved with a FWHM of 20″ (see Fig. 4). The line emission delineates well the warm molecular zone of the Bar. This warm PDR molecular zone is in between the ionization gas and the cold molecular gas. This is shown in Fig. 5 where the [NII] 122 μm emission map indicates the ionization front[4] (Bernard-Salas et al. 2012), the green contours show the position of the CH^+ J=3-2 emission, and the blue contours show the emission of $C^{18}O$ J=8-7 line. Most of the molecules are photodissociated in the ionized layer in the front of the Bar. Behind the Bar and as we move farther away, the conditions (low FUV flux, low temperature) are not favorable to form and/or excite CH^+.

We see knots of excess of emission in the Bar which correspond to the biggest clumps (α_{2000}=5^{h}35^{min}25.185^s, δ_{2000}= -5°24′34.6″ and α_{2000}=5^{h}35^{min}22.07^s, δ_{2000}=-5°25′13.4″) as detected from the ground by Lis & Schilke (2003). The knots have diameters of about ≃9″ or 0.02 pc and are marginally resolved. This is discussed further in Sect. 4. In the front of the Bar (closer to the ionizing stars) we see emission in the Western (Orion Ridge) and in the Northern part of the map. These excesses can also be seen in C^+ and [OI] (Bernard-Salas et al. 2012). We do not detect CH^+ J=3-2 line behind the Bar. While a background PDR is detected in the fine structure lines (Bernard-Salas et al. 2012) and also in the high-J CO (Parikka et al., in prep.), we do not detect CH^+ J=3-2 line there. The line is either too faint or not existent in the background PDR. In contrast, the CH^+ J=1-0, mapped with SPIRE, was found to extend over a large region around the Bar (see Fig. 3). We need to keep in mind, however, that we always have the OMC cloud behind the Bar as well (Goicoechea et al. 2015).

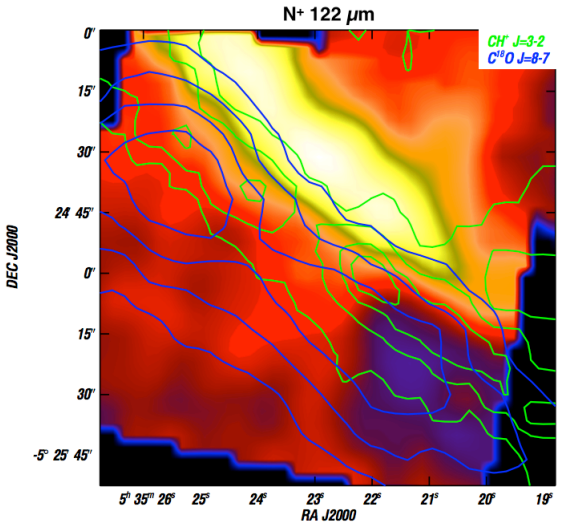

Fig. 5. [NII] 122 μm map with contours of CH^+ J=3-2 (green) and $C^{18}O$ J=8-7 (blue). Contours are with contour steps of 20 % of the peak emission in the Bar.

The OH ground-state rotational lines at 84 μm are well detected in the Bar and also in the Orion Ridge and Northern region in front of the Bar (see panel c in Fig. 3 and the right panel of Fig. 1). Like CH^+ J=3-2, the OH 84 μm emission is confined to the warm molecular zone, but is slightly wider than the CH^+ J=3-2 emission (see Fig. 6). Also like CH^+ J=3-2, the 84 μm line is not detected behind the Bar. There are two main knots of excess in the Bar, one of which may be associated with a dense structure (see Sect. 4 for discussion, referred to as core 3), and another with a source, which will be discussed in Sect. 7.

The OH ground-state rotational lines at 119 μm are clearly detected everywhere in the mapped area (see panel d in Fig. 3 and the left panel of Fig. 1). The OH 119 μm lines are more easily excited than other OH lines and thus they show a more extended spatial distribution (including the Orion Bar but also emission from the Orion molecular cloud complex). These lines are more affected by opacity and radiative transfer effects. Goicoechea et al. (2011) used nonlocal, non-LTE radiative transfer models, including FIR pumping, to fit several FIR OH rotational lines (~119 μm, ~84 μm, ~163 μm, ~79 μm, and ~65 μm lines) detected with *Herschel*/PACS towards a small region in the Orion Bar. The best fit was found for T_{kin} ~200 K, n(H_2)~10^6 cm^{-3} and a source-averaged OH column density of N(OH)=10^{15}cm^{-2}. For these conditions, the OH 119 μm lines are optically thick (τ >10), but the OH 84 μm lines are optically thin (or effectively optically thin, τ <5 and $T_{ex} \ll T_{kin}$). Therefore, OH 84 μm line intensities are expected to be proportional to N(OH).

To estimate whether the CH^+ J=3-2 and J=1-0 lines are optically thick, we use the PDR Meudon code using input parameters

[3] Draft available at: http://hal.archives-ouvertes.fr/hal-00765929, see also: http://www.ias.u-psud.fr/supreme/hipeplugin.php

[4] [NII] 122 μm peaks in the same place as other ionization front tracers, e.g. OI 1.32 μm (Lis & Schilke 2003), peak

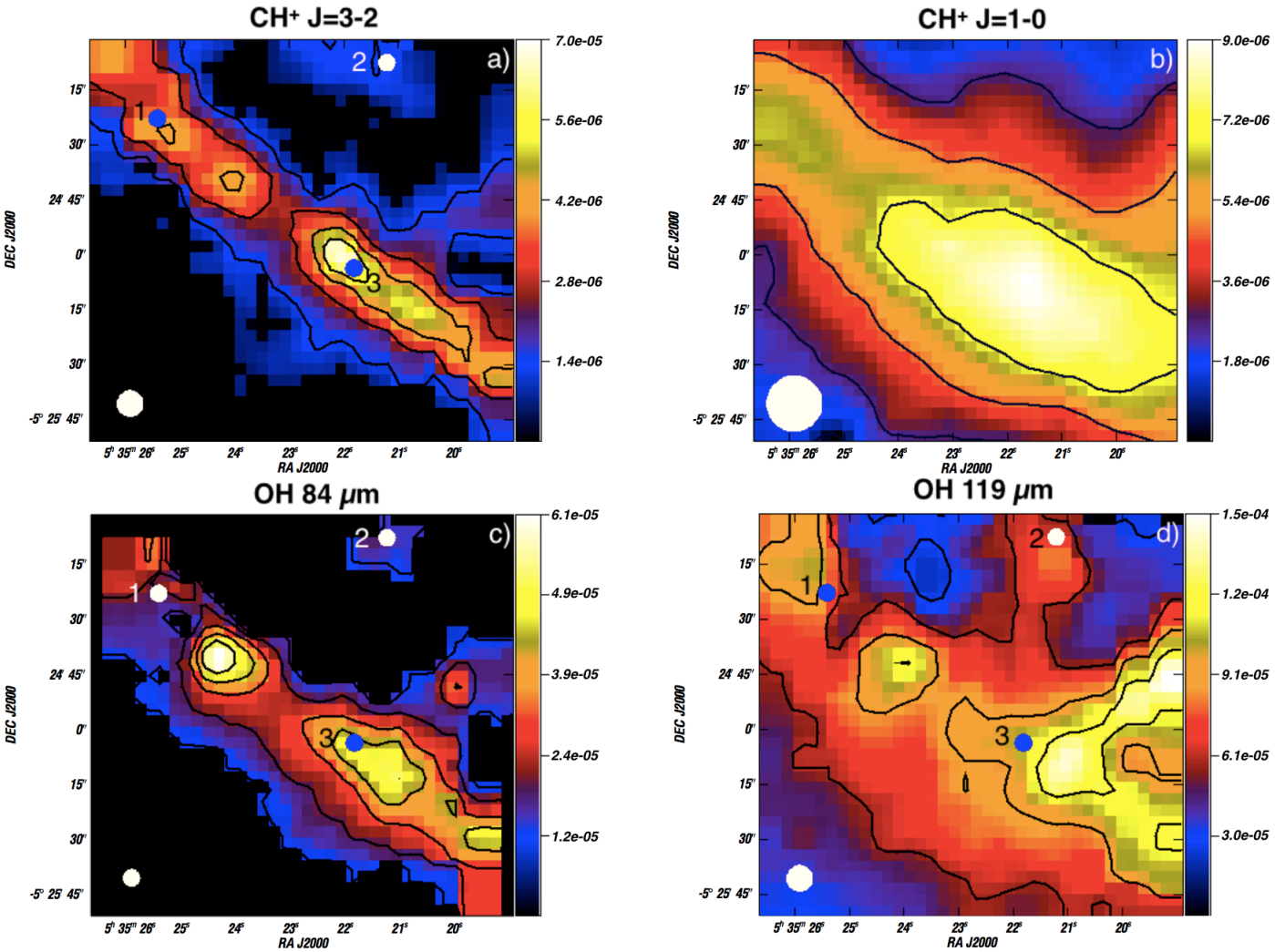

Fig. 3. Morphology of different lines: a) CH^+ J=3-2, b) CH^+ J=1-0, c) OH 84.6 μm, and d) OH 119.4 μm. Contours with contour steps of 20 % of the peak emission in the Bar. The intensities are in units of erg s^{-1} cm^{-2} sr^{-1}. The black pixels are pixels where lines are not detected. The beam size (6″ for OH 84 μm, 9″ for CH^+ J=3-2 and OH 119 μm, and 19″ for CH^+ J=1-0) is shown in the bottom left corner. The positions where the spectra in Fig. 1 have been taken from are also marked in the pictures with corresponding numbers.

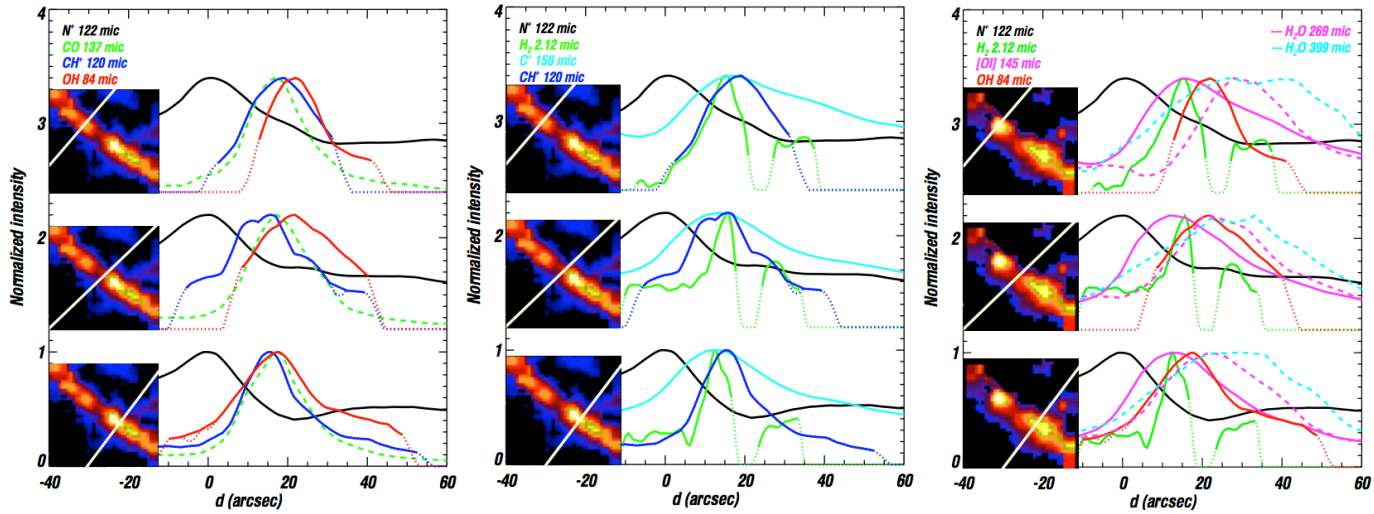

Fig. 4. Profile cuts across the Bar at positions indicated in the small CH^+ J=3-2 and OH 84 μm maps. The intensity of the lines have been normalized to the maximum emission in the Bar and the lines are not convolved to the same beam, so that the structures seen in the unconvolved maps are not lost. The distance is from the ionization front marked by the peak of N^+ emission. The dashed part of the H_2 profile in the cuts indicates the slit seen in the map and the positions of the cuts are indicated in the maps.

from Joblin et al (in prep.). This model reproduces all the rotational transitions observed with Herschel/PACS in the CO^+ peak position by Goicoechea et al. (2011). The code gives a lower optical thickness for CH^+ J=3-2 than for either of the lines of OH 84 μm Λ-doublet. Thus, we assume the CH^+ J=3-2 to be also effectively optically thin. In contrast, the CH^+ J=1-0 is likely to be optically thick.

In conclusion, the spatial distribution of OH 84 μm and CH^+ J=3-2 line emission share similar general characteristics. This is shown in the upper panel of Fig. 6 where we show a map of CH^+ J=3-2 with OH 84 μm contours. The correlation for the lines are shown in the same figure, below the map. The two line emissions correlate well, especially when the intensities are higher. We show the core 1 in red and core 3 (see Fig. 6 for the positions of the cores) in blue in the correlation. These points deviate from the general correlation, the core 3 as a whole and the higher CH^+ intensities for core 1. The similarity was expected because of the similar critical density and upper level energy temperature and a main formation route with H_2. This confirms the earlier work of Goicoechea et al. (2011) and suggests they originate in the same gas component. However, owing to our higher angular resolution and much larger map, we also observe some differences in the morphology. In order to interpret the differences and the common features, we compare these maps to other PDR tracers in the following sections.

4. Origin of the CH^+ and OH emission: clumps?

In this section we compare the CH^+ J=3-2 and OH 84 μm line maps with CO J=19-18 map of the same area (Parikka et al., in prep), to see if the previously found clumps (here referred as core 1 and 3, see Fig. 6 for their positions) coincide with the morphology of our maps. Here when we talk about clumps we mean the dense condensations in the Bar, detected by (Lis & Schilke 2003) in $H^{13}CN$.

4.1. Emission peaks of the CH^+ and OH lines

The comparison of the CH^+ J=3-2 and the CO J=19-18 maps is shown in the middle panel of Fig. 6. The morphology of the high-J CO line shows excess of emission at the positions of the biggest clumps detected from the ground in $H^{13}CN$ by Lis & Schilke (2003) and in CS J=2-1 by Lee et al. (2013). We can clearly see the cores 1 and 3[5], respectively at the North and South of the Bar. These clumps are seen both in CO and ^{13}CO (Parikka et al., in prep.). There is a shift of ∼5″ between the high-J CO and ^{13}CO.We have to keep in mind here and later, though, when talking about distances less than 10″ that the resolution of the high-J CO is only 9″, although the shift is still most likely real.

The ^{13}CO peaks in the same position as the $H^{13}CN$ probing the inner layer while high-J CO (J=19-18, 137 μm) originates in the outer regions of the clumps. The clumpy structure of the CO J=19-18 correlates well with CH^+ J=3-2 emission. Nevertheless, we note that for CH^+ J=3-2 (and J=1-0) the intensity peak is matched with core 3, while CO J=19-18 (and $C^{18}O$ J=8-7) peaks at core 1. Core 1 has a larger column density (Parikka et al., in prep.), suggesting that the optically thin high-J CO is more sensitive to the total column density of warm gas than CH^+. Like CH^+, most of the surface tracers, such as H_2 v=1-0 S(1) or optically thick lines (e.g., CO J=6-5 in Orion Bar), peak at the Southern part of the Bar. In the Bar, 56 % of the CH^+ J=3-2 emission comes from the interclump medium, while 44 % comes from the clumps. The clumpy morphology of the excited CH^+ emission leads to the conclusion that the CH^+ excitation must be sensitive to the density.

We compare OH 84 μm with CO J=19-18 in the left panel of Fig. 4 and in the right panel of Fig. 6. The two lines trace the warm molecular layer but the OH 84 μm line is more extended behind the Bar. The OH line emission peaks at the position of a compact source between the two cores (see Sect. 7). However, despite these differences, the morphologies of the excited OH and CO lines are similar enough to conclude that they originate from the warm and dense gas component.

The correlation of both lines with high-J CO is shown in Fig. 6. The correlation of CH^+ J=3-2 and CO J=19-18 is good behind the Bar (marked in magenta). The dividing line is in the middle of Bar seen in the high-J CO emission. OH 84 μm and CO J=19-18 differ more, especially in core 3 that is marked in blue in the correlation.

4.2. Spatial extension and distance from the ionization front

The spatial correlation between CH^+ J=3-2 and CO J=19-18 is clearly visible if we look at the cut made through the Bar in Fig. 6. Intensities have been normalized to the maximum intensity in the Bar for each line. We find a FWHM of ∼20″ for the Bar in CH^+ 120 μm, which is wider than the PSF of PACS (10″), thus, the emission is extended. The CH^+ J=3-2 and CO J=19-18 lines follow each other well especially in the cuts through the clumps (middle clump and core 3, see Fig. 4[6]). The spatial extension is the same for the CH^+ J=3-2 and CO J=19-18 lines, while OH 84 μm is more extended. This extension could be the result of projection effects along the line of sight (tilting) or it could be due to the clumpy structure allowing photons to penetrate deeper inside the PDR.

We find a large distance from the ionization front to the emission peak for CH^+ J=3-2 and OH 84 μm is about 15−20″ (0.03−0.04 pc at the distance of Orion). This is the same distance as the distance from the ionization front to the H_2 rotational and ro-vibrational lines emission (Allers et al. 2005). It is larger than what is expected by the standard PDR models (e.g., Allers et al. 2005; Goicoechea et al. 2011; Bernard-Salas et al. 2012; Joblin et al., in prep.). For example, the model presented by Bernard-Salas et al. (2012) predicts a distance of ∼8″ between the ionization front to the emission peak of CH^+ and OH. The large separation could be related to the changes of the physical properties, e.g., reduction in the dust FUV attenuation cross section, but could also be consistent with what we expect from the presence of clumps. Joblin et al. (in prep.) presents an isobaric model at high pressure (5×10^8 K cm^{-3}), including collisional and formation pumping, which reproduces the peak intensity of the high-J CO, OH and CH^+.

5. Formation and excitation of CH^+ and OH via vibrationally excited H_2

In this section, we compare the spatial distribution of the CH^+ J=3-2 line with those of H_2 v=1-0 S(1) and C^+ 158 μm, the components of the formation route in reaction $H_2 + C^+ \rightarrow CH^+ + H$. Similarly, we also compare the spatial distribution of the OH 84 μm emission to those of the H_2 v=1-0 S(1) and [OI] 145 μm, the components of reaction $H_2 + O \rightarrow H + OH$.

[5] We have adopted the numbering of the Lis & Schilke (2003) paper.

[6] The OH emission is not extended enough to get a useful cut through the core 1, however, CO and CH^+ follow each other well also in core 1.

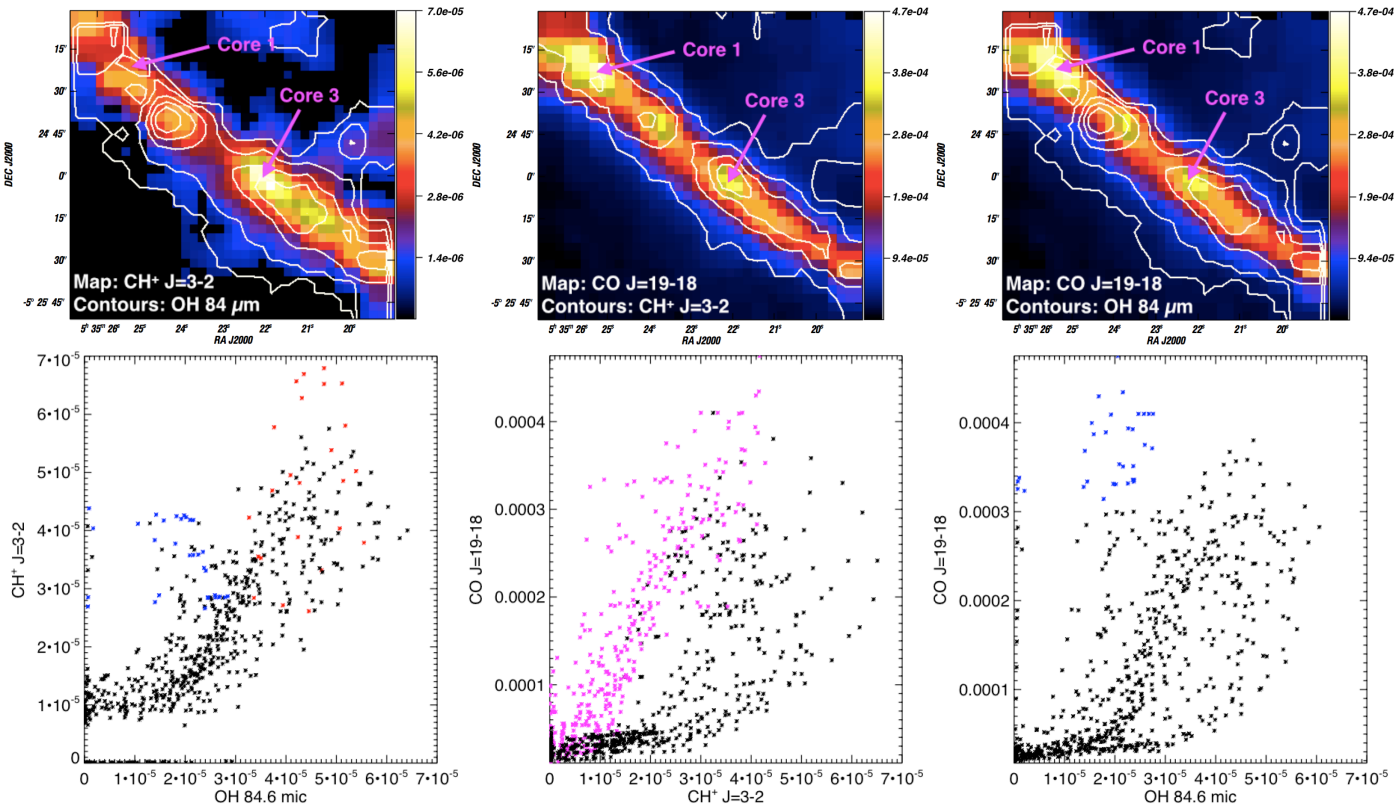

Fig. 6. Top row from left: Map of CH^+ J=3-2 integrated intensity with OH 84 μm contours (left). Maps of CO 137 μm integrated intensity with contours of CH^+ J=3-2 (middle) and OH 84.6 μm (right). All contours are with contour steps of 20 % of the peak emission in the Bar. The intensities are in units of erg s^{-1} cm^{-2} sr^{-1}. Cores 1 and 3 (Lis & Schilke 2003) are marked in all the figures. Bottom row from left: Correlations of the molecular lines shown in the maps above. Cores 1 (red) and 3 (blue) are marked in the correlation of CH^+ J=3-2 and OH 84.6 μm, the back of and behind the Bar (magenta, dividing line in the middle of the Bar) is marked in the correlation of CO J=19-18 and CH^+ J=3-2, and finally the core 3 (blue) is marked in the correlation of CO J=19-18 and CH^+ J=3-2.

5.1. Spatial comparison of CH^+ and excited H_2

Fig. 7 shows a map of H_2 v=1-0 S(1) at 2.12 μm and the CH^+ J=3-2 line. The H_2 v=1-0 S(1) was observed from the ground with a resolution of ∼1″ (Walmsley et al. 2000). The maps are not convolved, so that we do not blur the detailed structures. Fig. 7 shows a good correlation between the spatial distribution of the CH^+ J=3-2 emission and the vibrationally excited H_2 emission. The contours of the CH^+ emission trace in detail the structures seen in H_2. At the edge of the Bar, the CH^+ emission follows the excited H_2. In the clumps, the emission peaks are shifted by ∼5″.

In panel a of Fig. 8 we see the correlation between CH^+ J=3-2 and H_2. This correlation is done with the H_2 v=1-0 S(1) map of van der Werf et al. (1996), which has been convolved in the *Herschel* beam[7]. The convolved H_2 map with contours of the CH^+ J=3-2 line can be seen in Fig. 7. Except for core 3 (marked in red), the emission of the excited CH^+ and H_2 shows a good correlation, which indicates that CH^+ formation and/or excitation depends on the amount of the excited H_2.

In the clumps, the H_2 v=1-0 S(1) peaks nearer the clump's edge facing the stars than CH^+. This shift could be explained by H_2 (v>0) being mostly excited by UV pumping, which is only efficient at the edge of the Bar, while CH^+ J=3-2 is excited by nonreactive or reactive collisions that are sensitive to the local density. The CH^+ J=1-0 line emission is slightly more shifted (∼5″) to inside the Bar than the CH^+ J=3-2. It peaks closer to the ionization front than $C^{18}O$ by ∼5″ (see Fig. 5), while its upper level energy temperature is much lower (see Table 1). This further supports the idea that the excited H_2 (v>0) affects the formation and excitation of CH^+.

In the top row, middle panel, of Fig. 7, we show a map of C^+ 158 μm (Bernard-Salas et al. 2012). The C^+ 158 μm is also included in the cuts of Fig. 4, as it is the other component of the CH^+ formation route in reaction with excited H_2. We see a good correlation between the spatial distribution of the C^+ emission and the excited CH^+. In the Bar, we see a slight shift (less than 5″) between the C^+ and CH^+.

The correlation between CH^+ J=3-2 and C^+ 158 μm is shown in Fig. 8. Points in front of the Bar are marked in black and behind the Bar in magenta. The dividing line is in the middle of Bar seen in the high-J CO emission. Although there is a good overall correlation, we can clearly distinguish the two regions in the correlation. The shift between the front and behind is likely due to the physical conditions behind the Bar which are still favorable for C^+ emission, but not for excited CH^+. The cuts show that the C^+ emission is broader than the excited CH^+. This is due to C^+ 158 μm being easily excited with an upper level energy temperature of 91 K and a critical density of $5{\times}10^3$ cm^{-3}, and because there are diffuse regions where C^+ exists, but H_2 is not abundant. We see strong C^+ emission in front and behind the Bar, which has been interpreted as a background PDR (Bernard-Salas et al. 2012). We do not see excess of emission in CH^+ or H_2.

[7] The correlation could not be done with the map of Walmsley et al. (2000), because the slit distorted the correlation. The star that was covered by the slit is shown in the map by van der Werf et al. (1996), but has been blocked from the correlation.

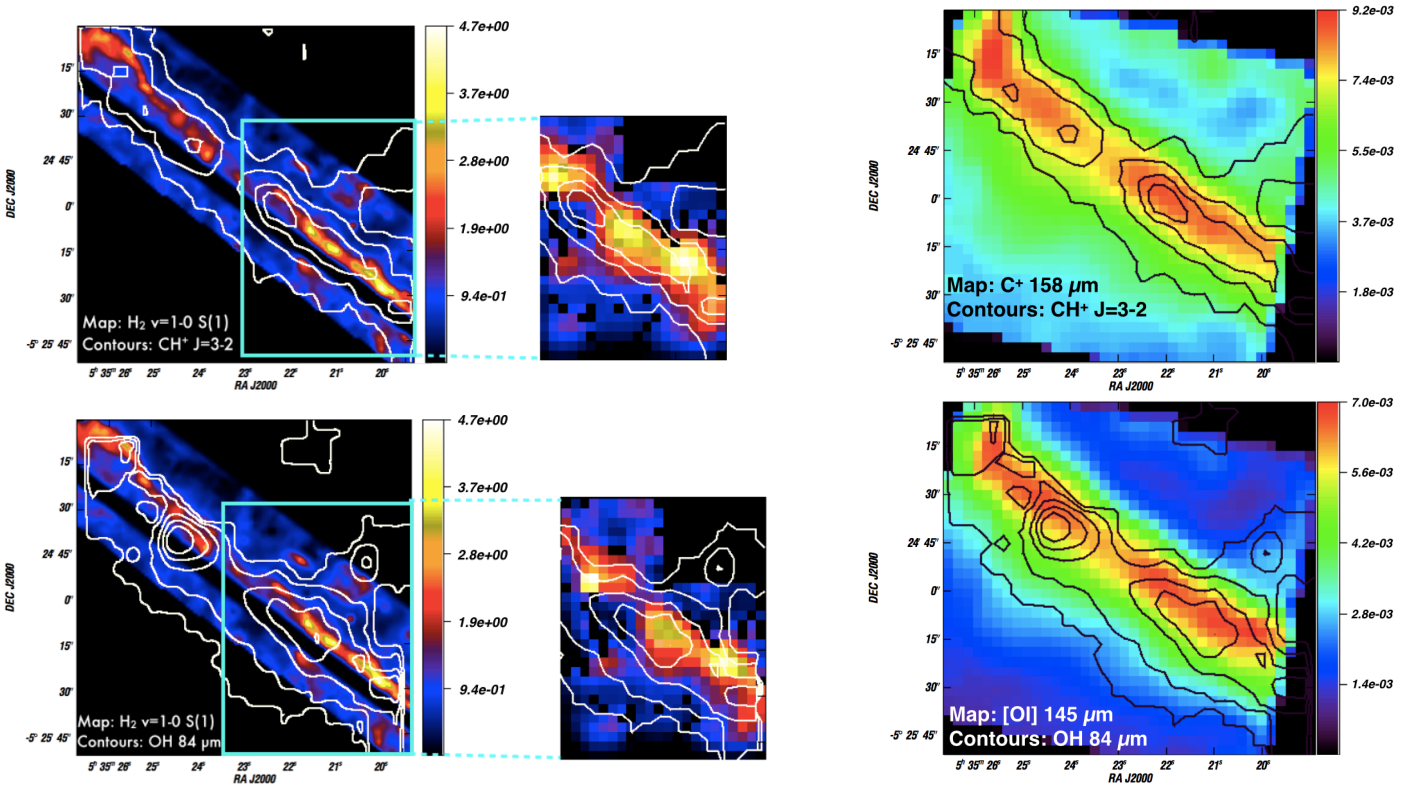

Fig. 7. Top row: CH^+ 120 μm compared with H_2 v=1-0 S(1) (Walmsley et al. 2000) and C^+ 158 μm (Bernard-Salas et al. 2012). CH^+ 120 μm contours overlaid on the H_2 map (left) and C^+ map (right). Zoom: map of vibrationally excited H_2 convolved to the spatial resolution of CH^+ J=3-2 map including contours of CH^+ J=3-2 with contour steps of 20 % of the peak emission in the Bar. Bottom row: OH 84 μm compared with H_2 v=1-0 S(1) and [OI] 145 μm (Bernard-Salas et al. 2012). OH 84 μm contours overlaid on the H_2 map (left) and [OI] map (right). All contours are with contour steps of 20 % of the peak emission, except for the zoomed picture where the contours are with contour steps of 10%. The maps are in units of erg s^{-1} cm^{-2} sr^{-1}.

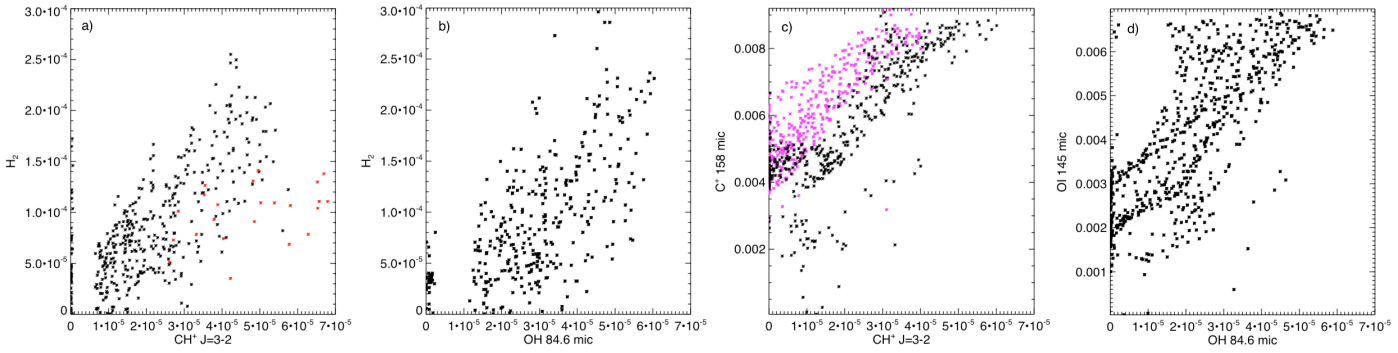

Fig. 8. Correlation for: a) vibrationally excited H_2 (van der Werf et al. 1996) and CH^+ J=3-2 with core 3 (red). b) Vibrationally excited H_2 (van der Werf et al. 1996) OH 84.6 μm. c) C^+ 158 μm (Bernard-Salas et al. 2012) and CH^+ J=3-2. The front (black) and back (magenta) are marked, the dividing line being in the middle of the Bar d) [OI] 145 μm (Bernard-Salas et al. 2012) and OH 84.6 μm.

In conclusion, our observations show a good spatial correlation between the emission of CH^+ J=3-2, H_2 v=1-0 S(1), and C^+ 158 μm. CH^+ was expected to be related to the amount of excited H_2, since excited H_2 is important to the formation of CH^+ (Agúndez et al. 2010; Godard & Cernicharo 2013; Nagy et al. 2013; Zanchet et al. 2013). Because CH^+ is easily destroyed, it is expected to be particularly sensitive to excitation via formation pumping and, thus, the excitation of CH^+ is also dependent on excited H_2. Formation pumping is predicted to be important to the excitation of all the CH^+ rotational lines for the physical conditions prevailing in the warm molecular zone of the Orion Bar. The chemical formation starts to be an important factor at J=3-2 transition. For higher transitions, chemical formation will dominate while for lower transitions non reactive collisions dominate (Godard & Cernicharo 2013; Zanchet et al. 2013). The fact that the CH^+ emission peak coincides with the excited H_2 emission peak, further supports the conclusion that formation pumping is important. However, our observations show a good overall correlation with CO, which suggests that nonreactive collisions are also important.

5.2. Spatial comparison of OH and excited H_2

The left panel in the bottom row of Fig. 7 compares a map of vibrationally excited H_2 (Walmsley et al. 2000) with contours of the OH 84 μm line. It is more extended and less correlated with

H_2 than CH^+. To investigate this further, we plot the correlation of OH 84 μm and the excited H_2 in the lower panel of Fig. 8. The convolved H_2 map with contours of the OH 84 μm line can be seen in Fig. 7. The correlation between the OH 84 μm and the excited H_2 emission is less clear than with CH^+ and H_2. This indicates that the OH formation is less sensitive to the presence of excited H_2 than CH^+, in agreement with theoretical expectations (see, e.g., Lambert & Danks 1986; Agúndez et al. 2010).

We have also compared OH 84 μm with [OI], the other component of the proposed formation route. The bottom right panel of Fig. 7 shows a map of [OI] 145 μm (Bernard-Salas et al. 2012) with OH 84 μm contours are shown in bottom row (left), a cut across the Bar of these two species is given in the right panel (see Fig. 4). In [OI] 145 μm we see the background PDR as in C^+, while it is not seen in OH 84 μm or H_2. The OH emission shows a sharper increase than the [OI] 145 μm emission at the PDR front. The [OI] 145 μm emission is slightly shifted (~5″) to the PDR front. In Fig 8 we show the correlation between [OI] 145 μm and OH 84 μm emission. We find that the increased OH emission matches the OI emission with a large dispersion. Giving the good correlation between [OI] and OH, the reaction with [OI] and H_2 should dominate the OH formation. This is in agreement with Agúndez et al. (2010), who found that the reaction $O + H_2\,(v = 0)$ dominates OH formation in the physical conditions prevailing in the Bar.

5.3. Spatial comparison of OH and H_2O

Alternatively, there is another formation route for OH via the photodissociation of H_2O. We compare the OH 84 μm line with two water lines at 269 μm (1_{11}-0_{00}, E_u/k=53 K) and 399 μm (2_{11}-2_{02}, E_u/k=137 K). Maps of the integrated line intensities of the waterlines are seen in Fig. 9 with contours of OH 84 μm.

Both H_2O lines, more easily excited than OH, peak behind the OH by ~15″ and are more extended (see the cut in Fig. 4). This could be explained by the lower gas temperature in the regions where the bulk of the H_2O arises compared to OH. The photodissociation is likely to limit the water abundance in the warm zone. Thus, the bulk of the OH and water emission arise from different depths, which is supported by the absence of high excitation water lines in the PACS spectra (Goicoechea et al. 2011). It also implies that this formation route is not as important as the $H_2 + O \rightarrow H + OH$ reaction.

6. CH^+ excitation and dynamics

In this section we discuss the CH^+ J=3-2 (120 μm) line in comparison with CH^+ J=1-0 (359 μm) line and the line width resolved observations of CH^+ J=2-1 (180 μm). First, the ratio of CH^+ J=3-2 and CH^+ J=1-0 is shown as a color map in Fig. 10. The contours of CH^+ J=3-2 are plotted for comparison. The ratio is an indicator of the excitation of CH^+. Thus, the excitation decreases further away from the θ Ori C and is linked to the UV radiation from the star.

To investigate the velocity structure and line width of CH^+, we examine the CH^+ J=2-1 (180 μm) line (HIFI), of which we have line width resolved data on a strip across the Southwestern part of the Bar (see Fig. 2 for configuration). A selection of the HIFI spectra obtained along the cut are shown in Fig. 10. Across the strip, the excitation conditions are different as can be seen from the ratio of CH^+ J=3-2 and CH^+ J=1-0. The ratio peaks at the edge of the PDR, right in front of the CH^+ J=3-2 emission, and it decreases further away from the star into the Bar. Optical

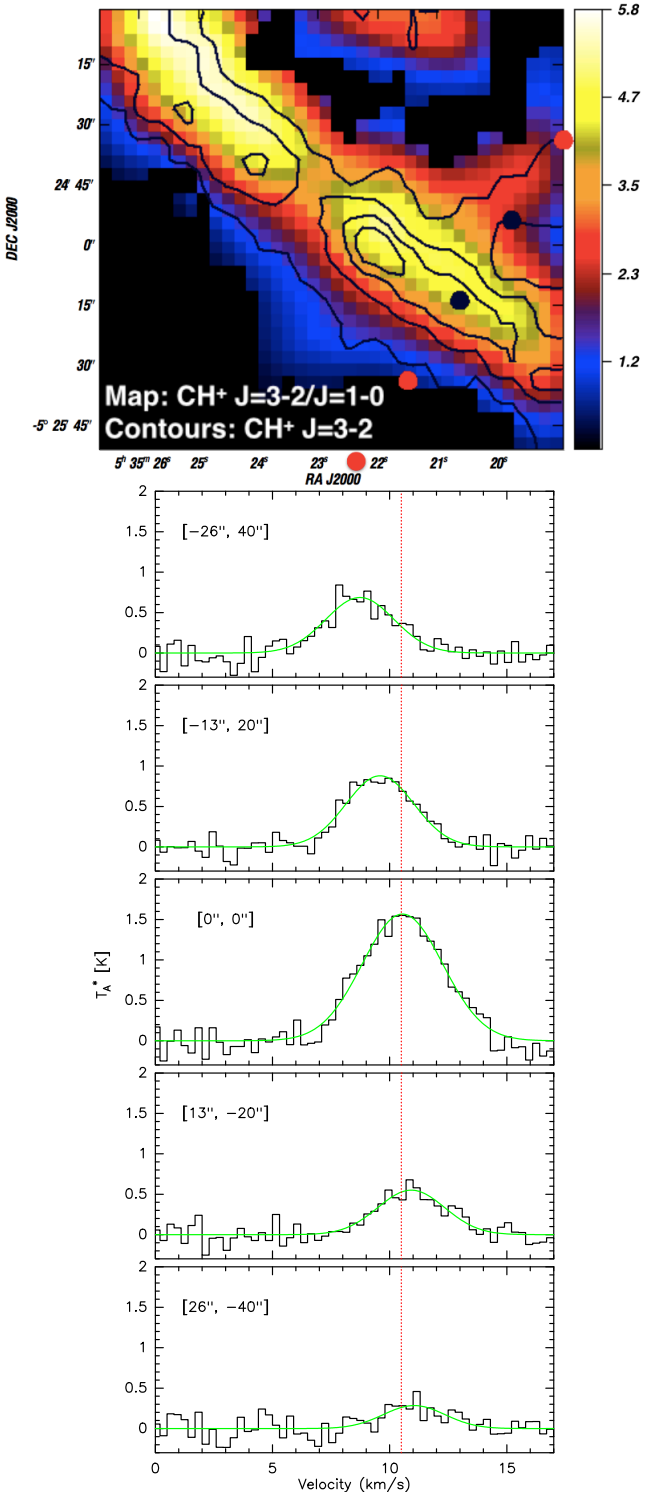

Fig. 10. The ratio of CH^+ J=3-2 and CH^+ J=1-0 integrated intensity with contours of CH^+ 120 μm with contour steps of 20 % of the peak emission to indicate the position of the Bar. The positions across the Bar are the positions of the CH^+ J=2-1 spectra below.

effect can enhance this ratio as the CH^+ J=1-0 is optically thick. The selected positions are ~23″ apart from each other (shown in the map above). The spectra have been obtained averaging all the scans that fall within 4″ of the selected position. The intensity scale is antenna temperature (T_A^*), and the typical rms is 0.12 K calculated at a resolution of 0.3 km s^{-1}. The offset (from the central position of α_{J2000}= $05^h35^{min}20.61^s$, δ_{J2000}= -05°25′14″)

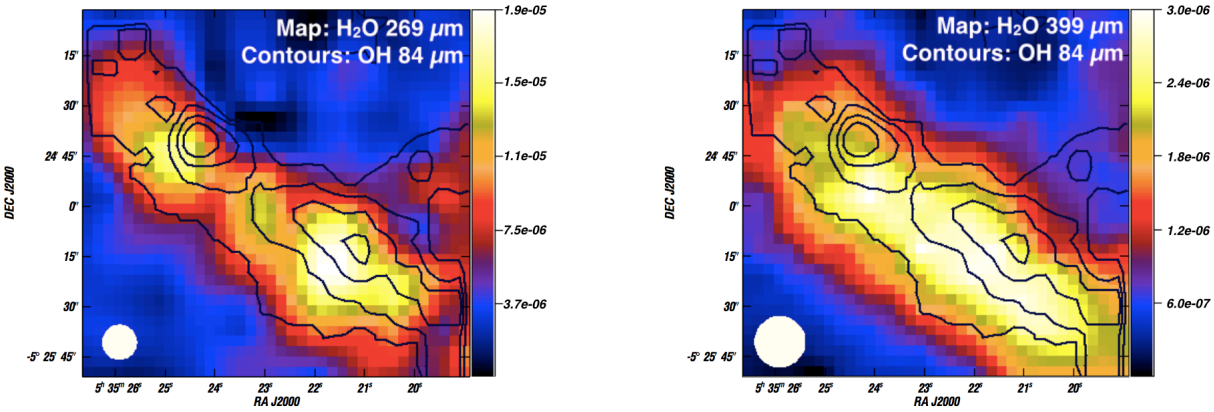

Fig. 9. Maps of H_2O 269 μm (left) and H_2O 399 μm (right) with contours of OH 84.6 μm with contour steps of 20 % of the peak emission. The maps are in units of erg s^{-1} cm^{-2} sr^{-1}.

Table 2. The results of CH^+ J=2-1: the offset from the central position of α_{J2000}: $05^h35^{min}20.61^s$, δ_{J2000}: -05°25′14″, the area [K], velocity ΔV [km s^{-1}], and the peak temperature [K]. The errors are marked in parenthesis.

Offset	Area [K]	V_{LSR} [km s^{-1}]	ΔV [km s^{-1}]	T_{peak} [K]
[-26″, 40″]	2.5 (0.2)	8.7 (0.1)	3.4 (0.3)	0.69
[-13″, 20″]	3.2 (0.2)	9.6 (0.1)	3.4 (0.2)	0.88
[0″, 0″]	6.8 (0.2)	10.6 (0.1)	4.0 (0.2)	1.57
[13″, -20″]	2.0 (0.2)	10.9 (0.1)	3.4 (0.3)	0.55
[26″, -40″]	0.9 (0.2)	11.1 (0.3)	3.1 (0.7)	0.28

of the spectra, the calculated area, the velocity (V_{LSR}), FWHM line width (ΔV) and the peak temperature [K] are listed in Table 2.

Fig. 10 and Table 2 show that the intensity of CH^+ J=2-1 is similar to the CH^+ J=3-2 emission as it is lower in front and behind the Bar and peaks at the same place as CH^+ J=3-2. The centroid velocity changes from 9 km s^{-1} in front of the Bar to 11 km s^{-1} in the Bar and behind the Bar. These velocities are similar to what Peng et al. (2012) found for CO transitions from J=6-5 to J=8-7.

The CH^+ J=1-0 and J=2-1 line widths (ΔV) measured by *Herschel*/HIFI show a much broader line width (ΔV ~4−5 km s^{-1}) than any other molecular tracers of dense gas in the Orion Bar (Nagy et al. 2013). We also find a broad line width of ~3−4 km s^{-1}, that seems to be narrower in front and behind the Bar, but considering the uncertainty, we cannot say that there is a difference between the different positions (see, Fig. 10 and Table 2).

The broad line width could be due to either interclump origin or formation pumping. CH^+ could originate from a low density interclump component (n~10^4 cm^{-3}), where the C^+ has been observed to have a line width of ~4 km s^{-1} (Nagy et al. 2013). However, the CH^+ spatial distribution and intensity suggests that CH^+ emission originates from small dense irradiated structures like the high-J CO with a narrower line profile (2.5 km s^{-1}, Joblin et al., in prep). Thus, we conclude that the broad line width is most likely an effect of formation pumping. If the broadening is due to the formation pumping, then there is no time for the CH^+ to thermalize, which would leave the line width unchanged (Nagy et al. 2013).

7. Proplyd in the Orion Bar

The OH 84 μm map reveals a clear emission peak of emission not detected in the other lines. In Fig. 11, we compare the 84 μm emission with an optical image from the Hubble Space Telescope (HST) by Robberto et al. (2013). The HST image reveals that there is an optical source which corresponds to the peak of the OH 84 μm emission. This source has been identified as a proplyd 244-440 (e.g., Bally et al. 2000). Proplyds, or externally illuminated dense protoplanetary disks, are a special class of low-mass young stellar objects modulated by the external environment. They are found embedded within or near a HII region and are identified by their typical cometary photoionized envelopes.

This is, to our knowledge, the first time that OH emission has been tentatively associated to a proplyd. In the Fig. 11, the

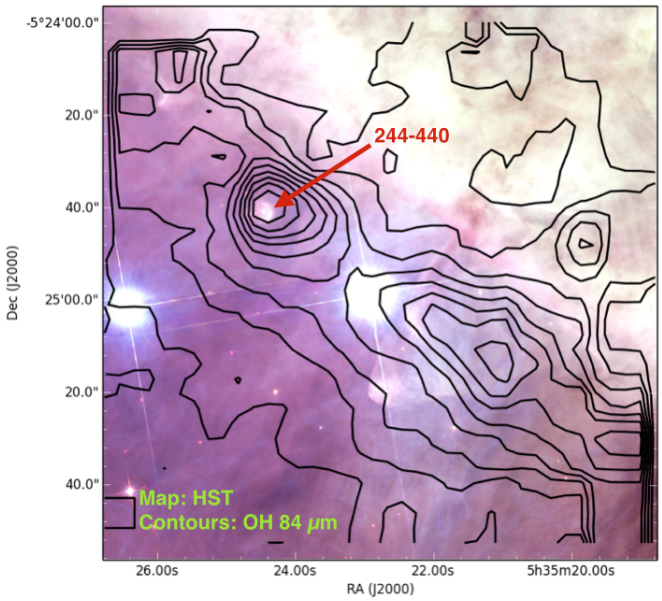

Fig. 11. Contours of OH 84.6 μm at every 10 % of the emission peak overlaid on image (Robberto et al. 2013).

highest OH contour level at the proplyd position is 8″ which corresponds to 3000 AU. While the disk is small (100-500 AU), the envelope can extend up to a couple of 1000 AU. The OH 84 μm line emission could either come from shocks or UV-radiation heating. The proplyd 244-440 shows microjets in HST optical images. If its origin is UV heating, the proplyd detection confirms that the OH does originate in dense and irradiated structures. To establish the origin of the OH line emission from the disk, outflows or jets, high spectral resolution observations are needed.

Like OH, CH^+ J=3-2 has been detected towards protoplanetary flared disks such as HD 100546 (Thi et al. 2011; Fedele et al. 2013). In the upper layers of the disks, which are directly exposed to the stellar radiation field and which resemble in many aspects PDRs, the reaction $H_2 + C^+ \rightarrow CH^+ + H$ is expected to be dominant. In a dense, strongly-UV irradiated gas reactions with H_2(v=0) are likely dominate. We do not see any excess of CH^+ J=3-2 in the Orion Bar, nor any excess of high-J CO emission usually associated with protoplanetary disks (Doppmann et al. 2011). As opposed to OH, CH^+ and high-J CO lines are usually faint in disks, and their emission is likely overshadowed by the strong nebular emission in the region.

8. Summary and conclusions

In this paper we examine the morphology of CH^+ J=3-2 line and the OH Λ-doublets at 84 μm and 119 μm observed with *Herschel*/PACS instrument in the Orion Bar. We use fully sampled maps (total area of $\sim 110'' \times 110''$) across the Bar. We compare these maps to maps of other molecular and atomic lines from the same area. The main findings of the paper are as follows:

- The CH^+ and OH were clearly detected in the Bar. We find that, having similar critical densities, upper level energies, and a main formation route through reactions of C^+ or O atoms with H_2, the morphologies of these lines are similar. Comparison with high-J CO shows that the CH^+ J=3-2 emission originates in the same gas component. Thus, the emission comes mostly from the warm and dense gas at the edge of the PDR. Our observations confirm the clumpy structure of the Bar and CH^+ J=3-2 and OH 84 μm and 119 μm trace these dense irradiated structures. Nevertheless, we observe emission from these lines in all the Bar and emission also comes from the interclump region.
- When comparing the spatial morphologies of the lines, we find that the CH^+ formation route with the vibrationally excited H_2 and C^+ must be the dominant chemical route. Although they have similar overall spatial distribution, there are also slight differences in CH^+ J=3-2 and OH 84 μm. This is most likely due to CH^+ being more susceptible to the formation pumping in its excitation. The OH is less correlated with the vibrationally excited H_2 as already pointed out by Agúndez et al. (2010) who predicted that the reaction $O + H_2\,(v = 0) \rightarrow H + OH$ dominates the OH formation.
- We also find a broad line width of ∼3−4 km s^{-1} for CH^+ J=2-1. This agrees with the paper of Nagy et al. (2013), who found a broad line width of ∼5 km s^{-1} in the Bar, which is broader than any other molecular line tracing dense gas in Orion Bar. Since the spatial correlation between CH^+ and high-J CO shows that they come from similar physical conditions (warm and dense gas) this difference may be due to the fast destruction of CH^+. In addition, comparison with vibrationally excited H_2 v=1-0 S(1) supports the effect of formation pumping. The CH^+ needs vibrationally excited H_2 to form and the excess of energy equivalent to 5360 K corresponds to 4.4 km s^{-1}, which is comparable to the observed line width.
- Interestingly, a peak in the OH 84 μm emission corresponds to a bright young object, identified as a proplyd 244-440. This link between dense structures and the excess of OH 84 μm emission in light of star formation is very exciting and needs to be studied further with new FIR high resolution telescopes like the currently operating SOFIA or JWST.

References

Agúndez, M., Goicoechea, J. R., Cernicharo, J., Faure, A., & Roueff, E. 2010, ApJ, 713, 662
Allers, K. N., Jaffe, D. T., Lacy, J. H., Draine, B. T., & Richter, M. J. 2005, ApJ, 630, 368
Baan, W. A., Rhoads, J., & Haschick, A. D. 1992, ApJ, 401, 508
Bally, J., O'Dell, C. R., & McCaughrean, M. J. 2000, AJ, 119, 2919
Bernard-Salas, J., Habart, E., Arab, H., et al. 2012, A&A, 538, A37
Cernicharo, J., Liu, X.-W., González-Alfonso, E., et al. 1997, ApJ, 483, L65
Darling, J. & Giovanelli, R. 2002, AJ, 124, 100
Dawson, J. R., Walsh, A. J., Jones, P. A., et al. 2014, MNRAS, 439, 1596
de Graauw, T., Helmich, F. P., Phillips, T. G., et al. 2010, A&A, 518, L6
Doppmann, G. W., Najita, J. R., Carr, J. S., & Graham, J. R. 2011, ApJ, 738, 112
Elitzur, M. & Watson, W. D. 1978, ApJ, 222, L141
Falgarone, E., Godard, B., Cernicharo, J., et al. 2010a, A&A, 521, L15
Falgarone, E., Ossenkopf, V., Gerin, M., et al. 2010b, A&A, 518, L118
Fedele, D., Bruderer, S., van Dishoeck, E. F., et al. 2013, A&A, 559, A77
Flower, D. R. 2001, J. Phys. B At. Mol. Opt. Phys., 34, 2731
Godard, B. & Cernicharo, J. 2013, A&A, 550, A8
Godard, B., Falgarone, E., Gerin, M., et al. 2012, A&A, 540, A87
Godard, B., Falgarone, E., & Pineau des Forêts, G. 2009, A&A, 495, 847
Goicoechea, J. R., Joblin, C., Contursi, A., et al. 2011, A&A, 530, L16
Goicoechea, J. R., Teyssier, D., Etxaluze, M., et al. 2015, ApJ, 812, 75
Green, S., Maluendes, S., & McLean, A. D. 1993, ApJS, 85, 181
Griffin, M. J., Abergel, A., Abreu, A., et al. 2010, A&A, 518, L3
Hammami, K., Owono Owono, L., Jaidane, N., & Ben Lakhdar, Z. 2008, J. Mol. Struct. THEOCHEM, 860, 45
Hammami, K., Owono Owono, L. C., & Stäuber, P. 2009, A&A, 507, 1083
Hollenbach, D., Kaufman, M. J., Neufeld, D., Wolfire, M., & Goicoechea, J. R. 2012, ApJ, 754, 105
Jones, M. E., Barlow, S. E., Ellison, G. B., & Ferguson, E. E. 1986, Chem. Phys. Lett., 130, 218
Köhler, M., Habart, E., Arab, H., et al. 2014, A&A, 569, A109
Lambert, D. L. & Danks, A. C. 1986, ApJ, 303, 401
Lebouteiller, V., Cormier, D., Madden, S. C., et al. 2012, A&A, 548, A91
Lee, K., Looney, L. W., Schnee, S., & Li, Z.-Y. 2013, ApJ, 772, 100
Lim, A. J., Rabadán, I., & Tennyson, J. 1999, MNRAS, 306, 473
Lis, D. C. & Schilke, P. 2003, ApJ, 597, L145
Müller, H. S., Schlöder, F., Stutzki, J., & Winnewisser, G. 2005, J. Mol. Struct., 742, 215
Nagy, Z., Van der Tak, F. F. S., Ossenkopf, V., et al. 2013, A&A, 550, A96
Naylor, D. A., Dartois, E., Habart, E., et al. 2010, A&A, 518, L117
Offer, A. R. & van Dishoeck, E. F. 1992, MNRAS, 257, 377
Offer, A. R., van Hemert, M. C., van Dishoeck, E. F., van Hemert, M. C., & van Dishoeck, E. F. 1994, J. Chem. Phys., 100, 362
Peng, T.-C., Wyrowski, F., Zapata, L. A., Güsten, R., & Menten, K. M. 2012, A&A, 538, A12
Pety, J. 2005, SF2A-2005 Sem. l'Astrophysique Fr.
Pineau des Forets, G., Flower, D. R., Hartquist, T. W., & Dalgarno, A. 1986, MNRAS, 220, 801
Poglitsch, A., Waelkens, C., Geis, N., et al. 2010, A&A, 518, L2
Rangwala, N., Maloney, P. R., Glenn, J., et al. 2014, ApJ, 788, 147
Robberto, M., Soderblom, D. R., Bergeron, E., et al. 2013, ApJS, 207, 10
Schmelz, J. T., Baan, W. A., Haschick, A. D., & Eder, J. 1986, AJ, 92, 1291
Spinoglio, L., Pereira-Santaella, M., Busquet, G., et al. 2012, ApJ, 758, 108
Storey, J. W. V., Watson, D. M., & Townes, C. H. 1981, ApJ, 244, L27
Thi, W.-F., Ménard, F., Meeus, G., et al. 2011, A&A, 530, L2
van der Werf, P. P., Stutzki, J., Sternberg, A., & Krabbe, A. 1996, A&A
Walmsley, C. M., Natta, A., Oliva, E., & Testi, L. 2000, A&A
White, R. E. 1984, ApJ, 284, 695
Zanchet, A., Godard, B., Bulut, N., et al. 2013, ApJ, 766, 80

7.4 PERSPECTIVES

The paper examines the morphology of CH^+ J=3-2 line and the OH Λ-doublets at 84 μm and 119 μm observed with *Herschel*/PACS instrument in the Orion Bar. The maps of a total area of ~110″ × 110″ are compared to maps of other atomic and molecular tracers observed in the same area.

The CH^+ and OH emission originates in the warm and dense gas component and the clumps in the Bar are clearly detected. We can also confirm the CH^+ formation route via vibrationally excited H_2. The peak in the OH 84 μm emission corresponds to a bright young object, identified as the proplyd 244-440. OH has been found in protoplanetary disks also in other studies (Sturm et al., 2010; Fedele et al., 2012). Unfortunately, due to limitations of our observations, the emission could not be reliably isolated from the rest of the region because our data is not resolved in line width. In order to confirm the proplyd finding, high spectral resolution observations are required to separate the expected different velocities of the proplyd and the surrounding nebula.

To confirm the detection of the proplyd we will be observing the proplyd 244-440 in the OH 163 μm line with *SOFIA*/GREAT during cycle 3. GREAT provides similar wavelength range to *Herschel*/PACS (in 60−200 μm range), but has a better spectral resolution, thus, the line width can be resolved. The 84 μm was not available for cycle 3 and instead we chose the OH 163 μm line, which is of similar upper level energy temperature as the 84 μm line (see Fig. 3.3). In addition Goicoechea et al. (2011) found both OH 163 μm doublets to be of similar magnitude as the OH 84 μm, 163 μm doublets being 1.34 (163.4 μm) and 2.74 (163.0 μm) 10^{-5} erg s^{-1} cm^{-2} sr^{-1} and 84 μm doublets 4.07 (84.6 μm) and 2.38 (84.4 μm) 10^{-5} erg s^{-1} cm^{-2} sr^{-1}. They also showed similar morphology and are both optically thin.

The OH 163 μm doublet will be observed also in three other proplyds along with [OI] 63 μm line[3]. We will use line width resolved observations from GREAT to constrain the excitation mechanism of the OH line (shocks vs. UV radiation) in the four proplyds.

3 [OI] 63 μm line observations will be the responsibility of Silvia Vicente.

8

HIGH-J CO IN THE ORION BAR

8.1 INTRODUCTION

CO is the most abundant molecule in the ISM after H_2. It was observed the first time in the ISM by Wilson et al. (1970) in the Orion Nebula. Since then, the CO J=1-0 line has been used to trace the molecular component of the ISM, and several surveys have been conducted to understand the distribution of CO in the Galaxy (e.g., Schwartz et al., 1973; Burton et al., 1975; Scoville and Solomon, 1975; Burton and Gordon, 1978; Dame and Thaddeus, 1985; Dame et al., 1987; Solomon et al., 1987). In addition CO has been observed in many environments, e.g., PDRs, protoplanetary disks, young stellar objects (YSOs) (see, e.g., Martín et al., 2009; Sturm et al., 2010; Furukawa et al., 2014), and different extragalactic environments, e.g., low surface brightness galaxies, high-redshift galaxies, and Ultra Luminous Infrared Galaxies (ULIRGs) (e.g., O'Neil et al., 2000; Schleicher et al., 2010; Papadopoulos et al., 2010).

The high-J CO is expected to trace the warm (T_{gas} ~100−150 K) and dense (n_H ~10^{6-7} cm^{-3}) medium due to its high upper level energy temperature and critical density, like the CH^+ and OH (Parikka et al., in prep., see Chapter 7). In the ISM, high-J CO can originate from FUV-illuminated surfaces of dense clumps or filaments with a small filling factor. Alternatively chemical pumping, shocks, cosmic rays, turbulence, or advection in the interclump medium can excite the CO to high-J levels. The dominating excitation process of CO depends on the local physical conditions of the interstellar gas. The competing excitation mechanisms may result in different spatial morphologies. UV heating is only efficient at the surface of the PDR, while the IR pumping, caused by the IR radiation from dust, excites gas further in the cloud. Cosmic rays can penetrate the cloud and they affect the entire PDR. Shocks can be detected in velocity structures, when examining the kinematics of the CO lines. Studying the excitation of CO will, thus, give information on the structure of the PDR as a whole.

With *Herschel* we have, for the first time, access to high excited lines of CO as *Herschel* that emit in the far-infrared (FIR) range. This range is critical in the study of PDRs, as bulk of dust, namely big grains, and important atomic and molecular species emit in FIR. The Orion Bar is an ideal target to study the warm gas as it is an active site of star formation, and it is considered to be a prototypical PDR with an almost edge-on orientation (Tielens et al., 1993).

Arab et al. (2012) used *Herschel* observations to model the dust continuum in the Orion Bar[1] and towards the ionizing stars. In addition, the main cooling lines of PDRs, like [OI] and [CII] have been studied in detail by

1 see Chapter 2.3.2

Bernard-Salas et al. (2012). In this chapter I use *Herschel* observations described in Chapter 4 to spatially resolve the emission of high excited CO and examine its main excitation mechanisms. This continues the work of Habart et al. (2010), who studied sparse sampled maps of several molecular lines including many CO and ^{13}CO transitions. I compare the high-J CO with other CO transitions, ^{13}CO transitions, other important molecules in PDRs like vibrationally excited H_2, and PAH emission.

8.2 SPATIAL DISTRIBUTION OF CO IN THE ORION BAR

We observed the CO J=19-18 transition (137 μm) in the Orion Bar with *Herschel*/PACS instrument (Poglitsch et al., 2010). We have also mapped the same area with SPIRE which gives us CO transitions from J=4-3 to J=13-12, ^{13}CO transitions from J=5-4 to J=13-12, and C^{18}O transitions from J=5-4 to J=13-12. I will highlight the comparison between the high-J CO (J=19-18) with the mid-J CO (J=12-11) and ^{13}CO (J=12-11), but all the SPIRE CO, ^{13}CO, and C^{18}O show the same trends and these maps are presented in Appendix B. In this Section I will also compare the high-J CO to other tracers of denser gas, like CS, and H^{13}CN. I also compare the high-J CO to vibrationally excited H_2, which is sensitive to the UV field (e.g., Tielens and Hollenbach, 1985a,b; Sternberg and Dalgarno, 1989) and seen in front of dense structures where UV radiation from the star is still high. Finally, the ratio of high-J and mid-J CO is compared to the emission of the high-J CO and 8 μm emission, which traces the emission of the PAHs that heat the gas via photoelectric heating.

The CO J=19-18 transition is detected unambiguously everywhere in the observed region (see Fig. 8.1). The highest signal-to-noise ratio (~130 σ) is

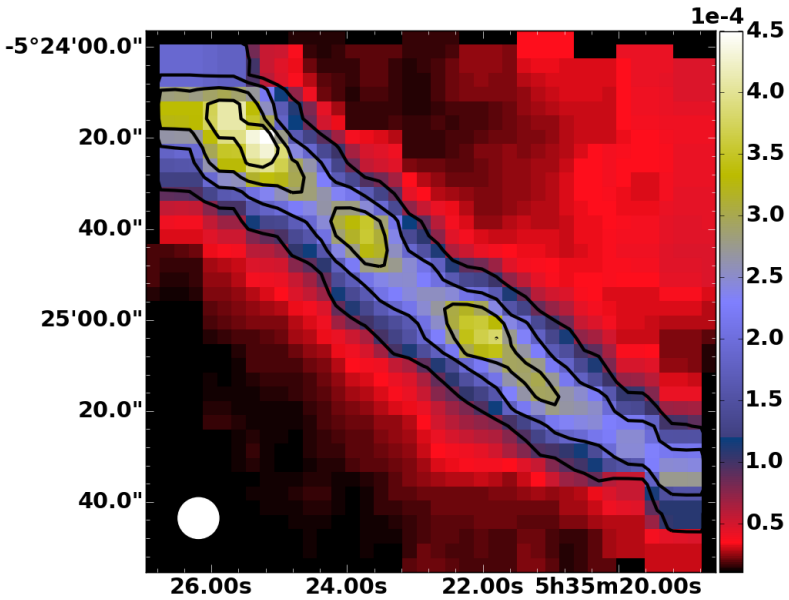

Figure 8.1: Map of CO J=19-18 integrated intensity. The contours are at levels of 0.2, 0.4, 0.6, and 0.8 of the peak emission. Beam size is indicated in the bottom left corner.

reached in the Bar, as expected, but the detection is clear ($\sigma \geqslant 10$) outside the Bar as well. The map shows a clumpy structure in the Bar and extended detection in front of the Bar (closer to the ionizing stars) and behind the Bar. There are three clear clumps in the Bar, and the maximum intensity (4.75×10^{-4} erg s^{-1} cm^{-2} sr^{-1}) is found in the northwestern clump. Strong emission appears also to originate from the interclump regions of the Bar, while 31 % of emission originates from the clumps (where the emission >60 % of the peak emission).

In Fig. 8.2 I compare the CO J=19-18 map to the ^{13}CO J=12-11. Low-J ^{13}CO is a well-known tracer of dense structures (see, e.g., Casoli et al., 1986; Meier et al., 2000; Wyrowski et al., 2006; Hily-Blant and Falgarone, 2007; Qian et al., 2012) and the higher transitions have a smaller beam size due to smaller wavelength. The morphologies of the two lines coincide well in

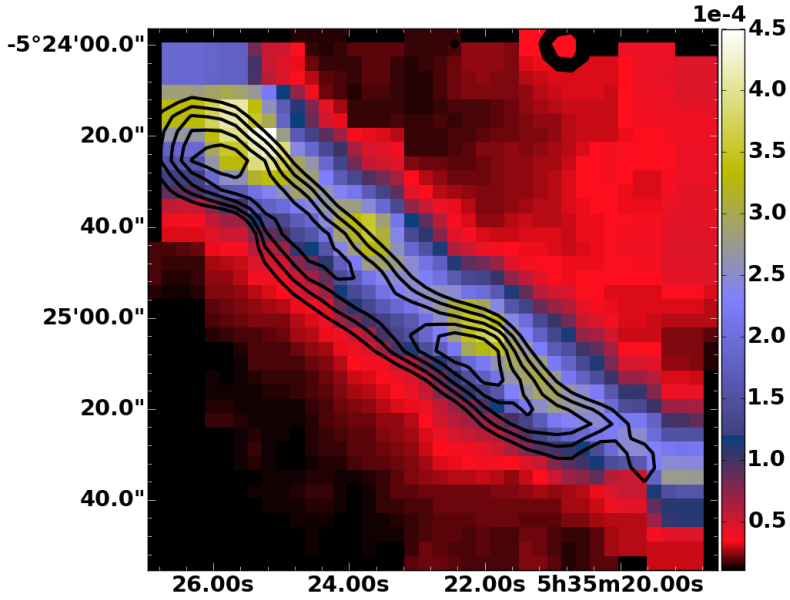

Figure 8.2: Map of CO J=19-18 integrated intensity. The contours of ^{13}CO J=12-11 are at levels of 0.5, 0.6, 0.7, 0.8, and 0.9 of the peak emission in the Bar.

the Bar, and both transitions trace the same clumps. The J=19-18 transition is shifted ~5″ relative to ^{13}CO towards the ionizing stars. This is expected as the ^{13}CO is a lower transition and it will peak deeper in the Bar. The similar morphologies indicate that the high-J CO is also sensitive to dense structures.

Fig. 8.3 shows a map from the Orion Bar in CO J=6-5 observed by Lis and Schilke (2003). In the same picture we see also the H_2 v=1-0 S(1) in black (Walmsley et al., 2000). The blue contours show the H^{13}CN J=1-0 emission (Lis and Schilke, 2003), a tracer of dense cores. Lis and Schilke (2003) identified several cores from the H^{13}CN emission, marked by numbers, from 1 to 10 in the map. Two of these cores (1 and 3) were also lately mapped by Lee et al. (2013) in CS J=2-1 (see Fig. 8.4), which is also known to originate in the dense cores of the clumps in PDRs. These two starless cores fall in the area we have mapped with CO J=19-18.

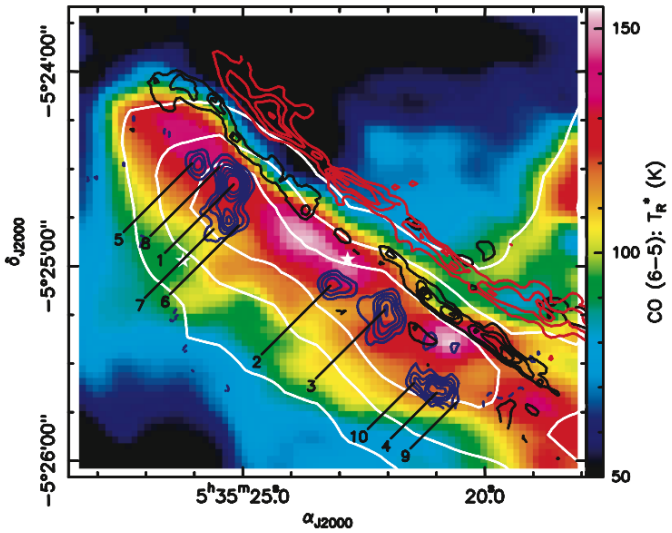

Figure 8.3: Distribution of the CO J=6-5 peak brightness temperature (color image) and ^{13}CO J=3-2 integrated intensity (white contours) in the Orion Bar. Red and black contours show the distribution of the OI 1.32 μm fluorescent emission and H_2 v=1-0 S(1) emission. Blue contours show the distribution of the H^{13}CN J=1-0 emission (Lis and Schilke, 2003).

In the right panel of Fig. 8.4 we have plotted the contours of CO J=19-18 in red on top of a *Herschel* 500 μm map (top: core 1, bottom: core 3), the same area as shown by Lee et al. (2013) on the left panel. For comparison, the H_2 v=1-0 S(1) emission (Walmsley et al., 2000) is plotted in blue. The CS J=2-1 map shows smaller structures, but this map has a higher resolution (5″)[2]. The CO J=19-18 emission is shifted ~5″ towards the ionizing stars from the H^{13}CN and CS J=2-1 emission as well as ^{13}CO J=12-11 (see Fig. 8.2). In addition, the H_2 v=1-0 S(1) emission is shifted ~5″ towards the ionizing stars from the CO J=19-18 emission.

The H_2 v=1-0 S(1) map with contours of CO J=19-18, for the whole area where the high-J CO was observed, is plotted in the Fig. 8.5. The figure shows that the edge of the Bar seen CO J=19-18 emission coincides with the edge of the Bar of the vibrationally excited H_2 emission. The maps in Fig. 8.4 and 8.5 are not convolved, but the displacement can be seen also in the convolved map. This is further evidence that the high-J CO originates in the irradiated dense structures. We can also make a link between the core tracers like H^{13}CN and CS J=2-1 and the CO J=19-18, which traces the edge of the dense clumps based on Fig. 8.4 and 8.5.

8.3 HIGH-J CO EXCITATION

The emission of fine structure lines and molecular lines dominate the cooling in PDRs. In this section I first examine the role of CO in the cooling of the PDR. The major cooling lines in Orion Bar are [CII] 158 μm and [OI] 63

2 From the contours in Fig. 8.4 we assume that the clumps would be seen also if convolved to 9″, which is the resolution of our high-J CO map.

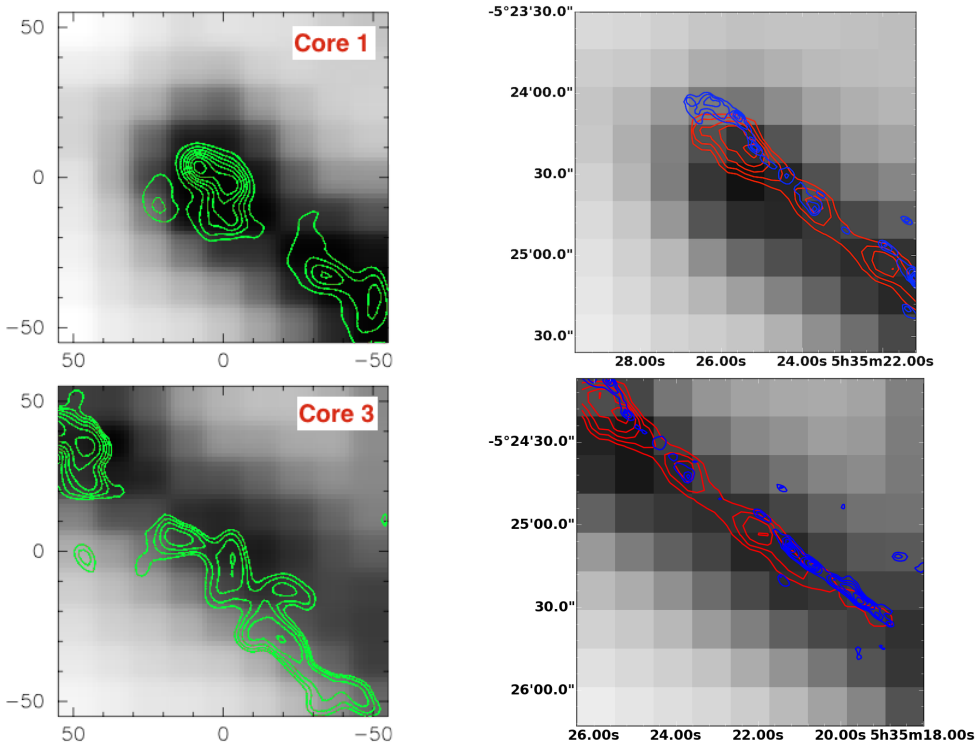

Figure 8.4: Top: core 1, bottom: core 3. Left: *Herschel* 500 µm with contours of CS J=2-1 (Lee et al., 2013). Right: *Herschel* 500 µm with contours of CO J=19-18 at levels from 50 % of the emission maximum and H_2 v=1-0 S(1) emission (Walmsley et al., 2000) from 40 % of the emission maximum, both with contour steps 10 % of relevant peak value. The (0, 0) coordinates for core 1 are RA: $05^h35^m25.4^s$ and DEC: -05°24′33″, and RA: $05^h35^m22.2^s$ and DEC: for -05°25′10″ for core 3. See also Fig. 8.5 for comparison of CO J=19-18 and H_2.

and 145 µm lines which account for 90 % of the power emitted by all the relevant FIR cooling lines (Bernard-Salas et al., 2012), [OI] 63 µm contributing 72 % of the cooling effect of these three lines. CO and H_2 are the most important molecular cooling lines, contributing 5 % and 4 %, respectively, of the total cooling at the FIR peak, where the cooling budget has been estimated.

The integrated intensities of ^{12}CO and ^{13}CO observations convolved to 26″, the largest beam size (after SUPREME cube making, see Chapter 4.3.2) are shown in Fig. 8.6. I include all the observed transitions of ^{12}CO from J=4-3 to J=13-12 and J=19-18 and ^{13}CO from J=5-4 to J=13-12. The properties of these lines are summarized in Table 8.1. The observations are shown for the three positions indicated in the map: in front of the Bar (blue), in the Bar (red), and behind the Bar (green). The three positions were chosen to evaluate the emission as a function of depth within the Bar. The position in the Bar is the position of core 3 seen in CO J=19-18, this position was chosen instead of core 1, because we could get a more straight line for the in front and behind positions. The final positions had to be adjusted since some of the higher ^{13}CO lines were not visible in all pixels of the map. The

Table 8.1: The properties of the observed lines: wavelength (λ), transition, critical density (n_{crit}), upper level energy temperature (E_u/k), and Einstein coefficient (A_{ij}). Numbers in parenthesis are power of 10. The critical densities have been calculated with ortho-H_2 (PDR Meudon code, Le Petit et al., 2006) and with a temperature of 100 K.

	λ [μm]	transition	n_{crit} [cm^{-3}]	E_u/k [K]	A_{ij} [s^{-1}]
CO	649.7	J=4-3	8 (04)	55.3	6.13 (-06)
CO	520.2	J=5-4	2 (05)	83.0	1.22 (-05)
CO	433.6	J=6-5	3 (05)	116	2.14 (-05)
CO	371.7	J=7-6	4 (05)	155	3.42 (-05)
CO	325.2	J=8-7	6 (05)	199	5.13 (-05)
CO	289.1	J=9-8	8 (05)	249	7.33 (-05)
CO	260.2	J=10-9	1 (06)	304	1.01 (-04)
CO	236.6	J=11-10	1 (06)	365	1.34 (-04)
CO	216.9	J=12-11	2 (06)	431	1.74 (-04)
CO	200.3	J=13-12	2 (06)	503	2.20 (-04)
CO	137.3	J=19-18	5 (06)	1050	5.70 (-04)
^{13}CO	546.2	J=5-4	1 (05)	79.3	1.07 (-05)
^{13}CO	455.2	J=6-5	2 (05)	111	1.87 (-05)
^{13}CO	390.2	J=7-6	4 (05)	148	2.99 (-05)
^{13}CO	341.5	J=8-7	5 (05)	190	4.49 (-05)
^{13}CO	303.6	J=9-8	7 (05)	238	6.41 (-05)
^{13}CO	273.2	J=10-9	1 (06)	291	8.80 (-05)
^{13}CO	248.4	J=11-10	1 (06)	349	1.17 (-04)
^{13}CO	226.9	J=12-11	2 (06)	412	1.52 (-04)
^{13}CO	209.5	J=13-12	2 (06)	481	1.92 (-04)

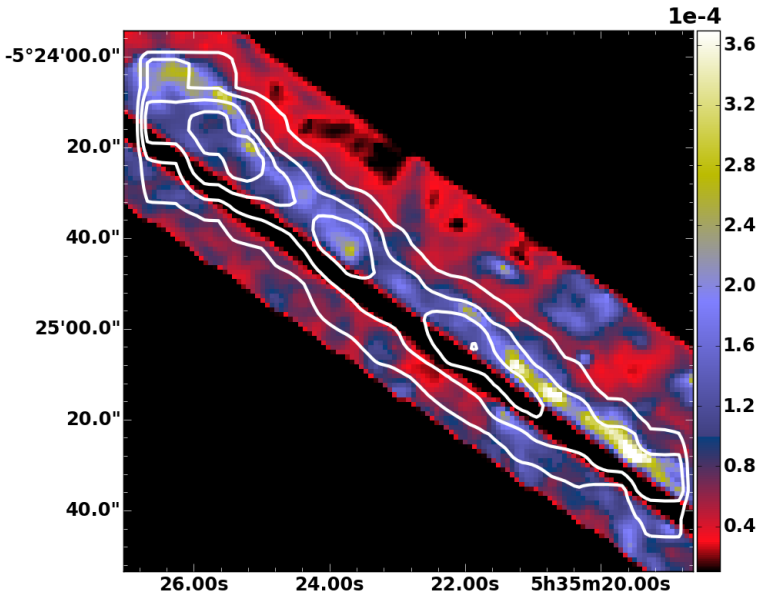

Figure 8.5: Map of excited H_2 (Walmsley et al., 2000) with overplotted contours of CO J=19-18. The observations are not convolved, so that smaller structures can be seen.

Table 8.2: Positions of the three points in Fig. 8.6.

Position	α (J2000)	δ (J2000)
In front of the Bar (blue)	5 35 20.5	-5 24 44
In the Bar (red)	5 35 22.1	-5 25 02
Behind the Bar (green)	5 35 22.6	-5 25 32

positions are listed in Table 8.2. In the plot the integrated line intensity is plotted against the upper level energy temperature.

The ^{12}CO intensity is higher than the ^{13}CO, as expected. The ^{12}CO is optically thick in all the observed transitions, except for the J=19-18 transition (see optical depth in Fig. 8.8), thus, the mostly optically thin ^{13}CO will help constrain the model used to evaluate the hydrogen density, CO column density, and temperature in the region presented in Sect. 8.4. The integrated intensity is higher in the Bar than in the front or behind the Bar.

In Fig. 8.6 we compare the high-J CO J=19-18 and mid-J CO J=12-11 to examine the temperature in the three positions. High-J CO is a tracer of warm gas, with its higher upper level energy temperature, while mid-J CO traces cooler gas. Thus, the larger the ratio is, the warmer is the gas. Fig. 8.6 shows that the temperature is highest in front of the Bar. The Bar is also warm, as the high-J and mid-J CO are comparable. Behind the Bar the temperature is lower, but the gas is still warm. This is evidence of contribution from a warm background PDR as has been discussed previously by Bernard-Salas et al. (2012). The temperature in the region is further discussed in Sect. 8.4 with a RADEX analysis.

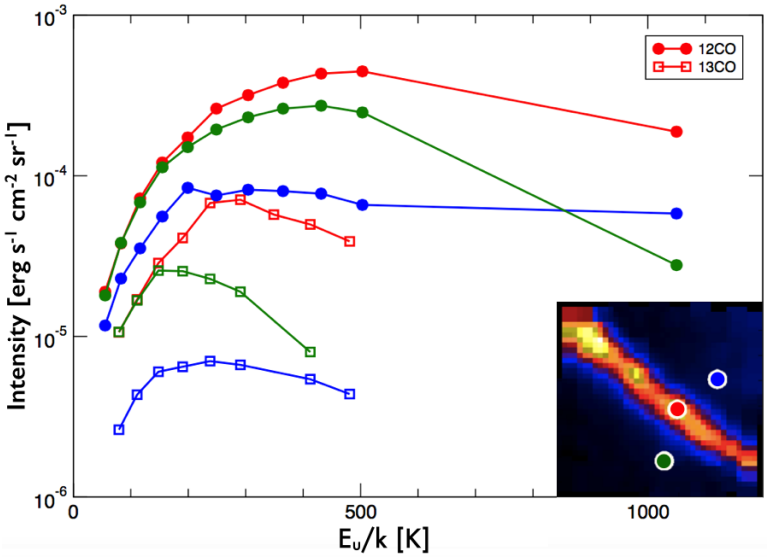

Figure 8.6: Top: Integrated line intensity plotted against the upper level energy temperature of the observed transitions. ^{12}CO (circles) and ^{13}CO (squares) in front of the Bar (blue), in the Bar (red), and behind the Bar (green) as indicated in the map.

Fig. 8.5 compares the CO J=19-18 to the vibrationally excited H_2, which is sensitive to the UV field (e.g., Tielens and Hollenbach, 1985a,b; Sternberg and Dalgarno, 1989). Since the excited H_2 traces the edge of the PDR and is sensitive to the UV radiation, the similar morphology of high-J CO with the excited H_2 indicates that the high-J CO is also sensitive to the UV radiation. To investigate further the excitation of high excited CO, we show in Fig. 8.7 the contour of the ratio of CO J=19-18 to CO J=12-11 (left panel) on top of CO J=19-18 emission. This figure shows that the ratio peaks in front of the

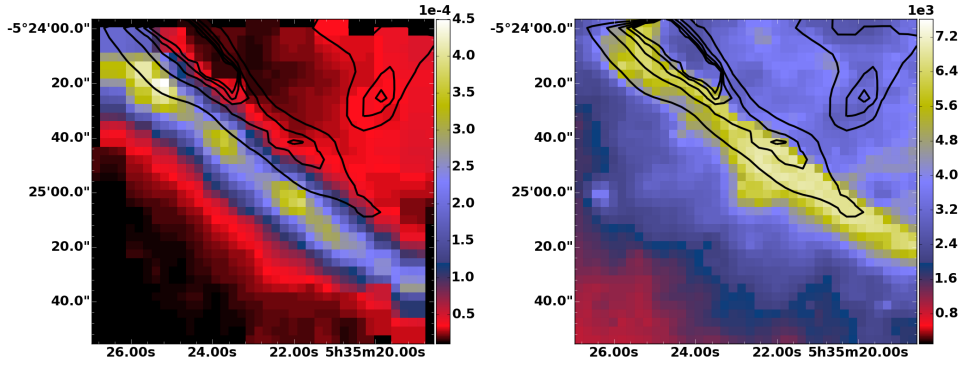

Figure 8.7: The contours of CO J=19-18 / CO J=12-11 ratio overplotted on the CO J=19-18 emission (left). The contours of CO J=19-18 / CO J=12-11 ratio overplotted on the IRAC 8 μm (right). The IRAC map is in units of MJy sr^{-1}.

CO J=19-18 emission. The UV radiation can excite the CO via photoelectric heating through the PAHs or direct UV pumping. It was already concluded in the previous section that the high-J CO is sensitive to the UV radiation, however, this needs to be confirmed with modeling. Previously PDR mod-

els have predicted for G_0 ~10^4 and $n > 10^5$ cm^{-3}, that the main heating processes at the PDR surface are the photoelectric effect on small grains and the H_2 formation and pumping (e.g., Le Bourlot et al., 2012).

We will now compare the CO ratio with Spitzer IRAC 8 μm (left panel), which traces the PAH emission. The left panel of Fig. 8.7 shows that PAH emission coincides with the high-J to mid-J CO ratio. Given that the PAHs dominate the photoelectric heating, it is likely that the photoelectric heating caused by UV radiation are important in the excitation of CO in the Orion Bar. The fact that the high/mid-J CO ratio peaks in where the high-J CO is excited and peaks in front or coincides with PAH emission gives further evidence that the high-J CO is excited by the UV radiation. We exclude the effect of cosmic rays, as we do not see excitation effect beyond the diffuse region in the front of the PDR. We define the Bar being Bar is defined as the region where the emission is higher than 75 % of the peak emission for carbon (Bernard-Salas et al., 2012). We cannot totally exclude the effect of IR pumping on the excitation of CO, but the effect is likely to be minor as the excitation can be explained by the UV radiation.

8.4 RADEX ANALYSIS

To assess the physical conditions in the Orion Bar, we analyze the integrated intensities of ^{12}CO and ^{13}CO observations with RADEX[3], a non-LTE local radiative transfer code (van der Tak et al., 2007). Fitting RADEX models to observations, we can find solutions for the gas density, kinetic temperature, line optical depth, column density, and abundance of the species[4].

We consider a grid of models and derive the gas temperature (T_g), CO column density (N_{CO}), filling factor (η), thermal pressure (P), and length (l) along the line-of-sight. We consider gas densities of 10^4–10^7 cm^{-3}, kinetic temperatures of 10 K–1000 K, and CO column densities of 10^{15}–5×10^{19} cm^{-2}. We use the cosmic microwave background radiation temperature of 2.73 K and assume a standard carbon isotopic ratio ^{12}C/^{13}C of 70 (Wilson, 1999).

8.4.1 *Fit by a thin slab of gas at high thermal pressure inclined along the line-of-sight*

In Fig. 8.8 we plot the results of the RADEX model at the position where the high-J CO is at maximum, using all the observed transitions for ^{12}CO and ^{13}CO. We plot the integrated line intensities against the upper energy levels of the transitions. The observations are plotted in black and the fits for different hydrogen densities, n_H: 10^5, 10^6, and 10^7 cm^{-3}, are plotted in colored lines, red, green, and blue, respectively. Both ^{12}CO and ^{13}CO were fitted simultaneously. Because the ^{12}CO line is optically thick in most of the observed transitions the ^{13}CO helps finding the more accurate solution. We cannot properly fit the n_H=10^4 cm^{-3} with RADEX as we would need a high column density and temperature and for this RADEX did not give real

3 http://www.sron.rug.nl/vdtak/radex/index.shtml
4 For more information on RADEX, see Chapter 3.6

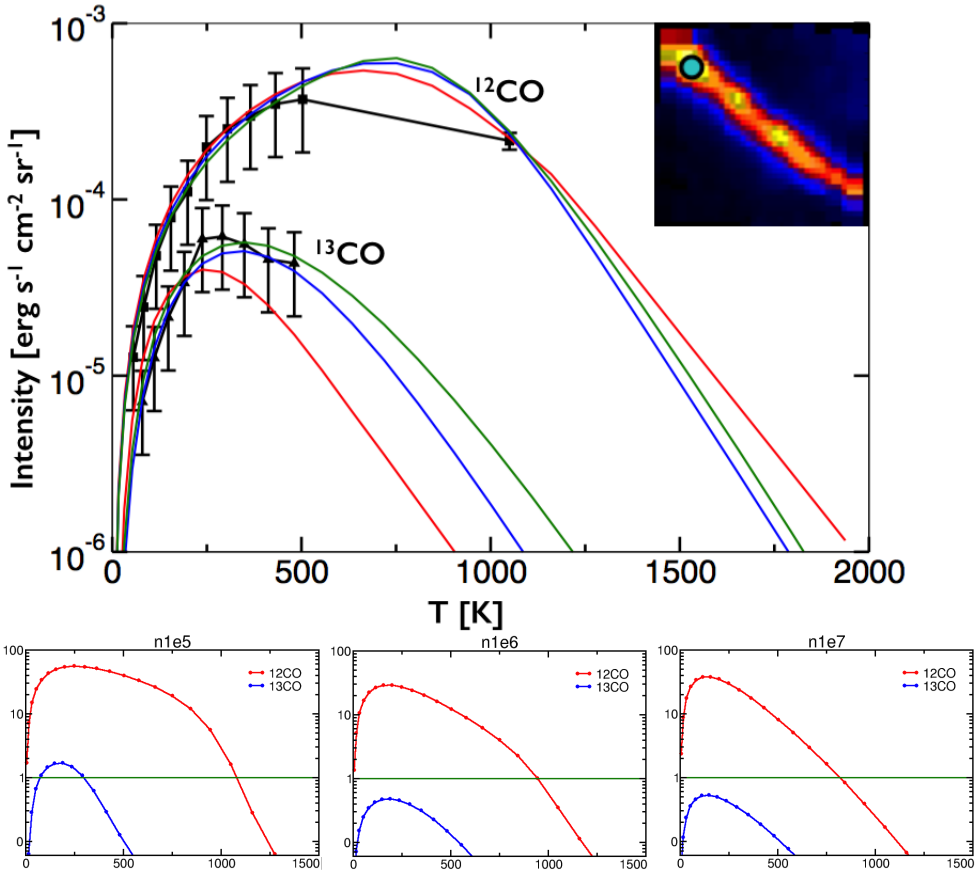

Figure 8.8: Top: The integrated line intensities of ^{12}CO observations from J=5-4 to J=13-12 and J=19-18 (black squares) and ^{13}CO observations from J=5-4 to J=13-12 (black triangles) are plotted against the upper energy levels of the transitions. The colored lines are the different RADEX fits for different hydrogen densities (n_H): 10^5 (red), 10^6 (blue), and 10^7 (green). The results of the fits are shown in Table 8.3. Bottom: Optical depth plotted against the upper level energy temperature for the best fits for each hydrogen density show in the top figure.

results, since the convergence for very high column densities causes issues in the fit. The results for the fits with different gas densities in this position are shown in Table 8.3.

The Orion Bar is inclined by a few degrees from the line-of-sight ($\theta \sim 6-7^\circ$ Hogerheijde et al., 1995; Pellegrini et al., 2009). The emission length or physical thickness of warm CO along the line-of-sight is given by $l = e/\sin(\theta) = 10 \times e$, e being the physical thickness of the warm CO emission. This length should be small, since it traces the surface of the irradiated dense structures. Assuming $e \sim 0.002$ pc, or $1''$ as predicted by PDR models (Allers et al., 2005; Joblin et al., in prep.), we find that the length, l, along the line-of-sight should be of the order of ~ 0.02 pc or $10''$ (see Fig. 8.9).

Comparing l to the one derived from the N_{CO}/n_H ratio from RADEX models (see Table 8.3), we estimate the gas density to be $n \sim 10^6$ cm^{-3}. For a density of 10^5 cm^{-3} the l is too long, since n is small and it does not match the geometrical view of the Orion Bar. Also we can exclude the gas

Table 8.3: Results for RADEX modeling for the selected position in the Bar. The fits are shown in Fig. 8.8.

n_H [cm^{-3}]	N_{CO} [10^{18} cm^{-2}]	T_g [K]	η	P [K cm^{-3}]	l [pc]	l [']
10^5	10	230	0.3	2.3×10^7	0.58	230
10^6	4	160	0.4	1.6×10^8	0.026	13
10^7	4	120	0.5	1.2×10^9	0.003	1.3

density of 10^4 cm^{-3}, which we could not fit, but would yield even longer distance than 10^5 cm^{-3}. For a density of 10^7 cm^{-3}, l is too small, since n is high. The density is about ten times lower than the density derived from density tracers such as CS that trace colder dense gas (Lee et al., 2013). For n ~10^6 cm^{-3}, the kinetic temperature is estimated to be ~150–200 K. The derived thermal pressure is high, $1-2\times10^8$ K cm^{-3}, and similar to the one obtained using the PDR code (3×10^8 K cm^{-3}, Joblin et al. in prep.). The high-J CO intensity is very sensitive to the pressure.

Considering that the Bar is a slab of 0.3 pc long inclined at 7° on the line of sight, we can account for the observed width of the warm CO emission (E~ L × sin(θ), equalling to 15–20″ or 0.03–0.04 pc). The warm CO column density of $N_H \simeq 4\times10^{18}\times2\frac{H_2}{CO} \simeq 8\times10^{22}$ cm^{-2} represents about 40 % of the total column along the line of sight (~2×10^{23} cm^{-2}, Johnstone et al., 2003). A filling factor, η, was used to fit the observations with RADEX (See results in Table 8.3). We find that the warm CO emission covers on average 50 % of the Herschel SPIRE beams (~25″). The high thermal pressure and small length along the line-of-sight confirm the presence of small irradiated dense structures in the Bar.

8.4.2 *Temperature and column density variations across the Bar*

In this section we examine the temperature and CO column density in the entire region for different gas densities. We obtain the temperature from the CO J=19-18/ CO J=12-11 ratio and a reference CO column density, and the CO column density from the CO J=8-7/^{13}CO J=8-7 and the found temperature. The ratio maps are shown in Fig. 8.10

We use the CO J=19-18/CO J=12-11 and CO J=8-7/^{13}CO J=8-7 ratios to derive the temperature and column density in the whole region pixel by pixel. First, we use a reference position fitted for all the transitions, shown in Fig. 8.8. From that position, we go pixel by pixel and find the best match for the two ratios. To do this we use a grid that includes temperatures from 10 K to 1000 K with steps of 10 K and column densities from 10^{15} to $5\times$ 10^{19} cm^{-2}. The steps for column densities are 10^{15} up to 10^{16}, 10^{16} up to 10^{17} and so on. As the temperature and column density should not vary too much from pixel to pixel, we use the previous pixel as a starting position and find the temperature using a limit of ±30 K for temperature

and 2×10^{18} cm^{-2} for the column density. Column density is then found with the same column density limit, but using the found temperature. The maps produced are shown in Fig. 8.11.

All the maps show similar tendencies. The gas temperature is higher in front of the Bar and the gas cools down the further the position is from the ionizing stars. The change is especially clear in the fits with n_H=10^5. Column density is higher in the Bar and lower in the front and behind the Bar. With higher gas densities we obtain lower temperatures and column densities. Maximum temperature is 790 K for n_H=10^5 cm^{-3}, 420 K for n_H=10^6 cm^{-3}, and 360 K for n_H=10^7 cm^{-3}. The maximum column densities were 10^{19} cm^{-2}, 5×10^{18} cm^{-2}, and 5×10^{18} cm^{-2}, respectively. Nevertheless, RADEX uses uniform density and pressure, and it is clear that neither the pressure or density are uniform in the region.

Arab et al. (2012) find that to fit the observed dust emission stratification, an increase of density is needed, in agreement of our column density maps. Using the DustEM model they found a temperature of 50 K, gas density of 1.5×10^5 cm^{-3}, and length of 0.45 pc in the Bar. We find a higher gas density (10^6 cm^{-3}) to fit the high-J CO. Our results do not necessarily contradict the results of Arab et al. (2012). The difference might be due to the bulk of the dust originating in a lower density medium. Cores and their fragments are typically higher density concentrations embedded in a larger filamentary structure at a lower density.

8.5 CONCLUSIONS AND PERSPECTIVES

We present for the first time high spatial resolution images of high excited CO over a large area of $\sim$110″$\times$ 110″ using *Herschel*. We find a clear detection of CO J=19-18 over the whole region. The morphology shows a clumpy structure in the Bar and we establish a link between the dense core of the clumps, traced in CS J=2-1 by Lee et al. (2013) and in H^{13}CN by Lis and Schilke (2003), and the edge of the PDR, traced in CO J=19-18 and vibrationally excited H_2. We have shown that UV heating excites the high-J CO.

We use RADEX models to derive the hydrogen density, ^{12}CO column density, and temperature in the region. We also calculate the length in the line-of-sight and the thermal pressure. The RADEX modeling gives several solutions, the best fits being with a thermal pressure of $\sim2\times10^8$ K cm^{-3}. This supports the conclusion that there are irradiated and dense structures (10^6 cm^{-3}) in the Bar.

We are planning to model the CO observations with the Meudon PDR code (Le Bourlot et al., 2012) to examine how the radiation field and thermal pressure vary. This code is one-dimensional, but solves the thermal balance and statistical equilibrium equations for excitation of selected species at each position in the cloud. In addition, it would be interesting to look at CO excitation in other PDRs with different conditions and different radiation fields, since there is evidence of strong dependence of CO excitation from G_0. We also have CO observations of MM3 young stellar object in

NGC 2023. If we could constrain the CO excitation in this object, it would help in understanding CO excitation in PDR-like structures.

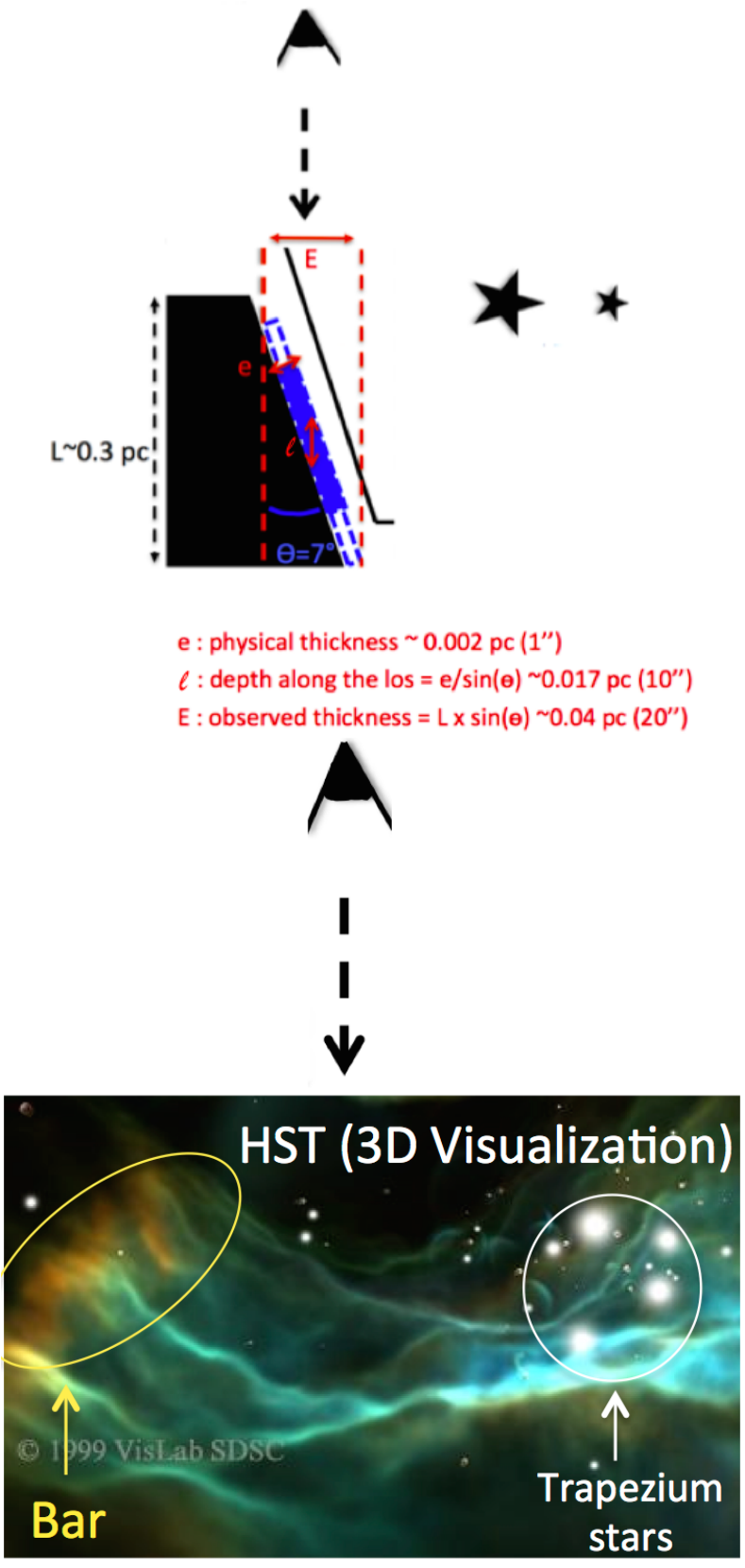

Figure 8.9: Top: Inclination of the Orion Bar, not in scale. Bottom: 3D visualization of the Orion Bar from HST observations (Nadeau et al., 2001). This picture shows the same geometry than the schematic above, there is a concave between the stars and the Bar.

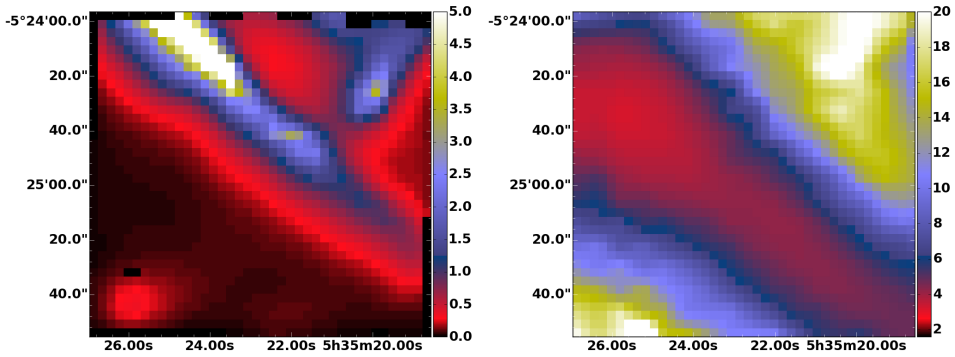

Figure 8.10: Ratio of CO J=19-18 and CO J=12-11 (left) and CO J=8-7 and ^{13}CO J=8-7 (right). The maximum of CO J=19-18/CO J=12-11 is 17 and 59 for CO J=8-7/^{13}CO J=8-7, although we show the scale only up to 5 and 20, respectively, here. These maxima are only few positions in the map and giving a lower scale will show better the changes in the ratios.

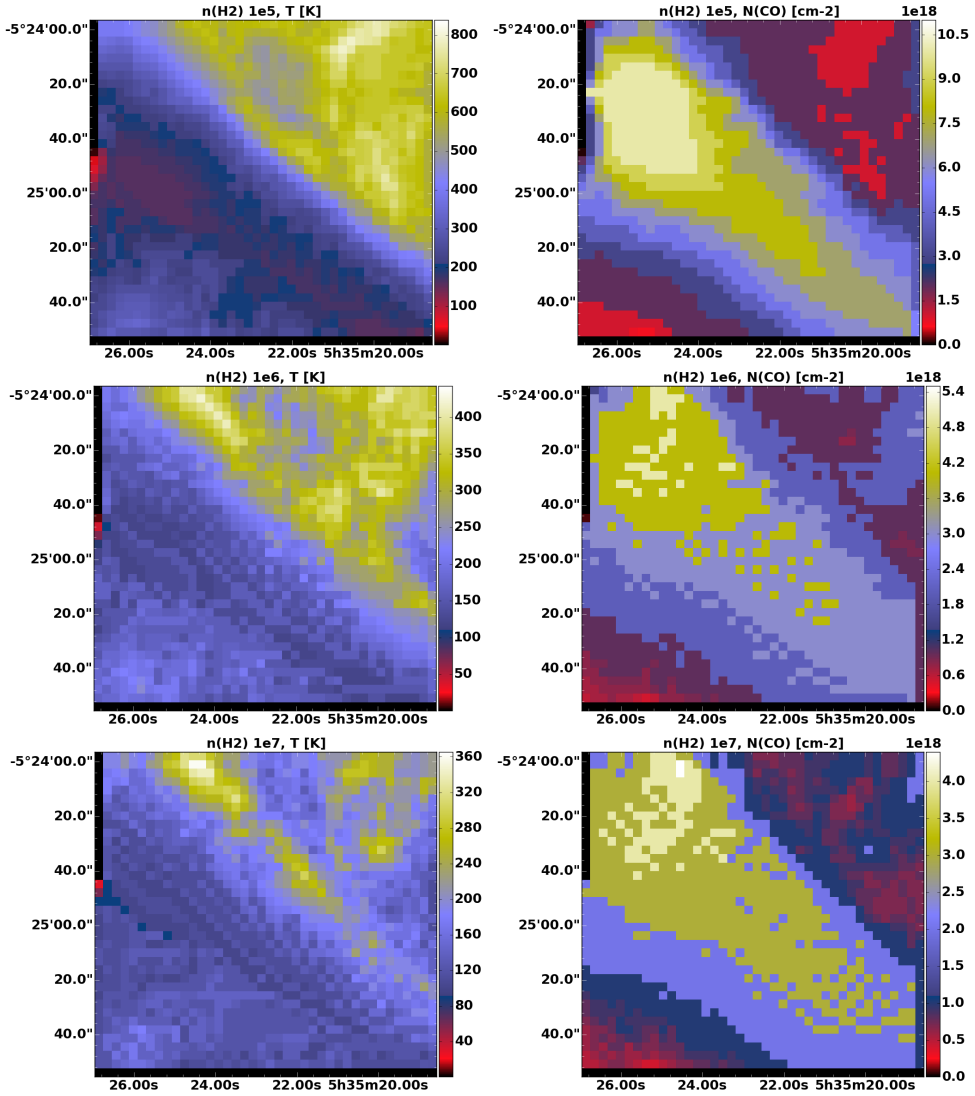

Figure 8.11: Temperature and CO column density maps for hydrogen densities of 10^5 cm^{-3}, 10^6 cm^{-3}, and 10^7 cm^{-3}. The left column shows the temperature maps from the lowest density (top) to the highest (bottom). The right column shows the CO column density, respectively.

Part V

CONCLUSIONS AND PERSPECTIVES

9 CONCLUSIONS AND PERSPECTIVES

In this thesis I have discussed the dense structures and initial conditions of star formation in the ISM. I have discussed both cold and warm dense structures and their physical and chemical properties in relation to star formation. I investigated the physical properties and self-gravitation and the influence of UV radiation on the structure, chemistry and thermal balance of the PDRs, and the nature, properties and evolution of irradiated dense structures inside PDRs. I summarize here the main conclusions of my work and will add suggestions how to extend and describe future lines of research in this area with current and future facilities.

9.1 CONCLUSIONS

COLD CLUMPS. In Chapter 6 we used ground based molecular line observations and *Herschel* dust continuum observations to investigate the physical properties and self-gravitation of 21 cold clumps. These clumps are bright and show low dust color temperatures (T~10−15 K) in the *Herschel* observations. We calculated the masses and compared them to the virial and Bonnor-Ebert masses. The main conclusions are:

- The dust and gas morphologies were comparable, and the hydrogen column densities calculated from the dust continuum and molecular line observations were similar.
- Only five of the 21 clumps had high enough mass to be gravitationally bound and, thus, could be prestellar.
- N_2H^+ is present in three of the five possible prestellar cores, which further suggests their prestellar nature.
- Using modeling to compare dust continuum and line data, we found ^{13}CO abundance close to the canonical value of 10^{-6}. However, the abundance ratio of ^{13}CO and $C^{18}O$ was ~10.

In collaboration with the Helsinki group, a Chinese group[1] have plans to observe other clumps and other density and temperature tracers to further understand the properties of the dense clumps and find evidence of possible shocks and outflows. This will continue the cold cores work, although I am not directly involved in it.

CH^+ AND OH IN THE ORION BAR. In Chapter 7 I examine the morphologies of CH^+ J=3-2 line, and the OH Λ-doublets at 84 μm and 119 μm

1 Wu et al. (2012) and Meng et al. (2013) have conducted similar studies on different set of clumps.

observed with *Herschel*/PACS instrument in the Orion Bar. These unique observations cover a total area of ~110″ × 110″ across the Bar. The main conclusions are:

- The emission of these lines comes mostly from the warm and dense gas at the edge of the PDR.
- The lines trace dense irradiated structures in the Bar.
- The CH^+ forms via vibrationally excited H_2.
- The peak in the OH 84 μm emission corresponds to a bright young object, identified as the proplyd 244-440.

CO IN THE ORION BAR. In Chapter 8 I examine the morphology of high-J CO (J=19-18) line observed with PACS in the Orion Bar. Like with CH^+ and OH, the total area of the observations is ~110″ × 110″ across the Bar. The main conclusions are:

- The high-J CO is sensitive to the UV radiation field.
- The main excitation route of CO is UV heating (most likely photoelectric heating, needs to be confirmed with more detailed modeling).
- The PDR has a high thermal pressure (~2×10^8 K cm^{-3}) and high H_2 density (10^6 cm^{-3}) in the Bar.

9.2 PERSPECTIVES

IMMEDIATE PERSPECTIVES. Following my studies on OH, I will conduct a pilot survey of OH emission in proplyds. In Chapter 7 we could not confirm that the OH 84 μm emission is associated with the proplyd. This is because the OH emission could not be reliably isolated from the rest of the region. In order to confirm the detection and separate the expected different velocities of the proplyd and the surrounding nebula, we will be observing the proplyd 244-440 in the OH 163 μm line with *SOFIA*/GREAT in cycle 3. This line was chosen, since the 84 μm is not currently covered by the GREAT bands. The 163 μm line has similar upper level energy temperature to the 84 μm line, and Goicoechea et al. (2011) found both OH 163 μm doublets to be of similar magnitude as the OH 84 μm. The lines are also both optically thin and have showed similar morphology. We will observe the OH 163 μm doublet also in three other proplyds. The line width resolved observations will be used to constrain the excitation mechanism of the OH line (shocks vs. UV radiation) in the proplyds.

In Chapter 8 we used RADEX to model the CO and ^{13}CO emission. RADEX is very useful for obtaining physical parameters for the gas, but it assumes uniform density and temperature layer. Thus, we will need to use a full radiative transfer code to examine how the radiation field and thermal pressure vary across the region. I plan to use the PDR Meudon code (Le Bourlot et al., 2012) to solve the radiative transfer in each point of

the cloud taking into account the absorption in the continuum by dust and in discrete transitions of H and H_2. In addition to the PDR modeling we plan to look at CO excitation in other PDRs with different conditions and different radiation fields, since there is evidence of strong dependence of CO excitation from the UV field.

SOFIA. SOFIA offers a great opportunity to study the dense interstellar structures. As part of my postdoc in Cologne, I will use this facility to observe other PDRs, like the Horsehead PDR, from which there are already [OI] observations at my disposal. When the OH 84 μm line becomes observable with GREAT, we will be able to study the OH 84 μm emission in proplyds complementing our current approved observations for the OH 163 μm line.

FUTURE OPPORTUNITIES. Current and future observatories — such as ALMA, NOEMA, JWST, and SPICA — with their improved sensibilities, spatial resolution, and wavelength coverage, provide a great opportunity to expand the studies of interstellar dense structures and star formation.

ALMA is a millimeter/submillimeter array, that has a high angular (0.7″ at 675 GHz to 4.8″ at 110 GHz in the most compact configuration) and velocity resolution (highest resolution at 110 GHz is 0.01 km s^{-1}). With ALMA we can observe the interstellar medium, PDRs and proplyds, in more lines and with better spatial resolution. Also with ALMA it is possible to spatially resolve the physical properties within the clumps, like the size and density of the clumps. Furthermore, with improved spectral resolution we can obtain information on gas dynamics. NOEMA, in addition to ALMA, will provide a similar resolution (0.5″ at 230 GHz) in the Northern Hemisphere.

JWST is scheduled for launch in late 2018 and will offer unprecedented resolution and sensitivity, compared to Spitzer. In particular, MIRI instrument will provide spectroscopy from 5—28 μm, enabling the study of PAH emission at extremely high spatial resolution (See Fig. 9.1). JWST can trace the earliest stages of stellar evolution, penetrating the dense cold cloud cores where stars are born. With JWST we can observe, e.g., features of H_2O (energies up to ~1400 K), CO (energies up to ~12000 K), and OH (energies up to ~580 K) in high excited states. With this level of sensitivity the conditions in protoplanetary disks as well as exoplanets can also be studied in greater detail.

SPICA is a proposed (M5) far-infrared observatory with high spatial resolution. It is similar to *Herschel* but it is cooled down, thus, it will achieve higher sensitivity (See Fig. 9.2). SAFARI (SpicA FAR-infrared Instrument) is a FIR imaging spectrometer (30—210 μm). While this instrument is still in configuration it will allow to expand Herschel studies to fainter regions of the ISM. With SAFARI we can detect many molecules (e.g., CH^+ and OH) in extragalactic environments and my current work will help in interpreting these tracers in the new environment.

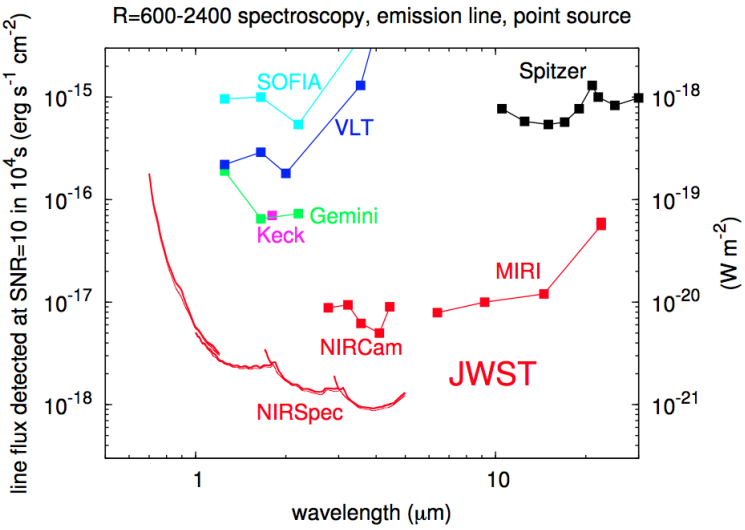

Figure 9.1: Sensitivity of JWST spectroscopic instruments compared to other platforms[2]. The faintest line flux that can be detected at SNR=10 in a point source in a 10^4 s integration is plotted.

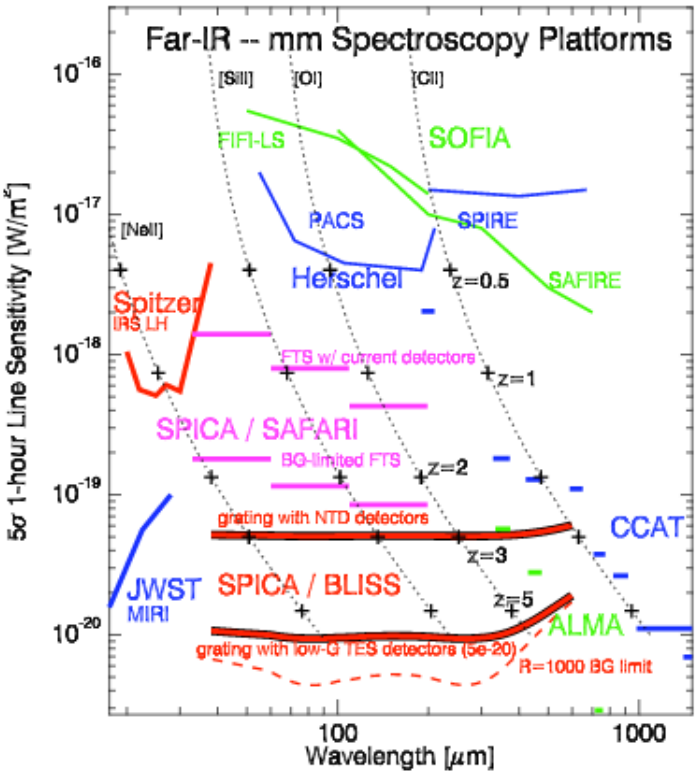

Figure 9.2: Sensitivity of far-IR spectroscopy platforms, particularly SPICA instruments (Bradford et al., 2008).

This is a very exciting time to be studying the ISM. The new facilities will improve our understanding of the dense structures and the details of star formation processes in ISM.

2 From http://www.stsci.edu/jwst/science/sensitivity

Part VI

APPENDIX

A

HERSCHEL KEY PROGRAMS

Herschel guaranteed time key programs on ISM / star formation:

- Evolution of interstellar dust, PI: Alain Abergel
- PRISMAS: PRobing InterStellar Molecules with Absorption line Studies, PI: Maryvonne Gerin
- The warm and dense ISM, PI: Volker Ossenkopf
- Probing the origin of the stellar initial mass function: A wide-field Herschel photometric survey of nearby star-forming cloud complexes, PI: Philippe André
- The earliest phases of star formation: From low- to high-mass objects, PI: Oliver Krause
- HIFI Spectral Surveys of Star Forming Regions, PI: Cecilia Ceccarelli
- Stellar Disk Evolution, PI: Göran Olofsson
- HOBYS: the Herschel imaging survey of OB Young Stellar objects, PI: Frédérique Motte
- HEXOS: Herschel Observations of EXtra-Ordinary Sources: The Orion and Sgr B2 Star-Forming Regions, PI: Edwin Bergin
- WISH: Water in Star Forming Regions with Herschel, PI: Ewine van Dishoeck

Herschel open time key programs on ISM / star formation:

- Gas in Protoplanetary Systems (GASPS), PI: Bill Dent
- DEBRIS: Disc Emission via a Bias-free Reconnaissance in the Infrared/Submillimetre, PI: Brenda Matthews
- Cold Disks around Nearby Stars. A Search for Edgeworth-Kuiper Belt analogues (DUNES: DUst disks around NEarby Stars), PI: Carlos Eiroa
- HIGGS: The Herschel Inner Galaxy Gas Survey, PI: Christopher Martin
- Galactic Cold Cores: A Herschel survey of the source populations revealed by Planck, PI: Mika Juvela
- Dust, Ice, and Gas In Time (DIGIT), PI: Neal Evans
- Herschel Oxygen Project, PI: Paul Goldsmith

- Hi-GAL: the Herschel infrared Galactic Plane Survey, PI: Sergio Molinari
- The Herschel Orion Protostar Survey (HOPS), PI: Tom Megeath
- State of the Diffuse ISM: Galactic Observations of the Terahertz CII Line (GOT CPlus), PI: William Langer

B

ORION BAR MAPS IN ^{12}CO, ^{13}CO, AND C^{18}O

In Fig. B.1 are presented the ^{12}CO maps transitions from J=4-3 to J=13-12. Maps of ^{13}CO transitions from J=5-4 to J=13-12 are shown in Fig. B.2 and C^{18}O transitions from J=5-4 to J=13-12 are shown in Fig. B.3. All maps are projected to the area of ^{12}CO J=19-18 map and the beam size from Supreme reduction is shown in the bottom left corner.

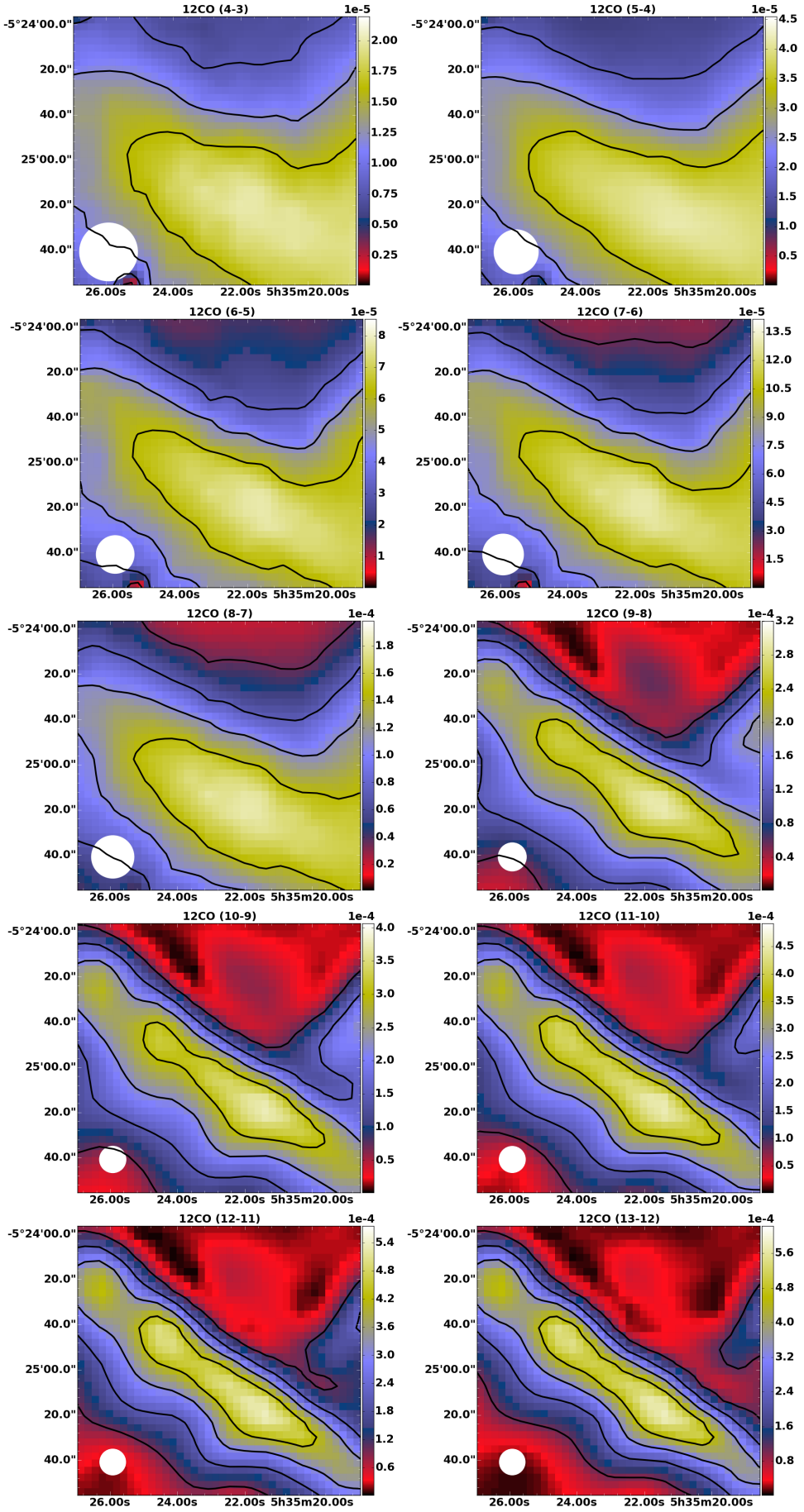

Figure B.1: ^{12}CO SPIRE maps. The beam size is indicated in the bottom left corner.

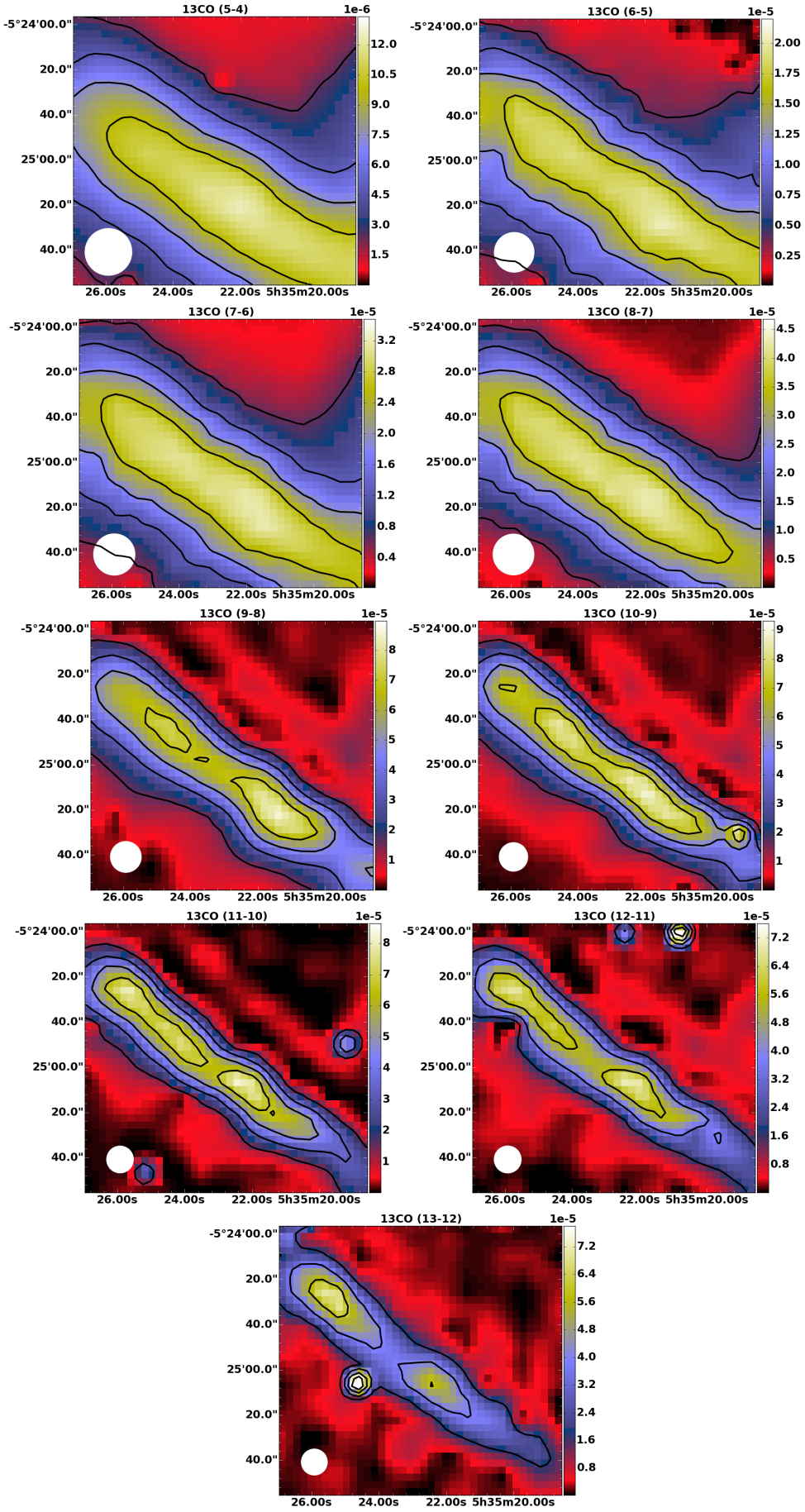

Figure B.2: ^{13}CO SPIRE maps. The beam size is indicated in the bottom left corner.

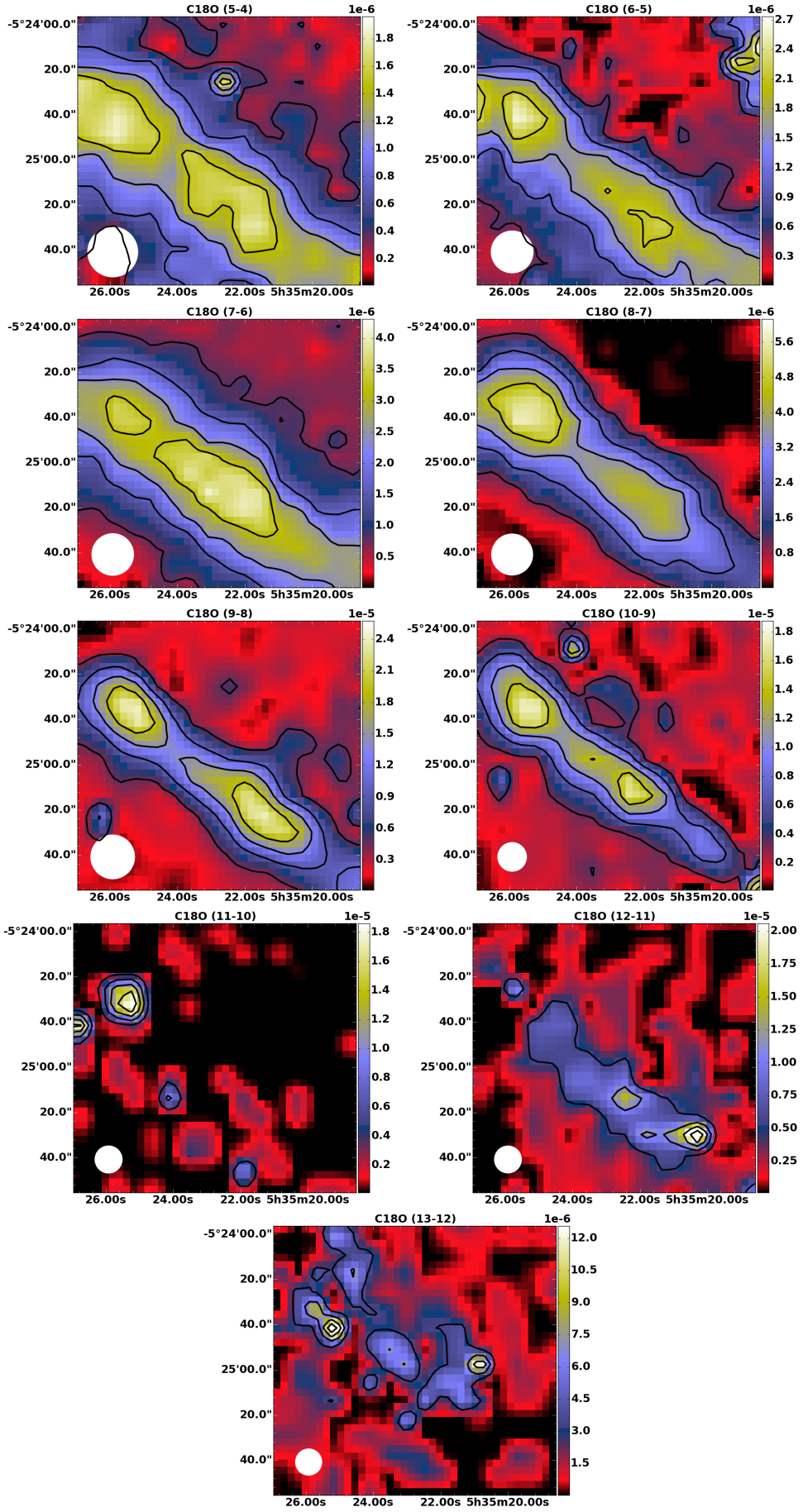

Figure B.3: C^{18}O SPIRE maps. The beam size is indicated in the bottom left corner.

BIBLIOGRAPHY

Agúndez, M., Goicoechea, J. R., Cernicharo, J., Faure, A., and Roueff, E. (2010). The Chemistry of Vibrationally Excited H2 in the Interstellar Medium. *ApJ*, 713(1):662–670.

Allers, K. N., Jaffe, D. T., Lacy, J. H., Draine, B. T., and Richter, M. J. (2005). H2 Pure Rotational Lines in the Orion Bar. *ApJ*, 630(1):368–380.

ALMA Partnership, Brogan, C. L., Pérez, L. M., et al. (2015). The 2014 ALMA Long Baseline Campaign: First Results from High Angular Resolution Observations toward the HL Tau Region. *ApJ*, 808(1):L3.

Alonso-Albi, T., Fuente, A., Crimier, N., et al. (2010). Chemical study of intermediate-mass (IM) Class 0 protostars. *A&A*, 518:A52.

Alves, F. O., Frau, P., Girart, J. M., et al. (2014). On the radiation driven alignment of dust grains: Detection of the polarization hole in a starless core. *A&A*, 569:L1.

Alves, J. F., Lada, C. J., and Lada, E. A. (2001). Internal structure of a cold dark molecular cloud inferred from the extinction of background starlight. *Nature*, 409(6817):159–161.

André, P., Basu, S., and Inutsuka, S. (2009). The formation and evolution of prestellar cores. *Struct. Form. Astrophys.*

André, P., Di Francesco, J., Ward-Thompson, D., et al. (2013). From Filamentary Networks to Dense Cores in Molecular Clouds: Toward a New Paradigm for Star Formation. *eprint arXiv:1312.6232*.

André, P., Men'shchikov, A., Bontemps, S., et al. (2010). From filamentary clouds to prestellar cores to the stellar IMF: Initial highlights from the Herschel Gould Belt Survey. *A&A*, 518:L102.

André, P., Ward-Thompson, D., and Barsony, M. (2000). From Prestellar Cores to Protostars: the Initial Conditions of Star Formation. *Protostars Planets IV (b. - Tucson Univ. Arizona Press. eds Mannings*.

Andrillat, Y. and Duchesne, M. (1974). Morphology of the central region of the Orion nebula in the near infrared. *A&A*, 35:467–472.

Arab, H., Abergel, A., Habart, E., et al. (2012). Evolution of dust in the Orion Bar with Herschel. *A&A*, 541:A19.

Arzoumanian, D., André, P., Peretto, N., and Könyves, V. (2013). Formation and evolution of interstellar filaments. *A&A*, 553:A119.

Asanok, K., Etoka, S., Gray, M. D., et al. (2010). OH and H2O masers towards the star-forming region S140-IRS1. *MNRAS*, 404(1):120–133.

Bacmann, A., Lefloch, B., Ceccarelli, C., et al. (2002). The degree of CO depletion in pre-stellar cores. *A&A*, 389(1):L6–L10.

Bally, J., O'Dell, C. R., and McCaughrean, M. J. (2000). Disks, Microjets, Windblown Bubbles, and Outflows in the Orion Nebula. *AJ*, 119(6):2919–2959.

Bally, J., Sutherland, R. S., Devine, D., and Johnstone, D. (1998). Externally Illuminated Young Stellar Environments in the Orion Nebula: Hubble Space Telescope Planetary Camera and Ultraviolet Observations. *AJ*, 116(1):293–321.

Bate, M. R. and Bonnell, I. A. (2005). The origin of the initial mass function and its dependence on the mean Jeans mass in molecular clouds. *MNRAS*, 356(4):1201–1221.

Bates, D. R. and Spitzer, Lyman, J. (1951). The Density of Molecules in Interstellar Space. *ApJ*, 113:441.

Belloche, A., Garrod, R. T., Müller, H. S. P., and Menten, K. M. (2014). Detection of a branched alkyl molecule in the interstellar medium: iso-propyl cyanide. *Science*, 345(6204):1584–7.

Benson, P. J. and Myers, P. C. (1989). A survey for dense cores in dark clouds. *ApJS*, 71:89.

Bergin, E. A., Alves, J., Huard, T., and Lada, C. J. (2002). N2H+ and C18O Depletion in a Cold Dark Cloud. *ApJ*, 570(2):L101–L104.

Bergin, E. A. and Langer, W. D. (1997). Chemical Evolution in Preprotostellar and Protostellar Cores. *ApJ*, 486(1):316–328.

Bergin, E. A. and Tafalla, M. (2007). Cold Dark Clouds: The Initial Conditions for Star Formation. *ARA&A*, 45(1):339–396.

Bernard-Salas, J., Habart, E., Arab, H., et al. (2012). Spatial variation of the cooling lines in the Orion Bar from Herschel /PACS. *A&A*, 538:A37.

Blake, G. A., Sutton, E. C., Masson, C. R., and Phillips, T. G. (1987). Molecular abundances in OMC-1 - The chemical composition of interstellar molecular clouds and the influence of massive star formation. *ApJ*, 315:621.

Bolatto, A. D., Leroy, A. K., Rosolowsky, E., Walter, F., and Blitz, L. (2008). The Resolved Properties of Extragalactic Giant Molecular Clouds. *ApJ*, 686(2):948–965.

Bradford, C. M., Kenyon, M., Holmes, W., Bock, J., and Koch, T. (2008). Sensitive far-IR survey spectroscopy: BLISS for SPICA. In Duncan, W. D., Holland, W. S., Withington, S., and Zmuidzinas, J., editors, *SPIE Astron. Telesc. + Instrum.*, pages 70201O–70201O–12. International Society for Optics and Photonics.

Bruderer, S., Benz, A. O., van Dishoeck, E. F., et al. (2010). Herschel /HIFI detections of hydrides towards AFGL 2591. *A&A*, 521:L44.

Burton, M. G., Hollenbach, D. J., and Tielens, A. G. G. M. (1990). Line emission from clumpy photodissociation regions. *ApJ*, 365:620.

Burton, W. B. and Gordon, M. A. (1978). Carbon monoxide in the Galaxy. III - The overall nature of its distribution in the equatorial plane. *A&A*, 63:7–27.

Burton, W. B., Gordon, M. A., Bania, T. M., and Lockman, F. J. (1975). The overall distribution of carbon monoxide in the plane of the Galaxy. *ApJ*, 202:30.

Cambrésy, L. (1999). Mapping of the extinction in giant molecular clouds using optical star counts. *A&A*.

Casoli, F., Combes, F., Dupraz, C., Gerin, M., and Boulanger, F. (1986). (C-13)O and (C-12)O observations of cold IRAS unidentified point sources in the Galaxy. *A&A*, 169:281–297.

Ceccarelli, C., Caux, E., White, G. J., et al. (1998). The far infrared line spectrum of the protostar IRAS 16293-2422. *A&A*.

Cernicharo, J., Liu, X.-W., González-Alfonso, E., et al. (1997). Discovery of Far-Infrared Pure Rotational Transitions of CH+ in NGC 7027. *ApJ*, 483(1):L65–L68.

Chen, C.-Y. and Ostriker, E. C. (2014). Formation of Magnetized Prestellar Cores with Ambipolar Diffusion and Turbulence. *ApJ*, 785(1):69.

Chen, H., Bally, J., O'Dell, C. R., et al. (1998). 2.12 Micron Molecular Hydrogen Emission from Circumstellar Disks Embedded in the Orion Nebula. *ApJ*, 492(2):L173–L176.

Clemens, D. P. and Barvainis, R. (1988). A catalog of small, optically selected molecular clouds - Optical, infrared, and millimeter properties. *ApJS*, 68:257.

Combes, F. (1991). Distribution of Co in the Milky Way. *ARA&A*, 29(1):195–237.

Courtès, G. and Viton, M. (1965). Un filtre à bandes passantes multiples, réglables et simultanées destiné à l'analyse spectrophotométrique des images télescopiques. *Ann. d'Astrophysique*, 28.

Cox, D. P. (2005). The Three-Phase Interstellar Medium Revisited. *ARA&A*, 43(1):337–385.

Crutcher, R. M., Wandelt, B., Heiles, C., Falgarone, E., and Troland, T. H. (2010). Magnetic Fields in Interstellar Clouds from Zeeman Observations: Inference of Total Field Strengths by Bayesian Analysis. *ApJ*, 725(1):466–479.

Csengeri, T., Menten, K. M., Wyrowski, F., et al. (2012). SOFIA observations of far-infrared hydroxyl emission toward classical ultracompact HII/OH maser regions. *A&A*, 542:L8.

Dalgarno, A. (2008). A Serendipitous Journey. *ARA&A*, 46(1):1–20.

Dame, T. M. and Thaddeus, P. (1985). A wide-latitude CO survey of molecular clouds in the northern Milky Way. *ApJ*, 297:751.

Dame, T. M., Ungerechts, H., Cohen, R. S., et al. (1987). A composite CO survey of the entire Milky Way. *ApJ*, 322:706.

Daniel, F., Cernicharo, J., and Dubernet, M. (2006). The Excitation of N2H+ in Interstellar Molecular Clouds. I. Models. *ApJ*, 648(1):461–471.

Davidson, J. A., Li, Z.-Y., Hull, C. L. H., et al. (2014). Testing Magnetic Field Models for the Class 0 Protostar L1527. *ApJ*, 797(2):74.

Dawson, J. R., Walsh, A. J., Jones, P. A., et al. (2014). SPLASH: the Southern Parkes Large-Area Survey in Hydroxyl - first science from the pilot region. *MNRAS*, 439(2):1596–1614.

de Graauw, T., Helmich, F. P., Phillips, T. G., et al. (2010). The Herschel -Heterodyne Instrument for the Far-Infrared (HIFI). *A&A*, 518:L6.

de Jong, T., Dalgarno, A., and Chu, S.-I. (1975). Carbon monoxide in collapsing interstellar clouds. *ApJ*, 199:69.

de Vries, C. P. and van Dishoeck, E. F. (1988). Detection of CH and CH+ in a high latitude molecular cloud. *A&A*, 203.

di Francesco, J., Evans, N. J., I., Caselli, P., et al. (2007). An Observational Perspective of Low-Mass Dense Cores I: Internal Physical and Chemical Properties. *Protostars Planets V*.

Dobashi, K., Uehara, H., Kandori, R., et al. (2005). Atlas and Catalog of Dark Clouds Based on Digitized Sky Survey I. *PASJ*.

Douglas, A. E. and Herzberg, G. (1941). Note on CH+ in Interstellar Space and in the Laboratory. *ApJ*, 94:381.

Douglas, A. E. and Morton, J. R. (1960). An Extension of the 1Π-1Σ System of CH+ an the Identification of the λ 3579 Interstellar Line. *ApJ*, 131:1.

Draine, B. T. (1978). Photoelectric heating of interstellar gas. *ApJS*, 36:595.

Dunham, T., J. (1937). Interstellar Neutral Potassium and Neutral Calcium. *PASP*, 49:26.

Elitzur, M. and Watson, W. D. (1978). Formation of molecular CH+ in interstellar shocks. *ApJ*, 222:L141.

Evans, N. J. (1999). Physical Conditions in Regions of Star Formation. *ARA&A*, 37(1):48.

Falgarone, E., Godard, B., Cernicharo, J., et al. (2010a). CH+ (1-0) and 13CH+ (1-0) absorption lines in the direction of massive star-forming regions. *A&A*, 521:L15.

Falgarone, E., Ossenkopf, V., Gerin, M., et al. (2010b). Strong CH+ J = 1-0 emission and absorption in DR21. *A&A*, 518:L118.

Fedele, D., Bruderer, S., van Dishoeck, E. F., et al. (2012). Warm H2O and OH in the disk around the Herbig star HD 163296. *A&A*, 544:L9.

Fedele, D., Pascucci, I., Brittain, S., et al. (2011). Water Depletion in the Disk Atmosphere of Herbig AeBe Stars. *ApJ*, 732(2):106.

Ferrière, K. M. (2001). The interstellar environment of our galaxy. *Rev. Mod. Phys.*, 73(4):1031–1066.

Field, G. B., Goldsmith, D. W., and Habing, H. J. (1969). Cosmic-Ray Heating of the Interstellar Gas. *ApJ*, 155:L149.

Flower, D. R., Pineau des Forêts, G., and Walmsley, C. M. (2005). Freeze-out and coagulation in pre-protostellar collapse. *A&A*, 436(3):933–943.

Furukawa, N., Ohama, A., Fukuda, T., et al. (2014). The Jet and Arc Molecular Clouds toward Westerlund 2, RCW 49, and HESS J1023-575 12CO and 13CO (J = 2-1 and J = 1-0) observations with NANTEN2 and Mopra Telescope. *ApJ*, 781(2):70.

Galli, D., Walmsley, M., and Gonçalves, J. (2002). The structure and stability of molecular cloud cores in external radiation fields. *A&A*, 394(1):275–284.

Geers, V. C., van Dishoeck, E. F., Visser, R., et al. (2007). Spatially extended polycyclic aromatic hydrocarbons in circumstellar disks around T Tauri and Herbig Ae stars. *A&A*, 476(1):279–289.

Godard, B. and Cernicharo, J. (2013). A complete model of CH+ rotational excitation including radiative and chemical pumping processes. *A&A*, 550:A8.

Godard, B., Falgarone, E., Gerin, M., et al. (2012). Comparative study of CH + and SH + absorption lines observed towards distant star-forming regions. *A&A*, 540:A87.

Godard, B., Falgarone, E., and Pineau des Forêts, G. (2009). Models of turbulent dissipation regions in the diffuse interstellar medium. *A&A*, 495(3):847–867.

Goicoechea, J. R., Cernicharo, J., Lerate, M. R., et al. (2006). Far-Infrared Excited Hydroxyl Lines from Orion KL Outflows. *ApJ*, 641(1):L49–L52.

Goicoechea, J. R., Joblin, C., Contursi, A., et al. (2011). OH emission from warm and dense gas in the Orion Bar PDR. *A&A*, 530:L16.

Goldreich, P. and Scoville, N. (1976). OH-IR stars. I - Physical properties of circumstellar envelopes. *ApJ*, 205:144.

Goldsmith, P. F. and Langer, W. D. (1978). Molecular cooling and thermal balance of dense interstellar clouds. *ApJ*, 222:881.

Goldsmith, P. F. and Langer, W. D. (1999). Population Diagram Analysis of Molecular Line Emission. *ApJ*, 517(1):209–225.

Gorenstein, P. (1975). Empirical relation between interstellar X-ray absorption and optical extinction. *ApJ*, 198:95.

Green, S., Montgomery, J. A., J., and Thaddeus, P. (1974). Tentative identification of U93.174 as the molecular ion N2H+. *ApJ*, 193:L89.

Griffin, M. J., Abergel, A., Abreu, A., et al. (2010). The Herschel -SPIRE instrument and its in-flight performance. *A&A*, 518:L3.

Güver, T. and Özel, F. (2009). The relation between optical extinction and hydrogen column density in the Galaxy. *MNRAS*, 400(4):2050–2053.

Habart, E., Dartois, E., Abergel, A., et al. (2010). SPIRE spectroscopy of the prototypical Orion Bar photodissociation region. *A&A*, 518:L116.

Hacar, A. and Tafalla, M. (2011). Dense core formation by fragmentation of velocity-coherent filaments in L1517. *A&A*, 533:A34.

Hacar, A., Tafalla, M., Kauffmann, J., and Kovács, A. (2013). Cores, filaments, and bundles: hierarchical core formation in the L1495/B213 Taurus region. *A&A*, 554:A55.

Hartmann, L. (2002). Flows, Fragmentation, and Star Formation. I. Low-Mass Stars in Taurus. *ApJ*, 578(2):914–924.

Helmich, F. P., Jansen, D. J., de Graauw, T., Groesbeck, T. D., and van Dishoeck, E. F. (1994). Physical and chemical variations within the W3 star-forming region. 1: SO2, CH3OH, and H2CO. *A&A*, 283:626–634.

Henney, W. J. and O'Dell, C. R. (1999). A Keck High-Resolution Spectroscopic Study of the Orion Nebula Proplyds. *AJ*, 118(5):2350–2368.

Herbst, E., Green, S., Thaddeus, P., and Klemperer, W. (1977). Indirect observation of unobservable interstellar molecules. *ApJ*, 215:503.

Heyer, M., Krawczyk, C., Duval, J., and Jackson, J. M. (2009). Re-Examining Larson's Scaling Relationships in Galactic Molecular Clouds. *ApJ*, 699(2):1092–1103.

Hily-Blant, P. and Falgarone, E. (2007). Dissipative structures of diffuse molecular gas. *A&A*, 469(1):173–187.

Hobbs, L. M. (1973). Interferometric studies of interstellar CH+ molecules. *ApJ*, 181:79.

Hogerheijde, M. R., Jansen, D. J., and van Dishoeck, E. F. (1995). Millimeter and submillimeter observations of the Orion Bar. 1: Physical structure. *A&A*, 294:792–810.

Hollenbach, D. and Tielens, A. (1999). Photodissociation regions in the interstellar medium of galaxies. *Rev. Mod. Phys.*, 71(1):173–230.

Hollenbach, D. J. and Tielens, A. G. G. M. (1997). Dense Photodissociation Regions (PDRs) 1. *ARA&A*, 35(1):179–215.

Hotzel, S., Harju, J., and Walmsley, C. M. (2004). The NH3/N2H+ abundance ratio in dense cores. *A&A*, 415(3):1065–1072.

Indebetouw, R., Mathis, J. S., Babler, B. L., et al. (2005). The Wavelength Dependence of Interstellar Extinction from 1.25 to 8.0 μm Using GLIMPSE Data. *ApJ*, 619(2):931–938.

Jeans, J. H. (1928). Astronomy and cosmogony. *Cambridge [Eng.] Univ. Press*.

Jewell, P. R. (2002). Millimeter Wave Calibration Techniques. *Single-Dish Radio Astron. Tech. Appl.*, 278:313–328.

Jijina, J., Myers, P. C., and Adams, F. C. (1999). Dense Cores Mapped in Ammonia: A Database. *ApJS*, 125(1):161–236.

Johnstone, D., Boonman, A. M. S., and van Dishoeck, E. F. (2003). Astrochemistry of sub-millimeter sources in Orion. Studying the variations of molecular tracers with changing physical conditions. *A&A*, 412(1):157–174.

Jones, M. E., Barlow, S. E., Ellison, G. B., and Ferguson, E. E. (1986). Reactions of C+ He+ and Ne+ with vibrationally excited H2 and D2. *Chem. Phys. Lett.*, 130(3):218–223.

Juvela, M. (2005). Efficient Monte Carlo methods for continuum radiative transfer. *A&A*, 440(2):531–546.

Juvela, M. and Padoan, P. (2003). Dust emission from inhomogeneous interstellar clouds: Radiative transfer in 3D with transiently heated particles. *A&A*, 397(1):201–212.

Juvela, M., Pelkonen, V.-M., Padoan, P., and Mattila, K. (2008). A Corona Australis cloud filament seen in NIR scattered light. *A&A*, 480(2):445–458.

Juvela, M., Ristorcelli, I., Montier, L. A., et al. (2010). Galactic cold cores: Herschel study of first Planck detections. *A&A*, 518:L93.

Juvela, M., Ristorcelli, I., Pagani, L., et al. (2012). Galactic cold cores. III. General cloud properties. *A&A*, 541:A12.

Juvela, M., Ristorcelli, I., Pelkonen, V.-M., et al. (2011). Galactic cold cores. II. Herschel study of the extended dust emission around the first Planck detections. *A&A*, 527:A111.

Kandori, R., Nakajima, Y., Tamura, M., et al. (2005). Near-Infrared Imaging Survey of Bok Globules: Density Structure. *AJ*, 130(5):2166–2184.

Kaufman, M. J., Wolfire, M. G., Hollenbach, D. J., and Luhman, M. L. (1999). Far-Infrared and Submillimeter Emission from Galactic and Extragalactic Photodissociation Regions. *ApJ*, 527(2):795–813.

Keto, E., Broderick, A. E., Lada, C. J., and Narayan, R. (2006). Oscillations of Starless Cores. *ApJ*, 652(2):1366–1373.

Klessen, R. S. and Burkert, A. (2000). The Formation of Stellar Clusters: Gaussian Cloud Conditions. I. *ApJS*, 128(1):287–319.

Köhler, M., Habart, E., Arab, H., et al. (2014). Physical structure of the photodissociation regions in NGC 7023. *A&A*, 569:A109.

Könyves, V., André, P., Men'shchikov, A., et al. (2010). The Aquila prestellar core population revealed by Herschel. *A&A*, 518:L106.

Kritsuk, A. G., Lee, C. T., and Norman, M. L. (2013). A supersonic turbulence origin of Larson's laws. *MNRAS*, 436(4):3247–3261.

Lacy, J. H., Knacke, R., Geballe, T. R., and Tokunaga, A. T. (1994). Detection of absorption by H2 in molecular clouds: A direct measurement of the H2:CO ratio. *ApJ*, 428:L69.

Lada, C. J., Bergin, E. A., Alves, J. F., and Huard, T. L. (2003). The Dynamical State of Barnard 68: A Thermally Supported, Pulsating Dark Cloud. *ApJ*, 586(1):286–295.

Lambert, D. L. and Danks, A. C. (1986). On the CH(+) ion in diffuse interstellar clouds. *ApJ*, 303:401.

Laques, P. and Vidal, J. L. (1979). Detection of a new type of condensations in the center of the Orion Nebula by means of S20 photocathode cells associated with a Lallemand electronic camera. *A&A*, 73:97–106.

Larson, R. B. (1981). Turbulence and star formation in molecular clouds. *MNRAS*, 194:809–826.

Larsson, B., Liseau, R., and Men'shchikov, A. B. (2002). The ISO-LWS map of the Serpens cloud core. *A&A*, 386(3):1055–1073.

Le Bourlot, J., Le Petit, F., Pinto, C., Roueff, E., and Roy, F. (2012). Surface chemistry in the interstellar medium. *A&A*, 541:A76.

Le Petit, F., Nehme, C., Le Bourlot, J., and Roueff, E. (2006). A Model for Atomic and Molecular Interstellar Gas: The Meudon PDR Code. *ApJS*, 164(2):506–529.

Lebouteiller, V., Cormier, D., Madden, S. C., et al. (2012). Physical conditions in the gas phases of the giant H II region LMC-N 11 unveiled by Herschel. *A&A*, 548:A91.

Lee, J., Evans II, N. J., Shirley, Y. L., and Tatematsu, K. (2003). Chemistry and Dynamics in Pre-protostellar Cores. *ApJ*, 583(2):789–808.

Lee, K., Looney, L., Johnstone, D., and Tobin, J. (2012). Filamentary Star Formation: Observing the Evolution toward Flattened Envelopes. *ApJ*, 761(2):171.

Lee, K., Looney, L. W., Schnee, S., and Li, Z.-Y. (2013). Earliest Stages of Protocluster Formation: Substructure and Kinematics of Starless Cores in Orion. *ApJ*, 772(2):100.

Lehtinen, K., Russeil, D., Juvela, M., Mattila, K., and Lemke, D. (2004). ISO far infrared observations of the high latitude cloud L1642. *A&A*, 423(3):975–982.

Leisawitz, D., Bash, F. N., and Thaddeus, P. (1989). A CO survey of regions around 34 open clusters. *ApJS*, 70:731.

Lim, A. J., Rabadán, I., and Tennyson, J. (1999). Electron-impact rotational excitation of CH+. *MNRAS*, 306(2):473–478.

Lindberg, J. E., Jørgensen, J. K., Green, J. D., et al. (2014). Warm gas towards young stellar objects in Corona Australis. *A&A*, 565:A29.

Lippok, N., Launhardt, R., Semenov, D., et al. (2013). Gas-phase CO depletion and N2H+ abundances in starless cores. *A&A*, 560:A41.

Lis, D. C. and Schilke, P. (2003). Dense Molecular Clumps in the Orion Bar Photon-dominated Region. *ApJ*, 597(2):L145–L148.

Liu, T., Wu, Y., Mardones, D., et al. (2014). Follow-up observations toward Planck cold clumps with ground-based radio telescopes. *eprint arXiv:1410.6979*.

Liu, T., Wu, Y., and Zhang, H. (2012). Molecular Environments of 51 Planck Cold Clumps in the Orion Complex. *ApJS*, 202(1):4.

Lombardi, M. and Alves, J. (2001). Mapping the interstellar dust with near-infrared observations: An optimized multi-band technique. *A&A*, 377(3):1023–1034.

Lombardi, M., Alves, J., and Lada, C. J. (2010). Larson's third law and the universality of molecular cloud structure. *A&A*, 519:L7.

MacLaren, I., Richardson, K. M., and Wolfendale, A. W. (1988). Corrections to virial estimates of molecular cloud masses. *ApJ*, 333:821.

Maeda, K., Wall, M. L., and Carr, L. D. (2015). Hyperfine structure of the hydroxyl free radical (OH) in electric and magnetic fields. *New J. Phys.*, 17(4):045014.

Makiwa, G., Naylor, D. A., Ferlet, M., et al. (2013). Beam profile for the Herschel-SPIRE Fourier transform spectrometer. *Appl. Opt.*, 52(16):3864–75.

Marconi, A., Testi, L., Natta, A., and Walmsley, C. M. (1998). Near infrared spectra of the Orion bar. *A&A*, 330:696–710.

Martín, S., Martín-Pintado, J., and Viti, S. (2009). Photodissociation Chemistry Footprints in the Starburst Galaxy NGC 253. *ApJ*, 706(2):1323–1330.

Mathews, G. S., Klaassen, P. D., Juhász, A., et al. (2013). ALMA imaging of the CO snowline of the HD 163296 disk with DCO+. *A&A*, 557:A132.

Mathis, J. S., Mezger, P. G., and Panagia, N. (1983). Interstellar radiation field and dust temperatures in the diffuse interstellar matter and in giant molecular clouds. *A&A*, 128:212–229.

McKee, C. F. and Ostriker, E. C. (2007). Theory of Star Formation. *ARA&A*, 45(1):565–687.

McKee, C. F. and Ostriker, J. P. (1977). A theory of the interstellar medium - Three components regulated by supernova explosions in an inhomogeneous substrate. *ApJ*, 218:148.

Meier, D. S., Turner, J. L., and Hurt, R. L. (2000). Molecular Gas Properties of the Starburst Nucleus of IC 342: High-Resolution 13 CO (2-1) Imaging. *ApJ*, 531(1):200–209.

Melnick, G. J., Genzel, R., and Lugten, J. B. (1987). Interpretation of rotationally excited far-infrared OH emission in Orion-KL. *ApJ*, 321:530.

Meng, F., Wu, Y., and Liu, T. (2013). Mapping Study of 71 Planck Cold Clumps in the Taurus, Perseus, and California Complexes. *ApJS*, 209(2):37.

Men'shchikov, A., André, P., Didelon, P., et al. (2010). Filamentary structures and compact objects in the Aquila and Polaris clouds observed by Herschel. *A&A*, 518:L103.

Menten, K. M., Reid, M. J., Forbrich, J., and Brunthaler, A. (2007). The distance to the Orion Nebula. *A&A*, 474(2):515–520.

Miville-Deschênes, M.-A., Martin, P. G., Abergel, A., et al. (2010). Herschel - SPIRE observations of the Polaris flare: Structure of the diffuse interstellar medium at the sub-parsec scale. *A&A*, 518:L104.

Molinari, S., Swinyard, B., Bally, J., et al. (2010). Hi-GAL: The Herschel Infrared Galactic Plane Survey. *PASP*, 122(889):314–325.

Motte, F., Andre, P., and Neri, R. (1998). The initial conditions of star formation in the rho Ophiuchi main cloud: wide-field millimeter continuum mapping. *A&A*.

Motte, F., Zavagno, A., Bontemps, S., et al. (2010). Initial highlights of the HOBYS key program, the Herschel imaging survey of OB young stellar objects. *A&A*, 518:L77.

Myers, A. T., Klein, R. I., Krumholz, M. R., and McKee, C. F. (2014). Star cluster formation in turbulent, magnetized dense clumps with radiative and outflow feedback. *MNRAS*, 439(4):3420–3438.

Myers, P. C. (1983). Dense cores in dark clouds. III - Subsonic turbulence. *ApJ*, 270:105.

Nadeau, D. R., Genetti, J. D., Napear, S., et al. (2001). Visualizing Stars and Emission Nebulas. *Comput. Graph. Forum*, 20(1):27–33.

Nagy, Z., Van der Tak, F. F. S., Ossenkopf, V., et al. (2013). The chemistry of ions in the Orion Bar I. - CH+, SH+, and CF+. *A&A*, 550:A96.

Naylor, D. A., Dartois, E., Habart, E., et al. (2010). First detection of the methylidyne cation (CH +) fundamental rotational line with the Herschel /SPIRE FTS. *A&A*, 518:L117.

Neufeld, D. A., Kaufman, M. J., Goldsmith, P. F., Hollenbach, D. J., and Plume, R. (2002). Submillimeter Wave Astronomy Satellite and Arecibo Observations of H2O and OH in a Diffuse Cloud along the Line of Sight to W51. *ApJ*, 580(1):278–284.

Neufeld, D. A., Wolfire, M. G., and Schilke, P. (2005). The Chemistry of Fluorine-bearing Molecules in Diffuse and Dense Interstellar Gas Clouds. *ApJ*, 628(1):260–274.

Nishiyama, S., Tamura, M., Hatano, H., et al. (2009). Interstellar Extinction Law Toward the Galactic Center III: J, H, KS Bands in the 2MASS and the MKO Systems, and 3.6, 4.5, 5.8, 8.0 μm in the Spitzer/IRAC System. *ApJ*, 696(2):1407–1417.

Öberg, K. I., Guzmán, V. V., Furuya, K., et al. (2015). The comet-like composition of a protoplanetary disk as revealed by complex cyanides. *Nature*, 520(7546):198–201.

O'Dell, C. R. and Hu, X. (1994). Comparison of HST and VLA images at 0.1" of the Orion nebula. *Very high angular Resolut. imaging; Proc. 158th Int. Astron. Union Symp.*

O'Dell, C. R., Muench, A., Smith, N., and Zapata, L. (2008). Star Formation in the Orion Nebula II: Gas, Dust, Proplyds and Outflows. *Handb. Star Form. Reg.*, 4.

O'Dell, C. R., Wen, Z., and Hu, X. (1993). Discovery of new objects in the Orion nebula on HST images - Shocks, compact sources, and protoplanetary disks. *ApJ*, 410:696.

O'Dell, C. R. and Wong, K. (1996). Hubble Space Telescope Mapping of the Orion Nebula. I. A Survey of Stars and Compact Objects. *AJ*, 111:846.

Okada, Y., Requena-Torres, M. A., Güsten, R., et al. (2015). Velocity resolved [CII], [CI], and CO observations of the N159 star-forming region in the

Large Magellanic Cloud: a complex velocity structure and variation of the column densities. *A&A*, 580:16.

Oliveira, I., Pontoppidan, K. M., Merín, B., et al. (2010). A Spitzer Survey of Protoplanetary Disk Dust in the Young Serpens Cloud: How do Dust Characteristics Evolve with Time? *ApJ*, 714(1):778–798.

O'Neil, K., Hofner, P., and Schinnerer, E. (2000). First Detection of CO in a Low Surface Brightness Galaxy. *ApJ*, 545(2):L99–L102.

Orieux, F., Giovannelli, J.-F., Rodet, T., and Abergel, A. (2013). Estimating hyperparameters and instrument parameters in regularized inversion Illustration for Herschel /SPIRE map making. *A&A*, 549:A83.

Orieux, F., Giovannelli, J.-F., Rodet, T., et al. (2012). Super-resolution in map-making based on a physical instrument model and regularized inversion. *A&A*, 539:A38.

Ossenkopf, V., Koumpia, E., Okada, Y., et al. (2015). Fine-structure line deficit in S 140. *A&A*, 580:A83.

Padoan, P. and Nordlund, A. (2002). The Stellar Initial Mass Function from Turbulent Fragmentation. *ApJ*, 576(2):870–879.

Pagani, L., Bacmann, A., Cabrit, S., and Vastel, C. (2007). Depletion and low gas temperature in the L183 (=L134N) prestellar core: the N2H+ -N2D+ tool. *A&A*, 467(1):179–186.

Palmeirim, P., André, P., Kirk, J., et al. (2013). Herschel view of the Taurus B211/3 filament and striations: evidence of filamentary growth? *A&A*, 550:A38.

Papadopoulos, P. P., Isaak, K., and van der Werf, P. (2010). CO J = 6-5 in Arp 220: Strong Effects of Dust on High-J CO Lines. *ApJ*, 711(2):757–763.

Parikka, A., Juvela, M., Pelkonen, V.-M., Malinen, J., and Harju, J. (2015). The physical state of selected cold clumps. *A&A*, 577:A69.

Parmar, P. S., Lacy, J. H., and Achtermann, J. M. (1991). Detection of low-J pure-rotational emission from H2 in the Orion Bar region - Evidence for small-scale clumpiness. *ApJ*, 372:L25.

Pellegrini, E. W., Baldwin, J. A., Ferland, G. J., Shaw, G., and Heathcote, S. (2009). Orion's Bar: Physical Conditions Across the Definitive H+/H0/H2 Interface. *ApJ*, 693(1):285–302.

Peretto, N., André, P., Könyves, V., et al. (2012). The Pipe Nebula as seen with Herschel : formation of filamentary structures by large-scale compression? *A&A*, 541:A63.

Pérez-Beaupuits, J. P., Wiesemeyer, H., Ossenkopf, V., et al. (2012). The ionized and hot gas in M17 SW. *A&A*, 542:L13.

Pineau des Forets, G., Flower, D. R., Hartquist, T. W., and Dalgarno, A. (1986). Theoretical studies of interstellar molecular shocks. III - The formation of CH(+) in diffuse clouds. *MNRAS*, 220:801–824.

Planck Collaboration VII (2011). Planck early results. VII. The Early Release Compact Source Catalogue. *A&A*, 536:A7.

Planck Collaboration XII (2011). Planck early results. XXII. The submillimetre properties of a sample of Galactic cold clumps. *A&A*, 536:A22.

Planck Collaboration XXIII (2011). Planck early results. XXIII. The first all-sky survey of Galactic cold clumps. *A&A*, 536:A23.

Planck Collaboration XXVIII (2015). Planck 2015 results. XXVIII. The Planck Catalogue of Galactic Cold Clumps. *eprint arXiv:1502.01599*.

Poglitsch, A., Waelkens, C., Geis, N., et al. (2010). The Photodetector Array Camera and Spectrometer (PACS) on the Herschel Space Observatory. *A&A*, 518:L2.

Porras, A. J., Federman, S. R., Welty, D. E., and Ritchey, A. M. (2014). OH+ in Diffuse Molecular Clouds. *ApJ*, 781(1):L8.

Predehl, P. and Schmitt, J. H. M. M. (1995). X-raying the interstellar medium: ROSAT observations of dust scattering halos. *A&A*.

Qian, L., Li, D., and Goldsmith, P. F. (2012). 13CO Cores in the Taurus Molecular Cloud. *ApJ*, 760(2):147.

Reina, C. and Tarenghi, M. (1973). X-ray Absorption and Optical Extinction in Interstellar Space. *A&A*, 26.

Requena-Torres, M. A., Güsten, R., Weiß, A., et al. (2012). GREAT confirms transient nature of the circum-nuclear disk. *A&A*, 542:L21.

Rickard, L. J., Turner, B. E., Palmer, P., Morris, M., and Zuckerman, B. (1977). Extragalactic carbon monoxide. *ApJ*, 213:673.

Roberts, H., Herbst, E., and Millar, T. J. (2003). Enhanced Deuterium Fractionation in Dense Interstellar Cores Resulting from Multiply Deuterated H+3. *ApJ*, 591(1):L41–L44.

Roberts, H. and Millar, T. J. (2000). Modelling of deuterium chemistry and its application to molecular clouds. *A&A*, 361:388–398.

Rodet, T., Orieux, F., Giovannelli, J.-F., and Abergel, A. (2008). Data Inversion for Over-Resolved Spectral Imaging in Astronomy. *IEEE J. Sel. Top. Signal Process.*, 2(5):802–811.

Russell, R. W., Melnick, G., Gull, G. E., and Harwit, M. (1980). Detection of the 157 micron /1910 GHz/ /C II/ emission line from the interstellar gas complexes NGC 2024 and M42. *ApJ*, 240:L99.

Sakai, T., Sakai, N., Foster, J. B., et al. (2013). ALMA Observations of the IRDC Clump G34.43+00.24 MM3: Hot Core and Molecular Outflows. *ApJ*, 775(1):L31.

Sakai, T., Sakai, N., Furuya, K., et al. (2015). ALMA Observations of the IRDC Clump G34.43+00.24 MM3: DNC/HNC Ratio. *ApJ*, 803(2):70.

Sánchez-Monge, Á., Cesaroni, R., Beltrán, M. T., et al. (2013). A candidate circumbinary Keplerian disk in G35.20-0.74 N: A study with ALMA. *A&A*, 552:L10.

Schleicher, D. R. G., Spaans, M., and Klessen, R. S. (2010). Probing high-redshift quasars with ALMA. I. Expected observables and potential number of sources. *A&A*, 513:A7.

Schöier, F. L., van der Tak, F. F. S., van Dishoeck, E. F., and Black, J. H. (2005). An atomic and molecular database for analysis of submillimetre line observations. *A&A*, 432(1):369–379.

Schwartz, P. R., Wilson, W. J., and Epstein, E. E. (1973). The Distribution of Galactic Carbon Monoxide: a Preliminary Survey. *ApJ*, 186:529.

Scoville, N. Z. and Solomon, P. M. (1975). Molecular clouds in the Galaxy. *ApJ*, 199:L105.

Shu, F. H., Adams, F. C., and Lizano, S. (1987). Star Formation in Molecular Clouds: Observation and Theory. *ARA&A*, 25(1):23–81.

Snow, T. P. and McCall, B. J. (2006). Diffuse Atomic and Molecular Clouds. *ARA&A*, 44(1):367–414.

Soam, A., Maheswar, G., Lee, C. W., et al. (2014). Magnetic field structure around cores with very low luminosity objects. *A&A*, 573:A34.

Sobolev, V. V. (1947). *Dvishushchuesia obolochki zvezd*. Izdatel'stvo leningradskogo gosudarstvennogo universiteta ordena Lenina universiteta, Leningrad.

Solomon, P. M., Rivolo, A. R., Barrett, J., and Yahil, A. (1987). Mass, luminosity, and line width relations of Galactic molecular clouds. *ApJ*, 319:730.

Stahler, S. W. and Palla, F. (2004). *The Formation of Stars*. WILEY-VCH Verlag GmbH & Co. KGaA.

Sternberg, A. and Dalgarno, A. (1989). The infrared response of molecular hydrogen gas to ultraviolet radiation - High-density regions. *ApJ*, 338:197.

Sternberg, A. and Dalgarno, A. (1995). Chemistry in Dense Photon-dominated Regions. *ApJS*, 99:565.

Storey, J. W. V., Watson, D. M., and Townes, C. H. (1981). Detection of interstellar OH in the far-infrared. *ApJ*, 244:L27.

Störzer, H., Stutzki, J., and Sternberg, A. (1995). CO+ in the Orion Bar, M17 and S140 star-forming regions. *A&A*.

Sturm, B., Bouwman, J., Henning, T., et al. (2010). First results of the Herschel key program "Dust, Ice and Gas In Time" (DIGIT): Dust and gas spectroscopy of HD 100546. *A&A*, 518:L129.

Tachihara, K., Onishi, T., Mizuno, A., and Fukui, Y. (2002). Statistical study of C18O dense cloud cores and star formation. *A&A*, 385(3):909–920.

Tafalla, M., Myers, P. C., Caselli, P., and Walmsley, C. M. (2004). On the internal structure of starless cores. I. Physical conditions and the distribution of CO, CS, N2H+, and NH3 in L1498 and L1517B. *A&A*, 416(1):191–212.

Tafalla, M. and Santiago, J. (2004). L1521E: The first starless core with no molecular depletion. *A&A*, 414(3):L53–L56.

Tafalla, M., Santiago-García, J., Myers, P. C., et al. (2006). On the internal structure of starless cores. II. A molecular survey of L1498 and L1517B. *A&A*, 455(2):577–593.

Tan, J. C., Kong, S., Butler, M. J., Caselli, P., and Fontani, F. (2013). The Dynamics of Massive Starless Cores with ALMA. *ApJ*, 779(2):96.

Tauber, J. A., Tielens, A. G. G. M., Meixner, M., and Foldsmith, P. F. (1994). Anatomy of a Photodissociation Region: High angular resolution images of molecular emission in the Orion Bar. *ApJ*, 422:136.

Thaddeus, P. and Turner, B. E. (1975). Confirmation of interstellar N2H+. *ApJ*, 201:L25.

Thi, W.-F., Ménard, F., Meeus, G., et al. (2011). Detection of CH+ emission from the disc around HD 100546. *A&A*, 530:L2.

Tielens, A. G., Meixner, M. M., van der Werf, P. P., et al. (1993). Anatomy of the photodissociation region in the orion bar. *Science (80-.).*, 262(5130):86–9.

Tielens, A. G. G. M. and Hollenbach, D. (1985a). Photodissociation regions. I. Basic model. *ApJ*, 291:722–746.

Tielens, A. G. G. M. and Hollenbach, D. (1985b). Photodissociation Regions II. A Model for the Orion Photodissociation Region. *ApJ*, 291:747–754.

Tilley, D. A. and Pudritz, R. E. (2004). The formation of star clusters - I. Three-dimensional simulations of hydrodynamic turbulence. *MNRAS*, 353(3):769–788.

Troland, T. H. and Crutcher, R. M. (2008). Magnetic Fields in Dark Cloud Cores: Arecibo OH Zeeman Observations. *ApJ*, 680(1):457–465.

Turner, B. E. (1974). U93.174 - A new interstellar line with quadrupole hyperfine splitting. *ApJ*, 193:L83.

Turner, B. E. (1995). The Physics and Chemistry of Translucent Molecular Clouds. IV. HCO+ and N2H+. *ApJ*, 449:635.

van der Tak, F. F. S., Black, J. H., Schöier, F. L., Jansen, D. J., and van Dishoeck, E. F. (2007). A computer program for fast non-LTE analysis of interstellar line spectra. *A&A*, 468(2):627–635.

van der Werf, P. P., Stutzki, J., Sternberg, A., and Krabbe, A. (1996). Structure and chemistry of the Orion bar photon-dominated region. *A&A*.

van Dishoeck, E. F. (2014). Astrochemistry of dust, ice and gas: introduction and overview. *Faraday Discuss.*, 168:9.

van Dishoeck, E. F. and Black, J. H. (1986). Comprehensive models of diffuse interstellar clouds - Physical conditions and molecular abundances. *ApJS*, 62:109.

van Dishoeck, E. F. and Black, J. H. (1987). The abundance of interstellar CO. *Phys. Process. interstellar clouds; Proc. NATO Adv. Study Inst.*, pages 241–274.

van Dishoeck, E. F., Kristensen, L. E., Benz, A. O., et al. (2011). Water in Star-forming Regions with the Herschel Space Observatory (WISH). I. Overview of Key Program and First Results. *PASP*, 123(900):138–170.

Vázquez-Semadeni, E., Banerjee, R., Gómez, G. C., et al. (2011). Molecular cloud evolution - IV. Magnetic fields, ambipolar diffusion and the star formation efficiency. *MNRAS*, 414(3):2511–2527.

Vázquez-Semadeni, E., Kim, J., Shadmehri, M., and Ballesteros-Paredes, J. (2005). The Lifetimes and Evolution of Molecular Cloud Cores. *ApJ*, 618(1):344–359.

Vicente, S., Berné, O., Tielens, A. G. G. M., et al. (2013). Polycyclic Aromatic Hydrocarbon Emission in the Proplyd HST10: What Is the Mechanism Behind Photoevaporation? *ApJ*, 765(2):L38.

Vladilo, G. and Centurion, M. (1990). The interstellar 12CH+/13CH+ ratio towards HD 26676. *A&A*, 240:476–480.

Walmsley, C. M., Flower, D. R., and Pineau des Forêts, G. (2004). Complete depletion in prestellar cores. *A&A*, 418(3):1035–1043.

Walmsley, C. M., Natta, A., Oliva, E., and Testi, L. (2000). The structure of the Orion bar. *A&A*.

Walsh, A. J., Myers, P. C., and Burton, M. G. (2004). Star Formation on the Move? *ApJ*, 614(1):194–202.

Wampfler, S. F., Bruderer, S., Karska, A., et al. (2013). OH far-infrared emission from low- and intermediate-mass protostars surveyed with Herschel -PACS. *A&A*, 552:A56.

Wampfler, S. F., Herczeg, G. J., Bruderer, S., et al. (2010). Herschel observations of the hydroxyl radical (OH) in young stellar objects. *A&A*, 521:L36.

Ward-Thompson, D., André, P., Crutcher, R., et al. (2007). An Observational Perspective of Low-Mass Dense Cores II: Evolution Toward the Initial Mass Function. *Protostars Planets V*.

Ward-Thompson, D., Kirk, J. M., André, P., et al. (2010). A Herschel study of the properties of starless cores in the Polaris Flare dark cloud region using PACS and SPIRE. *A&A*, 518:L92.

Ward-Thompson, D., Scott, P. F., Hills, R. E., and Andre, P. (1994). A Submillimetre Continuum Survey of Pre Protostellar Cores. *MNRAS*, 268.

Weinreb, S., Barrett, A. H., Meeks, M. L., and Henry, J. C. (1963). Radio Observations of OH in the Interstellar Medium. *Nature*, 200(4909):829–831.

White, R. E. (1984). Interstellar Matter Near the Pleiades - Part Two - CH Formation. *ApJ*, 284:695.

Wilson, R. W., Jefferts, K. B., and Penzias, A. A. (1970). Carbon Monoxide in the Orion Nebula. *ApJ*, 161:L43.

Wilson, T. L. (1999). Isotopes in the interstellar medium and circumstellar envelopes. *Reports Prog. Phys.*, 62(2):143–185.

Wolfire, M. G., Tielens, A. G. G. M., and Hollenbach, D. (1990). Physical conditions in photodissociation regions - Application to galactic nuclei. *ApJ*, 358:116.

Wu, Y., Liu, T., Meng, F., et al. (2012). Gas Emissions in Planck Cold Dust Clumps - A Survey of the J = 1-0 Transitions of 12CO, 13CO, AND C18O. *ApJ*, 756(1):76.

Wyrowski, F., Heyminck, S., Güsten, R., and Menten, K. M. (2006). Mid- and high- J CO observations towards ultracompact HII regions. *A&A*, 454(2):L95–L98.

Young Owl, R. C., Meixner, M. M., Wolfire, M., Tielens, A. G. G. M., and Tauber, J. (2000). HCN and HCO + Images of the Orion Bar Photodissociation Region. *ApJ*, 540(2):886–906.

Zanchet, A., Godard, B., Bulut, N., et al. (2013). H2(v = 0,1) + C+(2 P) -> H+CH+ State-to-state Rate Constants for Chemical Pumping Models in Astrophysical Media. *ApJ*, 766(2):80.

Zapata, L. A., Palau, A., Galvan-Madrid, R., et al. (2015). ALMA reveals a candidate hot and compact disc around the O-type protostar IRAS 16547-4247. *MNRAS*, 447(2):1826–1833.

Zinnecker, H. and Yorke, H. W. (2007). Toward Understanding Massive Star Formation *. *ARA&A*, 45(1):481–563.